Universität Rostock
Traditio et Innovatio

Leibniz Institute for Baltic Sea Research Warnemünde
IOW

Influences of surface buoyancy fluxes on circulation and mixing in estuaries

Kumulative Dissertation zur
Erlangung des akademischen Grades
doctor rerum naturalium (Dr. rer. nat.)
der Mathematisch-Naturwissenschaftlichen Fakultät
der Universität Rostock
vorgelegt von

Marvin Lorenz

geboren am 14. April 1993 in Eutin

Rostock, Oktober 2020

https://doi.org/10.18453/rosdok_id00002995

Dieses Werk ist lizenziert unter einer
Creative Commons Namensnennung 4.0 International Lizenz.

Reviewers

1. reviewer:
Prof. Dr. Hans Burchard,
Leibniz-Institut für Ostseeforschung Warnemünde

2. reviewer:
Prof. Dr. Julie Pietrzak, Delft University of Technology

3. reviewer:
Prof. Dr. Rob Hetland, Texas A&M University

Year of submission: 2020
Year of disputation: 2021

An expert is a person who has made all the mistakes that can be made in a very narrow field.

- Niels Bohr

Zusammenfassung

Klassische Ästuare sind Regionen, in denen sich Süßwasser eines Flusses mit salzigem Meerwasser vermischt. Die Austauschströmung eines klassischen Ästuars mit dem Ozean besteht aus einem bodennahen Einstrom von Salzwasser und einem oberflächennahen Ausstrom von gemischten Salz- und Süßwasser. Seit 1900 werden Austauschströmungen von Ästuaren durch Zahlenwerte für den Volumenstrom und den Salzgehalt für Ein- und Ausstrom quantifiziert. Jedoch wurde erst kürzlich eine Relation der Vermischung zur Austauschströmung gefunden. Diese Relation funktioniert sehr gut für klassische Ästuare, die durch den Einstrom von süßem Flusswasser angetrieben werden. Für inverse Ästuare ist diese Relation jedoch nicht anwendbar. In einem inversen Ästuar ist die Zirkulation invertiert, da Süßwasser durch Verdunstung entfernt wird. Die Folge ist ein Einstrom von salzigem Meerwasser nahe der Oberfläche und ein Ausstrom von Wasser mit höherem Salzgehalt als der des Ozeans nahe des Bodens.

Um die Vermischung in inversen Ästuaren zu untersuchen, wird in dieser Dissertation eine Relation für die Vermischung hergeleitet, die Süßwasserflüsse an der Oberfläche in Form von Verdunstung und Niederschlag einschließt. Für inverse Ästuare kann die Vermischung als Differenz von zwei Termen angenähert werden: Der erste Term ist das Produkt aus Salzgehalt des Einstroms, Salzgehalt des Ausstroms und Süßwasserverlust durch Verdunstung. Der zweite Term ist das Produkt von mittlerem Oberflächensalzgehalt zum Quadrat und Süßwasserverlust durch Verdunstung. Um die genannte Relation anzuwenden, werden repräsentative Zahlenwerte für die Austauschströmung benötigt. Das „Total Exchange Flow (TEF) analysis framework“ ist die aktuell beste Methode zur Bestimmung dieser repräsentativen Werte. Diese Dissertation verallgemeinert diese Methode, um numerisch robuste Werte für beliebig komplizierte Austauschströmungen zu erhalten. Zudem wurde diese Methode so erweitert, dass die Temperatur-Salzgehalt Struktur der Austauschströmung untersucht werden kann.

Die entwickelten Methoden und Relationen sind auf ein numerisches Modell eines großen, inversen Ästuars angewendet worden, den Persischen Golf. Die Ergebnisse zeigen, dass die Eigenschaften der Austauschströmung des Persischen Golfes mit dem Indischen Ozean einem saisonalen Zyklus folgen. Dieser ist angetrieben durch die Entstehung von sehr salzigen Persischen Golf Wassers, durch starke Verdunstung im Herbst und frühem Winter. Die Anwendung der Vermischungsrelationen zeigen, dass die Vermischung von Süßwasser durch Flusseinträge, sowie die Vermischung hervorgerufen durch Verdunstung etwa gleich groß sind, obwohl der Süßwasserverlust durch Verdunstung zehn mal größer ist, als der Flusseintrag von Süßwasser.

Abstract

Classical estuaries are regions where the freshwater of a river mixes with saline ocean water. The exchange flow of a classical estuary with the ocean consists of an inflow of saline ocean water near the bottom and an outflow of a mixture of saline water and riverine freshwater near the surface. Since 1900 estuarine exchange flows are quantified by bulk values for inflowing and outflowing volume transport and salinities of the two. Yet, the relation of the interior mixing to the exchange flow has just been recently derived. This relation works very well for classical estuaries, driven by river discharge. But for inverse estuaries, the relation does not work. In inverse estuaries, the circulation pattern is inverse due to evaporation that removes freshwater. This leads to a near-surface inflow of ocean water and a bottom outflow of water with salinities greater than the ocean salinity.

To study the mixing of inverse estuaries, this dissertation derives mixing relations that include surface freshwater fluxes, namely evaporation and precipitation. For inverse estuaries, the mixing can be estimated by the difference of two terms: the first term is the product of inflowing salinity, outflowing salinity, and freshwater loss due to evaporation. The second term is the product of the surface salinity squared and the freshwater loss due to evaporation. For the derived mixing relations, robust and representative bulk values of the exchange flow are needed. The Total Exchange Flow (TEF) analysis framework is the state-of-the-art method to compute these representative bulk values. This dissertation generalizes this method to calculate numerically robust bulk values for multi-layered exchange flows. Furthermore, the TEF analysis framework is extended to analyze the temperature-salinity structure of the exchange flow.

The developed methods and mixing relations are applied to a realistic simulation of a large inverse estuary, the Persian Gulf. The results show that the properties of the exchange flow of the Persian Gulf with the Indian Ocean follow a seasonal cycle, driven by the formation of very saline Persian Gulf Water due to strong evaporation in fall and early winter. The application of the mixing relations shows that the mixing due to river discharge and the mixing due to evaporation is comparable although the freshwater loss due to evaporation is ten times larger than the freshwater input by river discharge.

Contents

Zusammenfassung **v**

Abstract **vii**

Acknowledgements **xi**

Publications **xiii**

Conferences **xv**

1. Introduction **1**
1.1. Classical estuarine circulation 2
1.1.1. Gravitational circulation 2
1.1.2. Other mechanisms influencing the estuarine circulation 3
1.2. Inverse estuarine circulation 4
1.3. Exchange flow 5
1.3.1. Knudsen Relations 6
1.3.2. Total Exchange Flow (TEF) analysis framework 7
1.3.3. Relations between mixing and exchange flow 10
1.4. Numerical setup of the Persian Gulf using GETM 12

2. Key Results **15**
2.1. Numerical issues of the Total Exchange Flow (TEF) analysis framework for quantifying estuarine circulation 15
2.1.1. Two methods, one noise problem 15
2.1.2. A general mathematical formulation for the dividing salinity method 18
2.1.3. Application to a multi-layer case: the Gotland Basin 18
2.2. Numerical Study of the Exchange Flow of the Persian Gulf Using an Extended Total Exchange Flow Analysis Framework 20
2.2.1. TEF in temperature-salinity coordinates 20
2.2.2. Climatological exchange flow of the Persian Gulf 22
2.3. Impact of evaporation and precipitation on estuarine mixing relations . . 27
2.3.1. Inclusion of surface fluxes into existing mixing relations 27
2.3.2. A box model to explain the mixing in an inverse estuary 29
2.3.3. Mixing of the Persian Gulf 31

3. Summary and Conclusions **37**

Bibliography **41**

A. Declaration of my contributions to the publications **49**
A.1. Numerical issues of the Total Exchange Flow (TEF) analysis framework for quantifying estuarine circulation 49
A.2. Numerical Study of the Exchange Flow of the Persian Gulf Using an Extended Total Exchange Flow Analysis Framework 49
A.3. Impact of evaporation and precipitation on estuarine mixing relations . . 50

B. Publications **51**

Acknowledgements

If I told my 23-year old self four years ago that he would submit his dissertation during a global pandemic in 2020, he would have said, 'never'. At least to the first part. Yet, here I am, proudly submitting my dissertation. All of this is the fault of Hans Burchard, meant, of course, in its most positive sense. He showed me that I really enjoy scientific work in physical oceanography during my Master's and could convince me (quite easily) to do a Ph.D. with him. And I have not regretted any second of it. The last three years have been a great adventure. I have learned a lot, have been to many places, have met a lot of great people from all over the world, and of course, did some science. Thank you, Hans, for all of this.

Special thanks to Knut Klingbeil. You are an awesome colleague who taught me a lot. Without your GETM support and great discussions, this dissertation would have not only taken a lot longer but would not be half as good as it is now. I also have to thank Parker MacCready who has been a great collaborator as well. Unfortunately, I have not been able to visit you in Seattle this year, but there will always be a next time, right?

Another reason why time seemed to fly is the great working atmosphere because of the great colleagues I had and still have at IOW. Thanks to my office mates in room 214 and Ph.D. colleagues: Flo, Jen-Ping, Evridiki, Nicky, Jan, Madline, Selina, and Merten. Also, thanks to all the other colleagues who could always help me, either technical or science-related: Peter, Hagen, Martin, Ulf, and Xaver. Thanks to Markus, who gave great input on the readability of this thesis. Also, thank you to all the former and current colleagues: Berit, Lissi, Fatemeh, Claudia, Mahdi, Hadi, Natalia, Manja, Sadegh, Fernanda, Daniel, Lars, Thomas, Markus, and all the others I have forgotten to mention, sorry. Thanks to the whole Baltic Transcoast gang for being awesome.

An dieser Stelle gilt mein besonderer Dank meiner Familie. Ihr wusstet natürlich von Anfang an, dass ich irgendwann mal promovieren werden würde, auch wenn ich das für mich erst spät entdeckt habe. Danke für eure Unterstützung über die letzten Jahre. Egal, was ich in Zukunft auch machen werde, ich weiß, dass ihr immer für mich da sein werdet. Ein ganz besonderer Dank geht an Céline. Danke, dass Du immer für mich da bist!

Achievement unlocked: Ph.D.

Publications

Publications for the cumulative dissertation

Lorenz, M., Klingbeil, K., MacCready, P., and Burchard, H. (2019)
Numerical issues of the Total Exchange Flow (TEF) analysis framework for quantifying estuarine circulation
Ocean Science, 15, 601–614, https://doi.org/10.5194/os-15-601-2019

Lorenz, M., Klingbeil, K., and Burchard, H. (2020)
Numerical study of the exchange flow of the Persian Gulf using an extended Total Exchange Flow analysis framework
Journal of Geophysical Research: Oceans, 125, e2019JC015527. https://doi.org/10.1029/2019JC015527

Lorenz, M., Klingbeil, K., and Burchard, H. (submitted)
Impact of evaporation and precipitation on estuarine mixing relations
Journal of Physical Oceanography

Other peer-reviewed publications

Burchard, H., Gräwe, U., Klingbeil, K., Koganti, N., Lange, X., and **Lorenz, M.** (submitted)
Diahaline diffusivity in estuaries
Journal of Advances in Modeling Earth Systems

MacCready, P., McCabe, R.M., Siedlecki, S.A., **Lorenz, M.**, Giddings, S.N., Bos, J., Albertson, S., Banas, N.S., and Garnier, S. (submitted)
Estuarine Circulation, Mixing, and Resident Times in the Salish Sea
Journal of Geophysical Research: Oceans

Conferences

- Ocean Sciences Meeting, San Diego, California, USA, 2020/02/16 – 2020/02/21, oral presentation: 'Impact of Evaporation on Estuarine Mixing Estimates'
- COMMODORE, Hamburg, Germany, 2020/01/28 – 2020/01/31, poster presentation: 'Quantifying estuarine exchange flows in a thermohaline framework'
- Warnemünde Turbulence Days, Vilm, Germany, 2019/12/09 – 2019/12/12, oral presentation: 'An estuarine mixing relation including inverse estuaries'
- Gordon Research Conference, Manchester, New Hampshire, USA, 2019/06/16 - 2019/06/21, poster presentation: 'Total Exchange Flow (TEF) in temperature-salinity space – Further insights in exchange flows'
- Gordon Research Seminar, Manchester, New Hampshire, USA, 2019/06/15 - 2019/06/16, oral presentation: 'Total Exchange Flow (TEF) in temperature-salinity space – Further insights in exchange flows'
- MMS Days 2019, Kühlungsborn, Germany, 2019/03/20 -2019/03/22, poster presentation: 'Numerical issues of the Total Exchange Flow (TEF) analysis framework for quantifying estuarine circulation'
- Physics of Estuaries and Coastal Seas (PECS), Galveston, Texas, USA, 2018/10/15 – 2018/10/19, oral presentation: 'Variability of the exchange flow of the Persian Gulf'

Chapter 1.

Introduction

Estuaries have recently been named "mixing machines" by Wang et al. (2017) as this is what they tend to do. They transform inflowing ocean water by mixing it with riverine freshwater to an outflowing mixture of both. Or in cases of inverse estuaries, the inflowing ocean water is transformed by removing freshwater through evaporation to outflowing hypersaline water. Studying the mixing processes and quantification methods of mixing in estuaries have been and are the focus of many studies. Different measures for estuarine mixing have been proposed and discussed in the recent past. Currently, the destruction of salinity variance is agreed to be a suitable measure for estuarine mixing. This salt mixing in an estuary has recently been linked to the external river forcing and the estuarine exchange flow by MacCready et al. (2018) and Burchard et al. (2019) by combing the Knudsen relations (Knudsen, 1900) with the salinity variance budget. The key results link the salt mixing to the estuarine exchange flow, that is, volume and salt transports in and out of the estuary. Yet, these studies neglected surface freshwater fluxes in form of precipitation and evaporation that may drive an estuarine circulation as well. The inclusion and understanding of the influence of these surface buoyancy fluxes, especially evaporation, on estuarine salt mixing are the main focus of this dissertation.

On the path to this aim, the Total Exchange Flow (TEF) analysis framework (MacCready, 2011), the state-of-the-art method to study estuarine exchange flows, has been generalized and extended since this method is the basis needed to apply the mixing relations of MacCready et al. (2018) and Burchard et al. (2019). The generalization includes a mathematical formulation that allows a numerically robust computation of the bulk values for arbitrarily complicated exchange flows. The extension allows the decomposition of the exchange flow in potential temperature and salinity coordinates to study water masses involved in the exchange flow in greater detail. All these new methods, quantifying the exchange flow and salt mixing, have been applied to a realistic, hind-cast simulation for the first time. The study object is the Persian Gulf, a large, inverse estuary with a strong, seasonal forcing cycle.

This cumulative dissertation is structured as follows: first, the background is given in this Chapter by presenting basics and the current state of knowledge that are needed to understand estuarine circulation, estuarine mixing, used methods, and the study region of the Persian Gulf. The key results of the three publications are presented in Chapter 2. In Chapter 3 a short summary and conclusions are given.

1.1. Classical estuarine circulation

1.1.1. Gravitational circulation

Estuaries are semi-enclosed regions of a coastal ocean where external buoyancy forcing changes the density of the water in the form that it differs from the adjacent ocean density (Geyer and MacCready, 2014). Buoyancy is defined as the reduced gravitational acceleration due to density differences to a set reference:

$$b = -g\frac{\rho - \rho_0}{\rho_0}, \tag{1.1}$$

where $g = 9.81\,\mathrm{m\,s^{-2}}$ is the gravitational acceleration, ρ is the potential density of the fluid, and $\rho_0 = 1000\,\mathrm{kg\,m^{-3}}$ a reference density. Examples of estuaries are river deltas, fjords, bays, and several others (Valle-Levinson, 2010), often associated with a lot of anthropogenic influences adding a lot of stressors to the estuarine ecosystems. The most common and most studied estuary type in the mid-latitudes is forced by river discharge as the only buoyancy source. The river adds freshwater to the estuary, that is, water of high buoyancy (low density). In the absence of tides, due to the fresh river discharge on one side of the estuary and salty, thus dense and less buoyant, ocean water on the other side, a gravitational circulation establishes. The result is a circulation that consists of an inflow near the bottom of salty ocean water and outflow of brackish water near the surface which is a mixture of the salty ocean and fresh river water, see Fig. 1.1a. This form of a dense inflow at the bottom and a lighter outflow near the surface is referred to as classical estuarine circulation. It can be described by a tidally averaged balance of baroclinic (due to buoyancy) pressure gradients, barotropic (due to sea surface elevation) pressure gradients, and friction (Hansen and Rattray, 1965), see also MacCready and Geyer (2010):

$$\underbrace{-\partial_z\left(\overline{A_v \partial_z u}\right)}_{\text{friction}} = \underbrace{-g\partial_x\overline{\eta}}_{\text{barotropic}}\ \underbrace{-z\,\partial_x\bar{b}}_{\text{baroclinic}}, \tag{1.2}$$

with the eddy viscosity A_v, the horizontal velocity u, the sea surface elevation η, and the depth coordinate z, $-H \leq z \leq \eta$, where H is the maximum water depth. The bar denotes tidal averaging. Note that any quantity can be decomposed into a tidal mean and tidally fluctuating part, that is, $X = \overline{X} + X'$ with $\overline{X'} = 0$. The frictional component strongly depends on the assumptions made for the eddy viscosity A_v. Eddy viscosity is a parameterization for turbulence that relates the mean turbulent fluxes of momentum (Reynolds stresses; covariances of turbulent velocity components), to the mean velocity gradients. It is the analogous property to molecular kinematic viscosity, but for turbulent flows and is typically orders of magnitude larger. To find analytical solutions of eq. (1.2) for the classical estuarine circulation the gradients for buoyancy $\partial_x b$ and sea surface elevation $\partial_x \eta$ are often chosen to be constant. The eddy viscosity A_v can be assumed to be constant as well (Hansen and Rattray, 1965) or to

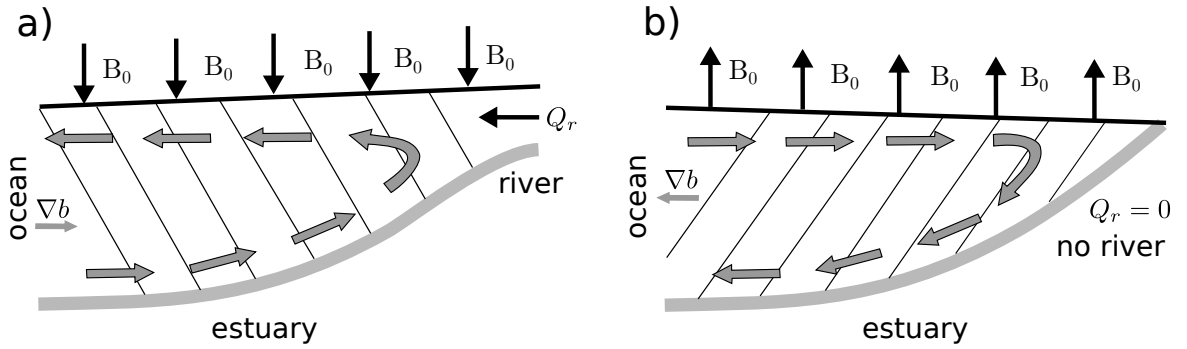

Figure 1.1.: Schematic of classical estuarine circulation in a) and inverse estuarine circulation in b). The ocean is on the left-hand side and the river on the right. The classical estuarine circulation is driven by a landward directed buoyancy gradient ∇b (black lines indicate lines of equal buoyancy) and river discharge Q_r (and/or downward surface buoyancy flux B_0, eq. (1.5)), creating an inflow near the bottom and an outflow near the surface. An inverse estuarine circulation is driven by a positive/upward surface buoyancy flux, decreasing the buoyancy inside the estuary, and therefore reversing the buoyancy gradient ∇b. The result is an inflow near the surface and an outflow near the bottom.

be a depth-dependent function, i.e. parabolic (Burchard and Hetland, 2010). Both solutions give a velocity profile that consists of landward velocities near the bottom and seaward velocities near the surface. In reality, the function of the eddy viscosity is more complicated. In realistic and complex numerical model simulations, the eddy viscosity is computed by a turbulence closure model. The turbulence closure model computes the turbulent kinetic energy (TKE) k and its dissipation rate ϵ which are used to compute the eddy viscosity A_v with

$$A_v = (c_\mu)^4 \frac{k^2}{\epsilon}, \tag{1.3}$$

where c_μ is a non-dimensional stability function that itself depends on shear, stratification, k, and ϵ, see a review by Umlauf and Burchard (2005) for details.

1.1.2. Other mechanisms influencing the estuarine circulation

In the presence of tides, the estuarine circulation is observed to be enhanced compared to the gravitational circulation, e.g. Simpson et al. (1990). This enhancement can be attributed to the eddy viscosity-shear covariance (ESCO) (Dijkstra et al., 2017) during the tidal cycle. The friction term in eq. (1.2) can be separated into a tidal mean part

(denoted by the bar) and a tidally fluctuating part (denoted by the prime):

$$\overline{A_v \partial_z u} = \underbrace{\overline{A_v} \partial_z \overline{u}}_{\text{mean}} + \underbrace{\overline{A_v' \partial_z u'}}_{\text{tidal flucuation}} \quad , \tag{1.4}$$

where the bar describes tidal averaging (Burchard and Hetland, 2010; Stacey et al., 2010). The latter term in eq. (1.4) describes the covariance between tidally varying eddy viscosity and tidally varying shear. Simply speaking: during flood, turbulence, and thus eddy viscosity, is strong since less buoyant water is pushed over buoyant water. Since the stratification is weakened, turbulence is strengthened and landward momentum is transported into the bottom layer enhancing the landward transport. During ebb, turbulence is weakened due to stronger stratification since buoyant water is stratified over dense water. Therefore, less seaward momentum is transferred into the bottom layer compared to flood and more momentum stays in the upper layer. Hence, the residual circulation due to the tidal asymmetries, also called *tidal straining circulation*, is in the same direction as the gravitational circulation, i.e. an inflow near the bottom and an outflow near the surface. Burchard and Hetland (2010) find that the tidal straining circulation can be twice as strong as the gravitational circulation for periodic stratified estuaries.

Despite tides, wind can strengthen or weaken circulation, depending on the direction. Generally speaking: winds blowing landward weaken the circulation, whereas seaward winds strengthen the circulation (Geyer, 1997; Lange and Burchard, 2019). But also winds blowing perpendicular to the estuary may influence the circulation, as upwelling and downwelling change the density of the coastal water and therefore the buoyancy gradient (Giddings and MacCready, 2017). Examples of estuaries with this classical circulation are the Hudson River (Warner et al., 2005; Ralston et al., 2008), the Columbia River (Jay and Smith, 1990; Baptista et al., 2005; MacCready, 2011; Kärnä et al., 2015), or the Elbe (Kappenberg et al., 1995; Burchard et al., 2004). Examples of estuaries, where tides are negligible, yet still showing a classical estuarine circulation flow, are the Warnow estuary (Lange et al., 2020), but also the Baltic Sea (Burchard et al., 2018; Placke et al., 2018).

1.2. Inverse estuarine circulation

In addition to riverine freshwater, further buoyancy forcing may come in form of precipitation and/or evaporation, as well as surface heat exchanges with the atmosphere. The upward surface buoyancy flux B_0 can be written as

$$B_0 = \frac{g\alpha}{c_p \rho} Q_{\text{net}} + g\beta s_{\text{surf}}(E - P), \tag{1.5}$$

with α the thermal expansion coefficient of seawater, c_p the specific heat capacity of seawater, Q_{net} the net heat flux (the sum of solar radiation, long-wave radiation,

sensible heat flux, and latent heat flux; negative when heat is taken up), β the haline contraction coefficient, s_{surf} the surface salinity of the ocean, E the evaporation rate, and P the precipitation rate (Cronin and Sprintall, 2009). A negative (downward) surface buoyancy flux (into the estuary), i.e. due to surface heating or precipitation, makes the water more buoyant (less dense), whereas a positive (upward) flux (out of the estuary), i.e. due to surface cooling and/or evaporation, makes the water less buoyant (denser). Evaporation and precipitation directly modify the surface buoyancy (latter term in eq. (1.5)). On the other hand, the short wave radiation is not fully absorbed at the surface, but penetrates the water column. It is gradually absorbed and converted into heat with depth, strongly depending on the turbidity of the water (Jerlov, 1976).

For a semi-enclosed bay with no river discharge, but strong evaporation, the water inside the bay becomes denser than the adjacent ocean water since the removal of fresh-water creates more saline water, so-called hypersaline water. Besides, the evaporation process causes a latent heat loss, i.e. a decrease in temperature. Both effects cause a positive buoyancy flux and increase the density inside the bay. As a result, the baroclinic pressure gradient changes its sign compared to the classical estuary described before, see Fig. 1.1b. Similarly, the sign of the opposing sea surface elevation gradient changes, due to the removal of water. The resulting circulation pattern changes its direction to a seaward bottom outflow of very dense water and an opposing inflow of ocean water near the surface, see Fig. 1.1b. This circulation pattern is often called *inverse estuarine circulation*. Estuaries that show this circulation pattern are therefore often referred to as inverse or negative estuaries. Examples of estuarine systems showing an inverse circulation are Shark Bay (Nahas et al., 2005; Hetzel et al., 2018), the Persian Gulf (Reynolds, 1993; Kämpf and Sadrinasab, 2006), and the Mediterranean Sea (Candela, 1991; Pinardi and Masetti, 2000).

1.3. Exchange flow

For a fixed transect, separating the estuary from the ocean, typically at the river mouth or bay entrance, the quantification of estuarine circulation through that cross-section is referred to as an exchange flow. The quantities that are mostly used to describe the exchange flow are volume transport of the inflow and outflow plus representative salinities of the two. Further quantities are temperatures and densities of the exchange flow. The exchange flow almost entirely controls the salt content of the estuary since river discharge, precipitation, and evaporation only add or remove negligible amounts of salt compared to the total salt of the system. In contrast, the temperature inside the estuary is primarily controlled by the heat exchange with the atmosphere, for example, solar radiation is heating the water whereas evaporation is cooling it.

1.3.1. Knudsen Relations

The earliest and simplest, yet very useful quantification of the exchange flow has been proposed by Knudsen (1900). By considering the volume and salt budget of the estuary, he was able to link the volume exchange to the salinities of the respective inflow and outflow, and the freshwater forcing. The volume of an estuary may change due to river discharge, precipitation, evaporation, and the net transport of the exchange flow. The salt content of an estuary is considered to only change if the net transport of salt is not zero. Therefore, the time-averaged volume budget and salt budget can be written as

$$\delta V \equiv \langle \partial_t V \rangle = Q_{\text{in}} + Q_{\text{out}} + Q_{\text{surf}} + Q_r, \tag{1.6}$$

$$\delta S \equiv \left\langle \partial_t \int_V s \, \mathrm{d}V \right\rangle = Q_{\text{in}} s_{\text{in}} + Q_{\text{out}} s_{\text{out}}, \tag{1.7}$$

with brackets denoting temporal averaging, V being the volume of the estuary, $Q_{\text{in}} \geq 0$ the inflowing volume transport, $Q_{\text{out}} \leq 0$ the outflowing volume transport, Q_{surf} being the sum of freshwater input from precipitation and freshwater loss due to evaporation, and Q_r the river discharge of zero salinity. s_{in} and s_{out} denote the representative salinities of the inflow and outflow. These equations describe a two-layer box model as depicted in Fig. 1.2. Combining eq. (1.6) and (1.7) leads to the following relations

$$Q_{\text{in}} = \frac{s_{\text{out}}}{s_{\text{in}} - s_{\text{out}}} \left(Q_r - \delta V + Q_{\text{surf}} \right) + \frac{1}{s_{\text{in}} - s_{\text{out}}} \delta S, \tag{1.8}$$

$$Q_{\text{out}} = \frac{s_{\text{in}}}{s_{\text{in}} - s_{\text{out}}} \left(\delta V - Q_r - Q_{\text{surf}} \right) - \frac{1}{s_{\text{in}} - s_{\text{out}}} \delta S, \tag{1.9}$$

that link exchange flow to external freshwater forcing and known representative salinities. For a stationary estuary, i.e. $\delta V = \delta S = 0$ and no surface freshwater exchange, $Q_{\text{surf}} = 0$, the relations simplify to the well-known Knudsen relations (Knudsen, 1900):

$$Q_{\text{in}} = \frac{s_{\text{out}}}{s_{\text{in}} - s_{\text{out}}} Q_r, \tag{1.10}$$

$$Q_{\text{out}} = -\frac{s_{\text{in}}}{s_{\text{in}} - s_{\text{out}}} Q_r. \tag{1.11}$$

These *Knudsen relations* relate the exchange flow to the freshwater forcing with known salinities of the inflow and outflow. The main advantage of this approach is that one can describe the whole exchange flow in terms of simple bulk values which represent the exchange flow as a result of complex dynamics. Applying the relations to the Baltic Sea in the year 1900, Knudsen (1900) was the first to quantify an exchange flow, see also Burchard et al. (2018) for a translation of the original paper of Knudsen (1900).

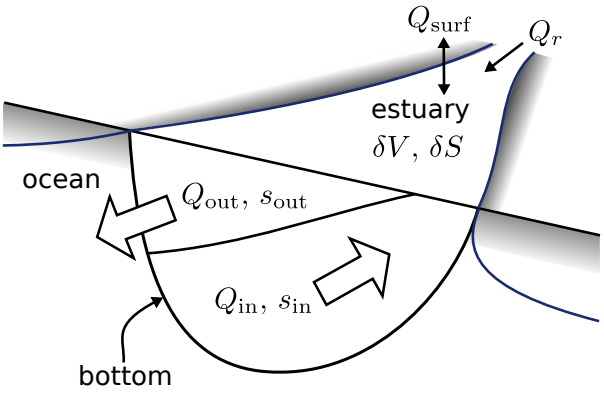

Figure 1.2.: Schematic depiction of the two-layer exchange flow of an estuary through a cross-section in terms of bulk values. The mean temporal change of the estuarine volume δV is the sum of volume transports in and out the estuary: i) inflow of river discharge Q_r, ii) the sum of precipitation and evaporation Q_{surf}, iii) inflowing volume transport Q_{in}, and iv) outflowing volume transport Q_{out}, see also eq. (1.6). The temporal mean change of salt in the estuary δS may only change due to the inflowing salt transport $Q_{\mathrm{in}}\, s_{\mathrm{in}}$ and the outflowing salt transport $Q_{\mathrm{out}}\, s_{\mathrm{out}}$, see also eq. (1.7).

1.3.2. Total Exchange Flow (TEF) analysis framework

The main challenge in applying the Knudsen relation is to find the correct values of s_{in} and s_{out} which should be representative of the exchange flow. To determine the most representative bulk values, the Total Exchange Flow (TEF) analysis framework was introduced by MacCready (2011) combining a continuous isohaline framework (Walin, 1977, 1982) and the bulk concept of Knudsen (1900). It analyzes the exchange flow in salinity coordinates rather than spatial coordinates since the dynamics of most estuaries are controlled by the salt distribution (Walin, 1977). Furthermore, the salt budget is entirely controlled by the exchange flow. It has been shown that this framework is necessary to correctly include the full salinity range during a tidal cycle into the bulk values since the temporal averaging is carried out in salinity coordinates (MacCready, 2011; Chen et al., 2012). Spatial (Eulerian) averaging over a tidal cycle on the other hand does not capture the highest/lowest salinities occurring during a tidal cycle and gives therefore different bulk values, see MacCready (2011) for a comparison.

Along a fixed transect, the time-averaged tracer transport $Q^c(S)$ through a cross-section $A(S)$ is defined as

$$Q^c(S) = -\left\langle \int_{A(S)} f^c \,\mathrm{d}A \right\rangle, \tag{1.12}$$

with

$$f^c = u_n c - K_h \partial_n c, \tag{1.13}$$

being the total tracer flux as the sum of advective ($u_n c$) and diffusive fluxes ($-K_h \partial_n c$, K_h is the horizontal diffusivity of tracer c) normal to the transect. $A(S)$ denotes the area where the salinity s is higher than the salinity class S, see the blue area in Fig. 1.3. Diffusion has just been recently added to the problem by Burchard et al. (2019). Before, only advection has been considered. The derivative with respect to S yields the tracer transport per salinity class:

$$q^c(S) = -\frac{\partial Q^c(S)}{\partial S}, \tag{1.14}$$

where the minus sign is necessary for the convention that positive values are part of the inflow into the estuary and negative values part of the outflow. The relation between Q^c and q^c as well as how the sorting works are schematically illustrated in Fig. 1.3 for a discrete example. The volume transport per salinity class $q^1 \equiv q$ is often called a *TEF-profile*, as it shows in which salinity classes the exchange flow occurs. This profile is the major advance to the two-layer Knudsen box model as it precisely shows in which salinity ranges the inflow and outflow are occurring. From the q^c profile, bulk values $Q^c_{\text{in}} \geq 0$ and $Q^c_{\text{out}} \leq 0$ can be obtained by the integration of the positive and negative parts of q^c, respectively:

$$Q^c_{\text{in}} = \int_0^{S_{\max}} (q^c)^+ \,\mathrm{d}S, \quad Q^c_{\text{out}} = \int_0^{S_{\max}} (q^c)^- \,\mathrm{d}S, \tag{1.15}$$

where the positive (negative) part of any function a is calculated as $(a)^+ = \max(0, a)$ ($(a)^- = \min(a, 0)$), see also the right panel of Fig. 1.3. Bulk tracer concentrations for inflow and outflow are obtained by the fraction of tracer transport and volume transport:

$$c_{\text{in}} = \frac{Q^c_{\text{in}}}{Q_{\text{in}}}, \quad c_{\text{out}} = \frac{Q^c_{\text{out}}}{Q_{\text{out}}}. \tag{1.16}$$

These bulk values have been shown to be representative of the exchange flow (MacCready, 2011). The TEF analysis framework has been applied to several estuaries since the introduction in 2011, e.g. MacCready (2011); Chen et al. (2012); Lemagie and Lerczak (2015); Wang et al. (2017); Burchard et al. (2018). When doing the TEF analysis for a numerical model, one has to define a discrete salinity axis, see also the schematic in Fig. 1.3. Lemagie and Lerczak (2015) noted that the TEF profile becomes noisy when choosing a too high number of salinity classes. In their study, increasing the number of salinity classes led to larger bulk values than before when a smaller number of salinity classes have been used. This brings up the question, which bulk values are correct. MacCready et al. (2018) noted in their Appendix that they used a dividing salinity by evaluating the maximum of $Q(S)$ to solve the noise problem, $Q_{\text{in}} = \max(Q)$, and therefore $Q_{\text{out}} = Q(0) - Q_{\text{in}}$. This method guarantees to give the

same bulk values, independently of the chosen number of salinity classes. The noise issue and diverging bulk values due to this noise motivated the first publication of this cumulative thesis. In Section 2.1 details of the numerical behavior of the bulk value computation is investigated and a general formulation of the method of MacCready et al. (2018) is presented. This general formulation includes inverse estuaries and allows evaluating TEF-profiles with more than two layers (in salinity coordinates). TEF so far uses salinity coordinates, but temperature is another contributor to the buoyancy. To explicitly consider temperature as well as salinity, a two-dimensional TEF analysis framework, using both salinity and temperature coordinates, is presented in the second publication in Section 2.2, where this framework is used to study the exchange flow of the Persian Gulf. Decomposing the exchange flow in thermohaline coordinates connects the TEF analysis framework to the water mass transformation framework (Hieronymus et al., 2014; Groeskamp et al., 2019) which is widely used for the world oceans.

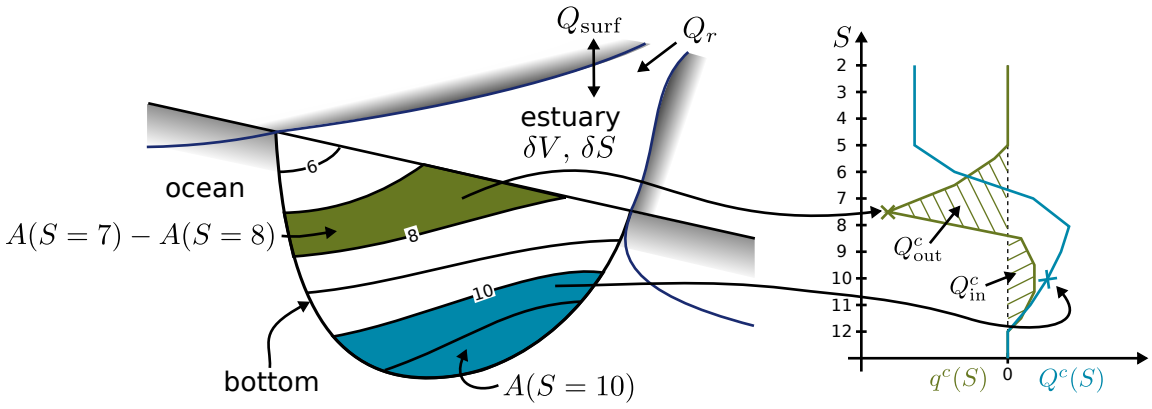

Figure 1.3.: Schematic depicting of how the TEF sorting of tracer transports through a cross-section is carried out according to the salinity distribution. In the left panel the same schematic is shown as in Fig. 1.2 but this time the cross-section shows a schematic salinity distribution with isohalines from $s = 6 - 11$ g/kg. In this example, the salinity axis for the TEF analysis is discretized in salinity classes of size $\Delta S = 1$ g/kg, see y-axis in the right panel. According to eq. (1.12), the area $A(S = 10)$ is the cross-section where $s > 10$ g/kg (shaded in blue). The integrated tracer transport through this cross-section is put into the corresponding salt class of $S = 10$ g/kg, see right panel blue cross. Eq. (1.14) states that q^c is the derivative of $Q^c(S)$, i.e. in this discrete case q^c is defined on the interfaces between two salinity classes, i.e. $(n + 0.5)\Delta S$, $n = 0, 1, 2, ...$ This is equal to the transport in an area between two isohalines divided by ΔS, e.g. between $S = 7$ and $S = 8$ g/kg (green area): $q^c(S = 7.5) = -\frac{Q^c(S=8)-Q^c(S=7)}{\Delta S}$, green cross in the right panel. This is done for all salinity classes and yields the profiles of q^c (green) and Q^c (blue) in the right panel. Q^c_{in} and Q^c_{out} can be obtained from $q^c(S)$ by integration over the positive and negative parts, see right panel and eq. (1.15). c_{in} and c_{out} are be obtained by the fraction of tracer transport to volume transport, see eq. (1.16).

1.3.3. Relations between mixing and exchange flow

Mixing in estuaries is often associated with eddy viscosity or diffusivity (Fischer, 1976; Basdurak et al., 2017). As mentioned in Section 1.1.1, the estuarine circulation does depend on the eddy viscosity, but also the length of the salt intrusion into the estuary depends on the eddy viscosity (Hetland and Geyer, 2004). Yet, it is not a suitable measure for estuarine mixing since in a well-mixed estuary, the salinity distribution is homogeneous, resulting in low salinity mixing, despite the highest eddy viscosity values. Therefore, a more suitable measure for estuarine mixing has been found to be the dissipation of salinity variance χ^s,

$$\chi^s = 2\left[K_h(\partial_x s)^2 + K_h(\partial_y s)^2 + K_v(\partial_z s)^2\right], \tag{1.17}$$

with K_h and K_v denoting the turbulent horizontal and vertical salinity diffusivities, see also Burchard and Rennau (2008). The dissipation of tracer variance, here salinity, is a widely used quantity in the ocean turbulence community, e.g. Nash and Moum (2002). For steady-state, homogeneous turbulence, χ^s equals the dissipation on molecular level, showing that χ^s is indeed a good measure for mixing.

Recently, MacCready et al. (2018) could link the volume integrated salinity mixing M inside an estuary to the Knudsen relations:

$$M \approx s_{\text{in}} s_{\text{out}} Q_r. \tag{1.18}$$

This simple, yet good approximation states that the total mixing inside the estuary is the product of the salinity of the inflow, salinity of the outflow, and river discharge, where the salinities have been computed with the TEF analysis framework, see Section 1.3.2. To illustrate this relation, let's revisit the Knudsen box model in Fig. 1.2. Similar to the budgets in eqs. (1.6) and (1.7) a budget for the salinity square can be evaluated:

$$\delta S^2 \equiv \left\langle \partial_t \int_V s^2 \,\mathrm{d}V \right\rangle = Q_{\text{in}} s_{\text{in}}^2 + Q_{\text{out}} s_{\text{out}}^2 = s_{\text{in}} s_{\text{out}} Q_r. \tag{1.19}$$

Eq. (1.19) shows that through the exchange flow the salinity square inside the estuary would constantly increase by $s_{\text{in}} s_{\text{out}} Q_r$. But as this system should be in steady-state, the salinity square must not change, showing that there is an internal sink term missing in eq. (1.19) that compensates the salinity square input through the exchange flow. This sink term is the volume integrated mixing of the estuary, $M = s_{\text{in}} s_{\text{out}} Q_r$, eq. (1.18), see also Burchard et al. (2019) for a detailed Knudsen box model.

Burchard et al. (2019) show that eq. (1.18) is an approximation of the exact relation between mixing, the exchange flow, and river discharge. They derive the volume, salinity, salinity squared, and salinity variance budgets and rephrase them in terms of bulk values. The budgets read for volume as:

$$\delta V = \langle \partial_t V \rangle = Q_{\text{in}} + Q_{\text{out}} + Q_r, \tag{1.20}$$

for salinity as:

$$\delta S = \left\langle \partial_t \int_V s \, \mathrm{d}V \right\rangle = Q_{\text{in}} s_{\text{in}} + Q_{\text{out}} s_{\text{out}} \tag{1.21}$$

for salinity square as:

$$\delta S^2 = \left\langle \partial_t \int_V s^2 \, \mathrm{d}V \right\rangle = Q_{\text{in}} \left(s^2\right)_{\text{in}} + Q_{\text{out}} \left(s^2\right)_{\text{out}} - M, \tag{1.22}$$

and for salinity variance, $s'^2 = (s - \bar{s})^2$ as:

$$\delta S'^2 = \left\langle \partial_t \int_V s'^2 \, \mathrm{d}V \right\rangle = Q_{\text{in}} \left(s'\right)^2_{\text{in}} + Q_{\text{out}} \left(s'\right)^2_{\text{out}} + \left\langle \bar{s}^2 \int_{A_r} u_n \, \mathrm{d}A \right\rangle - M, \tag{1.23}$$

with $\bar{s} = \frac{1}{V} \int_V s \, \mathrm{d}V$ being the average salinity of the estuary and the volume integrated, time-averaged salinity mixing M,

$$M = \left\langle \int_V \chi^s \, \mathrm{d}V \right\rangle \geq 0. \tag{1.24}$$

The bulk values $(s^2)_{\text{in}}$, $(s^2)_{\text{out}}$, $\left(s'\right)^2_{\text{in}}$, and $\left(s'\right)^2_{\text{out}}$ are computed similar to s_{in} and s_{out} by eq. (1.16).

The rephrasing in terms of bulk values allows relating the M to the external forcing, similarly to the Knudsen relations. Indeed, eqs. (1.20) and (1.21) lead to the relations in eq. (1.8) and (1.9) without surface freshwater fluxes which are neglected by both MacCready et al. (2018) and Burchard et al. (2019). M occurs in both the salt squared and the salt variance equation. Yet, the application of the variance equation requires knowledge of the temporal evolution of the mean salinity, an internal quantity, and the covariance of mean salinity and river discharge (the second term from the left in eq. (1.23)). The salinity square equation on the other hand is easier to apply as it only depends on external quantities. Therefore, eqs. (1.20)-(1.22) are combined below. The combination yields an exact mixing relation M_e, connecting the Knudsen bulk values with the volume integrated salt mixing as presented in Burchard et al. (2019):

$$M_e = \frac{s_{\text{out}}(s^2)_{\text{in}} - s_{\text{in}}(s^2)_{\text{out}}}{s_{\text{in}} - s_{\text{out}}} \left(Q_r - \delta V\right) + \frac{(s^2)_{\text{in}} - (s^2)_{\text{out}}}{s_{\text{in}} - s_{\text{out}}} \delta S - \delta S^2. \tag{1.25}$$

This very complex relation may be simplified by different assumptions and approximations. Assuming constancy, i.e. the time-average of the squared property is the same as the time-averaged quantity squared, here $(s^2)_{\text{in}} = (s_{\text{in}})^2$, $(s^2)_{\text{out}} = (s_{\text{out}})^2$, eq. (1.25) simplifies to

$$M_c = s_{\text{in}} s_{\text{sout}} \left(Q_r - \delta V\right) + \left(s_{\text{in}} - s_{\text{out}}\right) \delta S - \delta S^2. \tag{1.26}$$

For long-term averaging or periodicity, i.e. a tidally periodic estuary, the storage terms are approximately zero. Under these conditions, eq. (1.25) yields

$$M_p = \frac{s_{\text{out}}(s^2)_{\text{in}} - s_{\text{in}}(s^2)_{\text{out}}}{s_{\text{in}} - s_{\text{out}}} Q_r. \tag{1.27}$$

Considering both assumptions/approximations at the same time, eq. (1.25) reads as

$$M_{cp} = s_{\text{in}} s_{\text{out}} Q_r, \tag{1.28}$$

which is the key result of MacCready et al. (2018), as already presented before in eq. (1.18). Burchard et al. (2019) showed that for their idealized model simulations the relation of MacCready et al. (2018), eq. (1.28), approximates the exact mixing with a maximal error of only 10%. Since surface freshwater fluxes are neglected, the application of these mixing relations is not possible to a lot of estuaries. The question of how the exchange flow of an inverse estuary relates to its freshwater loss due to evaporation motivated the third publication of this dissertation, see Section 2.3. Simply replacing Q_r with a freshwater loss due to evaporation would result in $M \leq 0$ which is violating the strictly positive definition of M. The solution to this problem will be shown to be an additional salinity square flux due to evaporation that ensures a positive M as it will be shown in Section 2.3.

1.4. Numerical setup of the Persian Gulf using GETM

The Persian Gulf is chosen as the study site since it shows an inverse estuarine circulation driven by strong evaporation and has a large temperature range. Both make it an ideal candidate to employ the thermohaline TEF analysis framework and the salt mixing relations when surface freshwater fluxes are included. The Persian Gulf is a shallow (mean depth of $39\,$m), semi-enclosed marginal sea that is connected to the Gulf of Oman and the Indian Ocean via the Strait of Hormuz, see Fig. 1.4. Inside the Gulf evaporation rates up to 2 m/a (Privett, 1959; Ahmad and Sultan, 1991) dominate the freshwater budget, creating hyper-saline Persian Gulf Water (PGW), leaving the Persian Gulf as a bottom current. To replace the outflowing and evaporating water, an inflow of Indian Ocean Surface Water (IOSW) occurs. The PGW stratifies into the Gulf of Oman in around $250\,$m depth and propagates in form of mesoscale and sub-mesoscale eddies (Vic et al., 2015; Morvan et al., 2019). PGW T-S-signatures can be found for example in the Bay of Bengal (Jain et al., 2017) and also in front of Australia (Woo and Pattiaratchi, 2008). Measurements show that the outflow is relatively steady in time with small variabilities of scales between two and three weeks (Johns et al., 2003; Swift and Bower, 2003; Pous et al., 2004). Besides, pulses of high salinities are observed (Johns et al., 2003) which are explained by propagating mesoscale eddies transporting saline water through the Strait of Hormuz (Thoppil and Hogan, 2009).

The Persian Gulf is affected by the seasonal cycle of solar radiation and by seasonal atmospheric phenomena. The Shamal describes strong wind events all year long with the strongest south-westerly winds in late fall and winter, so-called winter Shamal, bringing dry air to the Gulf region (Reynolds, 1993; Thoppil and Hogan, 2010). This seasonal cycle of the forcing affects the stratification: in winter, the Gulf is almost everywhere in a well-mixed state (Reynolds, 1993); in summer, the Gulf is stably stratified due to surface heating and IOSW entering the Gulf (Reynolds, 1993). Lowest temperatures can be as cold as $18°$C to warmest temperatures $> 35°$C (Reynolds, 1993; Alessi et al., 1999). The stratification is destroyed in late summer and fall through increased vertical mixing due to stronger winds, higher evaporation, and heat loss (Yao and Johns, 2010a). Several model studies reproduced this seasonal cycle of stratification well and also indicate a seasonal dependency of the exchange flow with higher exchange flows in spring and summer than fall and winter (Kämpf and Sadrinasab, 2006; Yao and Johns, 2010b; Pous et al., 2015). Yet, all these model studies show different results and use different methods to quantify the exchange flow. Kämpf and Sadrinasab (2006) find a stronger exchange in spring (0.17 Sv (1 Sv$=10^6$ m^3 s^{-1})) than in fall (0.11 Sv). Yao and Johns (2010b) show monthly mean values for volume outflow that is larger in summer than in winter. Furthermore, they describe the spatial salinity, temperature, and velocity structure in the Strait of Hormuz in great detail. Pous et al. (2015) show annual mean values for five years for the volume transports of the inflow and outflow as well as a time series of inflow and outflow velocities and salinities in the Strait of Hormuz. These time series are taken at a certain position at a transect and no integrated/mean quantities of the exchange flow. Still, it shows larger outflowing velocities in winter/spring than summer/winter. It further shows that the outflowing salinity varies from $39-41$ g/kg in those five years. Yet, none of these studies provide a comprehensive analysis of the exchange flow in terms of Knudsen relations or the thermohaline structure of volume transports. Therefore, a great part of this dissertation focuses on a detailed analysis of the exchange flow utilizing the benefits of the TEF analysis framework, see Chapter 2.2. Furthermore, the salt mixing of the Gulf is analyzed using newly derived mixing relations that include surface freshwater fluxes in Chapter 2.3.

To have a model to apply the analysis to, a setup of the Persian Gulf has been created for the General Estuarine Transport Model (GETM, Burchard and Bolding, 2002). GETM is a three-dimensional coastal ocean model (Klingbeil et al., 2018), solving the hydrostatic Boussinesq equations. The turbulence closure is done using an eddy-viscosity approach with the k-ϵ-closure (Rodi, 1987; Burchard and Baumert, 1995). To do so, the turbulence library of the General Ocean Turbulence Model (GOTM, Burchard et al., 1999) is coupled to GETM. Vertically adaptive coordinates that minimize the numerical errors of the advection scheme are the unique feature of GETM (Hofmeister et al., 2010, 2011; Gräwe et al., 2015). By increasing the vertical resolution where stratification is highest, spurious numerical mixing is reduced. For further information on both the model and the setup validation, I refer to Lorenz et al. (2020).

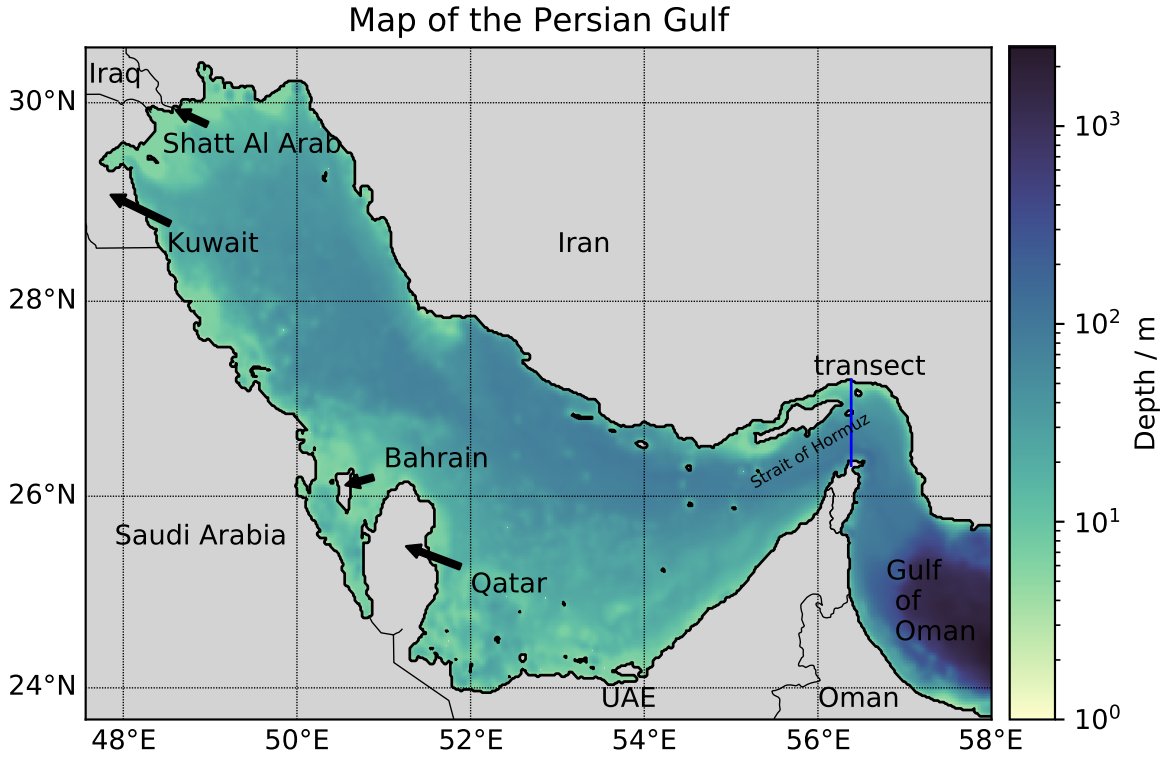

Figure 1.4.: Bathymetry and used model domain of the Gulf: the shallow north-west and southern regions are bounded by a trench in the north, which is deepening towards the Strait of Hormuz. Outside the Strait of Hormuz, the depth is increasing to $\sim 2000\,\mathrm{m}$ (note the non-uniform color scale). The blue line denotes the transect across which the exchange flow is analyzed. Source: Lorenz et al. (submitted).

Chapter 2.

Key Results

2.1. Numerical issues of the Total Exchange Flow (TEF) analysis framework for quantifying estuarine circulation

2.1.1. Two methods, one noise problem

The original method of MacCready (2011) to compute the bulk values of a TEF-profile relies on the separation of positive and negative parts of $q(S)$, see Section 1.3.2, eq. (1.15), and Fig. 1.3. This method is therefore called *sign method*. As briefly described before, Lemagie and Lerczak (2015) recognize in their study that the bulk values were sensitive to the chosen number of salinity classes. A TEF-profile may become noisy when choosing the number of discrete salinity classes too high. The noise may lead to many zero crossings and the bulk values are changing significantly. This leads to the question which bulk values are the correct ones or which number of salinity classes is optimal. A solution described by MacCready et al. (2018) considers the maximum of $Q(S)$ which corresponds to Q_{in} for a classical exchange flow ($s_{\text{in}} > s_{\text{out}}$). The salinity corresponding to the maximum divides the inflow and outflow as it corresponds to the zero-crossing of q and is therefore called dividing salinity which also gave the name for the method, *dividing salinity method*. The outflow can then be computed by considering all contributions below the dividing salinity. This method promises to be numerically converging towards the correct bulk values with an increasing number of salinity classes as shown below.

To study the convergence behavior of both methods and to illustrate the noise problem, an analytical example of a well-mixed tidal flow with oscillating salinity is considered, see also Burchard et al. (2019):

$$u(t) = u_r + u_a \cos(\omega t), \quad s(t) = s_r + s_a \cos(\omega t + \phi), \tag{2.1}$$

where $u_r < 0$ denotes the residual velocity, s_r the residual salinity, $u_a > 0$ the velocity amplitude, $s_r > 0$ the salinity amplitude, ω the tidal frequency, with $\omega = 2\pi/T$ with

T being the tidal period, and the tidal phase ϕ. As no diffusion is considered in this example, $f^c = c\,u$ in eq. (1.13). With this, $Q(S)$ and $Q^s(S)$ can be computed analytically and, therefore, also the bulk values, see the Appendix A of Lorenz et al. (2019) for details as well as Fig. 2.1d. With $A = 10000$ m^2, $u_r = -0.1$ m s^{-1}, $u_a = 1$ m s^{-1}, $s_r = 20$ g/kg and $s_a = 10$ g/kg, and $\phi = -1.16 = -0.185 \cdot 2\pi$, the inflow and outflow volume fluxes and salinities, Q_{in}, Q_{out}, s_{in}, and s_{out}, can then be calculated: $Q_{\text{in}} = 813.240$ m^{3}s^{-1}, $Q_{\text{out}} = -1813.240$ m^{3}s^{-1}, $s_{\text{in}} = 28.424$ g/kg, and $s_{\text{out}} = 12.748$ g/kg.

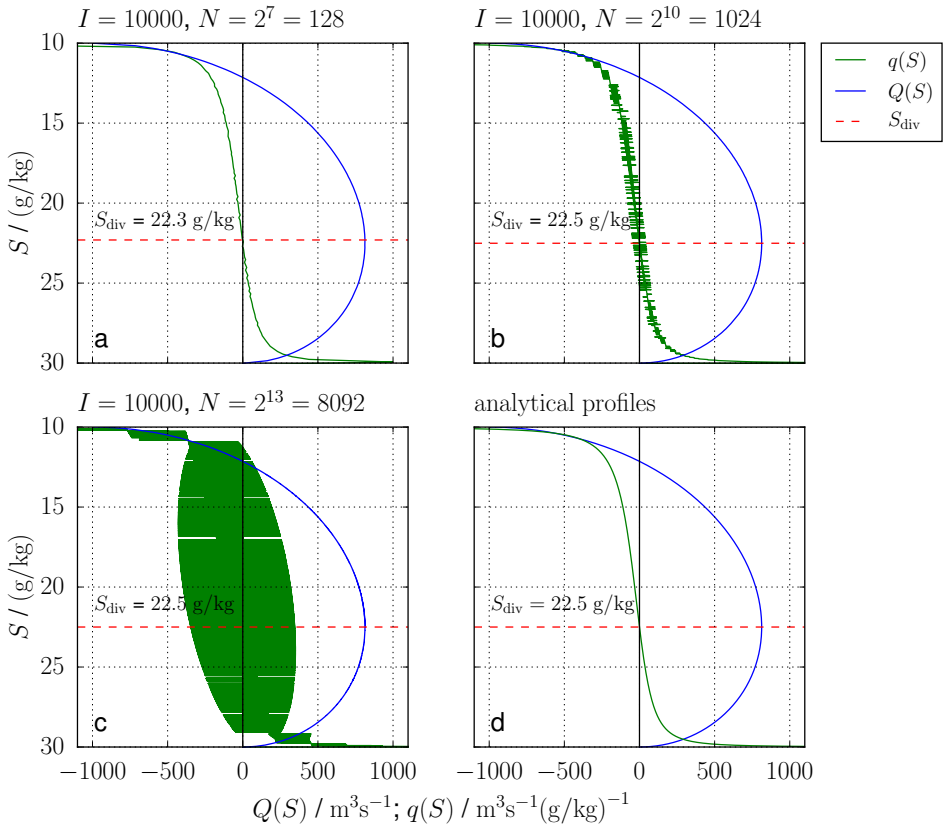

Figure 2.1.: Numerically, a)-c), and analytically, d), computed $Q(S)$ (blue), $q(S)$ (green) for the well-mixed tidal exchange flow, see eq. (2.1), for $I = 10^4$ time steps for one tidal cycle and varying number of salinity classes N. The computed dividing salinity, S_{div} is shown in dashed, red. With increasing N, q becomes more noisy, whereas Q seems unchanged. Source: Lorenz et al. (2019).

To compare the errors of the two methods, eqs. (2.1) are discretized for one tidal cycle with $I = 10,000$ time steps. For a varying number of salinity classes N between $S_{\text{min}} = 10$ g/kg and $S_{\text{max}} = 31$ g/kg, $q(S)$ and $Q(S)$ show different noise levels, see Fig. 2.1a-c. For a small number of salinity classes, Fig. 2.1a, both q and Q are very close to the analytical solution, Fig. 2.1d. Increasing the number of salinity classes, Fig. 2.1b, q becomes noisy, yet Q is closer to the analytical solution as the dividing salinity S_{div} now equals the analytical value of 22.5 g/kg. A further increase of the number of salinity classes, Fig. 2.1c, yields an even noisier q, which strongly deviates from the analytical solution, and by eye, one can see that separation by sign does not make much

sense anymore. Due to the discretization of the data, pairs of transport that would compensate each other in reality, i.e. one positive value and one negative value of equal salinity, could be put into different salinity classes because of the discretization. If the salinity class size is very small, this happens more often and the compensation that occurs analytically for each salinity class does not occur in the discrete profile. Fig. 2.1c shows this very clearly. This issue is true for both the discretization of analytical data and the output of a numerical model.

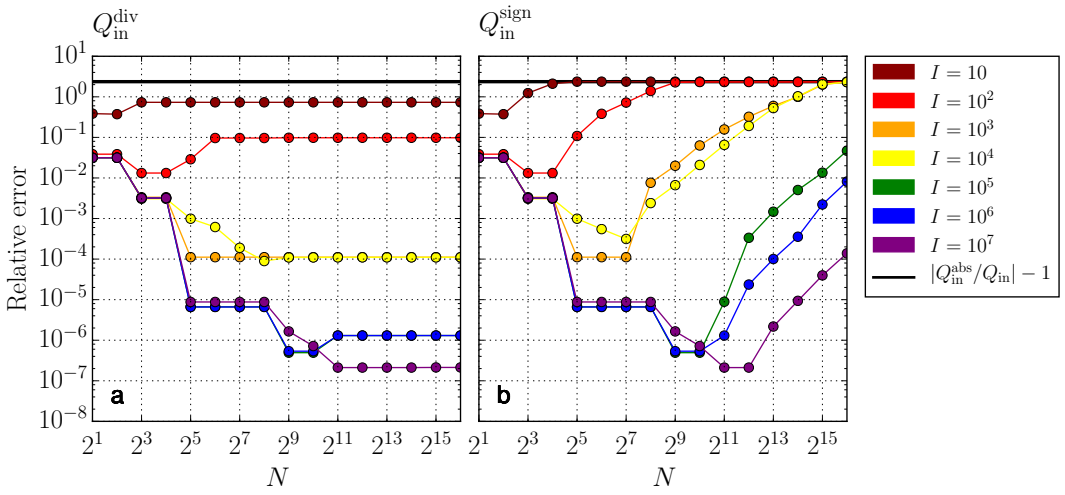

Figure 2.2.: The relative error of Q_{in} computed with a) the dividing salinity method and b) the sign method in dependency of the number of time steps I (color) and salinity classes N (x-axis). The error of the sign method converges in the limit of large N towards the error of the absolute bulk values (black line, (2.2)). In contrast, the error of the dividing salinity method converges towards a constant small value. The errors of both methods decrease with an increasing number of time steps I. Source: Lorenz et al. (2019).

The noise from the TEF-profiles translates into the computed bulk values. By increasing the number of salinity classes, the error of the sign method first decreases before converging against a value of maximum error, see Fig. 2.2b, where the convergence behavior of the sign method is shown for Q_{in}. This convergence is always the case, independent of the number of data points. The sign method converges against

$$Q_{\text{in}}^{\text{abs}} = \left\langle \int_A u^{+} \mathrm{d}A \right\rangle, \tag{2.2}$$

which describes the temporal average of all inflowing velocities during the averaging period, here one tidal cycle T. This is not the desired result as it does not account for partial compensation in the salinity classes, which is the major benefit of the TEF analysis framework. In contrast, the dividing salinity method converges to a constant small error when increasing the number of salinity classes, see Fig. 2.2a. For small N both methods coincide, yet only the dividing salinity method proofs to be a robust

method. As one would expect, the relative error to the analytical value decreases as the number of data points I increases, see Fig. 2.2a.

2.1.2. A general mathematical formulation for the dividing salinity method

As the dividing salinity method shows the desired convergence behavior, it is desirable to formulate a general framework that includes any type of estuary and allows the application to more complex TEF-profiles with more than two layers, e.g. a 4-layered system. In principle, one has to find the salinities that divide the different layers in the TEF-profile q^c. For smooth functions this is done by evaluating the zero crossings, i.e. solving $q^c(S) = 0$ for S. Yet, due to the noise that occurs in the discrete q^c, the evaluation of zero crossings is not suitable. But as shown before, the evaluation of the extrema of Q^c is numerically more robust and therefore the preferable choice. For known dividing salinities $S_{\text{div},j}$, the fluxes ΔQ^c_j in each layer can be calculated by

$$\Delta Q^c_j = \int_{S_{\text{div},j}}^{S_{\text{div},j+1}} q^c \, \mathrm{d}S = -\left(Q^c(S_{\text{div},j+1}) - Q^c(S_{\text{div},j})\right), \tag{2.3}$$

with the notation that inflow segments are $\Delta Q^c_j > 0$ and outflow segments are $\Delta Q^c_j < 0$. This integration corresponds to the shaded areas for Q^c_{in} and Q^c_{out} in the right panel of the TEF sketch in Fig. 1.3. With this, all Q_{in}'s and Q_{out}'s can be properly indexed. Accordingly, a representative salinity for each inflow and outflow can be computed with

$$s_{\text{in},m} = \frac{Q^s_{\text{in},m}}{Q_{\text{in},m}}, \quad s_{\text{out},m} = \frac{Q^s_{\text{out},m}}{Q_{\text{out},m}}, \tag{2.4}$$

where m denotes the index with $m = 1, 2, \ldots$, depending on the number of layers.

Determining the dividing salinities is the main challenge, as the wiggles of the noise of q^c propagate into Q^c, just smaller. This complicates the proper finding of the extrema. The solution is an algorithm that finds all extrema, but sorts out extrema that are caused by the noise by checking if the corresponding absolute value ΔQ^c_j is greater than a threshold value Q^c_{thresh}, see Appendix B of Lorenz et al. (2019) for a detailed description. By setting Q^c_{thresh} not only noise can be filtered but also a limit of relevance can be set. Lorenz et al. (2019) show an example for the exchange flow of the Baltic Sea where an additional inflow and outflow is occurring in the order of $10\,\mathrm{m^3\,s^{-1}}$ which is not relevant compared to the main exchange flow in the order of $10,000\,\mathrm{m^3\,s^{-1}}$.

2.1.3. Application to a multi-layer case: the Gotland Basin

To apply the general dividing salinity method to a complex system, a transect through the Gotland Basin in the central Baltic Sea is chosen. It is the deepest basin of the Baltic

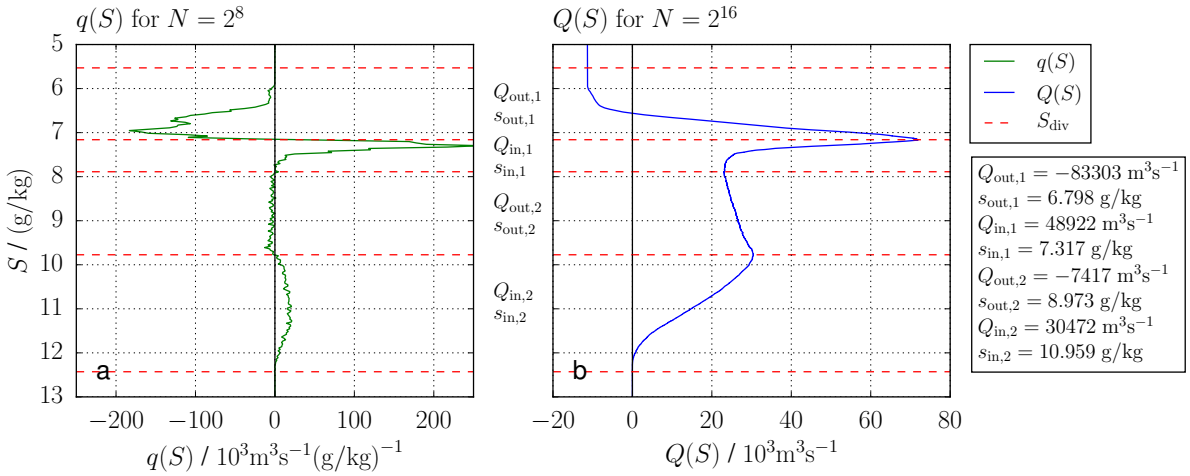

Figure 2.3.: Cross-section through Gotland Basin: profiles of q for $N = 2^8 = 256$, a), and Q for $N = 2^{16} = 65536$, b), for the Gotland transect in 2002/2003. Five dividing salinities separate two inflows (to the north) and two outflows (to the south). The corresponding TEF bulk values are listed on the right. Source: Lorenz et al. (2019).

Sea and consists of two counter clock-wise circulations, one in the surface layer above the halocline and one below the halocline. For the complex Major Baltic Inflow (MBI) of 2002/2003 (Feistel et al., 2006) model data of Burchard et al. (2018) is analyzed for the two-year period. In the resulting q profile, see Fig. 2.3a, a four-layer system is visible. A southward transport of salinities between 6 to 7 g/kg, and a northward transport between 7 to 8 g/kg can be assigned to the surface circulation. For the deep circulation, the northward transport corresponds to the inflow of saline (> 10 g/kg) water from the MBI. The southward transport is constant over a salinity range from 8 to 10 g/kg. The computed bulk values are computed according to eq. (2.3), where the dividing salinities were found by the algorithm set up with $Q_{\text{thresh}} = 700\,\text{m}^3\,\text{s}^{-1}$, and listed on the right in Fig. 2.3. The net southward transport is due to the river discharge since most rivers are located north of the transect. This example proves that the method is indeed capable of robustly computing a multi-layered exchange.

2.2. Numerical Study of the Exchange Flow of the Persian Gulf Using an Extended Total Exchange Flow Analysis Framework

2.2.1. TEF in temperature-salinity coordinates

The TEF analysis framework uses salinity coordinates. Yet over an annual cycle, temperature and therefore water masses occurring in the exchange flow may change significantly. Walin (1977) originally chose an isohaline framework since the density distribution is mainly controlled by salinity for most estuaries. Later, Walin (1982) introduced an isothermal framework to describe the heat transfer in the ocean. Speer (1993) used a combination of both frameworks to describe the conversion of water masses in the North Atlantic. On basis of these publications, the water mass transformation framework was developed by Hieronymus et al. (2014), see also Groeskamp et al. (2019). The seasonal cycle changes the temperature in many estuaries. Especially large, inverse estuaries experience a significant time lag between formation of outflowing water and the actual exchange of water with the ocean. For the example of the Persian Gulf, the time lag might be as long as half a year and even longer (Kämpf and Sadrinasab, 2006; Yao and Johns, 2010b). Therefore, the temperature of the outflow may give insights of the time and region of formation. To explicitly include the temperatures of the exchange flow of the Persian Gulf, a thermohaline decomposition of the exchange flow is carried out by extending the TEF analysis framework to consider potential temperature as a second coordinate. By modifying eq. (1.12) to

$$Q^c(S,\Theta) = -\left\langle \int_{A(S,\Theta)} f^c \,\mathrm{d}A \right\rangle, \tag{2.5}$$

where now $A(S,\Theta)$ denotes the area of the transect with salinities greater than S and temperatures greater than Θ. Differentiating $Q^c(S,\Theta)$ with respect to both salinity and potential temperature yields the tracer transport per salinity and per potential temperature class,

$$q^c(S,\Theta) \equiv q^c_{S,\Theta} = -\frac{\partial^2 Q^c(S,\Theta)}{\partial S \partial \Theta}. \tag{2.6}$$

$q_{S,\Theta}$ corresponds to the term $-\frac{\partial^2 M}{\partial T \partial S}$ in eq. (20) of Hieronymus et al. (2014). $q^c_{S,\Theta}$ allows analyzing and visualizing the exchange flow in form of a T-S diagram, a TEF-diagram, see Fig. 2.4.

The major benefit is that the different water masses are clearly depicted, e.g. in Fig. 2.4 the inflowing (red) IOSW of $S \approx 37$ g/kg and a wide temperature range, and the outflowing PGW (blue) of $S > 38$ g/kg and overall lower temperatures. One can integrate $q^c_{S,\Theta}$ over either coordinate to get the respective TEF-profile to compute the bulk values with the dividing salinity method, see Section 2.1 and eq. (2.3). For example,

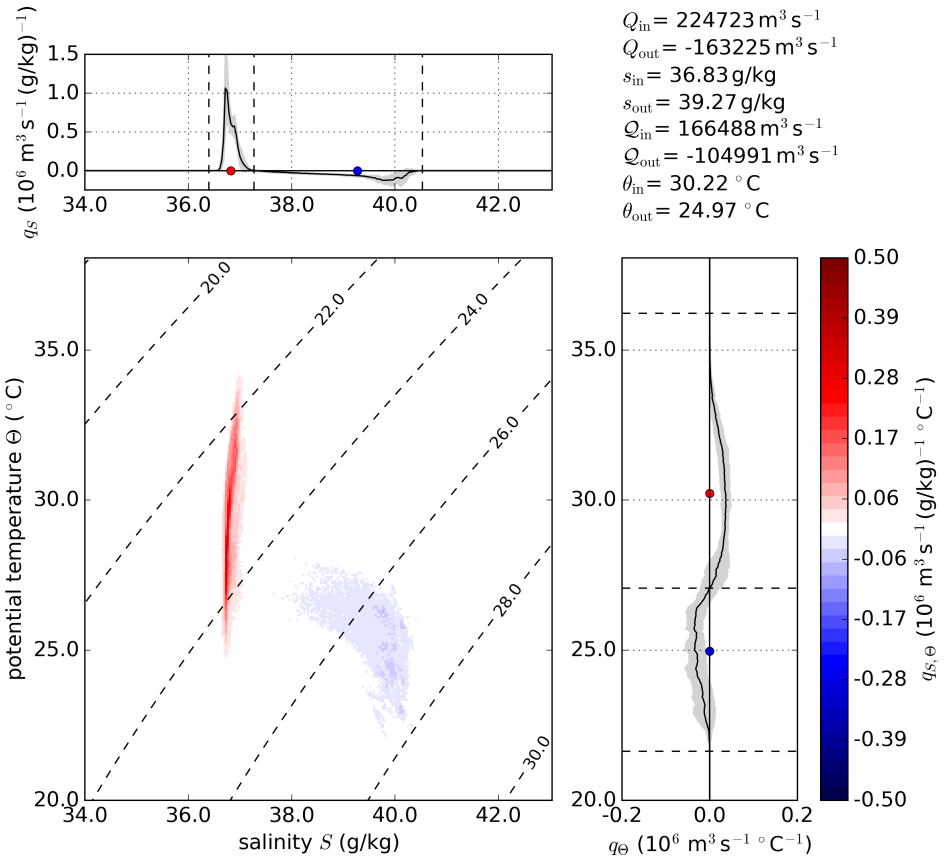

Figure 2.4.: TEF-diagram and TEF-profiles in salinity and potential temperature space for the climatological results of the exchange flow of the Persian Gulf in June. The main panel shows the color-coded volume transport per salinity and potential temperature class $q_{S,\Theta}$. By integration along one of the axes of $q_{S,\Theta}$ two different TEF-profiles are found with different volume fluxes for inflow and outflow: classic TEF-profile in salinity coordinates (top panel) and TEF-profile in potential temperature coordinates (right panel). In addition, the computed bulk values of the exchange flow are listed in the top right. Source: Lorenz et al. (2020).

integrating over all potential temperatures yields the original isohaline formulation in eq. (1.14):

$$q^c_S \equiv \int_{\Theta_{\min}}^{\Theta_{\max}} q^c_{S,\Theta}\, \mathrm{d}\Theta = q^c(S). \tag{2.7}$$

For Fig. 2.4 the one-dimensional TEF-profiles for salinity (top) and potential temperature (right) yield the bulk values listed in the upper right. There is a difference in the volume transport between both coordinate systems. Q_{in} and Q_{out}, computed from the isohaline volume transport function $Q_S = Q(S)$, are different values than $\mathcal{Q}_{\text{in}}$ and $\mathcal{Q}_{\text{out}}$, computed from the isothermal volume transport function $Q_\Theta = Q(\Theta)$. The reason is the partial compensation in the salinity and potential temperature classes.

When integrating over all potential temperatures, inflow and outflow are well separated in salinity coordinates. When integrating over all salinities, there are inflowing and outflowing parts between $\Theta = 25...27\,°\text{C}$. q_Θ in that range is the sum over both parts. Therefore, the values of $\mathcal{Q}_{\text{in}}$ and $\mathcal{Q}_{\text{out}}$ are smaller than Q_{in} and Q_{out}. Nevertheless, the bulk values for temperature and salinity are representative for the exchange flow, but maybe not so much for the different water masses.

2.2.2. Climatological exchange flow of the Persian Gulf

For the application of the TEF analysis framework to the exchange flow of the Persian Gulf, a 24-year numerical simulation using GETM was performed, see Section 1.4, and validated against observations (see Lorenz et al. (2020) for the validation). The first four years were discarded in the analysis of the exchange flow due to spin-up effects. The TEF-diagrams of the monthly climatology of the model run shows the changing T-S-distribution of the inflow of IOSW and outflow of PGW, see Fig. 2.5. The inflow (red) shows a constant narrow salinity range around $37\,$g/kg and a wider potential temperature range, depending on the season, with the highest temperatures in summer and lowest in winter. The outflow (blue) changes both its temperature and salinity range with the seasons. Overall, the outflow is more saline than the inflow and typically also colder than the inflow. Yet, in fall and winter, the outflow shows similar temperatures as the inflow except for December, where the inflow is colder than the outflow. What can be seen as well in the diagrams is that the highest salinities and lowest temperatures of the outflow are found in March and April ($\sim 41\,$g/kg, $\sim 21°$C), before decreasing the salinity and increasing the temperature until July ($\sim 40.5\,$g/kg, $\sim 24°$C). In August, there is more outflowing transport in colder and saltier water again ($\sim 41\,$g/kg, $\sim 22°$C). This indicates the arrival of a new water mass. Furthermore, the exchange flow is stronger in the first half of the year than the second, compare the color intensity in Fig. 2.5.

A closer look into the salinity distribution and salinity bulk values of the exchange flow confirms the points from before, see Fig. 2.6, where q_S (black line) and variability in form of the standard deviation (gray contour) are shown. First, the exchange flow is stronger in the first half compared to the second. Additionally, the maximum salinities and s_{out} show the seasonal behavior of the highest salinities in March/April, a decrease until July, before again more saline water arrives at the transect. This is well illustrated when looking at the core of the PGW (minimum of q_S). The profiles further show that both the inflow and outflow are variable on inter-annual time scales, indicated by the standard deviation, but have the same seasonal cycle each year. The inflow can be especially variable in February to May, where q_S partly can become negative at around $37\,$g/kg due to the high variability. The seasonal cycle of the exchange flow is best illustrated when plotting the bulk values for both the salt and heat exchange as a daily climatology, see Fig. 2.7. The volume transport of the exchange flow, Fig. 2.7a, shows again that the exchange flow is stronger in the first half of the year than the second, which is explained by stronger vertical mixing in the second half of the year

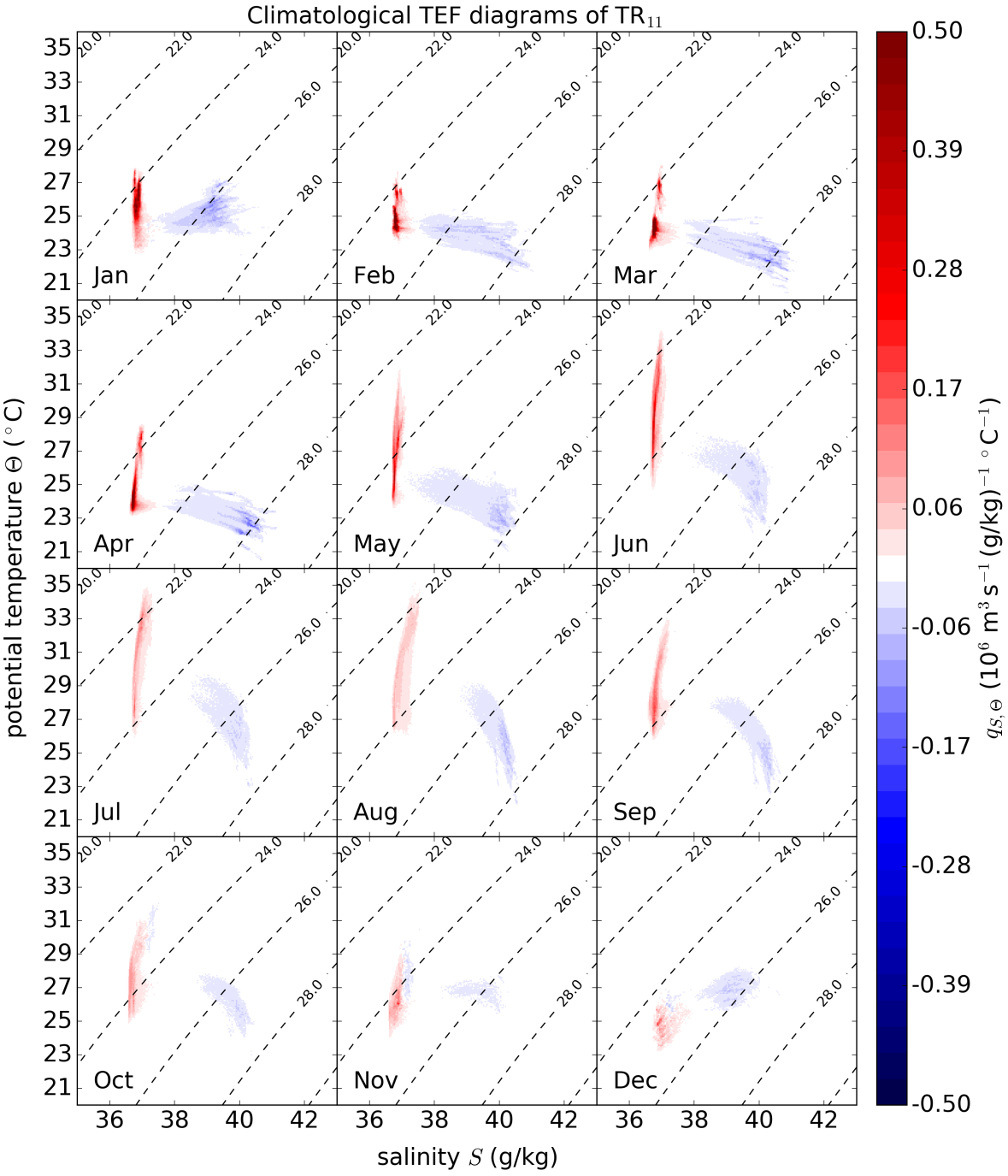

Figure 2.5.: Climatological TEF diagrams for the analysis period from 1997-2016. Each panel shows the climatological results for one month with color coded volume transport per salinity and potential temperature class. Source: Lorenz et al. (2020).

due to storms, higher evaporation and strong heat loss (Yao and Johns, 2010b). When the mixing stops in January, friction is removed and the exchange flow can reach its strongest state.

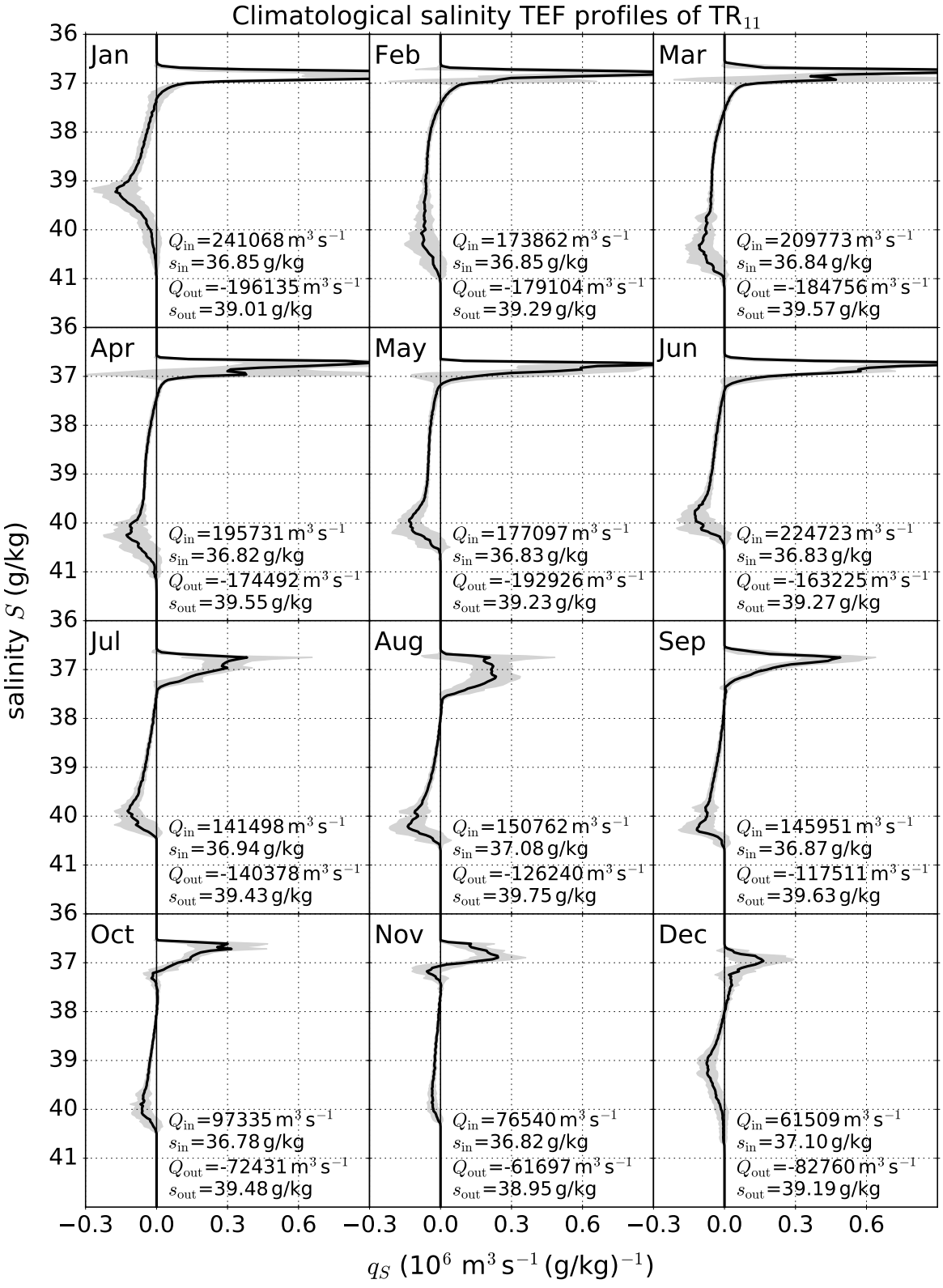

Figure 2.6.: Climatological TEF analysis for the analysis period from 1997-2016 in salinity coordinates. For each month, the bulk values for volume transport and representative salinities are computed with $N = 2^{16}$ salinity bins. Source: Lorenz et al. (2020).

The time series of the salinity of the outflow, s_{out} (Fig. 2.7b), the potential temperature of the outflow, θ_{out} (Fig. 2.7c), and therefore the potential density of the outflow, ρ_{out} (Fig. 2.7e) show the seasonal cycle described before with the sudden property changes in August. This increase in salinity, decrease in temperature, and thus increase in density can be associated with the change of the composition of the outflow. A tracer experiment, which marks the water where it was last in contact with the atmosphere and therefore the region of deep water formation, shows that in August the amount of water originating in the north increases (tracers 2,3 in Fig. 2.7f) compared to before. This water was formed approximately half a year before in winter and is therefore cold and saline, whereas the water marked with tracer 1 was formed only a few months before exiting as it was formed during winter in the southern shallows. The main contribution to the outflow is most of the time entrained water (tracer 4). The signature of the entrainment can also be seen clearly in Fig. 2.5 and Fig. 2.6. For the different regions marked with the tracer, see Fig. 1 of Lorenz et al. (2020). The salinity of the inflow is almost constant around $s_{\text{in}} \approx 37.0\,\text{g/kg}$ (Fig. 2.7b). The potential temperature of the inflow, θ_{in} (Fig. 2.7c), follows the seasonal cycle of short wave radiation, showing that the inflow is colder than the outflow in late fall and early winter. From the TEF in potential temperature coordinates, q_Θ, the heat budget can be illustrated, see Fig. 2.7d. What can be learned is that most of the time, except for November and December, the Persian Gulf imports heat from the Indian Ocean as it has to replace the annual mean net heat loss to the atmosphere ($-4.7\,\text{W}\,\text{m}^{-2}$ for the 24-year mean).

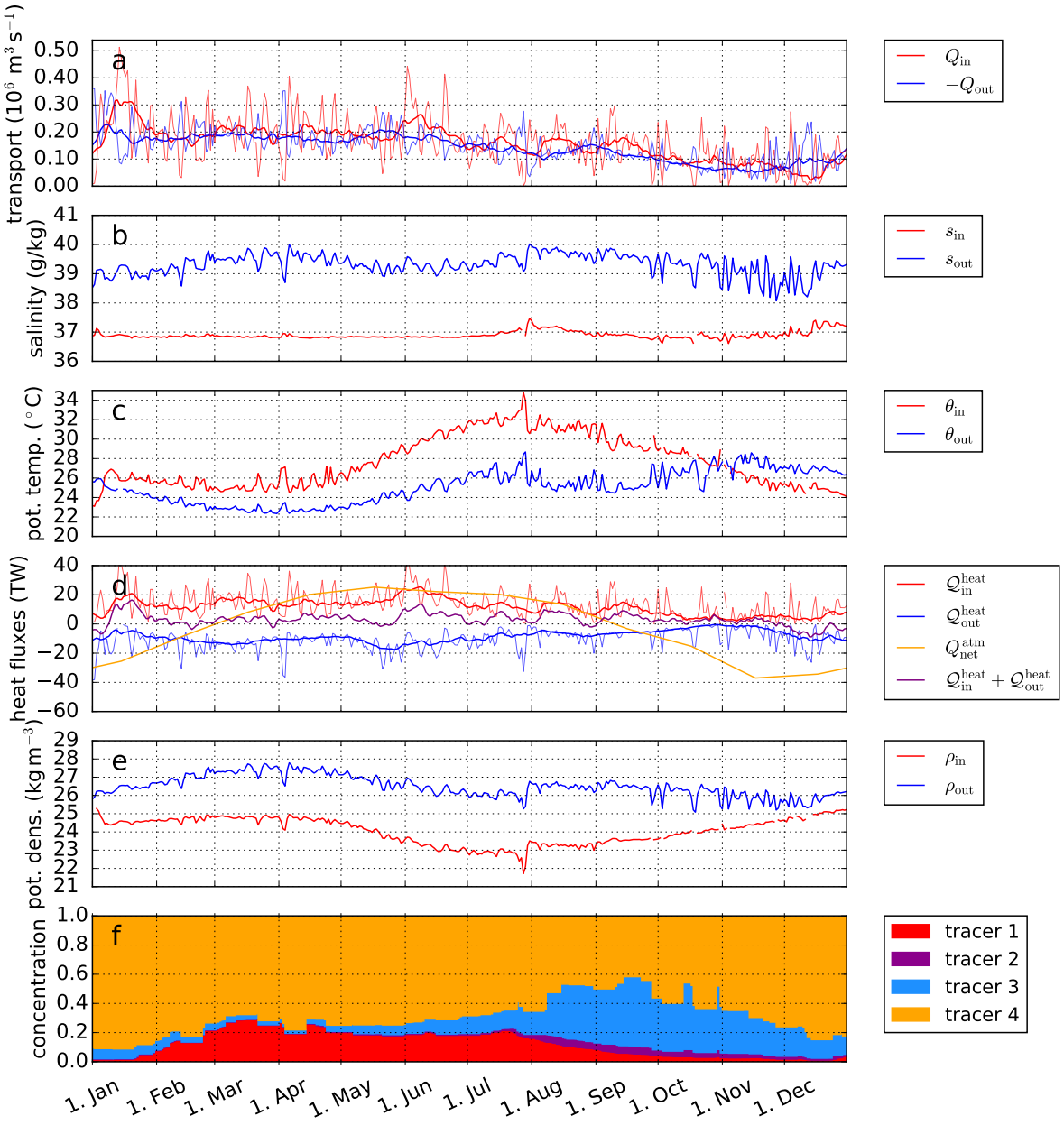

Figure 2.7.: Time series of climatological daily TEF bulk values: a) the transport (thick lines: 14-day running mean, thin lines: daily values), in b) the bulk salinities, in c) bulk potential temperatures, d) heat exchange (thick lines: 14-day running mean, thin lines: daily values) and surface heat fluxes (monthly mean) e) the bulk potential densities and in f) the tracer concentrations of the outflow. Blank spaces indicate that for that climatological day there was no two-layer exchange. Source: Lorenz et al. (2020).

2.3. Impact of evaporation and precipitation on estuarine mixing relations

2.3.1. Inclusion of surface fluxes into existing mixing relations

In the introduction, the existing mixing relations between exchange flow and freshwater forcing to the estuarine salt mixing are presented, summarizing the key results of MacCready et al. (2018) and Burchard et al. (2019). During the derivation, surface freshwater fluxes in form of evaporation and precipitation have been neglected. Yet these need to be included, for example, to describe inverse estuaries, which are driven by freshwater loss due to evaporation. Also, simply replacing the river discharge in eq. (1.28) with a negative volume transport due to evaporation would lead to $M \leq 0$ which breaks the strictly positive definition of M. The solution is an additional surface salinity squared flux due to evaporation that ensures a positive M, originating in the surface boundary condition. In the following, only the new budgets are listed and the resulting mixing relations are presented. For a detailed derivation, including the boundary conditions, I refer to Lorenz et al. (submitted).

The result of the volume integration, temporal averaging, and rephrasing in terms of TEF bulk values is done in one step here. The resulting volume budget as:

$$\delta V = \langle \partial_t V \rangle = Q_{\text{in}} + Q_{\text{out}} + Q_r + Q_{\text{surf}}, \tag{2.8}$$

which is the same as eq. (1.20) with the additional surface freshwater transport due to precipitation and evaporation,

$$Q_{\text{surf}} = -\left\langle \int_{A_{\text{surf}}} (E - P)\, \mathrm{d}A \right\rangle = Q_{\text{evap}} + Q_{\text{precip}}, \tag{2.9}$$

with $Q_{\text{evap}} \leq 0$, $Q_{\text{precip}} \geq 0$. The salinity budget is similar to eq. (1.21) since precipitation and evaporation do not add or remove salt from the system:

$$\delta S = \left\langle \partial_t \int_V s \, \mathrm{d}V \right\rangle = Q^s_{\text{in}} + Q^s_{\text{out}} = Q_{\text{in}} s_{\text{in}} + Q_{\text{out}} s_{\text{out}}. \tag{2.10}$$

The salinity square budget reads as:

$$\delta S^2 = \left\langle \partial_t \int_V s^2 \, \mathrm{d}V \right\rangle = Q_{\text{in}} \left(s^2\right)_{\text{in}} + Q_{\text{out}} \left(s^2\right)_{\text{out}} + F^{s^2}_{\text{surf}} - M, \tag{2.11}$$

with the new surface salinity square transport due to precipitation and evaporation:

$$F^{s^2}_{\text{surf}} = \left\langle \int_{A_{\text{surf}}} s^2 (E - P)\, \mathrm{d}A \right\rangle. \tag{2.12}$$

Although precipitation and evaporation do not add or remove salt, they remove or add salinity square. This is better understood when inspecting the salinity variance budget, that reads as:

$$\delta S'^2 = \left\langle \partial_t \int_V s'^2 \,\mathrm{d}V \right\rangle = Q_{\text{in}} {(s')^2}_{\text{in}} + Q_{\text{out}} {(s')^2}_{\text{out}} + F^{s^2}_{\text{surf}} + \left\langle \bar{s}^2 \int_{A_r} u_n \,\mathrm{d}A \right\rangle - \left\langle \int_{A_{\text{surf}}} \bar{s}^2 (E - P) \,\mathrm{d}A \right\rangle - M. \tag{2.13}$$

Here, precipitation and evaporation add variance to the system, similarly to river discharge in eq. (1.23). The difference to river discharge is that river discharge is assumed to occur at salinity $s = 0$, whereas precipitation and evaporation occur at the surface with a surface salinity, typically with $s \neq 0$. This results in the terms $F^{s^2}_{\text{surf}}$ and $-\left\langle \int_{A_{\text{surf}}} \bar{s}^2 (E - P) \,\mathrm{d}A \right\rangle$. The net variance transport of these two terms has to be compensated in the end by the mixing M, if the variance in the estuary should not change.

Similar to Section 1.3.3, one can combine eqs. (2.8)-(2.11). The combination leads to the following exact, new relation of M:

$$M_e = \frac{s_{\text{out}} (s^2)_{\text{in}} - s_{\text{in}} (s^2)_{\text{out}}}{s_{\text{in}} - s_{\text{out}}} (Q_r - \delta V + Q_{\text{surf}}) + \frac{(s^2)_{\text{in}} - (s^2)_{\text{out}}}{s_{\text{in}} - s_{\text{out}}} \delta S - \delta S^2 + F^{s^2}_{\text{surf}}. \tag{2.14}$$

The difference to eq. (1.25) (Burchard et al., 2019) is the additional freshwater transport Q_{surf} in the volume term and $F^{s^2}_{\text{surf}}$. Similarly to Section 1.3.3, one can make assumptions that simplify eq. (2.14). For the constancy assumption, i.e. the temporal average of the squared property is the same as the time-averaged quantity squared, e.g. $(s^2)_{\text{in}} = (s_{\text{in}})^2$, $(s^2)_{\text{out}} = (s_{\text{out}})^2$, eq. (2.14) reduces to

$$M_c = s_{\text{in}} s_{\text{sout}} (Q_r - \delta V + Q_{\text{surf}}) + (s_{\text{in}} - s_{\text{out}}) \delta S - \delta S^2 + F^{s^2}_{\text{surf}}. \tag{2.15}$$

For storage terms equal to zero, i.e. if one assumes periodicity or applies long-term averaging, eq. (2.14) yields

$$M_p = \frac{s_{\text{out}} (s^2)_{\text{in}} - s_{\text{in}} (s^2)_{\text{out}}}{s_{\text{in}} - s_{\text{out}}} (Q_r + Q_{\text{surf}}) + F^{s^2}_{\text{surf}}. \tag{2.16}$$

Considering both assumptions at the same time, (2.14) reads as

$$M_{cp} = s_{\text{in}} s_{\text{out}} (Q_r + Q_{\text{surf}}) + F^{s^2}_{\text{surf}}. \tag{2.17}$$

It is desirable to reformulate $F^{s^2}_{\text{surf}}$ in terms of a product of salinity bulk value squared times volume transport bulk value. Therefore, by defining a bulk surface salinity,

$$s_{\text{surf}} \equiv \left[(s^2)_{\text{surf}}\right]^{\frac{1}{2}} = \left(-\frac{F^{s^2}_{\text{surf}}}{Q_{\text{surf}}}\right)^{\frac{1}{2}}, \tag{2.18}$$

one can reformulate eq. (2.17) to

$$M_{cp} = s_{\text{in}} s_{\text{out}} Q_r + \left(s_{\text{in}} s_{\text{out}} - (s_{\text{surf}})^2\right) Q_{\text{surf}}. \tag{2.19}$$

This simple relation states that the mixing inside any estuary is the sum of mixing related to river discharge and mixing related to the surface freshwater transport. For $P = E = 0$, eq. (2.19) reads again as the well-known result of MacCready et al. (2018), see eq. (1.28).

2.3.2. A box model to explain the mixing in an inverse estuary

To illustrate relation (2.19) for an inverse estuary, a simple, two-layer box model is considered, see Fig. 2.8. A steady-state with a surface layer of V_{surf} with salinity s_{surf} and a bottom layer of V_{b} with salinity s_{out}, see Fig. 2.8a, is the result of evaporation and inverse estuarine circulation in an infinitesimal time interval Δt. The evaporation process is prescribed as a spatially constant removal of freshwater, $Q_{\text{surf}} \leq 0$, from the surface layer. This loss of freshwater increases the salinity of the upper layer from s_{surf} to s^*_{surf}, see Fig. 2.8b. The lost volume is refilled by the exchange flow with inflowing ocean water ($Q_{\text{in}} \geq 0$,s_{in}) and an outflow of the bottom water ($Q_{\text{out}} \leq 0$,s_{out}), see Fig. 2.8c. To compute the volume integrated mixing that is needed to keep the steady-state (Fig. 2.8a) the volume integrated salinity square budgets have to be evaluated. For the different states, the budgets read as:

$$\Sigma_a = V_{\text{surf}}(s_{\text{surf}})^2 + V_b(s_{\text{out}})^2, \tag{2.20}$$
$$\Sigma_b = (V_{\text{surf}} + \Delta t Q_{\text{surf}})(s^*_{\text{surf}})^2 + V_b(s_{\text{out}})^2, \tag{2.21}$$
$$\Sigma_c = (V_{\text{surf}} + \Delta t Q_{\text{surf}})(s^*_{\text{surf}})^2 + \Delta t Q_{\text{in}}(s_{\text{in}})^2 + (V_b + \Delta t Q_{\text{out}})(s_{\text{out}})^2. \tag{2.22}$$

The production of volume-integrated salinity square due to evaporation ($Q_{\text{surf}} \leq 0$) can be calculated as the difference of state b and state a:

$$\frac{\Sigma_b - \Sigma_a}{\Delta t} = -\frac{1}{1 + \frac{\Delta t Q_{\text{surf}}}{V_{\text{surf}}}}(s_{\text{surf}})^2 Q_{\text{surf}}, \tag{2.23}$$

where salt conservation between states a and b,

$$V_{\text{surf}} s_{\text{surf}} = (V_{\text{surf}} + \Delta t Q_{\text{surf}})\, s^*_{\text{surf}}, \tag{2.24}$$

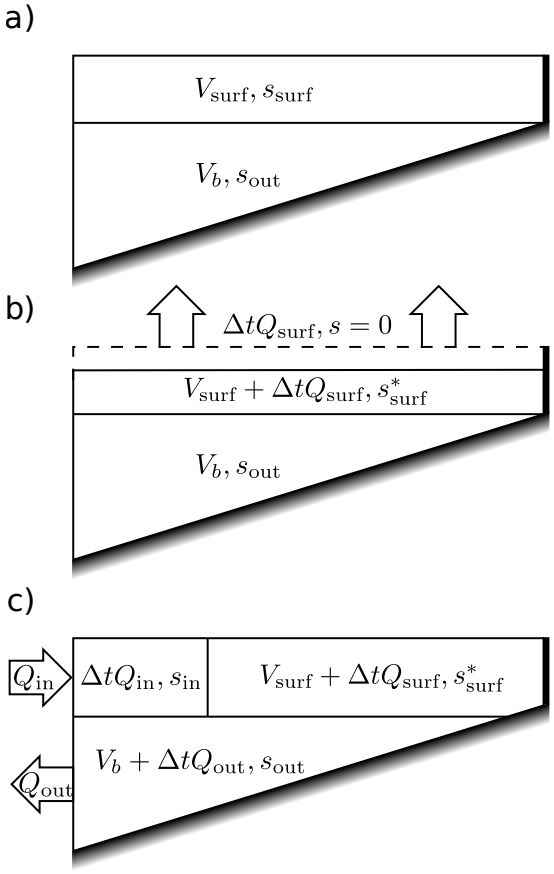

Figure 2.8.: Descriptive box model of a steady state, instantaneous process of an inverse estuarine circulation due to evaporation: a) The two-layered box with two well-mixed layers, a surface and bottom layer with different salinities. b) The fresh water volume, $\Delta t Q_{\mathrm{surf}}$, $Q_{\mathrm{surf}} < 0$, is removed from V_{surf} which reduces the volume of the surface layer to $V_{\mathrm{surf}} + \Delta t Q_{\mathrm{surf}}$. The salt left behind by the evaporation process is mixed into the reduced surface volume, increasing the salinity s_{surf} to s^*_{surf}. c) The exchange flow is added. Its net volume transport replaces the evaporated fresh water. The inflow Q_{in} of salinity s_{in} enters the estuary and V_{b} is reduced by the outflow Q_{out} to $V_{\mathrm{b}} + \Delta t Q_{\mathrm{out}}$. The salt content is not changed by the exchange flow. The state a) is the long-term average result of states b) and c). Source: Lorenz et al. (submitted).

has been used. With help of eqs. (1.8) and (1.9) for $\delta S = \delta V = Q_r = 0$, the change of volume-integrated salinity square due to the exchange flow can be quantified as the difference between state c and state b

$$\frac{\Sigma_c - \Sigma_b}{\Delta t} = s_{\mathrm{in}} s_{\mathrm{out}} Q_{\mathrm{surf}}. \tag{2.25}$$

The mixing required to mix state c back to state a is given by $\frac{\Sigma_c - \Sigma_a}{\Delta t}$ and thus in the limit of $\Delta t \to 0$,

$$M_{cp} = \lim_{\Delta t \to 0} \frac{(\Sigma_c - \Sigma_b) + (\Sigma_b - \Sigma_a)}{\Delta t} = \left(s_{\text{in}} s_{\text{out}} - (s_{\text{surf}})^2 \right) Q_{\text{surf}}, \tag{2.26}$$

which is the same result as in (2.17) with $Q_r = 0$. This simple box model shows that the salinity square change between state a and state b due to evaporation is equivalent to $F^{s^2}_{\text{surf}}$. It further illustrates the two processes that are included in M_{cp}: first, the salinity square increase due to evaporation ($-(s_{\text{surf}})^2 Q_{\text{surf}}$) and second, the salinity square loss due to the exchange flow ($s_{\text{in}} s_{\text{out}} Q_{\text{surf}}$).

2.3.3. Mixing of the Persian Gulf

To study the mixing of the Persian Gulf, a one-year simulation of Lorenz et al. (2020) has been repeated with an online computation of the TEF profiles which allows eq. (2.14) to exactly equal the directly diagnosed mixing during the model run with a method of Klingbeil et al. (2014). The chosen year is 2011 which shows a representative seasonal cycle, see Fig. 2.9.

The volume transport for Q_{in} and Q_{out}, Fig. 2.9a, is very similar to Fig. 2.7, yet, with a more clear spring-neap signal than the climatology. The surface freshwater transport Q_{surf}, Fig. 2.9e, also shows a typical seasonal cycle with more freshwater loss in the second half of the year than the first. Furthermore, events of large freshwater loss on time scales of around two weeks are occurring in fall, so-called Shamal winds (Thoppil and Hogan, 2009, 2010). The sum of the volume transports and river discharge is shown in Fig. 2.9c, which shows the volume storage term δV. s_{in} and s_{out}, Fig. 2.9b, also show the main seasonal features: s_{in} is more or less constant during the year, whereas s_{out} shows the seasonal increases in March/April and August/September, but here also spring-neap changes are visible. The bulk salinity squares obey the constancy assumption, i.e. $(s^2)_{\text{in}} = (s_{\text{in}})^2$ and $(s^2)_{\text{out}} = (s_{\text{out}})^2$, and are therefore not shown. The mean surface salinity of the model $s_{\text{surf,model}}$ shows the typical seasonal cycle of highest values in winter and lowest in summer (Kämpf and Sadrinasab, 2006). In contrast, the surface salinity bulk value s_{surf}, eq. (2.18), is very variable and has typically a greater value than the model surface salinity. This is due to the weighting of the surface salinity with the evaporation which is most of the year higher in the shallow coastal regions where also the surface salinities are highest.

As all the bulk values have a seasonal character, so does the mixing M_e, Fig. 2.9d. The mixing is generally higher in the second half of the year than the first. It is further modulated with a two-weekly signal, both due to the spring-neap cycle and also due to the Shamal events occurring on similar time scales. On diurnal time scales, the mixing is mainly dominated by the variability of the exchange flow, i.e. the storage terms. For this simulation, the constancy assumption is a very good approximation for the mixing as $M_c \approx M_e$, which is mainly due to physical and not numerical mixing.

To illustrate how mixing effects stratification and the overall state of the Persian Gulf, the basin-averaged potential energy relative to the mixed condition Φ (Simpson et al., 1978),

$$\Phi = \int_{-H}^{\eta} (b - \bar{b})\, z \, \mathrm{d}z, \tag{2.27}$$

with the buoyancy b, and the vertical mean buoyancy $\bar{b}$ is shown in Fig. 2.9f. Low values mean that less energy is needed to homogenize the water column, i.e. the water column is weakly stratified or already well-mixed. High values indicate strong stratification as a lot of energy is needed to homogenize the water column. Φ illustrates very nicely the seasonal cycle of stratification of the Persian Gulf. In winter, most regions of the Persian Gulf are well-mixed, indicated by small values of Φ. In spring, stratification starts to build up due to heat uptake from solar radiation, see also Fig. 2.7d in Section 2.2, but also due to inflowing IOSW. The maximum is reached in August before the stratification is weakening due to increased mixing. The increased mixing is due to stronger winds, higher evaporation, and thermal cooling as the Persian Gulf radiates heat into the atmosphere. $\widehat{\Phi}$ is the high-pass filtered Φ and illustrates that the stratification has also a strong variability on a two-weekly time scale. The relation between mixing, stratification, and surface salinity square flux, i.e. mixing due to evaporation, shows indeed that when mixing is high, Φ decreases since its time derivative, $\partial_t \Phi$, is negative, see Fig. 2.9g. Furthermore, since M_e and $F^{s^2}_{\text{surf}}$ are well correlated it suggests that most of the two-weekly variability of the mixing is due to the evaporation, e.g. in October, and not due to the spring-neap cycle.

The annual mean mixing of the Persian Gulf is $\sim 4.7 \cdot 10^6$ (g/kg)^2 m^3 s^{-1}, see Table 4 of Lorenz et al. (submitted) for a full list of annual bulk values for this simulation. The relative errors of the different assumptions for the mixing relations are:

$$\begin{aligned}
\text{constancy:} \quad & \left|\tfrac{M_c - M_e}{M_e}\right| = 1.4\%, \\
\text{periodicity:} \quad & \left|\tfrac{M_p - M_e}{M_e}\right| = 2.1\%, \\
\text{constancy and periodicity:} \quad & \left|\tfrac{M_{cp} - M_e}{M_e}\right| = 3.6\%, \\
\text{approx. } F^{s^2}_{\text{surf}}: \quad & \left|\tfrac{-\langle s_{\text{surf,model}}\rangle^2 \cdot Q_{\text{surf}} - F^{s^2}_{\text{surf}}}{F^{s^2}_{\text{surf}}}\right| = 1.2\%, \\
\text{constancy, periodicity, approx. } F^{s^2}_{\text{surf}}: \quad & \left|\tfrac{s_{\text{in}} s_{\text{out}} (Q_r + Q_{\text{surf}}) - (s_{\text{surf,model}})^2 \cdot Q_{\text{surf}} - M_e}{M_e}\right| = 2.2\%,
\end{aligned} \tag{2.28}$$

where $s_{\text{surf,model}}$ is the mean surface salinity of the model, see also Lorenz et al. (submitted). What this shows is that i) $F^{s^2}_{\text{surf}}$ may be well approximated with the basin-averaged surface salinity squared of the model times the mean freshwater transport due to evaporation and ii) that the average over one year is enough to represent an almost periodic state of the Persian Gulf. Since eq. (2.19) is a very good approximation, one can decompose it into riverine and surface fresh water contributions which contribute

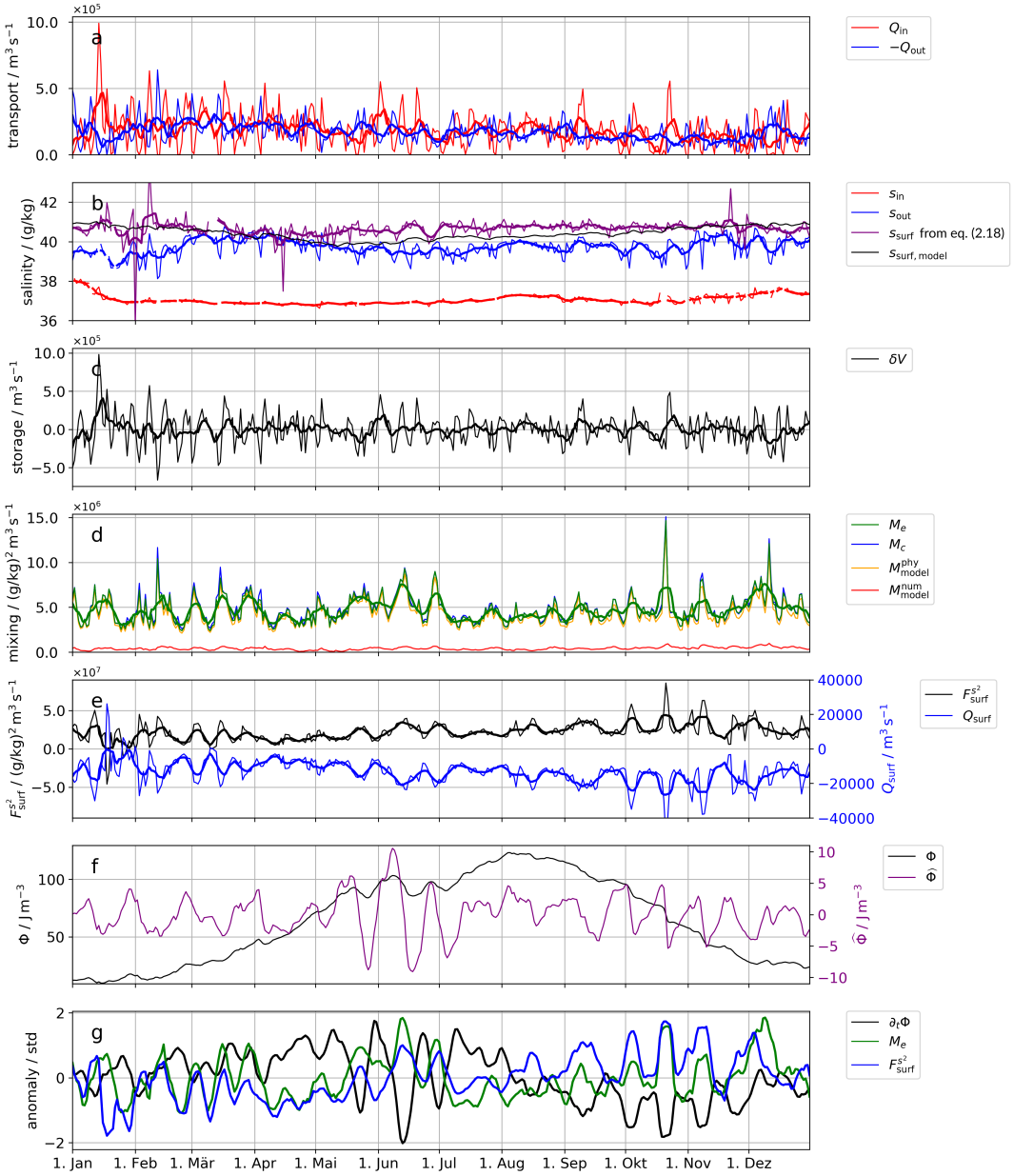

Figure 2.9.: Time series of the daily exchange flow and mixing quantities for 2011: a) bulk volume transport values, b) bulk salinities of the exchange flow and surface salinities, eq. (2.18), and model salinity, c) volume storage δV, d) mixing computed from the exchange flow bulk values using relation (2.14) and (1.26), and physical, numerical mixing of the model, e) surface freshwater flux Q_{surf} and surface salinity squared flux $F^{s^2}_{\text{surf}}$, f) potential energy relative to the mixed condition Φ (Simpson et al., 1978) and Φ without the seasonal signal, $\widehat{\Phi}$, and g) the temporal change of Φ, $\partial_t \Phi$, M_e and $F^{s^2}_{\text{surf}}$ (anomaly from the annual mean and scaled with the respective standard deviation). The thick lines are smoothed with a 1-week running mean filter. Note the different scaling of the y-axis in each panel. If there is a blank in the time series, e.g. in b), then the respective inflow or outflow is zero and the bulk values are zero as well. Further note that the bulk salinity squares are very closely following the squared bulk salinities. Source: Lorenz et al. (submitted).

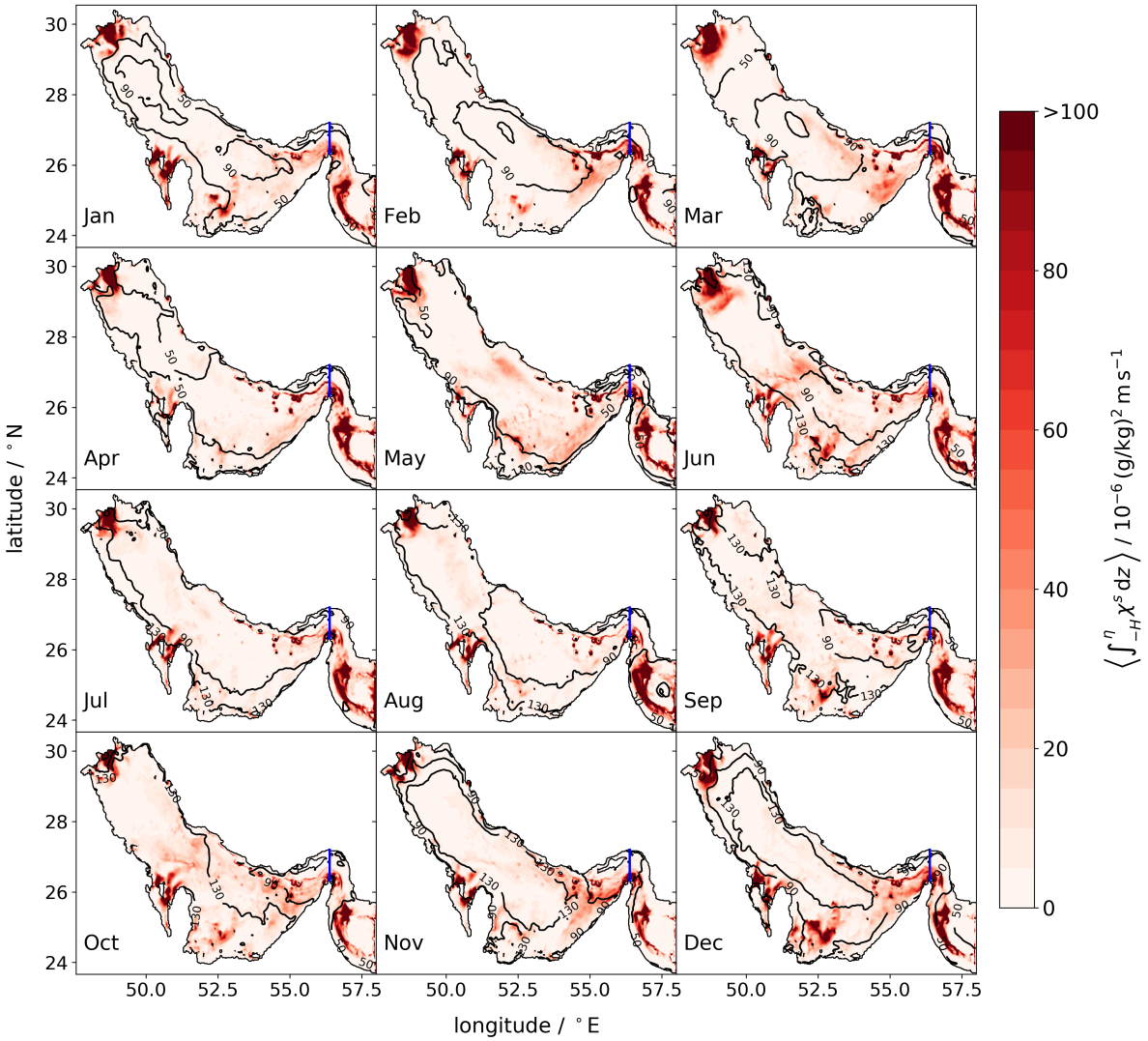

Figure 2.10.: Monthly mean mixing map of the Gulf for 2011: color coded is the vertically integrated local salt mixing, χ^s, see eq. (1.17). The black contour shows the surface salinity-square flux in 10^{-6} (g/kg)^2 m s^{-1}, see also eq. (2.12). The transect across the exchange flow analysis is carried out is shown in blue. Source: Lorenz et al. (submitted).

almost equally to the total mixing:

$$M_{\text{river}} = s_{\text{in}} s_{\text{out}} Q_r \approx 2.5 \cdot 10^6 \text{ g/kg}^2 \text{ m}^3 \text{ s}^{-1} \tag{2.29}$$

$$M_{\text{surface}} = \left(s_{\text{in}} s_{\text{out}} - \left(s_{\text{surf,model}}\right)^2\right) Q_{\text{surf}} \approx 2.1 \cdot 10^6 \text{ g/kg}^2 \text{ m}^3 \text{ s}^{-1}. \tag{2.30}$$

Despite $Q_r < 10|Q_{\text{surf}}|$, the mixing of both is similar. This can be explained by the fact that both are associated with different processes: for the surface mixing, the salinity gradients are very small, but occur over a large area, whereas the gradients of the riverine mixing are large, but confined to a small area. According to Burchard (2020)

the mixing inside a volume bound by an isohaline S is $M(S) = S^2 Q_r$. Assuming the riverine freshwater has to be mixed to the salinity of the outflow ($S \approx 40$ g/kg), the mixing would be $M = (40\,\text{g/kg})^2 Q_r$. This means that even though the river discharge is small compared to the evaporation transport, the mixing associated to this process is not since the salinity range is very large.

This can be well seen in Fig. 2.10, where the monthly integrated mean mixing per unit area is shown. In each month, there is high mixing occurring in the Shatt Al Arab river plume in the northwest. Another hotspot is the area west of Qatar and north of Bahrain, where water of high salinity (> 50 g/kg) enters into the basin of the Gulf. Despite the high density and mixing values, the water of this area does not contribute a lot to the composition of the outflow (Lorenz et al., 2020). The last hotspot inside the Gulf is the Strait of Hormuz where the exchange flow is occurring. The high mixing values there are explained by topographic features, strong tidal currents, and eddy activity (Swift and Bower, 2003). Outside of the Gulf, there is an area of high mixing on the western shelf of the Gulf of Oman, where the PGW stratifies into the water column of the Indian Ocean. This process is associated with strong mesoscale and submesoscale eddy activity (L'Hégaret et al., 2015; Vic et al., 2015; Morvan et al., 2019) formed by the interaction of the PGW and the steep topography. Since the model of this study is a hydrostatic model (Klingbeil et al., 2018), the mixing there is related to pressure gradient errors (Shchepetkin and McWilliams, 2003). The spatial distribution and temporal evolution of $F^{s^2}_{\text{surf}}$, contours in Fig. 2.10, show how it is growing from March onwards until November and moving from the shallow coasts to the deeper, open Gulf.

Chapter 3.

Summary and Conclusions

This dissertation contributed to the quantification of estuarine exchange flows and their relation to salt mixing inside the estuary. A general formulation of the dividing salinity method for the Total Exchange Flow (TEF) analysis framework (MacCready, 2011) was presented to solve the problem of noise when computing bulk values that characterize the estuarine exchange flow. Furthermore, the TEF analysis framework was extended to consider two coordinates at the same time, allowing decomposition of the exchange flow into TEF-diagrams, a T-S diagram with color-coded volume transport per salinity and temperature class. Additionally, general salt mixing relations for estuaries were derived by considering surface freshwater fluxes besides river discharge. These relations can now be applied to inverse estuaries as well. All these methods were applied to a numerical setup of the Persian Gulf to study its exchange flow and its mixing.

The general formulation of the dividing salinity method allows robust analysis of arbitrarily complicated exchange flows, independent of the number of discrete salinity classes. The dividing salinity method solves two problems evident from the originally proposed computation of bulk values of MacCready (2011). It allows the robust computation of the bulk values independent of any noise and it therefore also allows a proper description of exchange flows of more than two layers in salinity space. For any multi-layer flows the separation in the q^c profile would rely on distinct zero crossings, which might be interfered by noise as shown in Section 2.1 and Lorenz et al. (2019). The new dividing salinity method evaluates the extrema of Q^c, which has been shown to be robust against noise when a proper algorithm is applied (Lorenz et al., 2019).

The decomposition of the exchange flow into thermohaline coordinates leads to T-S diagrams of the exchange flow which help to differentiate between water masses involved in the exchange process. For the Persian Gulf, bulk values for salinity, potential temperature, and potential density have been computed for the outflow, revealing a change in the composition of the outflowing water into winter water formed in the southern shallows and the northern Gulf. By only considering salinity, this change might not have been a focus of interest, but together with the consideration of temperature, it indicated a change in water masses. This has been confirmed by the evaluation of passive tracers marking the different regions (Lorenz et al., 2020). This extension of TEF further spans the bridge to the water mass transformation framework (Hieronymus et al., 2014; Groeskamp et al., 2019) which is based on the isohaline and isothermal

frameworks presented in Walin (1977) and Walin (1982). The exchange flow $q_{S,\Theta}$ of Lorenz et al. (2020) corresponds to the term $-\frac{\partial^2 M}{\partial T \partial S}$ in eq. (20) of Hieronymus et al. (2014).

The last and maybe most important contribution of this dissertation has been made in understanding how the exchange flow of estuaries driven by surface buoyancy fluxes relates to the salt mixing inside the estuary. The relations introduced by MacCready et al. (2018) and Burchard et al. (2019) have been extended to include surface freshwater fluxes in both the volume, salinity square, and salinity variance budgets. The additional s^2-transport (variance transport) due to precipitation and evaporation fixes the issue of non-physical negative mixing when considering freshwater loss in the relation of MacCready et al. (2018), eq. (1.28), see also Section 2.3. For periodic or long-term averaged estuaries with non-negligible net surface freshwater transport, the mixing may be well approximated by

$$M \approx s_{\text{in}} s_{\text{out}} Q_r + \left(s_{\text{in}} s_{\text{out}} - (s_{\text{surf}})^2 \right) Q_{\text{surf}}, \tag{3.1}$$

see also eq. (2.19). This relation allows a decomposition of a riverine contribution to the mixing (first term of the right-hand-side of eq. (3.1)) and a surface freshwater contribution (second term of the right-hand-side of eq. (3.1)). For no surface freshwater transport it reduces to the well established relation by MacCready et al. (2018).

An application of the new extended methods to the Persian Gulf reveal the seasonal cycle of its exchange flow. The outflowing water consists of a mixture of cold and salty winter water, formed in either the southern shallows, i.e. the coast of the United Arabian Emirates, or in the northwestern region, and entrained water. During the first half of the year the exchange flow is stronger than in the second half due to the higher friction in the second half of the year (Yao and Johns, 2010b). Furthermore, most water (despite the entrained) water was formed in the southern shallow in the first half of the year, before in August water formed in winter in the northwest becomes the largest contributor to the outflow. This change in water mass is proven by passive tracer and is further well depicted in the temperature and salinity bulk values. The mixing of the Persian Gulf shows a seasonal cycle as well, with generally higher mixing in the second half than in the first. This is reflected by a build-up of stratification in the first half and the destruction of the same in the second half due to winds, evaporation, and heat loss to the atmosphere. On an annual time scale, eq. (3.1) allows the decomposition of a riverine part of mixing and mixing due to surface fluxes. For the Persian Gulf, both contribute almost equally, although the freshwater discharge due to rivers is a factor of ten smaller than the freshwater loss due to evaporation.

In this dissertation, existing estuarine methods have been extended and generalized allowing application to all kinds of estuaries, especially surface buoyancy flux driven ones. Yet, a lot of open questions remain that may be addressed in the future. A few closely linked to this dissertation will be mentioned in the following. With the introduction of isohaline mixing for classical estuaries by Burchard (2020), again the question remains of how to include the surface freshwater fluxes. Furthermore, the

application of the isohaline mixing theory including surface freshwater fluxes has to be proven to be applicable to realistic hind-cast models. In general, the isohaline framework has received a lot of attention in the estuarine community. Yet, in my opinion, the consideration of temperature should be continued, i.e. by working in a thermohaline framework. I imagine that combining the water mass transformation framework and the newly isohaline mixing could lead to great insights into how water masses are created and modified in estuaries. For the Persian Gulf, this dissertation showed how variable its exchange flow and the salt mixing can be. What now is needed to fully understand the transformation processes would be temperature mixing and the respective boundary fluxes, binned in T-S coordinates.

Despite further extending the analysis methods of estuarine exchange flows and mixing, the application of the presented methods to different estuary types should be carried out in the future. I imagine that especially decomposition of mixing in riverine and surface freshwater driven parts may be an important tool in the future when working with tropical estuaries that may change between classical and inverse estuarine circulation between wet and dry season (Valle-Levinson et al., 2003), as well as estuaries that may inhibit both types in the same time, i.e. by a formation of a salt-plug (Wolanski, 1986). Further, the application of the presented methods to glacier fjords with a floating ice tongue driven by subglacial discharge and melting at the ice-ocean interface may be very useful. If the melting of ice was included as another surface freshwater flux, one should be able to relate the melting to the exchange flow and the mixing. With these relations the sensitivity of the melting may be investigated in dependency of external forcing without running expensive numerical models. Further, the consideration of temperature into the equations is of importance for the glacier fjords since the melting is dependent on both temperature and salinity.

Bibliography

Ahmad, F., and S. Sultan, 1991: Annual mean surface heat fluxes in the Arabian Gulf and the net heat transport through the Strait of Hormuz. *Atmosphere-Ocean*, **29 (1)**, 54–61.

Alessi, C. A., H. D. Hunt, and A. S. Bower, 1999: Hydrographic Data from the US Naval Oceanographic Office: Persian Gulf, Southern Red Sea, and Arabian Sea 1923-1996. Tech. rep., WOODS HOLE OCEANOGRAPHIC INSTITUTION MA.

Baptista, A. M., and Coauthors, 2005: A cross-scale model for 3D baroclinic circulation in estuary–plume–shelf systems: II. Application to the Columbia River. *Continental Shelf Research*, **25 (7-8)**, 935–972.

Basdurak, B. N., K. D. Huguenard, A. Valle-Levinson, M. Li, and R. J. Chant, 2017: Parameterization of mixing by secondary circulation in estuaries. *Journal of Geophysical Research: Oceans*, **122 (7)**, 5666–5688.

Burchard, H., 2020: A Universal Law of Estuarine Mixing. *Journal of Physical Oceanography*, **50 (1)**, 81–93.

Burchard, H., and H. Baumert, 1995: On the performance of a mixed-layer model based on the k-ε turbulence closure. *Journal of Geophysical Research: Oceans*, **100**, 8523–8540.

Burchard, H., and K. Bolding, 2002: *GETM: A General Estuarine Transport Model; Scientific Documentation*. European Commission, Joint Research Centre, Institute for Environment and Sustainability.

Burchard, H., K. Bolding, and M. R. Villarreal, 1999: *GOTM, a general ocean turbulence model: theory, implementation and test cases*. Space Applications Institute.

Burchard, H., K. Bolding, and M. R. Villarreal, 2004: Three-dimensional modelling of estuarine turbidity maxima in a tidal estuary. *Ocean Dynamics*, **54**, 250–265.

Burchard, H., and R. D. Hetland, 2010: Quantifying the contributions of tidal straining and gravitational circulation to residual circulation in periodically stratified tidal estuaries. *Journal of Physical Oceanography*, **40 (6)**, 1243–1262.

Burchard, H., X. Lange, K. Klingbeil, and P. MacCready, 2019: Mixing estimates for estuaries. *Journal of Physical Oceanography*, **49 (2)**, 631–648.

Burchard, H., and H. Rennau, 2008: Comparative quantification of physically and numerically induced mixing in ocean models. *Ocean Modelling*, **20 (3)**, 293–311.

Burchard, H., and Coauthors, 2018: The Knudsen theorem and the Total Exchange Flow analysis framework applied to the Baltic Sea. *Progress in Oceanography*, 10.1016/j.pocean.2018.04.004.

Candela, J., 1991: The Gibraltar Strait and its role in the dynamics of the Mediterranean Sea. *Dynamics of Atmospheres and Oceans*, **15 (3-5)**, 267–299.

Chen, S. N., W. R. Geyer, D. K. Ralston, and J. A. Lerczak, 2012: Estuarine Exchange Flow Quantified with Isohaline Coordinates: Contrasting Long and Short Estuaries. *Journal of Physical Oceanography*, **42 (5)**, 748–763.

Cronin, M., and J. Sprintall, 2009: Wind and buoyancy-forced upper ocean. *Elements of Physical Oceanography: A derivative of the Encyclopedia of Ocean Sciences*, 237–245.

Dijkstra, Y. M., H. M. Schuttelaars, and H. Burchard, 2017: Generation of exchange flows in estuaries by tidal and gravitational eddy viscosity-shear covariance (ESCO). *Journal of Geophysical Research: Oceans*, **122 (5)**, 4217–4237.

Feistel, R., G. Nausch, and E. Hagen, 2006: Unusual Baltic inflow activity in 2002-2003 and varying deep-water properties. *Oceanologia*, **48**, 21–35.

Fischer, H. B., 1976: Mixing and dispersion in estuaries. *Annual Review of Fluid Mechanics*, **8 (1)**, 107–133.

Geyer, W., 1997: Influence of wind on dynamics and flushing of shallow estuaries. *Estuarine, Coastal and Shelf Science*, **44 (6)**, 713–722.

Geyer, W. R., and P. MacCready, 2014: The estuarine circulation. *Annual Review of Fluid Mechanics*, **46**, 175–197.

Giddings, S. N., and P. MacCready, 2017: Reverse Estuarine Circulation Due to Local and Remote Wind Forcing, Enhanced by the Presence of Along-Coast Estuaries. *Journal of Geophysical Research: Oceans*, **122 (12)**, 10 184–10 205.

Gräwe, U., P. Holtermann, K. Klingbeil, and H. Burchard, 2015: Advantages of vertically adaptive coordinates in numerical models of stratified shelf seas. *Ocean Modelling*, **92**, 56–68.

Groeskamp, S., S. M. Griffies, D. Iudicone, R. Marsh, A. G. Nurser, and J. D. Zika, 2019: The water mass transformation framework for ocean physics and biogeochemistry. *Annual Review of Marine Science*, **11**, 271–305.

Hansen, D. V., and M. Rattray, 1965: Gravitational circulation in straits and estuaries. *Journal of Marine Research*, **23**, 104–122.

Hetland, R. D., and W. R. Geyer, 2004: An idealized study of the structure of long, partially mixed estuaries. *Journal of Physical Oceanography*, **34 (12)**, 2677–2691.

Hetzel, Y., C. Pattiaratchi, and H. Mihanović, 2018: Exchange flow variability between hypersaline Shark Bay and the ocean. *Journal of Marine Science and Engineering*, **6 (2)**, 65.

Hieronymus, M., J. Nilsson, and J. Nycander, 2014: Water mass transformation in salinity–temperature space. *Journal of Physical Oceanography*, **44 (9)**, 2547–2568.

Hofmeister, R., J.-M. Beckers, and H. Burchard, 2011: Realistic modelling of the exceptional inflows into the central Baltic Sea in 2003 using terrain-following coordinates. *Ocean Modelling*, **39 (3-4)**, 233–247.

Hofmeister, R., H. Burchard, and J.-M. Beckers, 2010: Non-uniform adaptive vertical grids for 3D numerical ocean models. *Ocean Modelling*, **33 (1)**, 70–86.

Jain, V., and Coauthors, 2017: Evidence for the existence of Persian Gulf water and Red Sea water in the Bay of Bengal. *Climate Dynamics*, **48 (9-10)**, 3207–3226.

Jay, D. A., and J. D. Smith, 1990: Circulation, density distribution and neap-spring transitions in the Columbia River Estuary. *Progress in Oceanography*, **25 (1-4)**, 81–112.

Jerlov, N. G., 1976: *Marine optics*, Vol. 14. Elsevier.

Johns, W., F. Yao, D. Olson, S. Josey, J. Grist, and D. Smeed, 2003: Observations of seasonal exchange through the Straits of Hormuz and the inferred heat and freshwater budgets of the Persian Gulf. *Journal of Geophysical Research: Oceans*, **108 (C12)**.

Kämpf, J., and M. Sadrinasab, 2006: The circulation of the Persian Gulf: a numerical study. *Ocean Science*, **2 (1)**, 27–41.

Kappenberg, J., G. Schymura, and H.-U. Fanger, 1995: Sediment dynamics and estuarine circulation in the turbidity maximum of the Elbe River. *Netherland Journal of Aquatic Ecology*, **29 (3-4)**, 229–237.

Kärnä, T., A. M. Baptista, J. E. Lopez, P. J. Turner, C. McNeil, and T. B. Sanford, 2015: Numerical modeling of circulation in high-energy estuaries: A Columbia River estuary benchmark. *Ocean Modelling*, **88**, 54–71.

Klingbeil, K., F. Lemarié, L. Debreu, and H. Burchard, 2018: The numerics of hydrostatic structured-grid coastal ocean models: state of the art and future perspectives. *Ocean Modelling*, **125**, 80–105.

Klingbeil, K., M. Mohammadi-Aragh, U. Gräwe, and H. Burchard, 2014: Quantification of spurious dissipation and mixing – Discrete Variance Decay in a Finite-Volume framework. *Ocean Modelling*, **81**, 49–64.

Knudsen, M., 1900: Ein hydrographischer Lehrsatz. *Annalen der Hydrographie und Maritimen Meteorologie*, **28 (7)**, 316–320.

Lange, X., and H. Burchard, 2019: The relative importance of wind straining and gravitational forcing in driving exchange flows in tidally energetic estuaries. *Journal of Physical Oceanography*, **49 (3)**, 723–736.

Lange, X., K. Klingbeil, and H. Burchard, 2020: Inversions of Estuarine Circulation Are Frequent in a Weakly Tidal Estuary With Variable Wind Forcing and Seaward Salinity Fluctuations. *Journal of Geophysical Research: Oceans*, **125 (9)**, e2019JC015 789.

Lemagie, E. P., and J. A. Lerczak, 2015: A Comparison of Bulk Estuarine Turnover Timescales to Particle Tracking Timescales Using a Model of the Yaquina Bay Estuary. *Estuaries and Coasts*, **38**, 1797–1814.

L'Hégaret, P., R. Duarte, X. Carton, C. Vic, D. Ciani, R. Baraille, and S. Corréard, 2015: Mesoscale variability in the Arabian Sea from HYCOM model results and observations: impact on the Persian Gulf Water path. *Ocean Science*, **11 (5)**, 667–693.

Lorenz, M., K. Klingbeil, and H. Burchard, 2020: Numerical Study of the Exchange Flow of the Persian Gulf Using an Extended Total Exchange Flow Analysis Framework. *Journal of Geophysical Research: Oceans*, **125 (2)**, e2019JC015 527.

Lorenz, M., K. Klingbeil, and H. Burchard, submitted: Impact of evaportion and precipitation on estuarine mixing relations. *Journal of Physical Oceanography*.

Lorenz, M., K. Klingbeil, P. MacCready, and H. Burchard, 2019: Numerical issues of the Total Exchange Flow (TEF) analysis framework for quantifying estuarine circulation. *Ocean Science*, **15 (3)**, 601–614.

MacCready, P., 2011: Calculating estuarine exchange flow using isohaline coordinates. *Journal of Physical Oceanography*, **41 (6)**, 1116–1124.

MacCready, P., and W. R. Geyer, 2010: Advances in estuarine physics. *Annual Review of Marine Science*, **2 (1)**, 35–58.

MacCready, P., W. Rockwell Geyer, and H. Burchard, 2018: Estuarine Exchange Flow is Related to Mixing through the Salinity Variance Budget. *Journal of Physical Oceanography*, **48**, 1375–1384.

Morvan, M., P. L'Hégaret, X. Carton, J. Gula, C. Vic, C. de Marez, M. Sokolovskiy, and K. Koshel, 2019: The life cycle of submesoscale eddies generated by topographic interactions. *Ocean Science*, **15 (6)**, 1531–1543.

Nahas, E. L., C. B. Pattiaratchi, and G. N. Ivey, 2005: Processes controlling the position of frontal systems in Shark Bay, Western Australia. *Estuarine, Coastal and Shelf Science*, **65 (3)**, 463–474.

Nash, J. D., and J. N. Moum, 2002: Microstructure Estimates of Turbulent Salinity Flux and the Dissipation Spectrum of Salinity. *Journal of Physical Oceanography*, **32 (8)**, 2312–2333.

Pinardi, N., and E. Masetti, 2000: Variability of the large scale general circulation of the Mediterranean Sea from observations and modelling: a review. *Palaeogeography, Palaeoclimatology, Palaeoecology*, **158 (3-4)**, 153–173.

Placke, M., H. Meier, U. Gräwe, T. Neumann, C. Frauen, and Y. Liu, 2018: Long-term mean circulation of the Baltic Sea as represented by various ocean circulation models. *Frontiers in Marine Science*, **5**, 287.

Pous, S., X. Carton, and P. Lazure, 2004: Hydrology and circulation in the Strait of Hormuz and the Gulf of Oman—Results from the GOGP99 Experiment: 1. Strait of Hormuz. *Journal of Geophysical Research: Oceans*, **109 (C12)**.

Pous, S., P. Lazure, and X. Carton, 2015: A model of the general circulation in the Persian Gulf and in the Strait of Hormuz: Intraseasonal to interannual variability. *Continental Shelf Research*, **94**, 55–70.

Privett, D., 1959: Monthly charts of evaporation from the N. Indian Ocean (including the Red Sea and the Persian Gulf). *Quarterly Journal of the Royal Meteorological Society*, **85 (366)**, 424–428.

Ralston, D. K., W. R. Geyer, and J. A. Lerczak, 2008: Subtidal salinity and velocity in the hudson river estuary: Observations and modeling. *Journal of Physical Oceanography*, **38 (4)**, 753–770.

Reynolds, R. M., 1993: Physical oceanography of the Gulf, Strait of Hormuz, and the Gulf of Oman—Results from the Mt Mitchell expedition. *Marine Pollution Bulletin*, **27**, 35–59.

Rodi, W., 1987: Examples of calculation methods for flow and mixing in stratified fluids. *Journal of Geophysical Research: Oceans*, **92**, 5305–5328.

Shchepetkin, A. F., and J. C. McWilliams, 2003: A method for computing horizontal pressure-gradient force in an oceanic model with a nonaligned vertical coordinate. *Journal of Geophysical Research: Oceans*, **108 (C3)**.

Simpson, J., C. Allen, and N. Morris, 1978: Fronts on the continental shelf. *Journal of Geophysical Research: Oceans*, **83 (C9)**, 4607–4614.

Simpson, J. H., J. Brown, J. Matthews, and G. Allen, 1990: Tidal straining, density currents, and stirring in the control of estuarine stratification. *Estuaries*, **13 (2)**, 125–132.

Speer, K. G., 1993: Conversion among North Atlantic surface water types. *Tellus*, **45 (1)**, 72–79.

Stacey, M. T., M. L. Brennan, J. R. Burau, and S. G. Monismith, 2010: The tidally averaged momentum balance in a partially and periodically stratified estuary. *Journal of Physical Oceanography*, **40 (11)**, 2418–2434.

Swift, S. A., and A. S. Bower, 2003: Formation and circulation of dense water in the Persian/Arabian Gulf. *Journal of Geophysical Research: Oceans*, **108 (C1)**.

Thoppil, P. G., and P. J. Hogan, 2009: On the mechanisms of episodic salinity outflow events in the Strait of Hormuz. *Journal of Physical Oceanography*, **39 (6)**, 1340–1360.

Thoppil, P. G., and P. J. Hogan, 2010: Persian gulf response to a wintertime shamal wind event. *Deep Sea Research Part I: Oceanographic Research Papers*, **57 (8)**, 946–955.

Umlauf, L., and H. Burchard, 2005: Second-order turbulence closure models for geophysical boundary layers. A review of recent work. *Continental Shelf Research*, **25 (7-8)**, 795–827.

Valle-Levinson, A., 2010: Definition and classification of estuaries. *Contemporary Issues in Estuarine Physics*.

Valle-Levinson, A., C. Reyes, and R. Sanay, 2003: Effects of bathymetry, friction, and rotation on estuary–ocean exchange. *Journal of Physical Oceanography*, **33 (11)**, 2375–2393.

Vic, C., G. Roullet, X. Capet, X. Carton, M. J. Molemaker, and J. Gula, 2015: Eddy-topography interactions and the fate of the Persian Gulf Outflow. *Journal of Geophysical Research: Oceans*, **120 (10)**, 6700–6717.

Walin, G., 1977: A theoretical framework for the description of estuaries. *Tellus*, **29**, 128–136.

Walin, G., 1982: On the relation between sea-surface heat flow and thermal circulation in the ocean. *Tellus*, **34 (2)**, 187–195.

Wang, T., W. R. Geyer, and P. MacCready, 2017: Total exchange flow, entrainment, and diffusive salt flux in estuaries. *Journal of Physical Oceanography*, **47 (5)**, 1205–1220.

Warner, J. C., W. R. Geyer, and J. A. Lerczak, 2005: Numerical modeling of an estuary: A comprehensive skill assessment. *Journal of Geophysical Research: Oceans*, **110 (C5)**.

Wolanski, E., 1986: An evaporation-driven salinity maximum zone in Australian tropical estuaries. *Estuarine, Coastal and Shelf Science*.

Woo, M., and C. Pattiaratchi, 2008: Hydrography and water masses off the western Australian coast. *Deep Sea Research Part I: Oceanographic Research Papers*, **55 (9)**, 1090–1104.

Yao, F., and W. E. Johns, 2010a: A HYCOM modeling study of the Persian Gulf: 1. Model configurations and surface circulation. *Journal of Geophysical Research: Oceans*, **115 (C11)**.

Yao, F., and W. E. Johns, 2010b: A HYCOM modeling study of the Persian Gulf: 2. Formation and export of Persian Gulf Water. *Journal of Geophysical Research: Oceans*, **115 (C11)**.

Appendix A.

Declaration of my contributions to the publications

A.1. Numerical issues of the Total Exchange Flow (TEF) analysis framework for quantifying estuarine circulation

This paper was written during the first 14 months of my Ph.D. The concept for this study was initiated by my supervisor, Hans Burchard. He already started working on the manuscript, so the general structure was already there. Yet, less than 20% remained of this manuscript version. The analysis was completely redone with the new, converging computation method. In addition, I added a new analysis region, the Gotland Basin, to demonstrate the capability to describe multi-layered exchange flow cases. In the end, all plots and all analyses were done by myself. I have done more than 80% of the writing and 100% of the revisions with the valuable input of my co-authors during all stages of the study.

A.2. Numerical Study of the Exchange Flow of the Persian Gulf Using an Extended Total Exchange Flow Analysis Framework

The second paper was initiated again by my supervisor with the idea to analyze the exchange flow of an inverse estuary, the Persian Gulf, as an inverse Baltic Sea with the Total Exchange Flow (TEF) analysis framework. From there on, I designed the study from scratch. I set up the model setup, calibrated the model with input of my co-authors, and performed the numerical simulations. Furthermore, I extended the

TEF analysis framework to include potential temperature as a second coordinate, since the water masses of the exchange flow showed a significant temperature difference between inflow and outflow. Overall, the analysis and plots of the study were done 100% by myself. I also did all of the writing and the revisions, with valuable input and corrections from my co-authors.

A.3. Impact of evaporation and precipitation on estuarine mixing relations

The idea behind this paper came when working on the numerical model of the second paper. Recent studies, where my supervisor was involved in, derive mixing relations for estuaries driven by river discharge. The obvious question was then, how the estuarine mixing relations work for estuaries forced by evaporation or precipitation. From there on, I derived an expression that can describe these types of estuaries. I further designed the study from scratch, performed 100% of the numerical modeling, performed 100% of the analysis, and did 99% of the writing with valuable input and corrections from my co-authors throughout all stages of this study.

Appendix B.

Publications

Ocean Sci., 15, 601–614, 2019
https://doi.org/10.5194/os-15-601-2019
© Author(s) 2019. This work is distributed under
the Creative Commons Attribution 4.0 License.

Ocean Science Open Access EGU

Numerical issues of the Total Exchange Flow (TEF) analysis framework for quantifying estuarine circulation

Marvin Lorenz[1], **Knut Klingbeil**[1], **Parker MacCready**[2], **and Hans Burchard**[1]

[1]Leibniz Institute for Baltic Sea Research Warnemünde, Physical Oceanography and Instumentation, Rostock, Germany
[2]University of Washington, College of Environment, School of Oceanography, Seattle, WA, USA

Correspondence: Marvin Lorenz (marvin.lorenz@io-warnemuende.de)

Received: 18 December 2018 – Discussion started: 4 February 2019
Revised: 23 April 2019 – Accepted: 6 May 2019 – Published: 29 May 2019

Abstract. For more than a century, estuarine exchange flow has been quantified by means of the Knudsen relations which connect bulk quantities such as inflow and outflow volume fluxes and salinities. These relations are closely linked to estuarine mixing. The recently developed Total Exchange Flow (TEF) analysis framework, which uses salinity coordinates to calculate these bulk quantities, allows an exact formulation of the Knudsen relations in realistic cases. There are however numerical issues, since the original method does not converge to the TEF bulk values for an increasing number of salinity classes. In the present study, this problem is investigated and the method of dividing salinities, described by MacCready et al. (2018), is mathematically introduced. A challenging yet compact analytical scenario for a well-mixed estuarine exchange flow is investigated for both methods, showing the proper convergence of the dividing salinity method. Furthermore, the dividing salinity method is applied to model results of the Baltic Sea to demonstrate the analysis of realistic exchange flows and exchange flows with more than two layers.

1 Introduction

The Total Exchange Flow (TEF) analysis framework calculates time-averaged net volume and mass transport between enclosed volumes of the ocean and ambient water masses, sorted by salinity classes. Since oscillatory inflow and outflow components occurring at the same salinity compensate for one another, TEF characterises the net exchange flow with the ambient ocean. Salinity rather than density or temperature is used as a coordinate for calculating estuarine exchange flow, since only the salt budget is entirely controlled by the exchange flow. Therefore, salt is the only conserved quantity. In contrast, temperature and thus density are additionally affected by the freshwater runoff and the surface heat fluxes.

A first bulk approach based on inflow and outflow salinity and volume transport had been developed and applied to the exchange flow of the Baltic Sea by Knudsen (1900). The theoretical framework based on a continuous salinity space was first developed by Walin (1977) and was later applied to exchange flow in the Baltic Sea (Walin, 1981). A comparable framework had been applied by Döös and Webb (1994) for quantifying meridional overturning circulation in the Southern Ocean. Both the bulk concept by Knudsen (1900) and the continuous concept by Walin (1977) had been consistently combined by MacCready (2011), who also coined the term TEF.

The TEF analysis framework considers a time-averaged transport of a tracer c, Q^c, through the cross-sectional area $A(s > S)$, which has a salinity s above a specific value S. Q^c is defined as

$$Q^c(S) = \left\langle \int_{A(s>S)} c\,u\,\mathrm{d}A \right\rangle, \tag{1}$$

where u is the incoming velocity normal to $A(s > S)$ with the definition that positive u brings water into the estuary and $\langle\rangle$ denotes temporal averaging. The exchange profile of tracer flux per salinity as a function of the salinity is then obtained by differentiating $Q^c(S)$ with respect to S:

$$q^c(S) = -\frac{\partial Q^c(S)}{\partial S}, \tag{2}$$

such that Q^c can be also obtained via integration of q^c in salinity space:

$$Q^c(S) = \int\limits_{S'>S} q^c(S')\,\mathrm{d}S' = \int\limits_{S}^{S_{\max}} q^c(S')\,\mathrm{d}S'. \tag{3}$$

Based on these quantities, consistent Knudsen bulk values for inflowing and outflowing salinity (s_{in}, s_{out}), volume flux ($Q^1_{\mathrm{in}} = Q_{\mathrm{in}}$, Q_{out}) and salt flux (Q^s_{in}, Q^s_{out}), obeying

$$s_{\mathrm{in}} = \frac{Q^s_{\mathrm{in}}}{Q_{\mathrm{in}}}, \quad s_{\mathrm{out}} = \frac{Q^s_{\mathrm{out}}}{Q_{\mathrm{out}}}, \tag{4}$$

can be obtained. MacCready (2011) calculates the inflowing and outflowing bulk fluxes by integrating over positive and negative parts of q^c:

$$Q^{c,\,\mathrm{sign}}_{\mathrm{in}} = \int\limits_{S_{\min}}^{S_{\max}} (q^c)^+\,\mathrm{d}S, \quad Q^{c,\,\mathrm{sign}}_{\mathrm{out}} = \int\limits_{S_{\min}}^{S_{\max}} (q^c)^-\,\mathrm{d}S, \tag{5}$$

where, for any function a, the positive part is calculated as $(a)^+ = \max(a, 0)$ and the negative part is calculated as $(a)^- = \min(a, 0)$. In (5), $S_{\min}$ and $S_{\max}$ are the minimum and maximum salinities. We will call this method of integrating positive and negative contributions separately to obtain the Q^c_{in} and Q^c_{out} sign method in the following.

Recently, Klingbeil et al. (2019) showed the relation between TEF and thickness-weighted averaging. The concepts by Knudsen (1900), Walin (1977) and MacCready (2011) were focused on estuarine systems, which are characterised by distinct volume inflow Q_r of water masses of (almost) zero salinity. The exchange flow between the estuary and the ocean is described by the Knudsen bulk values. The TEF analysis framework provides one consistent calculation method for these bulk values, which for this case describe the net exchange flow. Since there is no clear definition of the Knudsen bulk values, we will call these "TEF bulk values" to distinguish between other bulk values which also fulfill the Knudsen relations, e.g. bulk values computed from a Eulerian version of TEF. The Knudsen relations have been reviewed in detail for exchange flow in the western Baltic Sea by Burchard et al. (2018). Recently, MacCready et al. (2018) showed how the bulk concept can be used to estimate the volume-integrated average mixing M (defined as the rate of reduction of the net salinity variance due to mixing) in estuaries: $M \approx s_{\mathrm{in}} s_{\mathrm{out}} Q_r$, i.e. the volume-integrated average mixing in an estuary is approximated by the product of inflow and outflow salinity with the estuarine freshwater supply. This mixing estimate by MacCready et al. (2018) approximates the TEF-based exact formulations developed by Burchard et al. (2018b).

Since the TEF analysis framework is continuous in salinity, a discretisation in salinity space is required when analysing data from numerical model simulations or field observations. In their Appendix A2, Klingbeil et al. (2019) presented the remapping of discrete data into bins. As a result, the output of a numerical model consists of a finite number of transport values associated with the same number of discrete salinities. Comparable to a histogram, the transport data are binned into salinity classes according to their associated salinities. As discussed by MacCready et al. (2018), the resulting TEF profiles can become noisy, i.e. the sign changes in q^c, when the number of discrete salinity classes N is chosen too high. For data sets with pairwise disjunct salinities, the number of transport values assigned to a single salinity bin decreases with the number of the salinity bins. After exceeding a threshold number of salinity classes, the bins will be sufficiently small to hold at most one transport value. In this case, $Q^{\mathrm{sign}}_{\mathrm{in}}$ is equal to $Q^{\mathrm{abs}}_{\mathrm{in}}$, with

$$Q^{\mathrm{abs}}_{\mathrm{in}} = \left\langle \int_A u^+ \mathrm{d}A \right\rangle. \tag{6}$$

In most practical applications, the salinity data are neither constant in space nor time, and in the limit of an infinite number of salinity classes $Q^{\mathrm{sign}}_{\mathrm{in}}$ will converge to $Q^{\mathrm{abs}}_{\mathrm{in}}$, which is not the desired result for Q_{in}.

In order to obtain robust bulk values, which are less sensitive to the number of salinity bins, MacCready et al. (2018) suggested an alternative to the sign method. Instead of finding an optimal number of bins (a problem well known for histograms; Knuth, 2006), they suggested to find a dividing salinity S_{div} which separates the inflow and outflow of a classical two-layer estuary with inflow at high and outflow at low salinity classes, i.e. $q^c(S_{\mathrm{div}}) = 0$ and $Q^c(S_{\mathrm{div}}) = \max(Q^c(S))$. The bulk values for inflow and outflow are then obtained by integrating

$$Q^{c,\,\mathrm{div}}_{\mathrm{in}} = \int\limits_{S_{\mathrm{div}}}^{S_{\max}} q^c\,\mathrm{d}S, \quad Q^{c,\,\mathrm{div}}_{\mathrm{out}} = \int\limits_{S_{\min}}^{S_{\mathrm{div}}} q^c\,\mathrm{d}S. \tag{7}$$

It should be noted that analytically, and for smooth q^c with only one zero crossing, both methods coincide. We will show in Sect. 2 the different convergence behaviours and will show that the dividing salinity method indeed converges towards robust TEF bulk values, e.g. $\lim\limits_{N\to\infty} Q^{\mathrm{div}}_{\mathrm{in}}(N) = Q_{\mathrm{in}}$, where $Q^{\mathrm{div}}_{\mathrm{in}}$ denotes the inflowing volume flux computed with the dividing salinity method (7) for $c = 1$.

Using the maximum of Q only works for classical two-layer exchange flows. In Sect. 3, we will introduce an extended formulation of the dividing salinity method which includes inverse estuaries (outflow at high salinities and inflow at low salinities) as well as exchange flows with more than two exchange layers in salinity space. Furthermore, in Sect. 3.2, the corresponding discrete description is presented. Afterwards, in Sect. 4, the extended method is applied to nu-

merical output from a model of the Baltic Sea, before we conclude in Sect. 5.

2 Convergence analysis for an analytical classical exchange flow

To demonstrate the different convergence behaviours of the sign method and the dividing salinity method, we take the analytical example from Burchard et al. (2019). It describes a well-mixed tidal flow with oscillating salinity as it occurs, e.g. in the Wadden Sea (Purkiani et al., 2015). The velocity and salinity are given by

$$u(t) = u_\mathrm{r} + u_\mathrm{a}\cos(\omega t), \quad s(t) = s_\mathrm{r} + s_\mathrm{a}\cos(\omega t + \phi), \tag{8}$$

with the residual velocity $u_\mathrm{r} < 0$, the residual salinity s_r, the velocity and salinity amplitudes $u_\mathrm{a} > 0$ and $s_\mathrm{a} > 0$, with $s_\mathrm{r} - s_\mathrm{a} \geq 0$, the tidal frequency $\omega = 2\pi/T$ with the tidal period T and the tidal phase ϕ. The tidally averaged salinity transport is given by

$$\frac{1}{T}\int_0^T us\,\mathrm{d}t = u_\mathrm{r}s_\mathrm{r} + \frac{u_\mathrm{a}s_\mathrm{a}}{2}\cos(\phi). \tag{9}$$

Zero residual salt transport therefore requires

$$\cos(\phi) = -2\frac{u_\mathrm{r}s_\mathrm{r}}{u_\mathrm{a}s_\mathrm{a}} \quad \text{with} \quad u_\mathrm{a}s_\mathrm{a} \geq 2|u_\mathrm{r}|s_\mathrm{r}. \tag{10}$$

Figure 1 shows an example for $u(t)$, $s(t)$ and $u(t)\cdot s(t)$, with $A = 10\,000\,\mathrm{m}^2$, $u_\mathrm{r} = -0.1\,\mathrm{m\,s^{-1}}$, $u_\mathrm{a} = 1\,\mathrm{m\,s^{-1}}$, $s_\mathrm{r} = 20\,\mathrm{g\,kg^{-1}}$ and $s_\mathrm{a} = 10\,\mathrm{g\,kg^{-1}}$, resulting in $\phi = -1.16 = -0.185\cdot 2\pi$. In this case, $Q(S)$, $Q^s(S)$ and S_div can be calculated analytically by either (5) or (7) (see Appendix A) and are shown in Fig. 2d. By means of (4), the inflow and outflow volume fluxes and salinities, Q_in, Q_out, s_in and s_out, can then be exactly calculated. The resulting analytical TEF bulk values are $Q_\mathrm{in} = 813.240\,\mathrm{m^3 s^{-1}}$, $Q_\mathrm{out} = -1813.240\,\mathrm{m^3 s^{-1}}$, $s_\mathrm{in} = 28.424\,\mathrm{g\,kg^{-1}}$ and $s_\mathrm{out} = 12.748\,\mathrm{g\,kg^{-1}}$.

We created a time series of $I = 10^5$ time steps of (8) and computed $q(S)$ and $q^s(S)$ for a varying number N of salinity classes between $S_\mathrm{min} = 10\,\mathrm{g\,kg^{-1}}$ and $S_\mathrm{max} = 31\,\mathrm{g\,kg^{-1}}$; see Fig. 2. In Fig. 2a ($N = 128$), the small N leads to smooth profiles for both q and Q. Profiles of higher numbers ($N = 1024$, $N = 8192$) of salinity classes exhibit more noisy q but apparently still smooth Q (Fig. 2b, c). Comparison with the analytical solution (Fig. 2d) shows that Q is similar for all N and q becomes more noisy. This is a result of the numerical discretisation of the data. Most likely, the numerical values (e.g. due to round-off errors) for these salinities are all different. Other than in continuous salinity space where inflows and outflows in the same salinity class partially compensate for one another, the corresponding discrete values could be associated with different salinity classes and the compensation does not occur anymore, resulting in noisy profiles, which

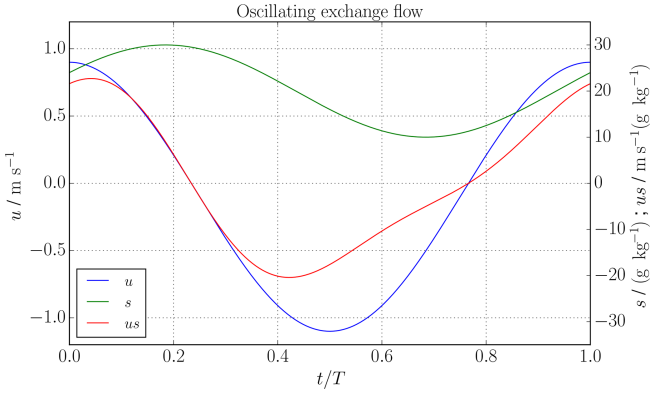

Figure 1. Oscillating exchange flow (see Sect. 2): time series of velocity (blue), salinity (green) and salinity flux (red) for the oscillating exchange flow scenario (8).

leads to errors in the results of the sign method. Q only appears to be smooth, but the noise is of course apparent since Q and q are dependent on each other. The integration process of the discrete q^c (see (3)) smooths the resulting Q^c.

To study the convergence of the two different methods (the sign method and dividing salinity method), one can compare the errors in discrete form to the analytical values. Figure 3 shows the relative error, $|Q_\mathrm{in}(I, N) - Q_\mathrm{in}|/|Q_\mathrm{in}|$, of the numerically computed inflow bulk values depending on the number of time steps I and the number of salinity classes N. For this analytical scenario, both methods coincide for a small number of salinity classes. For increasing N, the error of the sign method increases beyond a critical number of salinity classes and converges to the error of the absolute values (black line, 6), whereas the dividing salinity method converges towards a small constant relative error. The critical point where the error of the sign method increases is different for each number of time steps. The convergence analysis for different numbers of time steps I is done to gain experience in the impact of temporal resolution of the oscillating flow on the final bulk values. With the time step here being the equivalent to the output interval of a hydrodynamic model which provides data for TEF, the findings can directly be transferred to the analysis of model data. The error of the dividing salinity method decreases continuously with an increasing number of time steps I, showing that indeed the dividing salinity method converges towards the correct bulk values. Interestingly, there is almost no difference for $I = 10^3$ and $I = 10^4$, and $I = 10^5$ and $I = 10^6$, for the dividing salinity method, which is due to the compensation of the added values in the data of $u(t)$ and $s(t)$. For this scenario of a well-mixed estuary, one tidal period should be resolved with at least 1000 time steps, meaning one data point every minute or less, to find the transport Q_in with an error less than 0.1 % with the dividing salinity method. This is due the strong time dependency on the problem. For a stationary problem, one point in time would be sufficient to find the correct exchange flow.

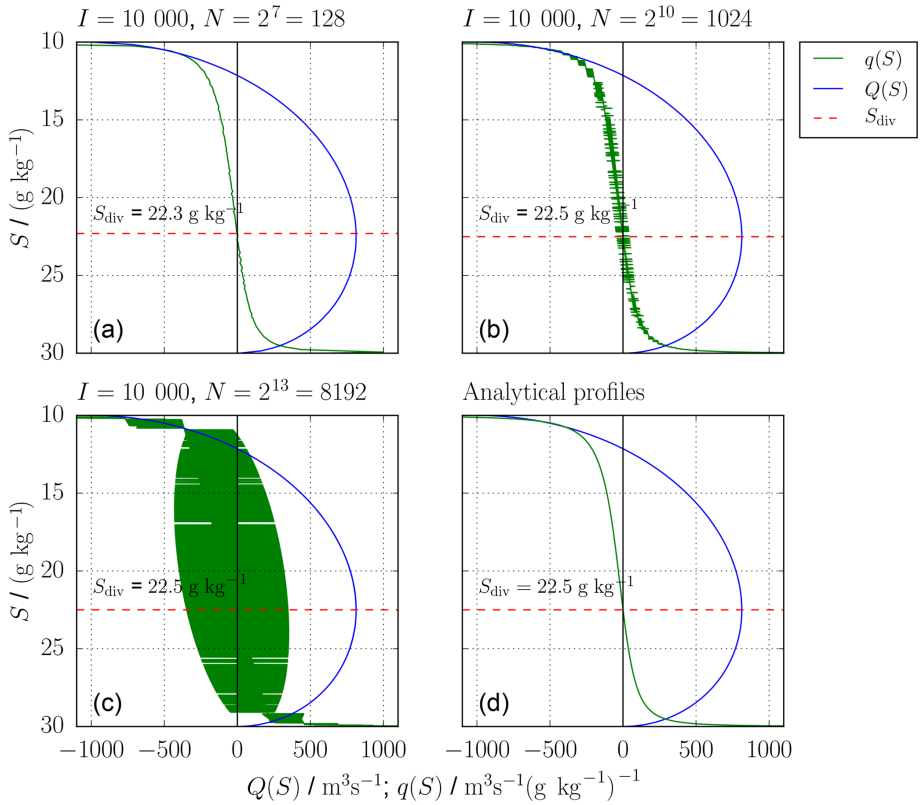

Figure 2. Oscillating exchange flow (see Sect. 2): from (14) and (15) numerically **(a–c)** and analytically **(d)** found $Q(S)$ (blue), $q(S)$ (green), dividing salinity, S_{div} (dashed, red), for $I = 10^4$ time steps for one tidal cycle and varying number of salinity classes N. With increasing N, q becomes more noisy, whereas Q seems unchanged.

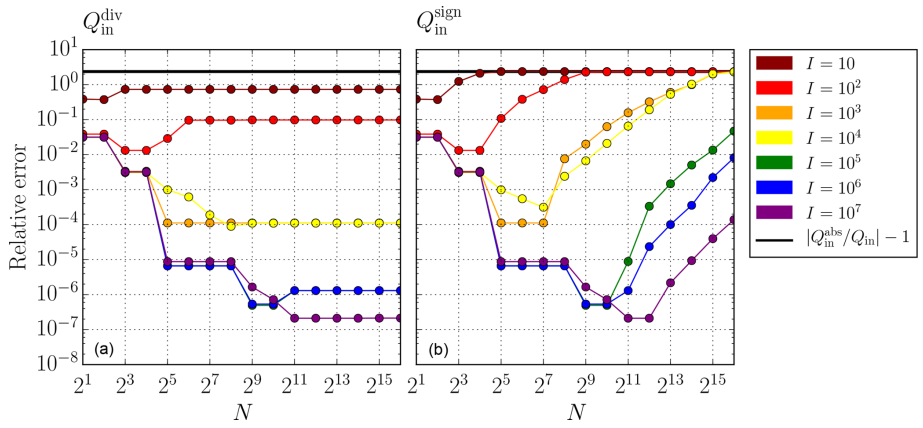

Figure 3. Oscillating exchange flow (see Sect. 2): relative error of Q_{in} computed with **(a)** the dividing salinity method and **(b)** the sign method depending on the number of time steps I (colour) and salinity classes N. The sign method (5) and the dividing salinity method (7) coincide for a small number of salinity classes, but the error of the sign method converges in the limit of large N towards the error of the absolute bulk values (black line, 6). In contrast, the error of the dividing salinity method converges towards a constant value. The errors of both methods decrease with increasing number of time steps I.

3 Extended dividing salinity method

3.1 Mathematical formulation

Encouraged by the good convergence behaviour of the dividing salinity method demonstrated in the previous section, we introduce here a general formulation which includes inverse estuaries and exchange flows with more than two layers. The general idea is to identify the salinities which divide q^c into inflowing and outflowing parts. This corresponds to zero crossings, dividing $q^c > 0$ and $q^c < 0$. Analytically, the zero crossings are calculated by solving $q^c(S_{\mathrm{div}}) = 0$ for S_{div}. However, as the discrete q^c might be very noisy with too many zero crossings (see Sect. 2), we propose finding the extrema of the discrete Q^c profiles, which share the same salinities as the zero crossings. Figure 4 shows a hypothetical exchange flows of four layers, separated by five dividing salinities which can be sorted in ascending order: $S_{\mathrm{min}} = S_{\mathrm{div},\,1} < S_{\mathrm{div},\,2} < S_{\mathrm{div},\,3} < S_{\mathrm{div},\,4} < S_{\mathrm{div},\,5} = S_{\mathrm{max}}$. The fluxes ΔQ^c_j in each layer can be calculated by

$$\Delta Q^c_j = \int_{S_{\mathrm{div},\,j}}^{S_{\mathrm{div},\,j+1}} q^c \,\mathrm{d}S = Q^c(S_{\mathrm{div},\,j+1}) - Q^c(S_{\mathrm{div},\,j}). \tag{11}$$

In the next step, inflow segments with $\Delta Q^c_j > 0$ and outflow segments with $\Delta Q^c_j < 0$ can be identified and indexed. For the example in Fig. 4, we index starting from S_{min}: $Q^c_{\mathrm{out},\,1} = \Delta Q^c_1$, $Q^c_{\mathrm{in},\,1} = \Delta Q^c_2$, $Q^c_{\mathrm{out},\,2} = \Delta Q^c_3$ and $Q^c_{\mathrm{in},\,2} = \Delta Q^c_4$. The representative salinities are calculated for each inflow and outflow similar to (4):

$$s_{\mathrm{in},\,m} = \frac{Q^s_{\mathrm{in},\,m}}{Q_{\mathrm{in},\,m}}, \quad s_{\mathrm{out},\,m} = \frac{Q^s_{\mathrm{out},\,m}}{Q_{\mathrm{out},\,m}}, \tag{12}$$

where m denotes the index with $m = 1, 2$ and so on. For a classical estuary, (11) reads as (7), where the only dividing salinity except S_{min} or S_{max} is $S_{\mathrm{div}} = S(\max(Q^c))$.

The mixing relations of MacCready et al. (2018) and Burchard et al. (2019) require only one value each for the inflow properties and outflow properties, respectively. These can be obtained from a multi-layer transect by applying weighted averages, i.e. for the inflowing bulk values:

$$Q^c_{\mathrm{in}} = \sum_m Q^c_{\mathrm{in},\,m},\; c_{\mathrm{in}} = \frac{\sum_m Q^c_{\mathrm{in},\,m}}{\sum_m Q_{\mathrm{in},\,m}} = \frac{\sum_m c_{\mathrm{in},\,m} Q_{\mathrm{in},\,m}}{\sum_m Q_{\mathrm{in},\,m}}, \tag{13}$$

and accordingly for Q^c_{out} and c_{out}.

3.2 Discrete formulation

The output from a numerical model along a transect across an estuary is assumed to consist of I time steps with $1 \le i \le I$ and $1 \le k \le K$, which are spatial increments per each time step. The output should include collocated model data s^i_k (salinity), c^i_k (tracer) and u^i_k (incoming normal velocity) which are available on cross-sectional area increments A^i_k. The salinity interval $[S_{1/2}, S_{N+1/2}]$, with $S_{1/2} < S_{\mathrm{min}}$ and $S_{\mathrm{max}} < S_{N+1/2}$, where $S_{\mathrm{min}} = \min(s)$ and $S_{\mathrm{max}} = \max(s)$, is divided into N equidistant intervals of length $\delta S = (S_{N+1/2} - S_{1/2})/N$; compare Fig. 5. The discrete profiles of q^c should be obtained directly without numerically calculating the volume flux profile Q^c before to avoid truncation errors due to numerical derivatives and to save computational time:

$$q^c_n = \frac{1}{I\delta S} \sum_{\substack{i \\ (\text{for } n = n^i_k)}} \sum_k u^i_k c^i_k A^i_k, \quad \text{with } n^i_k = \left\lfloor \left(\frac{s^i_k - S_{1/2}}{\delta S} \right) \right\rfloor, \tag{14}$$

where $\lfloor \cdot \rfloor$ is the integer truncation function. With this, the tracer flux increments are directly added to the respective salinity class; see the dots in the sketch of Fig. 5. Computation of $Q^c(S)$ can be easily carried out by summation of q^c_n:

$$Q^c_{n-1/2} = \delta S \sum_{n'=n}^{N} q^c_{n'}. \tag{15}$$

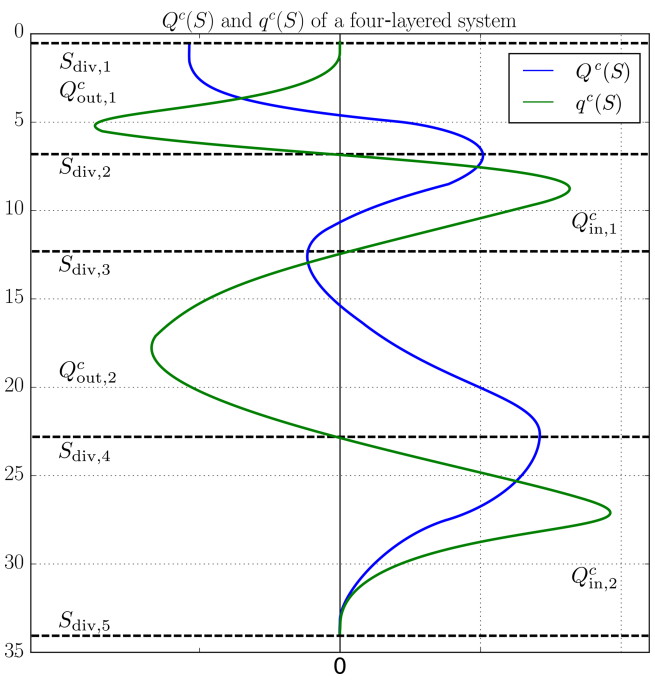

Figure 4. Sketch of hypothetical TEF profiles of a four-layered system with alternating inflows and outflows, $Q^c_{\mathrm{in},\,m}$ and $Q^c_{\mathrm{out},\,m}$. The respective inflows and outflows are divided by the zero crossings of $q^c(S)$ (green), so-called dividing salinities, $S_{\mathrm{div},\,j}$ (dashed, black), which correspond to the minima and maxima of $Q^c(S)$ (blue).

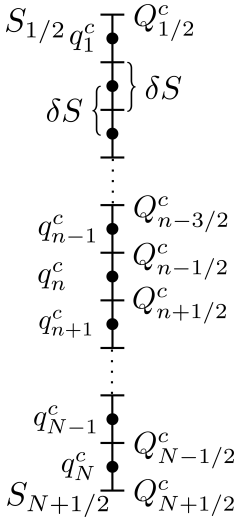

Figure 5. Sketch of how Q^c and q^c are located in a discrete salinity space. The salinity interval $[S_{1/2}, S_{N+1/2}]$ is divided into N equidistant salinity classes of length δS. The entries of Q^c (Q_n^c) are located on the lines, and the entries of q^c (q_n^c) are located on the dots.

Using the extended dividing salinity method defined in (11), the calculation for the transport reads

$$\Delta Q_j^c = Q_{n=n_{\mathrm{div},\,j+1}}^c - Q_{n=n_{\mathrm{div},\,j}}^c, \tag{16}$$

where $n_{\mathrm{div},\,j}$ and $n_{\mathrm{div},\,j+1}$ describe the indexes, where two consecutive extrema of Q^c are located. The dividing salinity indices are calculated with an algorithm which searches Q for local extrema by comparing every entry $Q_{n+1/2}$ to its nearest neighbours ($Q_{n-1/2}$ and $Q_{n+3/2}$). If $Q_{n+1/2}$ is greater (smaller) than its two neighbours, $n+1/2$ is stored as $n_{\mathrm{div},\,j}$ and denoted maximum (minimum). Afterwards, transport is computed according to (16), and only dividing salinities with transport greater than a threshold transport Q_{thresh} are considered. Please see Appendix B for a detailed description.

4 Application to exchange flow in the Baltic Sea

The Baltic Sea, shown in Fig. 6, can be considered as a large estuary with a long-term averaged river runoff of around $16\,000\,\mathrm{m^3 s^{-1}}$ and about balanced precipitation and evaporation (Matthäus and Schinke, 1999). In the estuarine classification diagram by Geyer and MacCready (2014), the Baltic Sea has been classified as a fjord type and a strongly stratified estuary, due to its relatively low runoff and relatively low mixing. The topography of the Baltic Sea consists of several basins of which the Gotland Basin in the central Baltic Sea, denoted as GB in Fig. 6, is the largest with a water depth of about 240 m. The shallow and narrow Danish Straits in the southwest provide the only connection to the saline North Sea.

Episodic inflow events of water consisting of a mixture of saline North Sea water and recirculated brackish Baltic Sea water (Meier et al., 2006) transport large amounts of salt and oxygen into the Baltic Sea. These inflows may either occur as major Baltic inflows (MBIs; i.e. as well-mixed, barotropic inflows) during winter months (Matthäus and Schinke, 1999; Mohrholz et al., 2015) or as baroclinic summer inflows (Feistel et al., 2004, 2006). These large inflow events propagate as dense bottom currents from basin to basin, where they are subject to entrainment of overlaying less saline water. The volume of the inflows increases and their salinity decreases on the way into the central Baltic Sea, where they ventilate the typically anoxic bottom layers (Reissmann et al., 2009). More frequent but weaker and less saline inflow events propagate through the western Baltic Sea (Sellschopp et al., 2006; Umlauf et al., 2007) and have the potential to ventilate intermediate layers but not the bottom layers in the central Baltic Sea (Reissmann et al., 2009). The major mixing process to transport saline bottom waters towards the surface of the central Baltic Sea has been identified as boundary mixing (Holtermann et al., 2012, 2014). However, recently double diffusion in the stratified interior has been discussed as another possibly efficient mixing process in the Baltic Sea (Umlauf et al., 2018). Finally, various surface mixed layer processes mix the salt into the surface layer of the Baltic Sea, such that a horizontal surface salinity gradient is established, with salinities varying from $25\,\mathrm{g\,kg^{-1}}$ in the Kattegat (K) to $5\,\mathrm{g\,kg^{-1}}$ in the Bothnian Bay (BoB). A permanent halocline separates these surface waters from the saline bottom waters. The halocline is located approximately in 70–90 m depth in the Gotland Basin. In addition, a seasonal thermocline develops during summer between 10 and 30 m (Reissmann et al., 2009). At times, salinity inversions occur in the strongly stratified thermocline, with surface waters being slightly more saline than waters in the thermocline (Burchard et al., 2017).

Above the halocline, driven by wind, inflows and Earth rotation, a cyclonic circulation is generally present in the central Baltic Sea, with net northward flow in the east of Gotland and southward flow in the west of Gotland (Meier, 2007; Omstedt et al., 2014). This cyclonic circulation is also present in the deeper layers of the central Baltic Sea, possibly driven by inflows and boundary mixing processes (Hagen and Feistel, 2007; Meier, 2007; Holtermann and Umlauf, 2012). This deep-water mean circulation is overlaid by topographic waves and inertial oscillations (Holtermann et al., 2014).

In the following, the numerical properties of the TEF analysis framework are tested against two transects of the Baltic Sea. The first transect is located across Darss Sill (D, red transect) in the western Baltic Sea over which part of the exchange with the North Sea is occurring; see Sect. 4.1. The second transect (green) is located in the Gotland Basin where we apply the extended dividing salinity method to the complicated multi-layer current system; see Sect. 4.2.

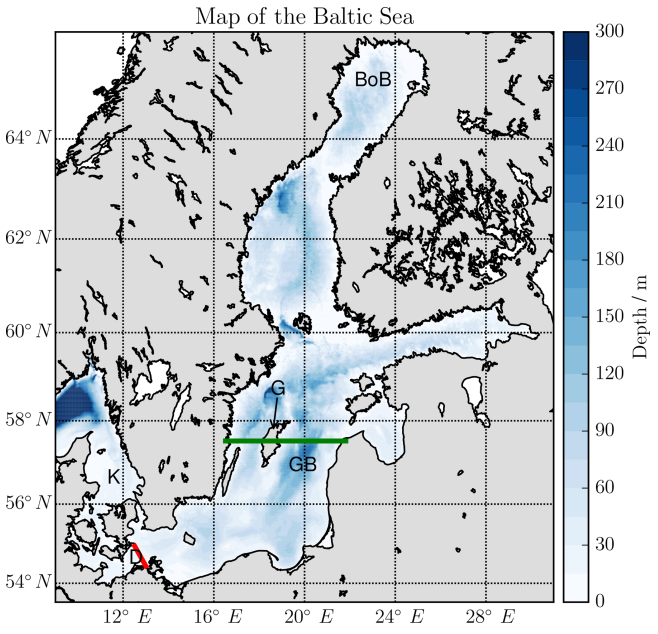

Figure 6. Map and bathymetry of the Baltic Sea. K: Kattegat, D: Darss Sill and the Darss Sill transect (red), G: the Gotland island, GB: Gotland Basin and the Gotland transect (green), BoB: Bothnian Bay.

4.1 Exchange flow over Darss Sill

In their recent review paper, Burchard et al. (2018) applied the Knudsen relations and the TEF analysis framework to analyse 65 years of high-resolution numerical model output for the western Baltic Sea using the General Estuarine Transport Model (GETM) (Burchard and Bolding, 2002; Hofmeister et al., 2010; Klingbeil and Burchard, 2013). Here, we investigate numerical properties of the TEF calculations based on the same numerical model output for the complex inflow years (2002/2003) with several barotropic and baroclinic inflows (Feistel et al., 2006) over the Darss Sill transect shown in Fig. 6.

The horizontal resolution of the model is about 600 m, and the water column is discretised by 42 vertical adaptive layers, the thickness of which vary in time and space (Gräwe et al., 2015). The salinity, velocity and layer thickness data are interpolated to 95 locations equally spaced by $\Delta x = 545\,\mathrm{m}$ along the 52 km long Darss Sill transect which is directed in northwest–southeast direction, such that the number of data points per time step is $K = 42 \cdot 95 = 3990$. The model output time step is $\Delta t = 3\,\mathrm{h}$, such that $I = 5840$ time steps for two simulation years are stored. These 3-hourly values are obtained by thickness-weighted averaging (Klingbeil et al., 2019) of the model layer values from all model time steps within the output interval.

Application of the TEF analysis framework for N different salinity classes is shown in Fig. 7, where a classical two-layer exchange flow with inflow at high salinities is seen. The upper panels show q and the respective TEF bulk values, computed with the sign method. q becomes more noisy with increasing N. The bulk values still change with increasing N. The lower panels show Q for the same N and the TEF bulk values computed with the extended dividing salinity method. These bulk values do converge for increasing N towards constant values. For this case, Q_{thresh} was set to $Q_{\mathrm{thresh}} = 100\,\mathrm{m^3\,s^{-1}}$.

The values found in this study with the dividing salinity method confirm that the found bulk values in Burchard et al. (2018) are correct and did not experience great errors from using the sign method.

Similar to the dependency of the TEF bulk values on I in the oscillating exchange flow in Sect. 2, we investigate the dependency of the TEF bulk values on the temporal resolution of the exchange flow. In order to do so, we repeated the TEF analyses for data obtained by thickness-weighted averaging of the 3-hourly model output to intervals of 12 h, and 1, 3, 5 and 10 d. For the dividing salinity method, the relative differences to estimated reference values for different time steps of the model output are calculated. The reference bulk values have been calculated by the dividing salinity method for $N = 2^{16} = 65\,536$ salinity classes and the 3-hourly output, since the exact values are not available. The hydrodynamic model was forced with 3-hourly atmospheric data, meaning that external processes of smaller timescales are not included. Therefore, the estimated bulk values can be considered as good estimations. Figure 8a shows $Q(S, \Delta t)$ with the corresponding dividing salinities. With coarser temporal resolution (larger Δt), the maximum of Q moves towards greater salinities and smaller transport values, showing a weakened exchange flow. For $\Delta t = 10\,\mathrm{d}$, the maximum shifts back to smaller salinities, indicating that some processes are not resolved anymore. Furthermore, the maximum salinities decrease with reduced temporal resolution, which indicates that the inflows of high salinities are not captured. In Fig. 8b, the relative deviations of the TEF bulk values are shown for the inflow. With increasing time step Δt, the deviations increase rapidly as one would expect since processes of smaller timescales are not resolved anymore. For $\Delta t \geq 3\,\mathrm{d}$, the deviations fluctuate around a constant value with the exception of $\Delta t = 5\,\mathrm{d}$. The deviations for this time step are smaller than expected. Figure 8a shows that the shape of $Q(S, 5\,\mathrm{d})$ is closer to the shape of the 3-hourly output, leading to more correct bulk values, which we expect to be accidental. The properties of the outflow follow a similar pattern with generally smaller deviations since the outflow does not depend as much on inflows events (not shown here). Figure 8b also shows that for this simulation 12-hourly model output is enough to resolve the exchange flow properly, i.e. errors of less than 1 %.

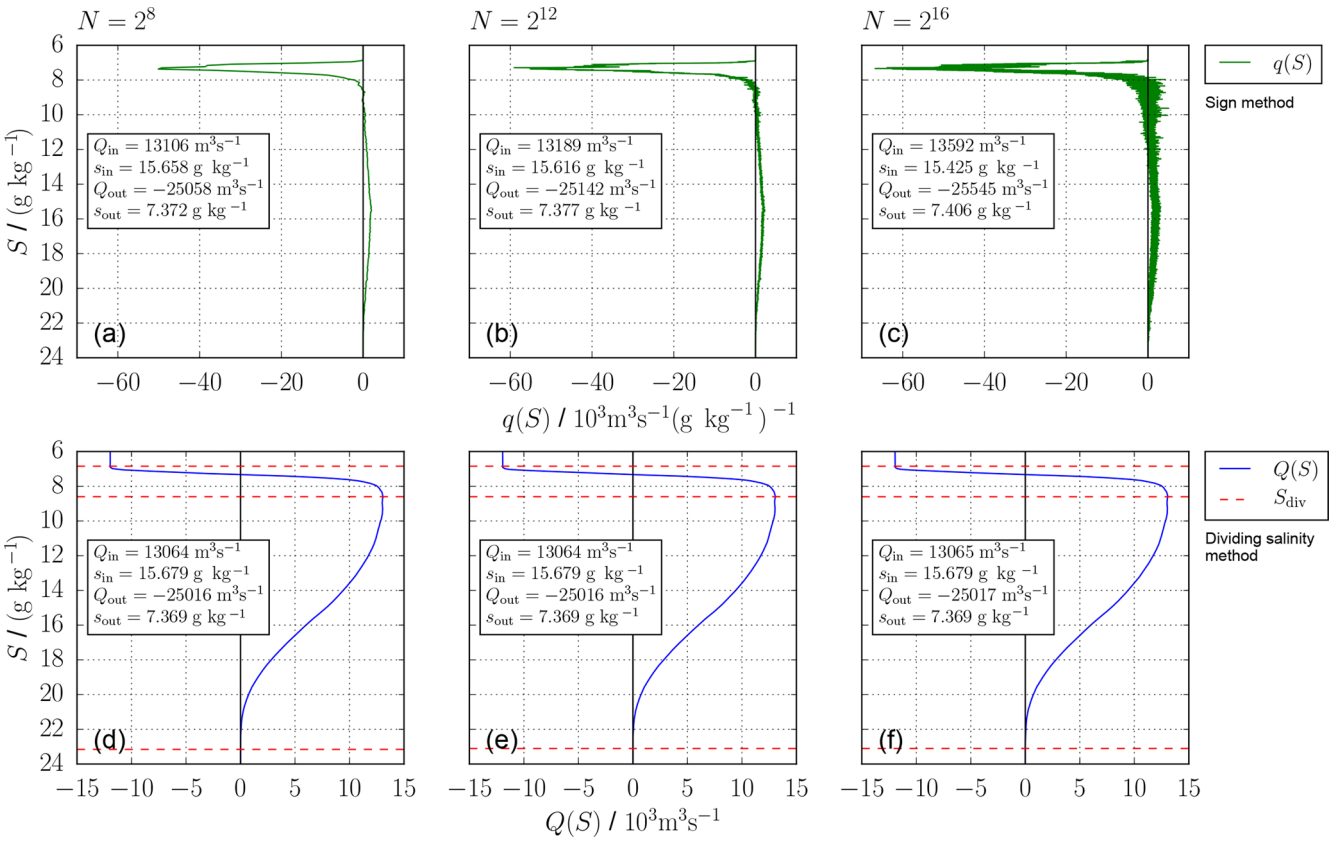

Figure 7. Exchange flow over Darss Sill: profiles of q **(a, b, c)** and Q **(d, e, f)** for the Darss Sill transect in 2002/2003 depending on the number of salinity classes N: **(a, d)** $N = 2^8 = 256$, **(b, e)** $N = 2^{12} = 4096$, **(c, f)** $N = 2^{16} = 65\,536$. The respective TEF bulk values are calculated with the sign method (5) in panels **(a, b, c)** and the extended dividing salinity method (11, 16) in panels **(d, e, f)**.

4.2 Cross section through the Gotland Basin

In this section, the capability of the extended dividing salinity method to be applied to exchange flows or transects with more than two layers is demonstrated. Here, example results are shown for model data of the Gotland Basin in the Baltic Sea. The analysed transect uses the model run from Burchard et al. (2018) consisting of 156 equally spaced locations with 1 nmi resolution and 50 vertical adaptive layers. Daily averages from 2 simulation years, 2002 and 2003, are analysed. These 2 years show a complex inflow activity, with baroclinic inflows during summer 2002 and summer 2003 and an MBI during winter 2002/2003 (Feistel et al., 2006).

Figure 9a shows q for $N = 2^8 = 256$ salinity classes to visualise the exchange flow, whereas Fig. 9b shows Q for $N = 2^{16} = 65\,536$, which is used to compute the bulk values using the extended dividing salinity method (11 and 16). For this data set, five dividing salinities are found using $Q_{\text{thresh}} = 0.01 \cdot \max(|Q|) \approx 700\,\text{m}^3\,\text{s}^{-1}$, separating two inflows ($Q_{\text{in},1}$ and $Q_{\text{in},2}$) and two outflows ($Q_{\text{out},1}$ and $Q_{\text{out},2}$). These are listed with their respective salinities ($s_{\text{in},1}$, $s_{\text{in},2}$, $s_{\text{out},1}$ and $s_{\text{out},2}$) on the right of Fig. 9 for $N = 2^{16}$ salinity classes.

The net southward transport of 11 300 m^3 s^{-1} results from the fact that most river input is entering the Baltic Sea north of the transect. $Q_{\text{in},1}$ and $Q_{\text{out},1}$ belong to the cyclonic surface circulation of the Gotland Basin described above. With the main river input in the north, the outflow $Q_{\text{out},1}$ is less saline than the inflow $Q_{\text{in},1}$ which experiences more entrainment of saline bottom waters during the recirculation. $Q_{\text{in},2}$ describes the net northward transport of the deep circulation which is fed with high salinities of the inflow events. $Q_{\text{out},2}$ is the corresponding deep net southward transport of less saline water which is homogeneous over a salinity range from ~ 8 to $\sim 10\,\text{g kg}^{-1}$; see Fig. 9a. Further and more detailed TEF analyses of the dynamics in the Gotland Basin should be carried out in the future but will be not part of this study, as the focus lies on the method and not the physics. Nevertheless, the extended dividing salinity method proves to be suitable to find robust bulk values for multi-layered exchange flows.

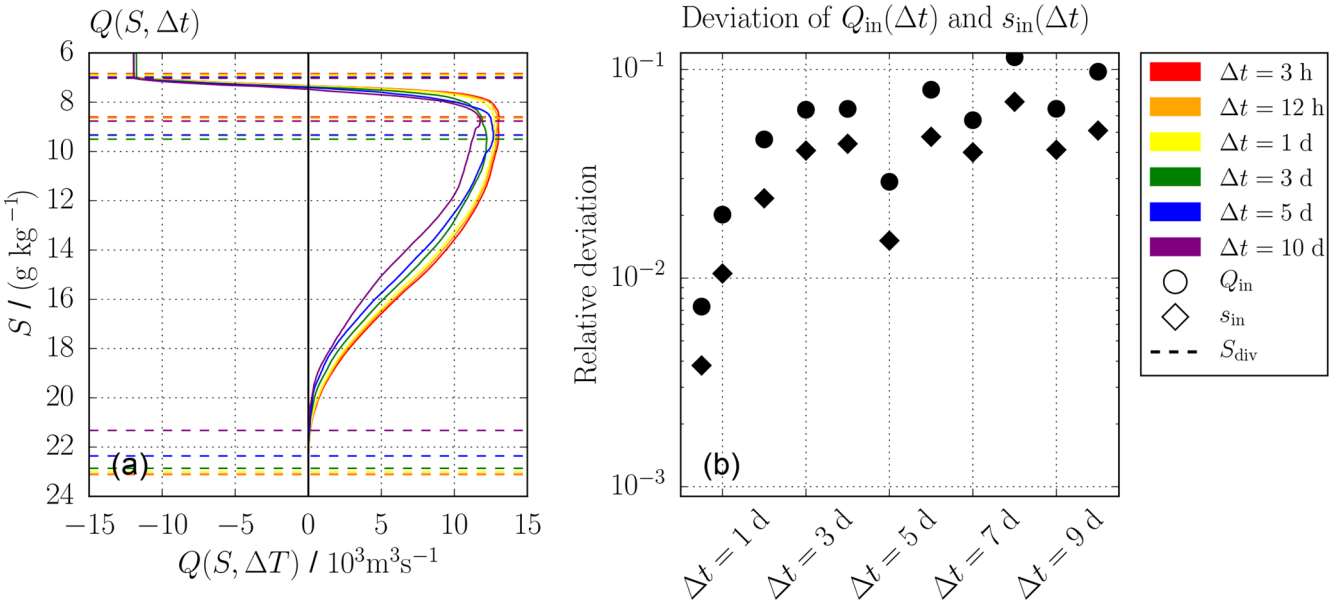

Figure 8. Exchange flow over Darss Sill: comparison of $Q(S)$ ($N = 2^{16} = 65\,536$) for different Δt in panel **(a)** and the relative deviations of Q_{in} and s_{in} in dependency Δt to the bulk values for $\Delta t = 3$ h in panel **(b)**. The bulk values were computed from $Q(\Delta t)$ using the extended dividing salinity method (11, 16). The dashed lines in panel **(a)** show the dividing salinities used to compute the bulk values in panel **(b)**. With different temporal resolutions, the shape of $Q(S)$ changes considerably and the resulting bulk values deviate significantly from the ones for 3-hourly data.

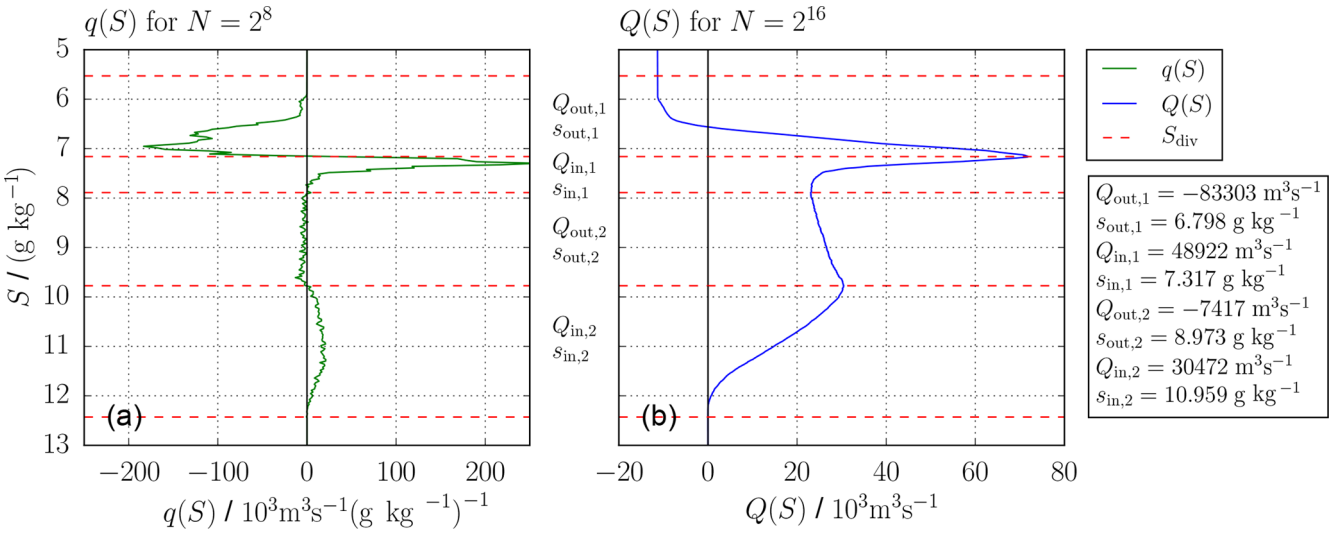

Figure 9. Cross section through Gotland Basin: profiles of q for $N = 2^8 = 256$ **(a)** and Q for $N = 2^{16} = 65\,536$ **(b)** for the Gotland transect in 2002/2003. Five dividing salinities separate two inflows and two outflows. The corresponding TEF bulk values are listed on the right.

5 Discussion and conclusions

This study investigated the numerical issues of the TEF analysis framework, proposed by MacCready (2011). Two existing calculation methods for the computation of the bulk values of an exchange flow, the sign method (5) (MacCready, 2011) and the dividing salinity method (7) (MacCready et al., 2018), were compared in their respective convergence behaviours for an analytical test case. We could show that only the dividing salinity method converges towards the analytical bulk values. The sign method relies on a smooth q profile, but q tends to become more noisy with increasing number of salinity classes (for constant temporal resolution), which leads to wrong convergence. The dividing salinity method on the other hand relies on a smooth Q. Although q is very noisy for a high number of salinity classes, Q allows a con-

vergent and robust calculation of TEF bulk values. An extended formulation of the dividing salinity method is presented which includes exchange flows of more than two layers as well as inverse exchange flows. We showed the application to two transects of the Baltic Sea. The main challenge of the extended dividing salinity method is finding the dividing salinities. We provide a detailed description of a robust algorithm to obtain extrema of Q which is required to determine the dividing salinities in Appendix B. Moreover, we investigated the dependency of the calculated bulk values on the frequency of model output. The results confirm that the output of the model for a transect which should be analysed by the application of TEF is strongly dependent on the physical mechanism controlling the exchange flow.

Based on our results, we propose a best-practice procedure for calculating TEF from a numerical model:

1. At the level of setting up a numerical model, the spatial (horizontal and vertical) resolution should be chosen as high as possible to reproduce return flows due to lateral eddies and smaller overturns.

2. Once a transect for the TEF analysis has been identified, the frequency for storing the output along that transect has to be chosen. For analytical correctness, the binning of data of volume and salt fluxes into salinity classes should be done online within the hydrodynamic model at every model time step. Time-averaged model output of these binned data can directly be used for the TEF analysis. If the model only provides output within the model layers, the binning and averaging must be done offline during postprocessing. This would induce different kinds of errors: (i) instantaneous data snapshots which skip intermediate model time steps do not conserve fluxes and do not consider intermediate salinity variations; (ii) model data obtained by thickness-weighted averaging over model time steps conserve fluxes but merge data of different salinities. Both types of errors can be reduced with a sufficiently high output frequency, such that the output data still resolve the dynamics of the flow.

3. If the binning is not done online, required output fields are the velocity component normal to the transect, the salinity and the grid box area along the transect. We suggest that these variables are stored as thickness-weighted averaged values (Klingbeil et al., 2019) between two output time steps to ensure the conservation of volume and salinity.

4. The results should be analysed for a large range of salinity classes N with the dividing salinity method (11) and (12) to check the convergence of the TEF bulk values. In this study, $N \approx 1000$ salinity classes ($\sim \delta S = 0.02\,\mathrm{g\,kg^{-1}}$) were sufficient enough for all three investigated examples with errors or deviations smaller than 0.1 %.

5. Visualisation of the exchange flow should still be done with a smooth q, since it shows the inflows and outflows more clearly. We suggest to choose $N \approx 250$ for estuaries with a wide range of salinities or a step size in salinity space of $\sim 0.05\,\mathrm{g\,kg^{-1}}$, i.e. 20 steps per $1\,\mathrm{g\,kg^{-1}}$, for estuaries with smaller salinity ranges.

Code availability. Please request the authors if you are interested in the code used for this publication.

Appendix A: Analytical solution for $Q(S)$ and $Q^s(S)$

For the oscillating exchange flow given in (8), the analytical solution is given here for the volume flux profile $Q(S)$ and the salinity flux profile $Q^s(S)$. According to (1), these profiles are calculated as

$$Q(S) = \left\langle \int_{A(S)} u \,\mathrm{d}A \right\rangle = \frac{A}{T} \int_{t^{(1)}(S)}^{t^{(2)}(S)} u(t) \,\mathrm{d}t = \frac{A}{\omega T} \left[u_\mathrm{r} \omega t + u_\mathrm{a} \sin(\omega t) \right]_{t^{(1)}(S)}^{t^{(2)}(S)}, \quad \text{(A1)}$$

and

$$\begin{aligned} Q^s(S) &= \left\langle \int_{A(S)} us \,\mathrm{d}A \right\rangle \\ &= \frac{A}{T} \int_{t^{(1)}(S)}^{t^{(2)}(S)} u(t) s(t) \,\mathrm{d}t \\ &= \frac{A}{\omega T} \Bigg[u_\mathrm{r} s_\mathrm{r} \omega t + u_\mathrm{a} s_\mathrm{r} \sin(\omega t) + u_\mathrm{r} s_\mathrm{a} \sin(\omega t + \phi) \\ &\quad + \frac{u_\mathrm{a} s_\mathrm{a} \cos(\phi)}{2} (\omega t + \sin(\omega t) \cos(\omega t)) \\ &\quad - \frac{u_\mathrm{a} s_\mathrm{a} \sin(\phi)}{2} \sin^2(\omega t) \Bigg]_{t=t^{(1)}(S)}^{t=t^{(2)}(S)}, \end{aligned} \quad \text{(A2)}$$

with

$$\begin{aligned} t^{(1)}(S) &= -\frac{1}{\omega} \left(\arccos\left(\frac{S - s_\mathrm{r}}{s_\mathrm{a}} \right) + \phi \right), \\ t^{(2)}(S) &= \frac{1}{\omega} \left(\arccos\left(\frac{S - s_\mathrm{r}}{s_\mathrm{a}} \right) - \phi \right), \end{aligned} \quad \text{(A3)}$$

which ensures that $s(t) \geq S$ for $t^{(1)}(S) \leq t \leq t^{(2)}(S)$ and $s(t) < S$ for $t^{(2)}(S) < t < t^{(1)}(S) + T$. $q(S)$ is calculated according to (2):

$$\begin{aligned} q(S) &= \frac{A}{\omega T \sqrt{s_\mathrm{a}^2 - (S - s_\mathrm{r})^2}} \left[u\left(t^{(1)}\right) + u\left(t^{(2)}\right) \right] \\ &= \frac{2A}{\omega T \sqrt{s_\mathrm{a}^2 - (S - s_\mathrm{r})^2}} \left[u_\mathrm{r} + u_\mathrm{a} \frac{S - s_\mathrm{r}}{s_\mathrm{a}} \cos(\phi) \right]. \end{aligned} \quad \text{(A4)}$$

The dividing salinity can be calculated by finding the root of $q(S)$. Solving (A4) with $q(S_\mathrm{div}) = 0$ for S_div:

$$S_\mathrm{div} = \frac{-s_\mathrm{a} u_\mathrm{r}}{u_\mathrm{a} \cos(\phi)} + s_\mathrm{r}. \quad \text{(A5)}$$

The TEF bulk values can be calculated according to (7) and (4).

Appendix B: Algorithm description

The algorithm finding the extrema of Q works as follows. First, every entry $Q_{n+1/2}$ of Q is compared with its nearest neighbours $Q_{n-1/2}$ and $Q_{n+3/2}$. If $Q_{n+1/2}$ is either the maximum (minimum) in this interval, the index $n + 1/2$ is stored and denoted by max (min), respectively. Afterwards, consecutive maxima or minima are deleted, leaving only the greatest maxima or the smallest minima. Now, minima and maxima should be alternating. At this stage, there are probably physically insignificant extrema found. Therefore, transport is calculated according to (16); their absolute values $|\Delta Q_j|$ are compared to a given threshold value Q_thresh, which we recommend to set to a value of $0.01 \cdot \max(|Q|)\,\mathrm{m^3\,s^{-1}}$. If the transport $|\Delta Q_j|$ is smaller than Q_thresh, $Q(S_{\mathrm{div},\,j})$ and $Q(S_{\mathrm{div},\,j+2})$ are compared and only the greater (smaller) of the two is kept to ensure that the greater maxima (smaller minima) remains. The two dividing salinities which belong to the smaller (greater) transport are then not considered anymore. If the first or last extremum is involved in this procedure, only the extremum which is not the first or last extremum is deleted. If this needs to be done, then the first or last extremum changes its property from either minimum to maximum or the other way round to ensure alternating minima and maxima. The last step is to adjust the first and last extrema to the index where $Q_{n+1/2}$ starts to differ from $Q_{1/2}$ (low salinities) or where $Q_{n+1/2}$ differs from 0 (high salinities). This step is not necessary for calculating the correct TEF bulk values since only the dividing part is important and not the exact value of the dividing salinity. Nevertheless, this procedure ensures that $S_{\mathrm{div},\,1}$ is the salinity class next to $\min(s)$ and $S_{\mathrm{div},\,J+1}$ is next to $\max(s)$, with J being the number of layers.

Figure B1 shows the sensitivity of the number of dividing salinities on Q_thresh for the data from Sect. 4.1 for $N = 4096$ salinity classes. In Fig. B1a, for $Q_\mathrm{thresh} = 10^{-10}\,\mathrm{m^3\,s^{-1}}$ (to filter out numerical noise of double-precision data), 135 dividing salinities, most between 8 and $10\,\mathrm{g\,kg^{-1}}$, are found. Most of them are noise carried on from the q profile to Q and have no physical meaning. However, two major transport values are found: $-24\,885$ and $12\,603\,\mathrm{m^3\,s^{-1}}$. For $Q_\mathrm{thresh} = 25\,\mathrm{m^3\,s^{-1}}$, noise-related transport values are filtered out, leaving two small transport values of 63 and $-44\,\mathrm{m^3\,s^{-1}}$. The two main transport values change to $-25\,016$ and $13\,045\,\mathrm{m^3\,s^{-1}}$. Increasing to $Q_\mathrm{thresh} = 50\,\mathrm{m^3\,s^{-1}}$, the $-44\,\mathrm{m^3\,s^{-1}}$ is not accounted for, and according to the algorithm the two involved dividing salinities are deleted. This deletes the $63\,\mathrm{m^3\,s^{-1}}$ transport as well. As a result the net transport of $19\,\mathrm{m^3\,s^{-1}}$, transport is now accounted to the major inflow, which increased from $13\,045$ to $13\,064\,\mathrm{m^3\,s^{-1}}$ if compared to Fig. B1b. These are

the exact same results as Fig. 7b, where $Q_{\text{thresh}} = 100\,\text{m}^3\,\text{s}^{-1}$ was used.

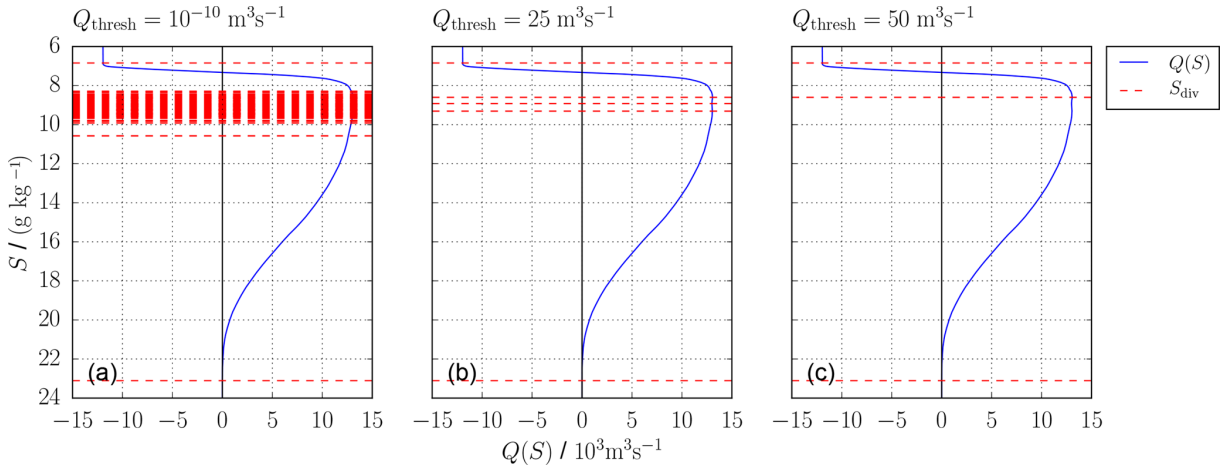

Figure B1. Comparison of the algorithm for **(a)** $Q_{\text{thresh}} = 10^{-10}\,\text{m}^3\,\text{s}^{-1}$, **(b)** $Q_{\text{thresh}} = 25\,\text{m}^3\,\text{s}^{-1}$ and **(c)** $Q_{\text{thresh}} = 50\,\text{m}^3\,\text{s}^{-1}$ for the Darss Sill data with $N = 4096$. The number of dividing salinities decreases with increasing threshold transport.

Competing interests. The authors declare that they have no conflict of interest.

Acknowledgements. This paper is a contribution to BMBF-GROCE FKZ 03F0778. Hans Burchard and Marvin Lorenz were supported by Research Training Group Baltic TRANSCOAST GRK 2000 funded by the German Research Foundation. Knut Klingbeil was supported by the Collaborative Research Centre TRR 181 on Energy Transfer in Atmosphere and Ocean funded by the German Research Foundation (project no. 274762653), and Parker MacCready was supported by US National Science Foundation (grant no. OCE-1736242).

Financial support. The publication of this article was funded by the Open Access Fund of the Leibniz Association.

Review statement. This paper was edited by Eric J. M. Delhez and reviewed by two anonymous referees.

References

Burchard, H. and Bolding, K.: GETM, A General Estuarine Transport Model: Scientific Documentation, Tech. Rep. EUR 20253 EN, Eur. Comm., 2002.

Burchard, H., Basdurak, N. B., Gräwe, U., Knoll, M., Mohrholz, V., and Müller, S.: Salinity inversions in the thermocline under upwelling favorable winds, Geophys. Res. Lett., 44, 1422–1428, 2017.

Burchard, H., Bolding, K., Feistel, R., Gräwe, U., Klingbeil, K., MacCready, P., Mohrholz, V., Umlauf, L., and van der Lee, E. M.: The Knudsen theorem and the Total Exchange Flow analysis framework applied to the Baltic Sea, Prog. Oceanogr., 165, 268–286, https://doi.org/10.1016/j.pocean.2018.04.004, 2018.

Burchard, H., Lange, X., Klingbeil, K., and MacCready, P.: Mixing Estimates for Estuaries, J. Phys. Oceanogr., 49, 631–648, https://doi.org/10.1175/JPO-D-18-0147.1, 2019.

Döös, K. and Webb, D. J.: The Deacon cell and the other meridional cells of the Southern Ocean, J. Phys. Oceanogr., 24, 429–442, 1994.

Feistel, R., Nausch, G., Heene, T., Piechura, J., and Hagen, E.: Evidence for a warm water inflow into the Baltic Proper in summer 2003, Oceanologia, 46, 581–598, 2004.

Feistel, R., Nausch, G., and Hagen, E.: Unusual Baltic inflow activity in 2002-2003 and varying deep-water properties, Oceanologia, 48, 21–35, 2006.

Geyer, W. R. and MacCready, P.: The estuarine circulation, Annu. Rev. Fluid Mech., 46, 175–197, 2014.

Gräwe, U., Holtermann, P., Klingbeil, K., and Burchard, H.: Advantages of vertically adaptive coordinates in numerical models of stratified shelf seas, Ocean Model., 92, 56–68, 2015.

Hagen, E. and Feistel, R.: Synoptic changes in the deep rim current during stagnant hydrographic conditions in the Eastern Gotland Basin, Baltic Sea, Oceanologia, 49, 185–208, 2007.

Hofmeister, R., Burchard, H., and Beckers, J.-M.: Non-uniform adaptive vertical grids for 3-D numerical ocean models, Ocean Model., 33, 70–86, 2010.

Holtermann, P. L. and Umlauf, L.: The Baltic Sea Tracer Release Experiment: 2. Mixing processes, J. Geophys. Res.-Oceans, 117, https://doi.org/10.1029/2011JC007445, 2012.

Holtermann, P. L., Umlauf, L., Tanhua, T., Schmale, O., Rehder, G., and Waniek, J. J.: The Baltic Sea Tracer Release Experiment: 1. Mixing rates, J. Geophys. Res.-Oceans, 117, https://doi.org/10.1029/2011JC007439, 2012.

Holtermann, P. L., Burchard, H., Graewe, U., Klingbeil, K., and Umlauf, L.: Deep-water dynamics and boundary mixing in a nontidal stratified basin: A modeling study of the Baltic Sea, J. Geophys. Res.-Oceans, 119, 1465–1487, 2014.

Klingbeil, K. and Burchard, H.: Implementation of a direct nonhydrostatic pressure gradient discretisation into a layered ocean model, Ocean Model., 65, 64–77, 2013.

Klingbeil, K., Becherer, J., Schulz, E., de Swart, H. E., Schuttelaars, H. M., Valle-Levinson, A., and Burchard, H.: Thickness-Weighted Averaging in tidal estuaries and the vertical distribution of the Eulerian residual transport, J. Phys. Oceanogr., accepted, 2019.

Knudsen, M.: Ein hydrographischer Lehrsatz, Annalen der Hydrographie und Maritimen Meteorologie, 28, 316–320, 1900.

Knuth, K. H.: Optimal Data-Based Binning for Histograms, arXiv e-prints, physics/0605197, 2006.

MacCready, P.: Calculating estuarine exchange flow using isohaline coordinates, J. Phys. Oceanogr., 41, 1116–1124, 2011.

MacCready, P., Rockwell Geyer, W., and Burchard, H.: Estuarine Exchange Flow is Related to Mixing through the Salinity Variance Budget, J. Phys. Oceanogr., 48, 1375–1384, 2018.

Matthäus, W. and Schinke, H.: The influence of river runoff on deep water conditions of the Baltic Sea, in: Biological, Physical and Geochemical Features of Enclosed and Semi-enclosed Marine Systems, edited by Blomqvist, E. M., Bonsdorff, E., and Essink, K., 1–10, Springer Netherlands, Dordrecht, 1999.

Meier, H. E. M.: Modeling the pathways and ages of inflowing salt- and freshwater in the Baltic Sea, Estuarine Coast. Shelf Sci., 74, 610–627, 2007.

Meier, H. M., Feistel, R., Piechura, J., Arneborg, L., Burchard, H., Fiekas, V., Golenko, N., Kuzmina, N., Mohrholz, V., Nohr, C., Paka, T. V., Sellschopp, J., Stips, A., and Zhurbas, V.: Ventilation of the Baltic Sea deep water: A brief review of present knowledge from observations and models, Oceanologia, 48, 2006.

Mohrholz, V., Naumann, M., Nausch, G., Krüger, S., and Gräwe, U.: Fresh oxygen for the Baltic Sea – an exceptional saline inflow after a decade of stagnation, J. Marine Syst., 148, 152–166, 2015.

Omstedt, A., Elken, J., Lehmann, A., Leppäranta, M., Meier, H., Myrberg, K., and Rutgersson, A.: Progress in physical oceanography of the Baltic Sea during the 2003–2014 period, Prog. Oceanogr., 128, 139–171, 2014.

Purkiani, K., Becherer, J., Flöser, G., Gräwe, U., Mohrholz, V., Schuttelaars, H. M., and Burchard, H.: Numerical analysis of stratification and destratification processes in a tidally energetic inlet with an ebb tidal delta, J. Geophys. Res.-Oceans, 120, 225–243, 2015.

Reissmann, J. H., Burchard, H., Feistel, R., Hagen, E., Lass, H. U., Mohrholz, V., Nausch, G., Umlauf, L., and Wieczorek, G.: Verti-

cal mixing in the Baltic Sea and consequences for eutrophication – A review, Prog. Oceanogr., 82, 47–80, 2009.

Sellschopp, J., Arneborg, L., Knoll, M., Fiekas, V., Gerdes, F., Burchard, H., Lass, H. U., Mohrholz, V., and Umlauf, L.: Direct observations of a medium-intensity inflow into the Baltic Sea, Cont. Shelf Res., 26, 2393–2414, 2006.

Umlauf, L., Arneborg, L., Burchard, H., Fiekas, V., Lass, H., Mohrholz, V., and Prandke, H.: Transverse structure of turbulence in a rotating gravity current, Geophys. Res. Lett., 34, https://doi.org/10.1029/2007GL029521, 2007.

Umlauf, L., Holtermann, P. L., Gillner, C. A., Prien, R., Merckelbach, L., and Carpenter, J. R.: Diffusive convection under rapidly varying conditions, J. Phys. Oceanogr., 48, 1731–1747, 2018.

Walin, G.: A theoretical framework for the description of estuaries, Tellus, 29, 128–136, 1977.

Walin, G.: On the deep water flow into the Baltic, Geofysica, 17, 75–93, 1981.

JGR Oceans

RESEARCH ARTICLE
10.1029/2019JC015527

Special Section:
Contributions from the Physics of Estuaries and Coastal Seas meeting, 2018

Numerical Study of the Exchange Flow of the Persian Gulf Using an Extended Total Exchange Flow Analysis Framework

Marvin Lorenz[1], Knut Klingbeil[1], and Hans Burchard[1]

[1]Leibniz Institute for Baltic Sea Research Warnemünde, Rostock, Germany

Key Points:
- The Total Exchange Flow analysis framework was extended by including potential temperature, which yields T-S diagrams of the exchange flow
- We conducted a 24-year simulation of the Persian Gulf using GETM
- We applied the extended TEF analysis framework to the simulation and analyzed the seasonality of the exchange flow

Supporting Information:
- Supporting Information S1

Correspondence to:
M. Lorenz,
marvin.lorenz@io-warnemuende.de

Citation:
Lorenz, M., Klingbeil, K., & Burchard, H. (2020). Numerical study of the exchange flow of the Persian Gulf using an extended Total Exchange Flow analysis framework. *Journal of Geophysical Research: Oceans*, *125*, e2019JC015527. https://doi.org/10.1029/2019JC015527

Received 26 JUL 2019
Accepted 8 JAN 2020
Accepted article online 16 JAN 2020

Abstract The Total Exchange Flow analysis framework computes consistent bulk values quantifying the estuarine exchange flow using salinity coordinates since salinity is the main contributor to density in estuaries and the salinity budget is entirely controlled by the exchange flow. For deeper and larger estuaries temperature may contribute equally or even more to the density. That is why we included potential temperature as a second coordinate to the Total Exchange Flow analysis framework, which allows gaining insights in the potential temperature-salinity structure of the exchange flow as well as to compute consistent bulk potential temperature and therefore heat exchange values with the ocean. We applied this theory to the exchange flow of the Persian Gulf, a shallow, semienclosed marginal sea, where dominant evaporation leads to the formation of hypersaline and dense Gulf water. This drives an inverse estuarine circulation which is analyzed with special interest on the seasonal cycle of the exchange flow. The exchange flow of the Persian Gulf is numerically simulated with the General Estuarine Transport Model from 1993 to 2016 and validated against observations. Results show that a clear seasonal cycle exists with stronger exchange flow rates in the first half of the year. Furthermore, the composition of the outflowing water is investigated using passive tracers, which mark different surface waters. The results show that in the first half of the year, most outflowing water comes from the southern coast, while in the second half most water originates from the northwestern region.

Plain Language Summary We studied the water exchange of the Persian Gulf with the Indian Ocean through the Strait of Hormuz. Due to evaporation, fresh water is removed in the Gulf but the salt of the water stays behind. This process creates hypersaline, thus dense water, which flows as a bottom current into the Indian Ocean. We performed a numerical simulation from 1993 to 2016, which we compared to observations and other model studies. Using the simulation's results, we could show that the water exchange follows a seasonal cycle with varying water properties, that is, salinity and temperature. Volume exchange is found to be stronger in the first half of the year than the second. The inflowing water has a nearly constant salinity but varies strongly in temperature. The salinity and temperature of the outflowing water are dependent on the origin of the water. Dense water, formed in fall and early winter in the southern Arabian coast, leaves the Gulf in late winter and spring. Dense water formed in the north at the same time arrives in the Strait of Hormuz in summer and fall. This change in origin can be found as a signature of colder and more saline outflowing water.

1. Introduction

Estuarine exchange flows can be described with simple yet precise bulk values (Knudsen, 1900), for residual volume fluxes, Q_{in} and Q_{out}, and bulk salinities s_{in}, s_{out}.The Total Exchange Flow (TEF) analysis framework (MacCready, 2011) offers a consistent calculation of the Knudsen bulk values using salinity coordinates instead of spatial coordinates since the salt budget is entirely controlled by the exchange flow. It successfully combined the concept of continuous salinity coordinates (Walin, 1977) with the bulk value concept of Knudsen (1900). Despite the bulk values, the other main result of TEF is profiles of the volume transport in salinity space, which provides a detailed insight in the salinity structure of the exchange flow. A numerically accurate and general computation of the bulk values from the TEF profiles has been discussed in Lorenz et al. (2019). Additionally, the bulk values were recently used to quantify estuarine mixing, defined as the destruction of salinity variance in estuaries (MacCready et al., 2018; Burchard et al., 2019).

©2020. American Geophysical Union. All Rights Reserved.

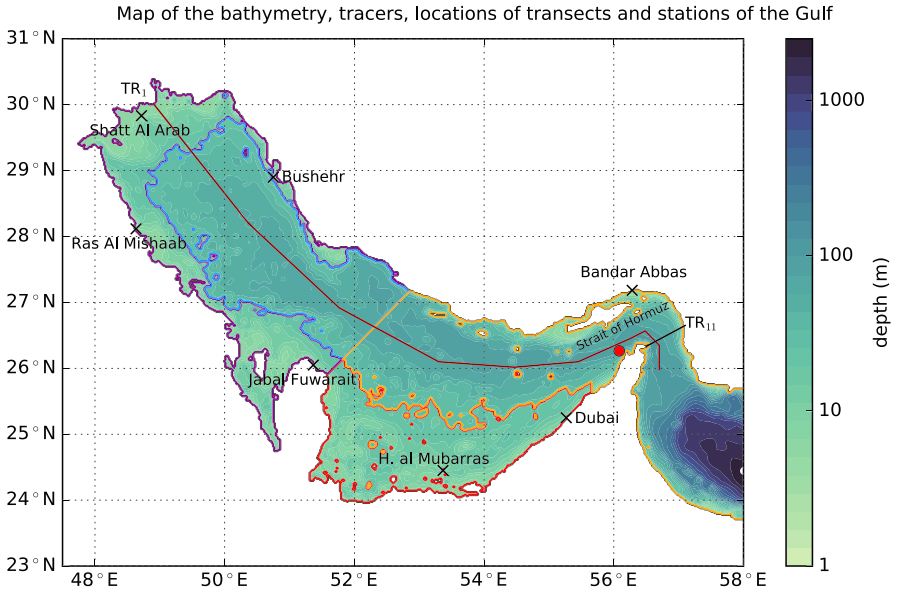

Figure 1. Map of the model domain and bathymetry of the Gulf. We marked different regions of the Gulf with different surface tracers when the water last was in contact with the atmosphere (colored contours). Tracer 1 (red) marks the shallow (<30 m) southern coast, Tracer 2 the shallow northern coast (purple), Tracer 3 the deeper northeastern part (blue), and Tracer 4 the central and western part (orange). Furthermore, the transects and stations used in this paper are marked: transects (along the Gulf axis: TR_1 and in the Strait of Hormuz: TR_{11}), tidal stations (black crosses), position of data from Johns et al. (2003) (red dot).

Whereas previous studies focused on freshwater dominated estuaries, we apply the TEF analysis framework in this study to the exchange flow of the Persian Gulf (also known as Arabian Gulf), an inverse estuary with dominating evaporation, to investigate the seasonality. With winter water temperatures below 20 °C and summer water temperatures above 35 °C (Alessi et al., 1999; Reynolds, 1993) the Gulf is heavily impacted by the seasonal solar radiation. For this purpose we extended TEF to include potential temperature space. This allows the decomposition of the potential temperature-salinity structure of the exchange flow (sections 2 and 4.1). This extended method is applicable to any estuarine exchange flow and allows the user to estimate the heat exchange through any transect. Similar decompositions have been applied to stream functions in the open ocean and to study water mass transformation processes (Döös et al., 2012; Groeskamp et al., 2019; Hieronymus et al., 2014; Speer, 1993; Worthington, 1981; Zika et al., 2013). The Gulf is a semienclosed marginal sea, connected through the Strait of Hormuz to the Gulf of Oman and Arabian Sea. The Gulf itself is shallow (mean depth of 39 m), consists of shallow coastal regions in the north and south, and has a deeper trench following the axis of the Gulf along the Iranian coast to the Strait of Hormuz; compare Figure 1. Very high Gulf-wide-averaged evaporation rates, up to 2 m/a and locally even more (Ahmad & Sultan, 1991; Privett, 1959), exceed the precipitation, resulting in the creation of hypersaline Persian Gulf Water (PGW) and drive an inverse estuarine circulation. PGW is leaving the Gulf as a bottom current and Indian Ocean Surface Water (IOSW) is entering through the Strait of Hormuz to compensate the volume loss. The PGW stratifies in relatively shallow depth into the Gulf of Oman (~250 m), mixes with ambient water due to mesoscale and submesoscale eddies (Morvan et al., 2019; Vic et al., 2015), and spreads into the Indian Ocean where PGW signatures can be found, for example, in the Bay of Bengal (Jain et al., 2017). Previous measurements showed that the outflow of the PGW does not follow a significant seasonal cycle and is relatively steady with only small variabilities one time scales of 2–3 weeks (Johns et al., 2003; Swift & Bower, 2003; Pous et al., 2004).

Other and more recent model studies find a seasonal cycle of weaker outflows in winter and stronger outflows in summer (Chao et al., 1992; Elhakeem et al., 2015; Kämpf & Sadrinasab, 2006; Pous et al., 2015; Yao & Johns, 2010b). In addition, the measurements of Johns et al. (2003) show episodic salinity pulses in the outflow from March to July 1997. Thoppil and Hogan (2009) investigated these pulses and showed that these are a signal of propagating mesoscale cyclonic eddies, formed in the vicinity of 26°N, 55.5°E due to

baroclinic instabilities. These are triggered by abrupt changes of the local circulation due to wind stress fluctuations. Yao and Johns (2010b) argued that longer pulses from the measurements are caused by spilling of saline water from the southern shallows.

Previous model studies that indicate a seasonality computed only inflowing and outflowing transports for monthly or annual values and described the PGW salinities by a range of minimum to maximum values. In addition, these studies did not utilize the benefits of TEF. Therefore, this study conducts an extensive analysis of the exchange flow and its properties for the climatological exchange flow as well as time series of bulk values.

Another question we want to answer is the question of the composition of the PGW. Previous studies discussed the origin of the PGW, which is known to mainly form in the north and in the south (Swift & Bower, 2003; Yao & Johns, 2010b) with highest densities found in winter in the north. The southern shallows form dense water in autumn and winter, which reaches the Strait of Hormuz in late winter and spring (Kämpf & Sadrinasab, 2006), while the water from the north is steady over the whole year (Yao & Johns, 2010b).

To provide a quantitative measure of the composition of the PGW, we conducted a tracer experiment by marking the surface waters of different regions where they were in last contact with the atmosphere. Then, we computed the composition of the outflowing water by calculating the respective concentration bulk values of the tracers. With this approach we are able to gain insights of the different composition and especially the ratio of water from northern and southern origin.

This paper is structured as following. In section 2 we provide a summary of the TEF computation and the extension of potential temperature as the second coordinate. In section 3 the model and the setup description are presented in detail including the validation of the model. The results of this study are shown in section 4, starting in section 4.1 with an example for the potential temperature-salinity TEF, before showing the results of the application on the Gulf. Discussion of the results is done in section 5 before we summarize and conclude in section 6.

2. Methods

2.1. TEF Analysis Framework

The TEF analysis framework (Burchard et al., 2018; Lorenz et al., 2019; MacCready, 2011) allows a consistent calculation of the transports and salinities of an exchange flow in salinity space. The main idea of TEF is that transports of volume and salinity in and out the estuary of the same salinity partially compensate since only the net exchange changes salinity and volume of the estuary. The transport of a tracer c using salinity coordinates S, $Q_S^c(S)$, through a cross section is defined as follows:

$$Q_S^c(S) = \left\langle \int_{A(S)} c\, u \, \mathrm{d}A \right\rangle, \tag{1}$$

where $A(S)$ denotes the area of a cross section with salinities greater than S, u is the velocity normal to the cross section (we define that positive values for u bring water into the estuary), and $\langle\ \rangle$ denotes temporal averaging. By differentiating $Q_S^c(S)$ with respect to S, one finds the exchange profile of tracer flux per salinity class:

$$q_S^c(S) = -\frac{\partial Q_S^c(S)}{\partial S}. \tag{2}$$

Lorenz et al. (2019) discussed in their paper two methods for computing the TEF bulk values, the *sign method*, which uses the positive and negative part of q_S^c (MacCready, 2011) and the *dividing salinity method*, which uses the extremum of Q_S^c as the salinity class, S_{div}, to separate the inflow and outflow (MacCready et al., 2018). The latter is used for this study and reads for an inverse estuary as

$$Q_{\mathrm{in}}^c = \int_{S_{\mathrm{min}}}^{S_{\mathrm{div}}} q_S^c \, \mathrm{d}S, \quad Q_{\mathrm{out}}^c = \int_{S_{\mathrm{div}}}^{S_{\mathrm{max}}} q_S^c \, \mathrm{d}S, \tag{3}$$

where S_{min} and S_{max} denote the minimum and maximum salinities of the used salinity space. The respective salinities are then calculated by the fraction of the salinity flux ($c = s$) and the volume flux ($c = 1$):

$$s_{\mathrm{in}} = \frac{Q_{\mathrm{in}}^s}{Q_{\mathrm{in}}}, \quad s_{\mathrm{out}} = \frac{Q_{\mathrm{out}}^s}{Q_{\mathrm{out}}}. \tag{4}$$

For most estuaries the density is mainly controlled by the salinity, which justifies the treatment in salinity space. But for the Persian Gulf, temperature gradients are not negligible and contribute to density gradients. Therefore, we will also investigate the exchange flow in potential density coordinates; that is, we replace S in (1)–(3) with the potential density ρ. For larger and especially deeper estuaries the exchange flow properties change with the season. This is also the case for the Persian Gulf where the bottom water in the Strait of Hormuz can be 10° colder than the surface waters (Reynolds, 1993), that is, summer water stratified over winter water. To study the seasonal exchange flow and the change of water masses, we take potential temperature Θ into account. We extend (1) by considering both salinity and potential temperature when computing the transports:

$$Q^c_{S,\Theta}(S,\Theta) = \left\langle \int_{A(S,\Theta)} c\, u \, \mathrm{d}A \right\rangle, \tag{5}$$

where $A(S,\Theta)$ now denotes the cross-sectional area with salinities greater than S and potential temperatures greater than Θ. Differentiation with respect to S and Θ allows the decomposition of the tracer flux in fluxes per salinity class and potential temperature class:

$$q^c_{S,\Theta}(S,\Theta) = -\frac{\partial^2 Q^c_{S,\Theta}(S,\Theta)}{\partial S\, \partial \Theta}, \tag{6}$$

which allows the analysis of the exchange flow in the form of a T-S diagram; see section 4.1. Equation (6) combines the TEF analysis framework with the T-S analysis framework used for the open ocean. Integration of (6) over all potential temperatures Θ yields (2), and the bulk values can be computed as described above:

$$q^c_S = \int_{\Theta_{\min}}^{\Theta_{\max}} q^c_{S,\Theta}\, \mathrm{d}\Theta. \tag{7}$$

Equivalently, by integrating over all salinities S (6) yields

$$q^c_\Theta(\Theta) = \int_{S_{\min}}^{S_{\max}} q^c_{S,\Theta}\, \mathrm{d}S = -\frac{\partial Q^c_\Theta(\Theta)}{\partial \Theta}, \tag{8}$$

which corresponds to the usual TEF using temperature instead of salinity as coordinates; see also Walin (1982). Using Q^c_Θ, one can similarly to (3) compute potential temperature fluxes, $\mathcal{Q}^\theta_{\mathrm{in,out}}$, and volume fluxes, $\mathcal{Q}_{\mathrm{in,out}}$, which then can be used to compute bulk potential temperatures:

$$\theta_{\mathrm{in}} = \frac{\mathcal{Q}^\theta_{\mathrm{in}}}{\mathcal{Q}_{\mathrm{in}}}, \quad \theta_{\mathrm{out}} = \frac{\mathcal{Q}^\theta_{\mathrm{out}}}{\mathcal{Q}_{\mathrm{out}}}, \tag{9}$$

where it should be noted that $\mathcal{Q}^\theta_{\mathrm{in,out}} \neq Q^\theta_{\mathrm{in,out}}$ and $\mathcal{Q}_{\mathrm{in,out}} \neq Q_{\mathrm{in,out}}$.

3. Model and Setup Description

The simulations in this study were performed with the General Estuarine Transport Model (GETM; Burchard & Bolding, 2002; Klingbeil & Burchard, 2013), which is a three-dimensional coastal ocean model (Klingbeil et al., 2018), solving the hydrostatic Boussinesq equations. Vertical turbulence is parameterized by an eddy-viscosity approach with k-ϵ closure in terms of stratification and shear (Burchard & Baumert, 1995; Rodi, 1987). For this the turbulence library from the General Ocean Turbulence Model (Burchard et al., 1999; Umlauf & Burchard, 2005) is linked to GETM. For lateral mixing we used the Smagorinsky (1963) parameterization with a Smagorinsky constant of 0.28 and a turbulent Prandtl number of 2 for tracers. The free surface is calculated by split-explicit mode splitting with drying-and-flooding capability (Burchard et al., 2004). For both the horizontal and vertical advection discretization, we used the Total Variation Diminishing-Superbee scheme (Pietrzak, 1998) to reduce the spurious numerical mixing of the transported quantities (Klingbeil et al., 2014)

The model setup, see Figure 1, uses a one nautical mile bathymetry based on ETOPO1 (Amante & Eakins, 2009), which is smoothed and adjusted to improve tide propagation. In the vertical 40 adaptive layers (Gräwe et al., 2015; Hofmeister et al., 2010, 2011) are used. The internal pressure gradient was discretized according to Shchepetkin and McWilliams (2003) to minimize errors due to the terrain-following coordinates. At 58°E

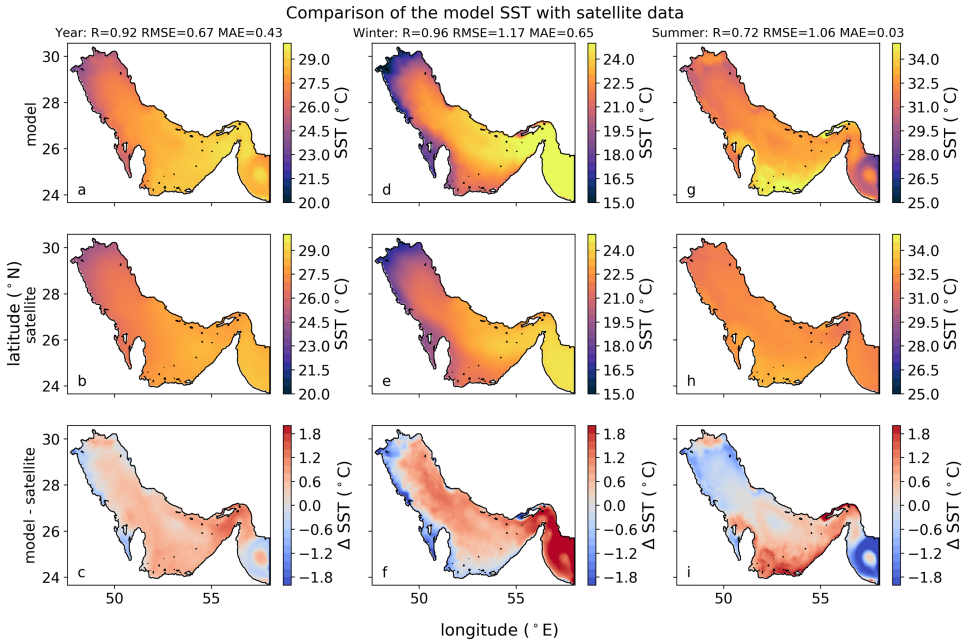

Figure 2. Comparison of the sea surface temperature of the model (a, d, and g) with OSTIA data (b, e, and h) (Stark et al., 2007) for the annual mean (a–c), winter (December, January, and February, d–f), and summer (June, July, and August, g–i) in 2015. Panels (c), (f), and (i) show the difference between model results and observations. In addition, the correlation *R*, the root-mean-square error (RMSE), and the mean absolute error (MAE) are provided for each column.

the open boundary is located, for which 3-hourly HYCOM data (Chassignet et al., 2007) with 1-hourly tide prescription by Oregon State University Tidal Prediction Software (OTPS, Egbert & Erofeeva, 2002) is used.

For meteorological forcing CFSR/CFS2 (Saha et al., 2010, 2011) is applied, using the Bignami bulk formula to compute longwave radiation (Bignami et al., 1995) and a Jerlov Type 1A water class (Jerlov, 1976), which suits the Gulf's water properties best (Al Azhar et al., 2016). The shortwave radiation is adjusted in a way that the mean value is reduced by 37 W/m^2 to account dust storms as Johns et al. (2003) described, based on Tragou et al. (1999). In addition, to account for the temporal change of the albedo due to the dust storms, we applied an additional cosine function with an amplitude of 20 W/m^2, which approximates the aerosol concentrations in the atmosphere quite well, as the greatest concentrations are found in June and July (Smirnov et al., 2002). The amplitude of 20 W/m^2 resulted in the least deviations in sea surface temperature (SST); see section 3.1.1. Rivers are prescribed by a constant value of 1,300 m^3/s for the Shatt Al Arab and by monthly climatologies from Kämpf and Sadrinasab (2006) for three other main rivers: Helleh, Mond, and Zohreh. To study the origin of the PGW, we marked the surface layer with different passive tracers in four areas: the shallow (< 30 m) south (Tracer 1, red), the northern shallow coast (Tracer 2, purple), the deeper (≥ 30 m) northeastern region (Tracer 3, blue), and the central and western part (Tracer 4, orange); see colored contours in Figure 1. For each baroclinic time step the tracers are passively transported and mixed. To guarantee that the sum of all tracers is less or equal to 1, the concentration of each tracer at the surface is reset to 0, except for the one in the specifically marked region, where it is set to 1. The model was initialized with temperature and salinity fields from HYCOM on 1 January 1993 and run until 1 January 2017. The spin-up time is 4 years, which is sufficient that the sum of all four tracers in each grid cell is 1.

3.1. Validation

3.1.1. SST

Comparison of the model's surface temperature with satellite measurements from the Operational Sea Surface Temperature and Sea Ice Analysis (Stark et al., 2007) is shown for 2015 in Figure 2 with computed correlation *R*, root-mean-square error, and mean absolute error (Willmott, 1981, 1982). The first row shows the model results for the annual mean, the winter season (December, January, and February), and summer season (June, July, and August). The second row shows the satellite SSTs and the third the difference between model and satellite. Comparing the annual distribution, the model is slightly warmer but agrees

Table 1
Dominant Tidal Constituents of the Persian Gulf

Station	M2	S2	K1	O1	N2	K2	P1
Bandar Abbas (mod)	92/195	35/228	34/7	20/7	22/176	10/222	11/5
Bandar Abbas (obs)	100/197	36/229	34/11	21/3	22/180	10/227	11/10
Bushehr (mod)	32/128	11/177	24/233	18/202	7/102	4/168	8/222
Bushehr (obs)	34/110	12/160	31/227	20/189	7/84	4/156	9/218
Shatt Al Arab (mod)	66/262	20/319	38/271	27/236	13/233	8/309	11/263
Shatt Al Arab (obs)	84/221	29/279	50/250	30/205	17/189	10/260	14/243
Ras Al Mishaab (mod)	13/328	3/28	29/281	21/245	3/276	1/22	9/269
Ras Al Mishaab (obs)	25/276	8/335	38/259	21/221	6/243	3/334	13/253
Jabal Fuwarait (mod)	23/42	7/73	16/72	9/32	6/14	2/74	5/65
Jabal Fuwarait (obs)	42/44	13/88	20/54	9/0	11/17	4/88	7/54
H. al Mubarras (mod)	24/287	10/342	30/119	19/80	5/265	4/330	9/109
H. al Mubarras (obs)	28/261	13/315	43/102	23/52	4/232	3/315	14/102
Dubai (mod)	37/248	12/286	14/106	13/69	8/223	4/279	5/91
Dubai (obs)	44/237	16/281	23/91	16/42	10/217	5/265	7/77

Note. The results are computed for the Year 2014 and are shown with amplitude (cm)/phase shift (°) compared to Greenwich for several stations in the Gulf; see Figure 1 for the locations. Observational data are taken from Pous et al. (2012) (Tables 1 and S2).

well with the observations ($R = 0.92$). The winter season shows colder northern and eastern coasts and warmer temperatures toward the Strait of Hormuz. The model and the observations show the same temperature distribution ($R = 0.96$) with the model being colder at the coasts and warmer in the deeper regions, especially in the Gulf of Oman near the open boundary. In summer, the model shows a very warm southern coast, which is deviating from the observations by up to 2 °C ($R = 0.72$). Again, the temperature distribution near the open boundary is up to 2 °C colder than the observations.

A comparison for all years is provided in Table 1 for SST products of National Oceanic and Atmospheric Administration Optimum Interpolation SST (Reynolds et al., 2007) and Operational Sea Surface Temperature and Sea Ice Analysis (Stark et al., 2007) in the supporting information of this publication. All simulation years show the described discrepancies in varying strengths, that is, colder coasts in winter and a warm southern coast, and being in general slightly warmer than the observations.

3.1.2. Heat and Fresh Water Fluxes

Heat and fresh water fluxes are besides wind the main drivers of the dynamics in the Gulf. Figure 3 shows the climatological annual cycle of the model simulation. The mean net heat flux of $-4.7\,W/m^2$ ($-8.3\,W/m^2$ for 1997) is in the range of other studies: -7 ± 4 to $4\,W/m^2$ (1997) (Johns et al., 2003), $-4\,W/m^2$ (Kämpf & Sadrinasab, 2006), $-3\,W/m^2$ (Thoppil & Hogan, 2010), and -7 to $-10.3\,W/m^2$ (Yao & Johns, 2010a). Precipitation $P = 0.11$ m/a and evaporation $E = 1.62$ m/a agree with other studies as well: $P = 0.15$ m/a, $E = 1.58$ m/a (Johns et al., 2003), $P = 0.21$ to 0.24 m/a, $E = 1.51$ to 1.61 m/a (Pous et al., 2015), and $E = 1.8$ m/a (Kämpf & Sadrinasab, 2006). The seasonal cycle of the heat fluxes and net fresh water flux is in agreement with previous studies (Yao & Johns, 2010a). The net fresh water fluxes show higher evaporation rates in fall than in spring. The error bars denote the standard deviation of the monthly means of the 24 simulation years. The greatest variations can be found for the evaporation rate, which transfers to the latent heat flux. The other heat fluxes show little annual variations. Since the incoming shortwave radiation, its distribution and strength is a major uncertainty in the Gulf region; we provide the model's calculated annual mean surface fluxes for heat and fresh water in Table S2 in the supporting information of this publication.

3.1.3. Tides

The Gulf experiences strong mixing due to tides especially in the Strait of Hormuz (Alosairi et al., 2011), and therefore, the model shall reproduce the tidal gauges. A harmonic analysis for the main tidal components was carried out and the results for the amplitude (cm) and phase (°) compared to Greenwich are listed in Table 1. Overall, the tidal wave is slightly faster and the amplitudes are slightly smaller than the observations show. Nevertheless, for the area of main interest, the Strait of Hormuz, the tidal components are correct (Bandar Abbas).

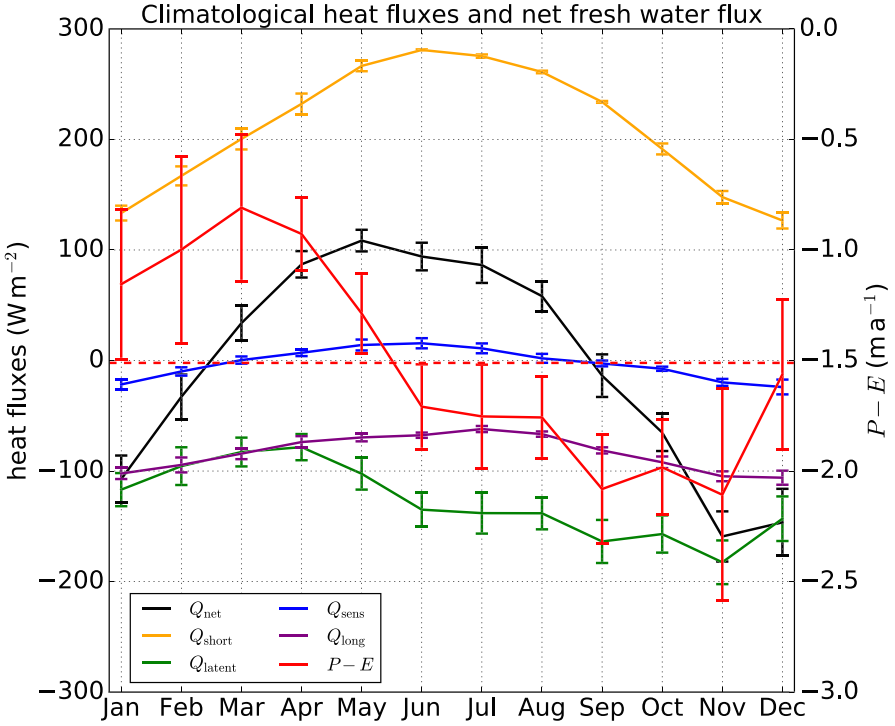

Figure 3. Climatological surface heat fluxes and fresh water fluxes (1993-2016): net heat flux Q_{net} (black), shortwave radiation Q_{short} (orange), latent heat flux Q_{heat} (green), sensible heat flux Q_{sens} (blue), longwave heat flux Q_{long} (purple), and the net surface fresh water flux as the difference of precipitation P and evaporation E, $P-E$, (red). Positive value denote a flux into the Gulf. The error bars denote the standard deviation to indicate the natural interannual variability.

3.1.4. Salinity and Potential Temperature Distribution Along the Gulf Axis

The structure along the Gulf axis, TR_1, for potential temperature and salinity shows two completely different states: a well-mixed state in winter (January) and a well-stratified state in summer (July); see Figure 4. Similar depictions can be found in Reynolds (1993) or Yao and Johns (2010b) for measurements of the Mt. Mitchell expedition or in Swift and Bower (2003) for climatological distributions, as well as for model studies, for example, Yao and Johns (2010b). The along-axis structures of this study compare well to the observations. In winter the Gulf is well mixed, that is, homogeneous water columns, with high salinities and cold potential temperatures in the northwest. Toward the Strait of Hormuz there is stratification occurring

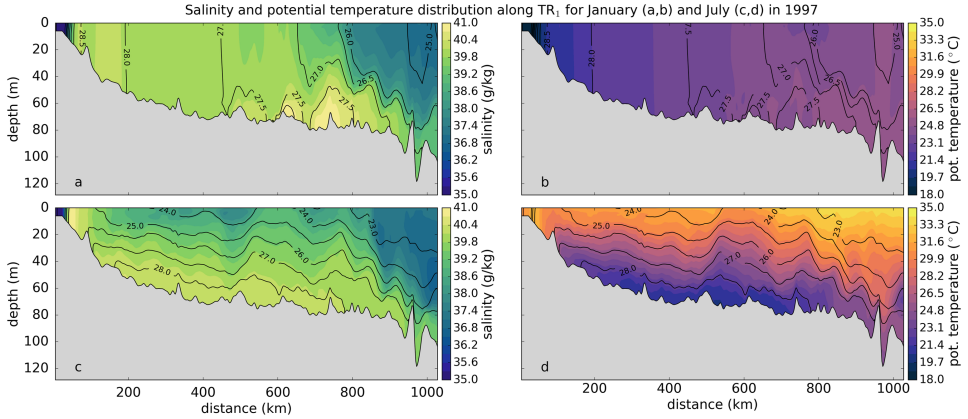

Figure 4. Model results of the mean salinity, mean potential temperature, and mean potential density anomaly (contour lines) distribution along the Gulf axis TR_1 for January (a, b) and July (c, d) 1997.

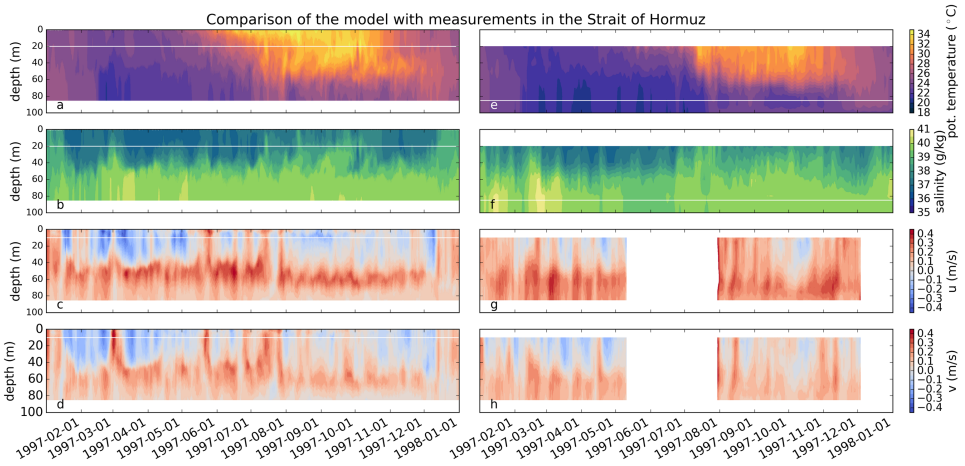

Figure 5. Comparison of model results (a–d) for potential temperature, salinity and zonal (u) and meridional (v) velocities in the Strait of Hormuz; see red dot in Figure 1, with measurements from Johns et al. (2003). (e–h) Both, the model data and the observations, were smoothed using a running mean of 24-hr width.

with IOSW stratifying over PGW due to the exchange flow. In summer the whole Gulf is vertically stably stratified with increasing salinity at the surface toward the northwest. In addition, the doming of the isolines shows the signature of the large cyclonic eddies of the Gulf wide circulation (Thoppil & Hogan, 2010).

3.1.5. Strait of Hormuz

We showed that the general structure of the Gulf is well represented in the model. Now we compare the model temporal evolution in the Strait of Hormuz to measurements of Johns et al. (2003) for potential temperature, salinity, and velocity components; see Figure 5. The data were smoothed, using a 24-hr running mean. Comparing Figures 5a and 5e, the temporal evolution of potential temperature agrees in terms of timing and depth of the thermocline. The cold winter water in the observations from mid-February to July is warmer in the model. Similarly, the summer potential temperatures above the thermocline are warmer. Comparing the salinity evolution in Figures 5b and 5f, the salinities match the observations in two important characteristics: first, the uplift of the halocline due to propagating eddies (Thoppil & Hogan, 2009) and second, the general uplift of the halocline from July to November, although the second is not as pronounced in the model as in the observations. In the supporting information of this publication we show time series for potential temperature and salinity at four depths, which show the agreements and the deviations in more detail. Comparing the velocity components u (zonal) and v (meridional), a general northeastward current is persistent below 40 m in both model and observations. Maximum velocities are found between 40 and 60 m in the model and 50–70 m in the observations. Propagating eddies are existent over the whole year in the model and in the first half of the observations.

4. Results

4.1. TEF Diagram

The extended TEF analysis as described in section 2.1 of the climatological results along TR_{11} in June is shown in Figure 6. The structure of the diagram is inspired by Döös and Webb (1994) who showed in a similar structure the volume transport depending on depth and density. The lower left panel shows $q_{S,\Theta}$ with the dashed line denoting the potential density, the upper panel shows q_S, and the right panel shows q_Θ. The dashed lines in the last two panels denote the dividing salinities/potential temperatures, separating inflow and outflow (Lorenz et al., 2019), the gray shade shows the standard deviation, and the red and blue dot the respective representative bulk value of salinity or potential temperature of the inflow and outflow.

$q_{S,\Theta}$ shows two distinct water masses. In red the inflowing IOSW with salinities of ~37 g/kg and a wide range of potential temperatures, 25–35 °C, and in blue the outflow of PGW with higher salinities and colder potential temperatures. The general wider spread of salinities and potential temperatures of the PGW indicates the entrainment process where both water masses are mixed. In contrast to this depiction, Figure 7 shows a conventional T-S diagram of the same data used for Figure 6, where color denotes the occurrence of the potential temperature-salinity combination. The occurrence value is weighted with the layer height,

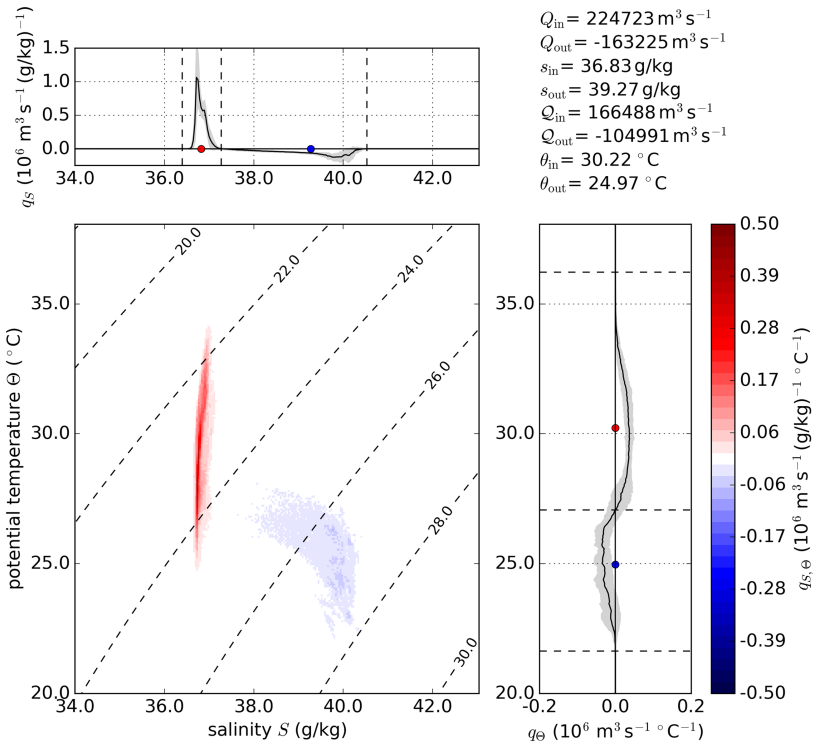

Figure 6. TEF diagram and TEF profiles in salinity and potential temperature space for the climatological results of TR_{11} in June. The main panel shows the color coded volume transport per salinity and potential temperature class $q_{S,\Theta}$. By integration along one of the axis of $q_{S,\Theta}$ two different TEF profiles are found with different volume fluxes for inflow and outflow: classic TEF profile in salinity coordinates (top panel) and TEF profile in potential temperature coordinates (right panel). In addition, the computed bulk values of the exchange flow are listed in the top right. The depiction structure is inspired by Döös and Webb (1994).

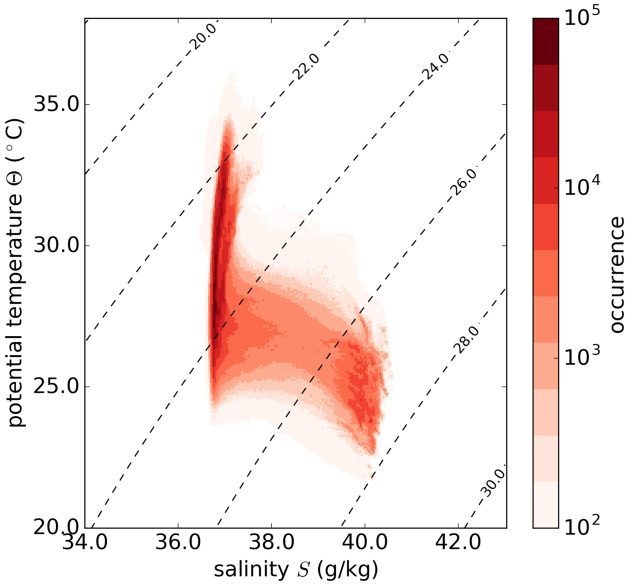

Figure 7. Conventional T-S diagram of the data behind the TEF diagram (Figure 6). Color depicts the occurrence of the potential temperature-salinity combination.

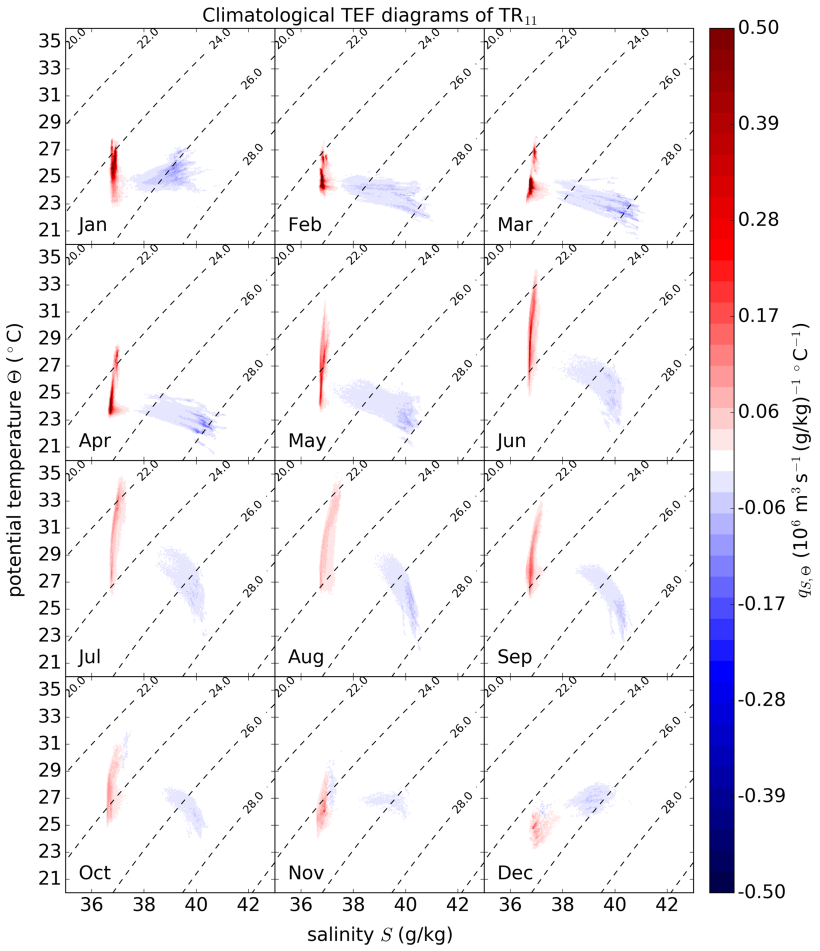

Figure 8. Climatological TEF diagrams for the analysis period from 1997–2016 along TR_{11}. Each panel shows the climatological results for one month with color coded volume transport per salinity and potential temperature class.

which is variable in time and space in the used model. Comparing both figures, one finds that many potential temperature-salinity combinations do not contribute to the exchange flow in terms of TEF. Especially, the mixture of both water masses and values that only rarely occur does not contribute. This could have two reasons: First, the transports for these combinations are very small, and second, the transport partially compensates each other, meaning positive and negative transport add up with no significant transport being left in the Θ-S combination. On the other hand, the cores of the inflow and outflow in the TEF diagram correspond to high numbers of occurrence.

Integration along Θ in Figure 6 yields to the classical TEF profile in salinity space (upper panel), which is then used to compute the bulk values Q_{in}, Q_{out}, s_{in}, and s_{out} using the dividing salinity method (Lorenz et al., 2019). The profile shows a clear signature of the IOSW as distinct positive values in salinity classes around 37 g/kg and the PGW as a less pronounced peak around 40 g/kg. The outflow from ~37.5 to ~39.5 g/kg is a mixture of both water masses due to entrainment as mentioned before. Integration along S yields a TEF profile in potential temperature space (right panel). The resulting profile shows one inflow and outflow as well, but while in salinity space inflow and outflow are clearly separated, there is additional compensation in potential temperature from ~25–28 °C. This compensation causes that $Q_{in} \neq \mathcal{Q}_{in}$ and $Q_{out} \neq \mathcal{Q}_{out}$. This result motivates that the representative potential temperatures must be computed in potential temperature space, because the heat flux in salinity space would not include the compensation and therefore overestimates the heat exchange.

Integration along isopycnals ρ will lead to an exchange profile in potential density coordinates. This will lead to additional values of volume transport, probably being different than the other two transport pairs.

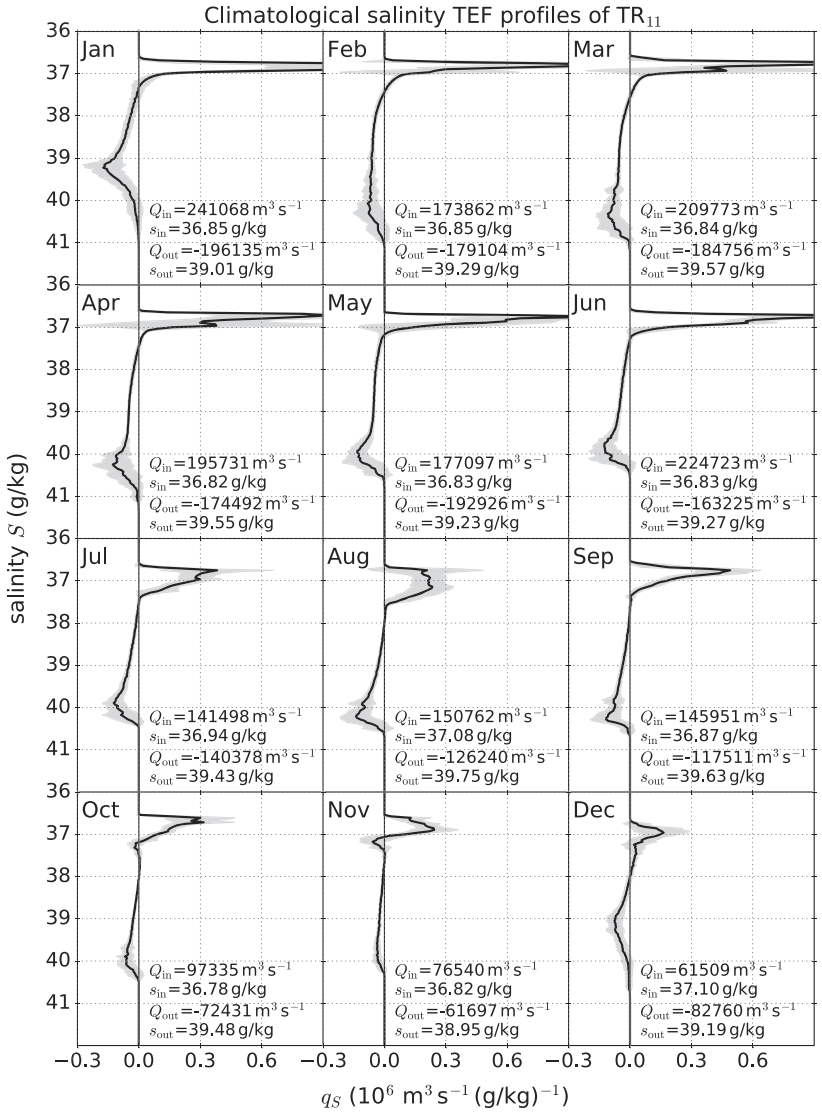

Figure 9. Climatological TEF analysis for the analysis period from 1997–2016 along TR_{11} in salinity coordinates. For each month, the bulk values for volume transport and representative salinities are computed with $N = 2^{16}$ salinity bins.

Yet this approach will find the correct representative bulk values for potential density. We elaborate more on this in the next section.

4.2. Climatological Exchange Flow

To analyze the seasonal exchange flow of the Gulf, we employ TEF diagrams for the monthly climatology in Figure 8. The diagrams show a distinct separation of the inflow (red) and outflow (blue) throughout the year. The inflow covers a narrow salinity range around 37 g/kg and dependent on the season a wider range in potential temperature for all months. Highest potential temperatures of the inflow are found in July and August, lowest in December. The outflow on the other hand covers a wider salinity and potential temperature range with changing properties in different seasons. First, the potential temperature of the outflow is overall colder than the inflow with December being the exception where the potential temperature of the inflow is colder. From January to March the potential temperatures are comparable, from April to September the potential temperatures are colder and in October and November the potential temperatures are again comparable. Whereas from December to May the transition from inflow to outflow seems continuous along the salinity axis, there is a salinity gap from June to November of more than 1 g/kg. Interestingly, in October, November, and December outflowing water can be found at high temperatures and salinities in the range

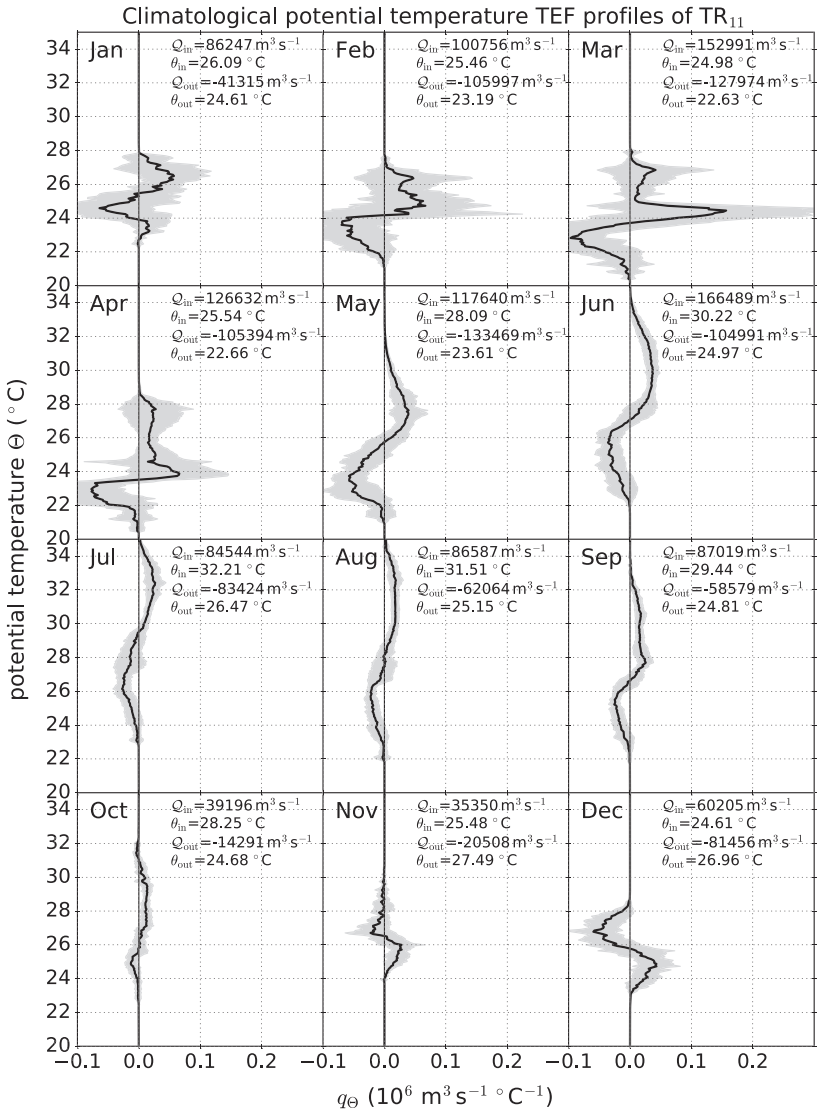

Figure 10. Climatological TEF analysis for the analysis period from 1997–2016 along TR_{11} in potential temperature coordinates. For each month, the bulk values for volume transport and representative potential temperatures are computed with $N = 2^{16}$ potential temperature bins.

of 37–37.5 g/kg. To follow the classical TEF analysis framework and to give more detailed insights into the salinity distribution, Figure 9 shows the TEF profile for q_S (black line) in salinity space, including the standard deviation (gray contour) and the respective TEF bulk values. Taking a closer look onto the shape of the profiles one recognizes the distinct peak for the inflow, which is highly variable from February to May. From July to December the salinity range widens. The bulk values show that the inflow is stronger during the first half of the year. The bulk salinity s_{in} is not changing much. The transition zone, which we mentioned before, shows one sharp crossing of the zero line from January to May, but q_S is very close to the zero line for ~1 g/kg before becoming clearly negative for the other months. This results in the gap between inflow and outflow one sees in Figure 8. The outflow extends over a broad salinity range from 37.5 to ~41 g/kg. The shape and the location of the maximum outflow per salinity class (minimum of q_S) vary over the season. The maximum is shifting from salinities around ~39 g/kg in December and January toward higher salinities between ~40 and 41 g/kg in March and April, then decreasing again toward lower salinities < 40 g/kg in June before increasing again in August and September, and finally decreasing toward the starting situation in December. s_{out} follows this seasonal dependency. Highest salinities are found in March and April

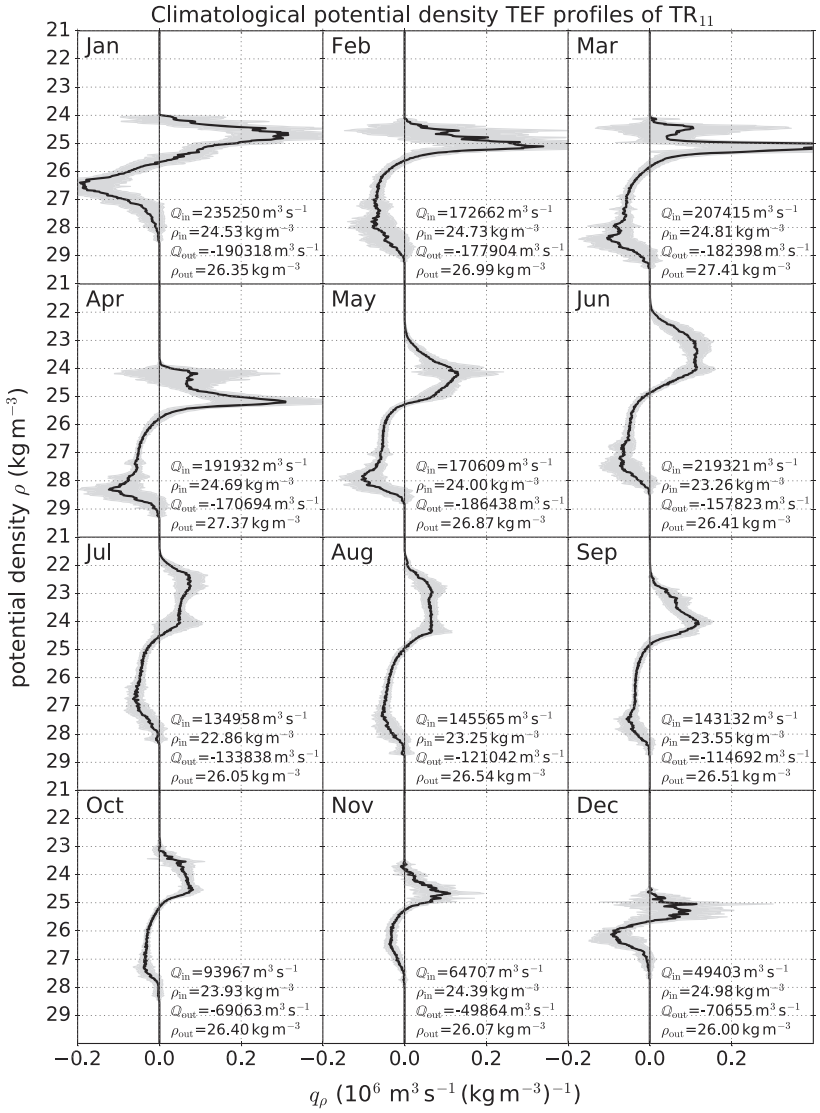

Figure 11. Climatological TEF analysis for the analysis period from 1997–2016 along TR_{11} in potential density coordinates. For each month, the bulk values for volume transport and representative potential densities are computed with $N = 2^{16}$ potential densities bins.

with salinities > 41 g/kg, but highest s_{out} is found in August. In October and November one sees the signature of an outflow at salinities around 37.5 g/kg, which was seen before in the TEF diagrams. Similarly to the inflow, the bulk values of the outflow show stronger transport in the first half of the year, and weaker transport in the second half with the lowest transport in November and strongest in January.

Similarly to Figure 9, Figure 10 shows the climatological potential temperature TEF profiles with the respective bulk values. The TEF potential temperature profiles show as the TEF salinity profiles a two-layered exchange flow (with the exception of January, but the shapes of the profiles change considerably over the year). The January profile shows a three-layered exchange flow. The bulk values in Figure 10 are the correct bulk values, which treat the two inflow layers as one. Separating the inflow into the two layers yields $Q_{in,1} = 11,892\,m^3/s$, $Q_{in,2} = 74,240\,m^3/s$, $\theta_{in,1} = 23.45\,°C$, and $\theta_{in,2} = 26.52\,°C$. All profiles show an inflow of warmer water and an outflow of colder water, except November and December where the situation is reversed. From January the potential temperatures of the inflow increases until July and the outflow potential temperature decreases until April, where the coldest potential temperatures are found as well. Warmest potential temperatures are found in July and August. From August the inflowing potential temperature

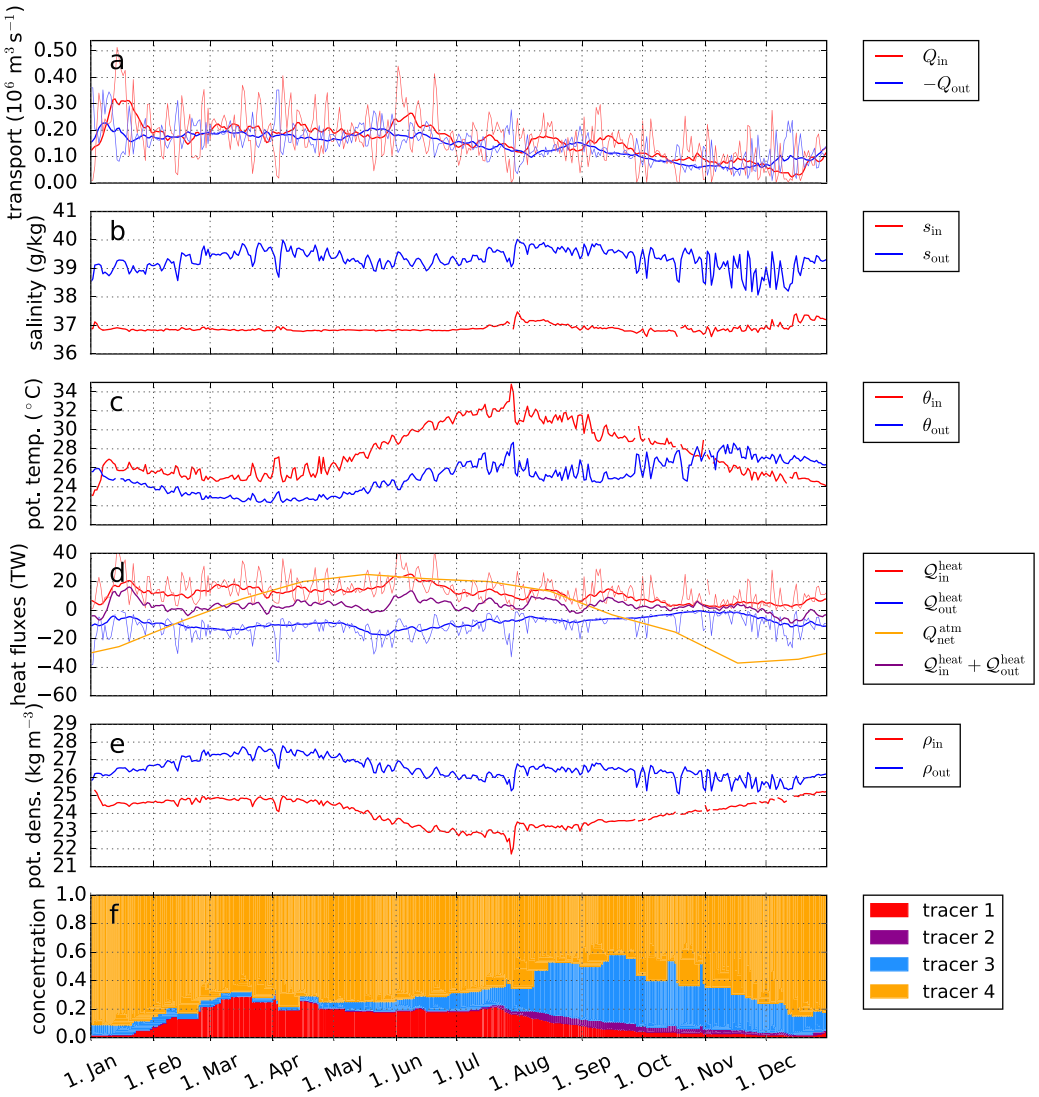

Figure 12. Time series of climatological daily TEF bulk values along TR_{11}: in (a) the transport (thick lines: 14-day running mean, thin lines: daily values), in (b) the bulk salinities, in (c) bulk potential temperatures, (d) heat exchange (thick lines: 14-day running mean, thin lines: daily values) and surface heat fluxes (monthly mean) (e) the bulk potential densities, and in (f) the tracer concentrations of the outflow. Blank spaces indicate that for that climatological day there was no two-layer exchange.

decreases until the the end of the year. The outflowing potential temperature is warmest in November and December. θ_{out} follows the cycle of s_{out} but inversed. When s_{out} shows the higher values, θ_{out} shows smaller values. This link of the properties of the outflow indicates a change in the origin of the water, which will be further investigated in the following section 4.3. The values for the volume transport also indicate a stronger exchange flow in the first half of the year.

Since density is the dynamical relevant quantity, we also integrated along isopycnals in the TEF diagram yielding potential density TEF profiles in Figure 11. The density TEF results show the seasonality as well as the change of the origin of the outflow in August/September. For these months the outflow's density bulk value increases. The volume flux bulk values are very close to the ones of salinity TEF with the exception of November and December as the inflow and outflow are well separated in salinity and density coordinates for these months. In November and December, there is additional compensation in density coordinates, decreasing the volume exchange bulk values.

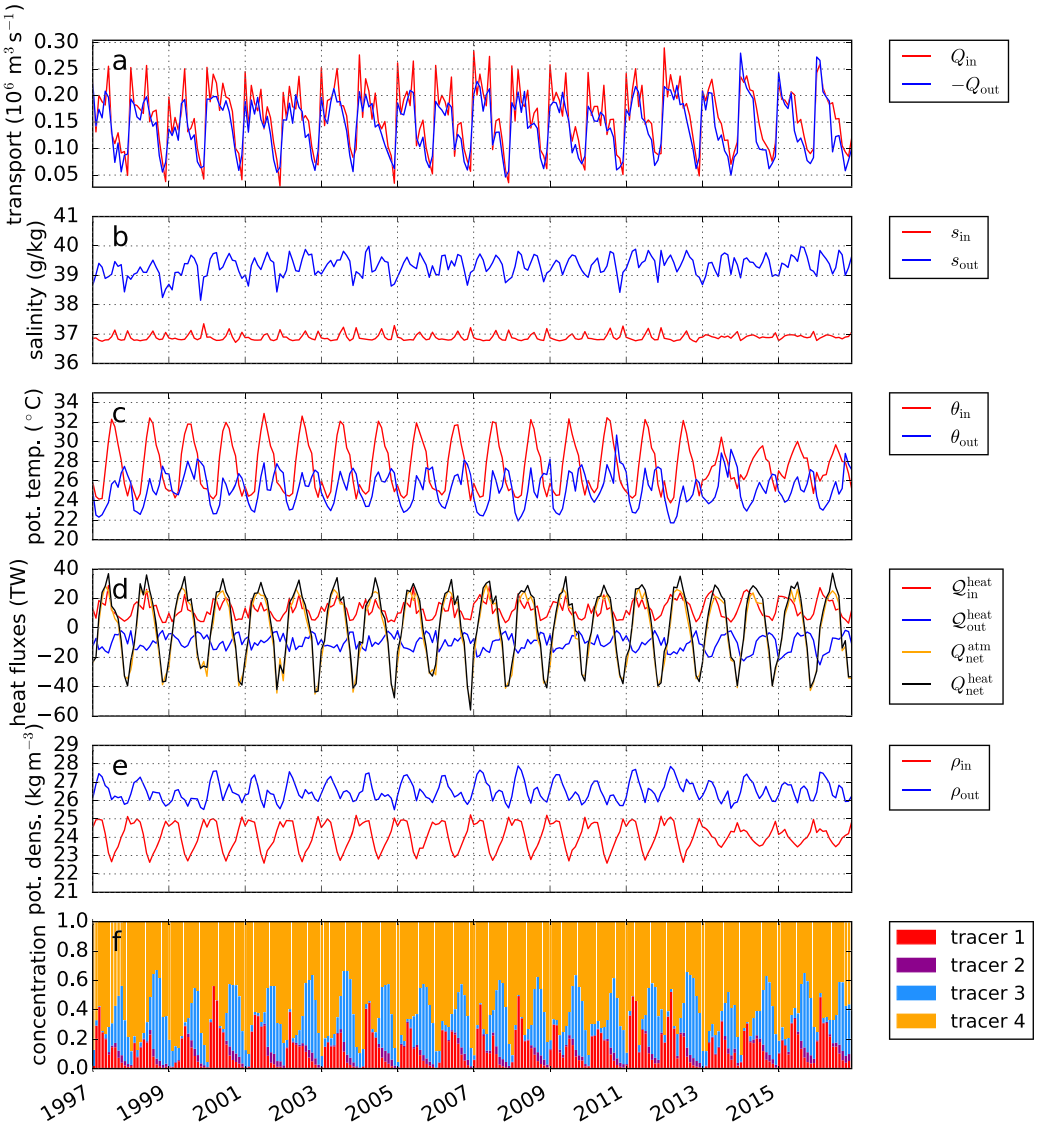

Figure 13. Time series of monthly TEF bulk values along TR_{11}: in (a) the transport, in (b) the bulk salinities, in (c) bulk potential temperatures, in (d) heat exchange and surface heat fluxes ($Q_{net}^{heat} = Q_{in}^{heat} + Q_{out}^{heat} + Q_{net}^{atm}$), in (e) the bulk potential densities, and in (f) the tracer concentrations of the outflow.

4.3. Time Series of the Exchange Flow

We have seen the climatological exchange flow and its salinity, potential temperature, and potential density distribution. In this section we take a closer look into the temporal evolution of the computed bulk values, the heat budget, and the composition of the outflow using the tracers we introduced in section 3. Figure 12 shows the climatological daily bulk values of the transport in (a), the salinities in (b), the potential temperatures in (c), the heat exchange in (d), the bulk potential densities in (e), and the tracer concentrations of the outflow in (f). It should be noted that the time series only shows one bulk value for one inflow and outflow or a blank if there was none on that climatological day. Multiple inflows or multiple outflows, like in January in Figure 10, were combined to one value by weighted averaging (Lorenz et al., 2019). All time series show a very high variability, especially for the volume transport. The climatological results from section 4.2 showed that s_{out} and the maximum salinities changed with the seasons and had two peaks: one in March/April and a second in August/September. The time series of s_{out} in Figure 12b shows these changes as well. Similar changes can be found in the potential temperatures of the outflow in Figure 12c where the potential temperature drops when the salinity increases. ρ_{out} in Figure 12e shows an increase at the same times. This

variability can be explained with the composition of the outflow in Figure 12f. It shows the respective outflow bulk values, that is, fraction of water origin with values between 0 and 1, for the different tracers $c_{i,\mathrm{out}}$ using the salinity coordinates as these represent the PGW properties. The sum of the tracers in each grid cell after the spin-up time is 1, meaning we can exactly decompose where the water was last in contact with the atmosphere. In orange, the eastern surface waters were marked which for the outflow can be interpreted as the fraction of entrained water. January, which showed the strongest exchange, shows the highest fraction of entrained water. For February to July most of the water, despite the entrained water, comes from the southern shallows (red), while from August to December most water comes from the deeper (<30 m) northern parts (blue) and only a small amount (<10%) comes from the northern shallows (purple). This regime shift from water of the southern shallows to water from the north explains the water property change in s_{out}, θ_{out}, and ρ_{out}. Before this shift there is a rapid increase of ~2 °C in θ_{in} and therefore a decrease in ρ_{in}. This coincides with a very small volume inflow at the surface. During the shift, the inflow properties show a short small increase in salinity and density, showing that for a short period the inflow consisted of a mixture of both water masses. Figure 12d shows the bulk values for heat c=$\theta\rho$cs, $Q^{\mathrm{heat}}_{\mathrm{in,out}}$ (ρ: potential density and c_s: specific heat capacity of water), the net surface heat flux $Q^{\mathrm{atm}}_{\mathrm{net}}$, and the net heat exchange with the Indian Ocean as the sum of $Q^{\mathrm{heat}}_{\mathrm{in,out}}$. The net heat transport through the transect is always positive, that is, importing heat into the Gulf, except in December, where heat is exported. This net heat import is highly variable on short timescales but on average replacing the net heat loss into the atmosphere; see also section 3.1.2. To study potential trends and interannual changes during the simulation period we computed monthly bulk values for each year; see Figure 13. The monthly bulk values for transport, salinity, potential temperature, potential density, and heat show similar annual cycles for each year until 2012. From there on the bulk values differ significantly from the years before, especially for the potential temperature the bulk values for θ_{in} are suddenly 2° colder. The reason for this is found in the change of the boundary data. From 2012 the HYCOM simulation changed and therefore the boundary data we apply. The data change from 3-hourly to daily values changes the inflow properties significantly, and the outflow properties insignificantly; see also section 5.2.

5. Discussion

5.1. TEF Diagram

The TEF diagram extends the presentation of the exchange flow by including potential temperature as a second coordinate. This allows gaining insight into the potential temperature-salinity structure, which provides a better understanding of the exchange flow and distinctions between different contributing water masses. Similar frameworks have been applied to study the water mass transformation and overturning circulation, that is, for the Atlantic Ocean (Döös et al., 2012; Groeskamp et al., 2019; Hieronymus et al., 2014; Speer, 1993; Worthington, 1981; Zika et al., 2013). In addition, it can be easily compared to other T-S diagrams with the restriction that the TEF diagram is a subset of a classical T-S diagram due to the partial compensation. Yet because of this reason, the TEF diagram reduces and simplifies the conventional T-S diagram to the relevant potential temperature-salinity combination, which contribute to the exchange flow. The two coordinates presented in this framework could be easily exchanged to other coordinate combinations, that is, potential density (driving the physics) and one being important for the biogeochemistry, for example, oxygen (Groeskamp et al., 2019).

The exchange flow in salinity and potential temperature coordinates yields T-S diagrams with color-coded transport per salinity and potential temperature class. By integration along either of the axis, one finds the classical TEF profile for the other. From these one can compute the bulk values via the dividing salinity method (Lorenz et al., 2019). The results from section 4.1 show that the TEF profiles for potential temperature and salinity do not provide the same bulk values for volume exchange. The reason is found in different compensation when sorting the respective fluxes into salinity or potential temperature bins. This opens the question which coordinate system should be used to compute the bulk values. For quantifying the exchange flow of an arbitrary tracer c we think that one should compute the respective bulk values using the tracer as coordinates. For the estuary only the net exchange is important and therefore the tracer flux per tracer class, that is, salinity space for salinity bulk values and potential temperature space for potential temperature bulk values.

Because of the different compensation in different coordinates, the TEF bulk values are not necessarily representative for the water bodies but definitely representative for the exchange flow. To be representative

for the water bodies, one would have to compute the bulk values from the two-dimensional $q_{S,\Theta}$ or $Q_{S,\Theta}$. For example, instead of finding one dividing salinity, one would have to find one line that separates the inflow and outflow, which aggravate the automatic computation of the volume fluxes. Especially for multilayer exchange flows, the inflows and outflows may not be as clearly separated as for the Persian Gulf.

5.2. Exchange Flow of the Gulf

The results show a seasonality of the exchange flow with stronger exchange flow in terms of transport in the first half of the year and a weaker exchange flow in the second half. The corresponding inflowing properties are a relatively stable value for salinity of $s_{\text{in}} \approx 37$ g/kg and a seasonal potential temperature, and therefore heat, which follows the seasonal cycle of solar radiation. The outflowing properties are dependent on the origin of the water and the amount of entrained water. For the first half of the year, most of the water originated at the southern shallows, which is entrained on its path toward the Strait of Hormuz. In the middle of the year, the waters origin changes from south to north with only a minor contribution of the northern shallows. This change of water masses changes the bulk salinity and potential temperature of the outflow toward higher salinities, colder potential temperatures, and therefore higher potential density. The heat budget is dominated by the surface heat fluxes, yet there is a net heat import through the Strait of Hormuz, which compensates for the net surface heat loss.

The computed transport of the outflow can be compared to the values of other studies with reservation since the TEF bulk values are different from the Eulerian transports (Burchard et al., 2018; MacCready, 2011). But the seasonality and different strength compares well to the results of Yao and Johns (2010b). Compared to the results of Pous et al. (2015), the seasonality compares, but the transports are generally higher in their study. The shape of the climatological TEF diagrams compares well to the T-S diagram provided in Kämpf and Sadrinasab (2006) with data from Alessi et al. (1999) and Pous et al. (2015). However, the maximum salinities in Pous et al. (2015) are less than the values in this study or the observation from Alessi et al. (1999) for the Strait of Hormuz.

We conclude from these results that the seasonal formation of PGW can be described as follows: In fall, when the evaporation rate is highest and the net surface heat flux becomes negative, the stratification of the Gulf vanishes due to buoyancy loss and leads to dense and hypersaline, cold water, especially in the shallow regions in the north and south. The water is well mixed in late fall/early winter; see Figure 4, and horizontal density gradients are formed, which create a bottom gravity current toward the Strait of Hormuz. When vertical mixing becomes weaker in late winter and spring, the exchange flow strengthens comparable to the removal of a lock in a lock exchange. The dense water from the southern shallows arrives in the Strait of Hormuz in winter until the end of spring, which was also found by Kämpf and Sadrinasab (2006). In summer the first water of the north arrives in the Strait and slowly replaces the water from the south, which has become to warm and thus too light. The southern water formed in spring becomes part of the surface recirculation (Yao & Johns, 2010b) during this time. In August/September most of the outflowing water originates from the north, creating the second peaks in s_{out}, θ_{out}, and ρ_{out}. The tracers suggest that most of the dense northern water is not formed in the shallow, but the deeper area (depth greater than 30 m) due to the well-mixed state of the Gulf and the greater volume. Although the water in the deeper northern part may not be as dense as the water from the northern shallows, the water is mixed down and becomes part of the bottom current. This formation is in agreement with Yao and Johns (2010b).

Despite the change in boundary forcing, which changed the bulk values, especially for the inflow θ_{in} and therefore also ρ_{in}, the exchange flows varies from year to year; see Figure 13 as well as the standard deviation in Figures 9 and 10. These can be related to interannual changes in the atmospheric forcing as the boundary potential temperatures and salinities in the upper layer of the boundaries do not show any significant variability except a seasonal cycle. Especially, the wind fields and potential temperatures play an important role for the evaporation, which is the major driver of the exchange flow. As the exchange flow varies annually we do not find any signal of timescales greater than 1 year in the bulk values. The internal interannual variability in the atmospheric forcing is of greater importance for the variability of the exchange flow than the bias in the boundary conditions. Even though the boundary conditions changed, the transformation of IOSW to PGW is robust in the simulation as the outflow properties are within the variability of the years before. Nevertheless, for future long-term studies consistent data sets to force the model would be of great benefit.

6. Summary and Conclusions

This study investigated the potential temperature-salinity structure of the exchange flow of the Gulf by applying the TEF analysis framework (MacCready, 2011) to the results of a 24-year high-resolution simulation using GETM. The TEF analysis framework was extended to include a second coordinate, potential temperature in this case, which leads to a TEF diagram instead of profiles. This two-dimensional decomposition of the exchange flow gives a more detailed insight on the composition of the exchange flow. The model reproduces the general overturning circulation of the Gulf, and the results are in agreement with other studies. We could show that the evolution of the exchange flow follows a seasonal cycle with stronger exchange in spring and summer, than in fall and early winter, that is, Yao and Johns (2010b) and Pous et al. (2015). This is also true for the potential temperature-salinity distribution of the water in the Strait of Hormuz, that is, Alessi et al. (1999). In addition to the volume transport, we provide bulk values for the salinity and potential temperature for the inflow and outflow, which completes the description of the exchange flow. The potential temperature coordinates allowed the computation of the heat exchange through the analyzed transect. Furthermore, the TEF profiles and TEF bulk values for s_{out}, θ_{out}, and ρ_{out} showed a change to higher salinities, lower potential temperatures, and therefore higher potential densities in August/September. We showed with a tracer experiment that this change is associated to a shift of the origin of the PGW. While in winter and spring the PGW originated in the southern shallows, in summer between August/September most water originated from the northern part of the Gulf. This finding underlines the benefits of the two-dimensional TEF analysis framework as it allows further quantification of the exchange flow properties. It can be furthermore easily applied to any estuarine exchange flow.

Acknowledgments
This study was conducted within the framework of the Research Training Group ' Baltic TRANSCOAST' funded by the DFG (Deutsche Forschungsgemeinschaft) under grant number GRK 2000 (www.baltic-transcoast.uni-rostock.de) which funded Marvin lorenz and Hans Burchard. This is Baltic TRANSCOAST publication no. GRK2000/0029. Marvin Lorenz was further supported by the Leibniz strategy fonds (Strategiefonds-2018-IOW-I_Population structure). Knut Klingbeil was supported by the Collaborative Research Centre TRR 181 on Energy Transfer in Atmosphere and Ocean funded by the DFG (Project 274762653). The numerical simulations were performed with resources provided by the North-German Supercomputing Alliance (HLRN). Most of the analysis work was performed by computers financed by PROSO (FKZ: 03F0779A). All data behind the plots and additional model data can be found here (https://iowmeta.io-warnemuende.de/geonetwork/srv/eng/catalog.search#/metadata/IOW-IOWMETA-Persian GulfExchangeFlowModel-1993-2016)

References

Ahmad, F., & Sultan, S. (1991). Annual mean surface heat fluxes in the Arabian Gulf and the net heat transport through the Strait of Hormuz. *Atmosphere-Ocean*, *29*(1), 54–61.

Al Azhar, M., Temimi, M., Zhao, J., & Ghedira, H. (2016). Modeling of circulation in the Arabian Gulf and the Sea of Oman: Skill assessment and seasonal thermohaline structure. *Journal of Geophysical Research: Oceans*, *121*, 1700–1720. https://doi.org/10.1002/2015JC011038

Alessi, C. A., Hunt, H. D., & Bower, A. S. (1999). Hydrographic data from the US Naval Oceanographic Office: Persian Gulf, Southern Red Sea, and Arabian Sea 1923-1996: Woods Hole Oceanographic Institution Ma.

Alosairi, Y., Imberger, J., & Falconer, R. A. (2011). Mixing and flushing in the Persian Gulf (Arabian Gulf). *Journal of Geophysical Research*, *116*, C03029. https://doi.org/10.1029/2010JC006769

Amante, C., & Eakins, B. W. (2009). *ETOPO1 1 arc-minute global relief model: Procedures, data sources and analysis*. Boulder, Colorado, USA: US Department of Commerce, National Oceanic and Atmospheric Administration, National Environmental Satellite, Data, and Information Service, National Geophysical Data Center, Marine Geology and Geophysics Division Colorado.

Bignami, F., Marullo, S., Santoleri, R., & Schiano, M. (1995). Longwave radiation budget in the Mediterranean Sea. *Journal of Geophysical Research*, *100*(C2), 2501–2514.

Burchard, H., & Baumert, H. (1995). On the performance of a mixed-layer model based on the k-ϵ turbulence closure. *Journal of Geophysical Research*, *100*, 8523–8540. https://doi.org/10.1029/94JC03229

Burchard, H., & Bolding, K. (2002). *GETM: A general estuarine transport model; scientific documentation*: European Commission, Joint Research Centre, Institute for Environment and Sustainability.

Burchard, H., Bolding, K., Feistel, R., Gräwe, U., Klingbeil, K., MacCready, P., et al. (2018). The Knudsen theorem and the total exchange flow analysis framework applied to the Baltic Sea. *Progress in Oceanography*, *165*, 268–286. https://doi.org/10.1016/j.pocean.2018.04.004

Burchard, H., Bolding, K., & Villarreal, M. R. (1999). *GOTM, a General Ocean Turbulence Model: Theory, implementation and test cases*. Ispra: Space Applications Institute.

Burchard, H., Bolding, K., & Villarreal, M. R. (2004). Three-dimensional modelling of estuarine turbidity maxima in a tidal estuary. *Ocean Dynamics*, *54*, 250–265. https://doi.org/10.1007/s10236-003-0073-4

Burchard, H., Lange, X., Klingbeil, K., & MacCready, P. (2019). Mixing estimates for estuaries. *Journal of Physical Oceanography*, *49*(2), 631–648.

Chao, S.-Y., Kao, T. W., & Al-Hajri, K. R. (1992). A numerical investigation of circulation in the Arabian Gulf. *Journal of Geophysical Research*, *97*(C7), 11,219–11,236.

Chassignet, E. P., Hurlburt, H. E., Smedstad, O. M., Halliwell, G. R., Hogan, P. J., Wallcraft, A. J., et al. (2007). The HYCOM (HYbrid Coordinate Ocean Model) data assimilative system. *Journal of Marine Systems*, *65*(1), 60–83.

Döös, K., Nilsson, J., Nycander, J., Brodeau, L., & Ballarotta, M. (2012). The world ocean thermohaline circulation. *Journal of Physical Oceanography*, *42*(9), 1445–1460.

Döös, K., & Webb, D. J. (1994). The Deacon cell and the other meridional cells of the Southern Ocean. *Journal of Physical Oceanography*, *24*(2), 429–442.

Egbert, G. D., & Erofeeva, S. Y. (2002). Efficient inverse modeling of barotropic ocean tides. *Journal of Atmospheric and Oceanic Technology*, *19*(2), 183–204.

Elhakeem, A., Elshorbagy, W., & Bleninger, T. (2015). Long-term hydrodynamic modeling of the Arabian Gulf. *Marine pollution bulletin*, *94*(1-2), 19–36.

Gräwe, U., Holtermann, P., Klingbeil, K., & Burchard, H. (2015). Advantages of vertically adaptive coordinates in numerical models of stratified shelf seas. *Ocean Modelling*, *92*, 56–68.

Groeskamp, S., Griffies, S. M., Iudicone, D., Marsh, R., Nurser, A. G., & Zika, J. D. (2019). The water mass transformation framework for ocean physics and biogeochemistry. *Annual Review of Marine Science*, *11*, 271–305.

Hieronymus, M., Nilsson, J., & Nycander, J. (2014). Water mass transformation in salinity–temperature space. *Journal of Physical Oceanography*, *44*(9), 2547–2568.
Hofmeister, R., Beckers, J.-M., & Burchard, H. (2011). Realistic modelling of the exceptional inflows into the central Baltic Sea in 2003 using terrain-following coordinates. *Ocean Modelling*, *39*(3-4), 233–247.
Hofmeister, R., Burchard, H., & Beckers, J.-M. (2010). Non-uniform adaptive vertical grids for 3D numerical ocean models. *Ocean Modelling*, *33*(1), 70–86.
Jain, V., Shankar, D., Vinayachandran, P., Kankonkar, A., Chatterjee, A., Amol, P., et al. (2017). Evidence for the existence of Persian Gulf Water and Red Sea Water in the Bay of Bengal. *Climate Dynamics*, *48*(9-10), 3207–3226.
Jerlov, N. G. (1976). *Marine optics*, vol. 14. Amsterdam; New York: Elsevier.
Johns, W., Yao, F., Olson, D., Josey, S., Grist, J., & Smeed, D. (2003). Observations of seasonal exchange through the Straits of Hormuz and the inferred heat and freshwater budgets of the Persian Gulf. *Journal of Geophysical Research: Oceans*, *108*(C12), 3391. https://doi.org/10.1029/2003JC001881
Kämpf, J., & Sadrinasab, M. (2006). The circulation of the Persian Gulf: A numerical study. *Ocean Science*, *2*(1), 27–41.
Klingbeil, K., & Burchard, H. (2013). Implementation of a direct nonhydrostatic pressure gradient discretisation into a layered ocean model. *Ocean Modelling*, *65*, 64–77. https://doi.org/10.1016/j.ocemod.2013.02.002
Klingbeil, K., Lemarié, F., Debreu, L., & Burchard, H. (2018). The numerics of hydrostatic structured-grid coastal ocean models: State of the art and future perspectives. *Ocean Modelling*, *125*, 80–105. https://doi.org/10.1016/j.ocemod.2018.01.007
Klingbeil, K., Mohammadi-Aragh, M., Gräwe, U., & Burchard, H. (2014). Quantification of spurious dissipation and mixing—Discrete variance decay in a finite-volume framework. *Ocean Modelling*, *81*, 49–64. https://doi.org/10.1016/j.ocemod.2014.06.001
Knudsen, M. (1900). Ein hydrographischer Lehrsatz. *Annalen der Hydrographie und Maritimen Meteorologie*, *28*(7), 316–320.
Lorenz, M., Klingbeil, K., MacCready, P., & Burchard, H. (2019). Numerical issues of the Total Exchange Flow (TEF) analysis framework for quantifying estuarine circulation. *Ocean Science*, *15*(3), 601–614. https://doi.org/10.5194/os-15-601-2019
MacCready, P. (2011). Calculating estuarine exchange flow using isohaline coordinates. *Journal of Physical Oceanography*, *41*(6), 1116–1124.
MacCready, P., Rockwell Geyer, W., & Burchard, H. (2018). Estuarine exchange flow is related to mixing through the salinity variance budget. *Journal of Physical Oceanography*, *48*, 1375–1384.
Morvan, M., L'Hégaret, P., Carton, X., Gula, J., Vic, C., de Marez, C., et al. (2019). The life cycle of submesoscale eddies generated by topographic interactions. *Ocean Science*, *15*(6), 1531–1543. https://doi.org/10.5194/os-15-1531-2019
Pietrzak, J. (1998). The use of TVD limiters for forward-in-time upstream-biased advection schemes in ocean modeling. *Monthly Weather Review*, *126*(3), 812–830.
Pous, S., Carton, X., & Lazure, P. (2004). Hydrology and circulation in the Strait of Hormuz and the Gulf of OmanResults from the GOGP99 experiment: 1. Strait of Hormuz. *Journal of Geophysical Research*, *109*, C12037. https://doi.org/10.1029/2003JC002145
Pous, S., Carton, X., & Lazure, P. (2012). A process study of the tidal circulation in the Persian Gulf. *Open Journal of Marine Science*, *2*(4), 131–140.
Pous, S., Lazure, P., & Carton, X. (2015). A model of the general circulation in the Persian Gulf and in the Strait of Hormuz: Intraseasonal to interannual variability. *Continental Shelf Research*, *94*, 55–70.
Privett, D. (1959). Monthly charts of evaporation from the N. Indian Ocean (including the Red Sea and the Persian Gulf). *Quarterly Journal of the Royal Meteorological Society*, *85*(366), 424–428.
Reynolds, R. M. (1993). Physical oceanography of the Gulf, Strait of Hormuz, and the Gulf of OmanResults from the Mt Mitchell expedition. *Marine Pollution Bulletin*, *27*, 35–59.
Reynolds, R. W., Smith, T. M., Liu, C., Chelton, D. B., Casey, K. S., & Schlax, M. G. (2007). Daily high-resolution-blended analyses for sea surface temperature. *Journal of Climate*, *20*(22), 5473–5496.
Rodi, W. (1987). Examples of calculation methods for flow and mixing in stratified fluids. *Journal of Geophysical Research*, *92*, 5305–5328. https://doi.org/10.1029/JC092iC05p05305
Saha, S., Moorthi, S., Pan, H.-L., Wu, X., Wang, J., Nadiga, S., et al. (2010). *NCEP Climate Forecast System Reanalysis (CFSR) Selected Hourly Time-Series Products, January 1979 to December 2010*. Boulder CO. https://doi.org/10.5065/D6513W89
Saha, S., Moorthi, S., Wu, X., Wang, J., Nadiga, S., Tripp, P., et al. (2011). *NCEP climate forecast system version 2 (CFSv2) selected hourly time-series products*. Boulder CO: Research Data Archive at the National Center for Atmospheric Research, Computational and Information Systems Laboratory. https://doi.org/10.5065/D6N877VB
Shchepetkin, A. F., & McWilliams, J. C. (2003). A method for computing horizontal pressure-gradient force in an oceanic model with a nonaligned vertical coordinate. *Journal of Geophysical Research*, *108*(C3), 3090. https://doi.org/10.1029/2001JC001047
Smagorinsky, J. (1963). General circulation experiments with the primitive equations: I. The basic experiment. *Monthly Weather Review*, *91*(3), 99–164.
Smirnov, A., Holben, B. N., Dubovik, O., O'Neill, N. T., Eck, T. F., Westphal, D. L., et al. (2002). Atmospheric aerosol optical properties in the Persian Gulf. *Journal of the Atmospheric Sciences*, *59*(3), 620–634.
Speer, K. G. (1993). Conversion among North Atlantic surface water types. *Tellus A*, *45*(1), 72–79.
Stark, J. D., Donlon, C. J., Martin, M. J., & McCulloch, M. E. (2007). OSTIA: An operational, high resolution, real time, global sea surface temperature analysis system. In *Oceans 2007-europe*, pp. 1–4.
Swift, S. A., & Bower, A. S. (2003). Formation and circulation of dense water in the Persian/Arabian Gulf. *Journal of Geophysical Research*, *108*(C1), 3004. https://doi.org/10.1029/2002JC001360
Thoppil, P. G., & Hogan, P. J. (2009). On the mechanisms of episodic salinity outflow events in the Strait of Hormuz. *Journal of Physical Oceanography*, *39*(6), 1340–1360.
Thoppil, P. G., & Hogan, P. J. (2010). A modeling study of circulation and eddies in the Persian Gulf. *Journal of Physical Oceanography*, *40*(9), 2122–2134.
Tragou, E., Garrett, C., Outerbridge, R., & Gilman, C. (1999). The heat and fresh water budgets of the Red Sea. *Journal of Physical Oceanography*, *29*(10), 2504–2522.
Umlauf, L., & Burchard, H. (2005). Second-order turbulence closure models for geophysical boundary layers. A review of recent work. *Continental Shelf Research*, *25*(7-8), 795–827.
Vic, C., Roullet, G., Capet, X., Carton, X., Molemaker, M. J., & Gula, J. (2015). Eddy-topography interactions and the fate of the Persian Gulf Outflow. *Journal of Geophysical Research: Oceans*, *120*, 6700–6717. https://doi.org/10.1002/2015JC011033
Walin, G. (1977). A theoretical framework for the description of estuaries. *Tellus*, *29*, 128–136.
Walin, G. (1982). On the relation between sea-surface heat flow and thermal circulation in the ocean. *Tellus*, *34*(2), 187–195.
Willmott, C. J. (1981). On the validation of models. *Physical Geography*, *2*(2), 184–194.

Willmott, C. J. (1982). Some comments on the evaluation of model performance. *Bulletin of the American Meteorological Society*, *63*(11), 1309–1313.

Worthington, L. (1981). 2 the water masses of the world ocean: Some results of a fine-scale census.

Yao, F., & Johns, W. E. (2010a). A HYCOM modeling study of the Persian Gulf: 1. Model configurations and surface circulation. *Journal of Geophysical Research*, *115*, C11017. https://doi.org/10.1029/2009JC005781

Yao, F., & Johns, W. E. (2010b). A HYCOM modeling study of the Persian Gulf: 2. Formation and export of Persian Gulf Water. *Journal of Geophysical Research*, *115*, C11018. https://doi.org/10.1029/2009JC005788

Zika, J. D., Sijp, W. P., & England, M. H. (2013). Vertical heat transport by ocean circulation and the role of mechanical and haline forcing. *Journal of Physical Oceanography*, *43*(10), 2095–2112.

Supporting Information for "Numerical study of the exchange flow of the Persian Gulf using an extended Total Exchange Flow analysis framework"

Marvin Lorenz[1], **Knut Klingbeil**[1]**and Hans Burchard**[1]

[1]Leibniz Institute for Baltic Sea Research Warnemnde, Rostock, Germany

1 SST validation

We provide in Tab. 1 a full table of the validation of the model against satellite products of SST from NOAA OI (Reynolds et al., 2007) and OSTIA (Stark et al., 2007).

2 Surface heat flux validation

Below in Tab. 2 we list all surface fluxes of the model run for the Persian Gulf.

3 Temperature and salinity validation in the Strait of Hormuz

To complement Fig. 6 in the publication, we provide a direct comparison of the model results with observations (Johns et al., 2003) at depths of salinity measurements in Fig. 1.

References

Egbert, G. D., & Erofeeva, S. Y. (2002). Efficient inverse modeling of barotropic ocean tides. *Journal of Atmospheric and Oceanic Technology*, *19*(2), 183–204.

Johns, W., Yao, F., Olson, D., Josey, S., Grist, J., & Smeed, D. (2003). Observations of seasonal exchange through the Straits of Hormuz and the inferred heat and freshwater budgets of the Persian Gulf. *Journal of Geophysical Research: Oceans*, *108*(C12).

Pous, S., Carton, X., & Lazure, P. (2012). A process study of the tidal circulation in the Persian Gulf. *Open Journal of Marine Science*, *2*(04), 131–140.

Reynolds, R. W., Smith, T. M., Liu, C., Chelton, D. B., Casey, K. S., & Schlax, M. G. (2007). Daily high-resolution-blended analyses for sea surface temperature. *Journal of Climate*, *20*(22), 5473–5496.

Stark, J. D., Donlon, C. J., Martin, M. J., & McCulloch, M. E. (2007). OSTIA: An operational, high resolution, real time, global sea surface temperature analysis system. In *Oceans 2007-europe* (pp. 1–4).

Willmott, C. J. (1981). On the validation of models. *Physical geography*, *2*(2), 184–194.

Willmott, C. J. (1982). Some comments on the evaluation of model performance. *Bulletin of the American Meteorological Society*, *63*(11), 1309–1313.

Corresponding author: Marvin Lorenz, `marvin.lorenz@io-warnemuende.de`

Table 1. Comparison values for correlation R (dimensionless), RMSE (°C) and MAE (°C) for the SST of the model and NOAA OI SST product (Reynolds et al., 2007) (top) and the SST derived from OSTIA (Stark et al., 2007) (bottom) for year/winter/summer.

year	R (annual/winter/summer)	RMSE	MAE
NOAA OI			
1993	0.94 / 0.94 / 0.32	0.75 / 1.34 / 1.32	0.63 / 0.77 / 0.01
1994	0.87 / 0.93 / 0.87	0.75 / 1.04 / 0.92	0.50 / 0.25 / 0.50
1995	0.91 / 0.94 / 0.75	0.67 / 1.07 / 0.81	0.39 / 0.43 / 0.17
1996	0.91 / 0.95 / 0.80	0.86 / 1.05 / 1.06	0.73 / 0.60 / 0.85
1997	0.93 / 0.95 / 0.88	0.72 / 1.11 / 0.96	0.53 / 0.58 / 0.60
1998	0.81 / 0.94 / 0.85	0.85 / 0.99 / 0.84	0.57 / 0.46 / 0.57
1999	0.83 / 0.91 / 0.82	0.91 / 1.16 / 1.02	0.62 / 0.57 / 0.73
2000	0.87 / 0.94 / 0.69	0.96 / 1.13 / 1.29	0.73 / 0.61 / 1.07
2001	0.85 / 0.93 / 0.76	0.85 / 1.07 / 0.97	0.56 / 0.49 / 0.63
2002	0.86 / 0.93 / 0.78	0.83 / 1.02 / 1.06	0.56 / 0.34 / 0.78
2003	0.90 / 0.94 / 0.76	0.88 / 1.15 / 1.14	0.69 / 0.67 / 0.84
2004	0.88 / 0.94 / 0.82	0.83 / 1.04 / 0.86	0.60 / 0.46 / 0.47
2005	0.89 / 0.95 / 0.78	0.78 / 1.02 / 0.87	0.50 / 0.49 / 0.56
2006	0.84 / 0.94 / 0.86	0.82 / 1.14 / 1.07	0.55 / 0.40 / 0.76
2007	0.88 / 0.95 / 0.88	0.91 / 1.20 / 1.14	0.70 / 0.65 / 0.90
2008	0.91 / 0.95 / 0.84	0.77 / 1.19 / 1.20	0.53 / 0.47 / 0.88
2009	0.91 / 0.96 / 0.82	0.71 / 1.09 / 1.02	0.43 / 0.52 / 0.69
2010	0.85 / 0.96 / 0.81	0.75 / 0.86 / 1.16	0.51 / 0.26 / 0.96
2011	0.94 / 0.96 / 0.79	0.59 / 0.98 / 0.96	0.26 / 0.36 / 0.54
2012	0.91 / 0.96 / 0.87	0.78 / 0.96 / 1.21	0.55 / 0.27 / 0.92
2013	0.94 / 0.95 / 0.77	0.64 / 1.24 / 1.03	0.41 / 0.56 / 0.17
2014	0.94 / 0.95 / 0.77	0.65 / 1.45 / 1.05	0.42 / 0.65 / 0.05
2015	0.92 / 0.96 / 0.61	0.73 / 1.20 / 1.28	0.52 / 0.47 / 0.50
2016	0.94 / 0.96 / 0.69	0.73 / 1.29 / 1.32	0.48 / 0.48 / 0.40
OSTIA			
2007	0.88 / 0.94 / 0.81	0.72 / 1.15 / 0.88	0.41 / 0.35 / 0.39
2008	0.90 / 0.94 / 0.84	0.76 / 1.25 / 1.12	0.50 / 0.31 / 0.80
2009	0.91 / 0.96 / 0.84	0.67 / 1.01 / 0.87	0.37 / 0.45 / 0.44
2010	0.85 / 0.97 / 0.78	0.74 / 0.84 / 0.99	0.50 / 0.48 / 0.71
2011	0.94 / 0.97 / 0.81	0.60 / 0.90 / 0.88	0.30 / 0.45 / 0.39
2012	0.91 / 0.97 / 0.84	0.75 / 0.84 / 1.18	0.54 / 0.45 / 0.88
2013	0.93 / 0.96 / 0.75	0.63 / 1.17 / 0.99	0.38 / 0.73 / -0.08
2014	0.93 / 0.95 / 0.77	0.62 / 1.37 / 1.02	0.35 / 0.73 / -0.24
2015	0.92 / 0.96 / 0.72	0.67 / 1.17 / 1.06	0.43 / 0.65 / 0.03
2016	0.94 / 0.96 / 0.73	0.64 / 1.20 / 1.15	0.31 / 0.48 / 0.02

Table 2. Table of the annual mean surface heat and fresh water fluxes of all model years. The unit for the heat fluxes is $\mathrm{W\,m^{-2}}$ and the unit for the fresh water fluxes is $\mathrm{m\,a^{-1}}$.

year	Q_{short}	Q_{long}	Q_{latent}	Q_{sens}	Q_{net}	P	E	$P-E$
1993	207.1	-83.9	-119.1	-4.3	-0.2	0.15	1.51	-1.35
1994	209.6	-85.2	-130.4	-3.3	-9.3	0.04	1.65	-1.60
1995	208.2	-84.6	-124.1	-3.6	-4.1	0.17	1.57	-1.40
1996	207.1	-83.3	-121.1	-5.2	-2.5	0.20	1.53	-1.34
1997	205.9	-83.5	-126.7	-4.1	-8.3	0.28	1.60	-1.32
1998	209.1	-82.2	-117.8	-3.5	5.6	0.12	1.49	-1.37
1999	211.3	-84.0	-132.9	-3.2	-8.9	0.10	1.68	-1.58
2000	211.5	-85.1	-130.8	-3.5	-8.0	0.09	1.65	-1.56
2001	212.4	-83.6	-126.4	-1.2	1.3	0.04	1.60	-1.56
2002	210.8	-85.7	-131.3	-4.8	-10.9	0.07	1.66	-1.59
2003	207.8	-82.1	-127.7	-2.6	-4.6	0.10	1.62	-1.52
2004	209.3	-83.7	-127.7	-3.4	-5.5	0.11	1.62	-1.51
2005	210.0	-84.2	-123.4	-2.5	-0.1	0.09	1.56	-1.48
2006	206.3	-82.2	-130.1	-5.0	-11.0	0.14	1.65	-1.50
2007	211.9	-84.5	-126.2	-2.7	-1.6	0.06	1.60	-1.53
2008	212.0	-85.4	-130.2	-3.2	-6.7	0.06	1.65	-1.58
2009	208.5	-83.2	-125.6	-1.0	-1.4	0.12	1.59	-1.47
2010	213.2	-84.7	-126.6	-2.1	-0.2	0.05	1.60	-1.56
2011	208.6	-82.9	-136.0	-2.3	-12.6	0.09	1.72	-1.63
2012	209.3	-83.4	-125.4	-2.8	-2.3	0.08	1.59	-1.51
2013	211.5	-85.4	-132.3	-2.2	-8.4	0.11	1.67	-1.56
2014	211.0	-83.0	-130.4	-1.4	-3.8	0.10	1.65	-1.55
2015	211.0	-82.1	-132.5	-1.7	-5.3	0.08	1.68	-1.60
2016	210.6	-81.5	-132.7	-1.5	-5.1	0.08	1.68	-1.59
mean	209.8	-83.7	-127.8	-3.0	-4.7	0.11	1.62	-1.51

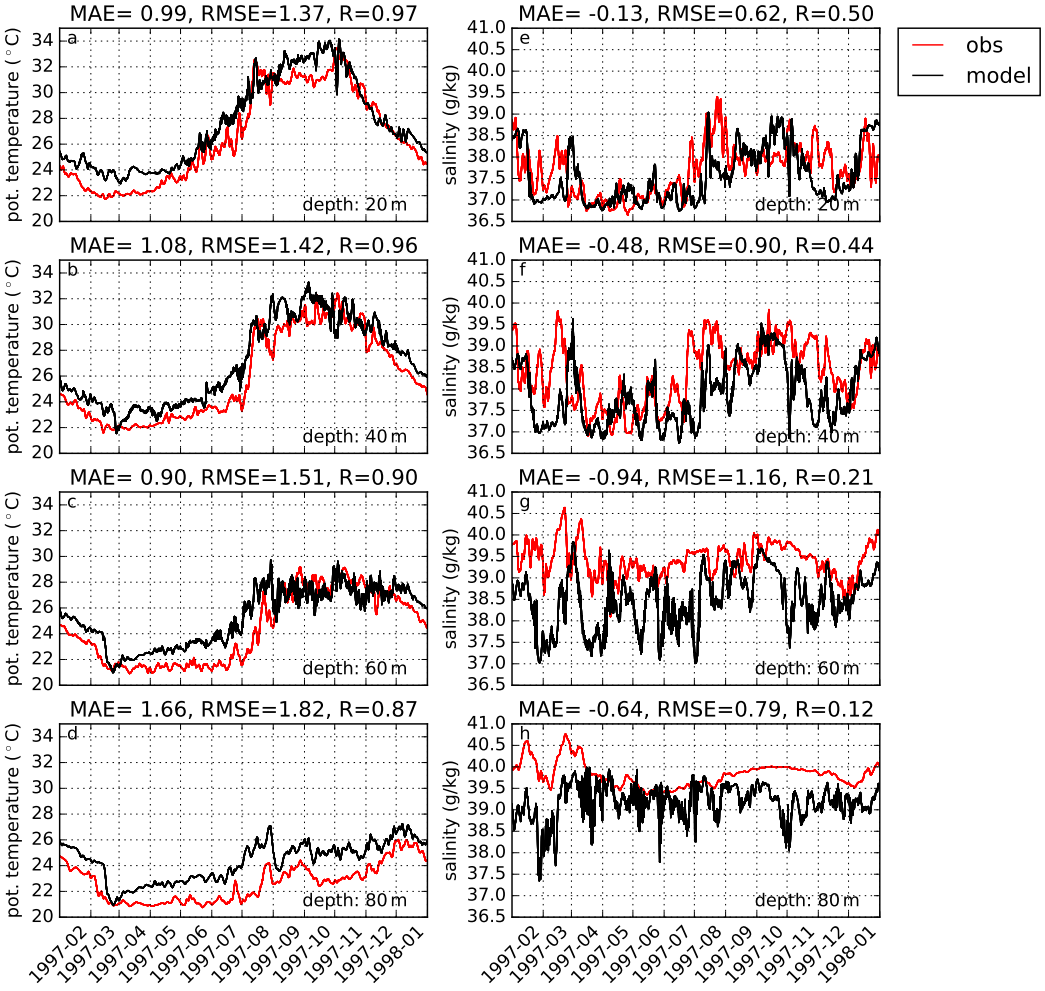

Figure 1. Times series for potential temperature and salinity for the model (black) and observations (Johns et al., 2003) (red) for depths of salinity measurements. For each depth, the MAE, the RMSE and correlation R are computed.

Generated using the official AMS LaTeX template v5.0

Impact of evaporation and precipitation on estuarine mixing relations

Marvin Lorenz*, Knut Klingbeil, Hans Burchard

Leibniz Institute for Baltic Sea Research Warnemünde, Rostock, Germany

Corresponding author: Marvin Lorenz, marvin.lorenz@io-warnemuende.de

ABSTRACT

Recent studies could link the quantities of estuarine exchange flows to the volume-integrated mixing inside an estuary, where mixing is defined as the destruction of salinity variance. These so-called mixing relations state that the mixing inside an estuary is given by its boundary fluxes which are quantified as Knudsen or Total Exchange Flow bulk values. So far, river runoff is the only freshwater flux included and the freshwater exchange due to precipitation and evaporation is neglected. Yet, the latter is the driving force of inverse estuaries, which could not be described by the existing relations. Therefore, this study adds evaporation and precipitation to complete the existing mixing relations. It is shown that these are included as an additional variance transport to the mixing relations. This further allows decomposing the mixing into a riverine and a surface transport contribution. The derived relations are tested against idealized two-dimensional numerical simulations of different combinations of freshwater forcing. The exact mixing, occurring in the model, can be directly diagnosed and compared to the estuarine mixing relations. Both agree exactly. Furthermore, the mixing relations are applied for the first time to a realistic three-dimensional numerical simulation, an annual hind-cast simulation of the Persian Gulf. The results show that the mixing contributions of river discharge and evaporation are almost equal, although the freshwater transport due to evaporation is about one order of magnitude larger than the river runoff.

1. Introduction

Estuaries are mixing hotspots where river water of zero salinity is mixed with inflowing saline ocean water to form brackish water, flowing out of the estuary into the ocean. Mixing is the key process that transforms the properties of the inflowing water into the properties of outflowing water, e.g. salinity, temperature, and suspended matter concentration. We define mixing in this study as the destruction of salinity variance per unit volume, χ^s (Nash and Moum 2002; Burchard and Rennau 2008; Burchard et al. 2009; Wang et al. 2017; MacCready et al. 2018; Burchard et al. 2019), since salinity is the major contributor to the density structure in estuaries. By the knowledge of inflow and outflow properties as well as river discharge, one can draw inferences about the mixing inside the estuary as shown recently by MacCready et al. (2018) and Burchard et al. (2019). By evaluating the salinity variance budget in terms of the Knudsen relations (Knudsen 1900), MacCready et al. (2018) relate the long-term average, estuary-wide mixing, M, to the characteristics of the exchange flow and river discharge,

$$M \approx s_{\mathrm{in}} s_{\mathrm{out}} Q_r, \tag{1}$$

where s_{in} and s_{out} are the bulk values of the salinities of the inflow and outflow, and Q_r is the river discharge. For the computation of the exchange flows bulk values, the Total Exchange Flow (TEF) analysis framework (MacCready 2011) is used. Burchard et al. (2019) generalized the mixing relation to a non-stationary relation, that can exactly compute the mixing inside a model estuary.

While these mixing relations can be applied to all estuaries which are driven by river discharge only, there is the whole class of inverse estuaries, which can not be described as evaporation is neglected in the previous studies (MacCready et al. 2018; Burchard et al. 2019). Furthermore, tropical and subtropical estuaries can be a combination of inverse and classical estuaries (Valle-Levinson 2010). Strong evaporation may form so-called salt plugs, a region of maximum salinities

greater than the ocean salinity inside the estuary (Wolanski 1986). For those types of an estuary, the freshwater forcing may change between seasons, i.e. the estuary may change from a classical estuary type during rain season to an inverse type in dry season (Valle-Levinson and Bosley 2003).

Simply replacing the incoming river runoff Q_r with the outgoing evaporation transport Q_{evap}, $Q_{\text{evap}} < 0$, in (1) would result in $M < 0$. For the exchange flow, this might make sense, as the inflowing water is transformed into more saline outflowing water which requires demixing of the inflowing water since no salt is added in the estuary. But M is by definition a strictly positive number. As we will show in this study, the solution is an additional boundary flux proportional to the square of the surface salinity, which is not considered in (1). The added variance by surface fluxes ensures $M \geq 0$. Stern (1968) already states that salt variance added by surface fluxes has to be destructed on micro-scales due to molecular diffusion to achieve a steady-state solution for the world ocean.

By this inclusion, not only estuaries may be described, but also bays, lagoons, and shallow coastal zones which are influenced by precipitation or evaporation.

The paper is structured as follows: first, we derive the exact mixing relations including the cross-surface freshwater transport in Section 2, as an extension to the relations presented in MacCready et al. (2018) and Burchard et al. (2019). In Section 3 we present a schematic box model explaining the new mixing relation for a strictly inverse estuary. In Section 4 we present the application of the new mixing relations to idealized, two-dimensional estuary simulations, and the first application to a realistic, three-dimensional simulation, the Persian Gulf. In Section 5 we discuss the results of this study and conclude.

2. Derivation of the mixing relations

a. Budget equations

Volume

Following the derivation of Burchard et al. (2019) we consider Cartesian coordinates (x, y, z), the time t and the velocity vector (u, v, w). We start at the Reynolds-averaged continuity equation in Boussinesq approximation,

$$\partial_x u + \partial_y v + \partial_z w = 0. \tag{2}$$

We consider the kinematic boundary conditions at the surface,

$$w(\eta) = \partial_t \eta + u(\eta)\partial_x \eta + v(\eta)\partial_y \eta + E - P \quad \text{for} \quad z = \eta, \tag{3}$$

where E is the evaporation rate and P the precipitation rate, both in $\mathrm{m\,s^{-1}}$, and the bottom,

$$w(-H) = -u(-H)\partial_x H - v(-H)\partial_y H \quad \text{for} \quad z = -H. \tag{4}$$

Carrying out the volume integration over the whole volume of the estuary and considering the kinematic boundary conditions, (3) and (4), the continuity equation (2) reads as

$$\partial_t V = -\int_{A_b} u_n \,\mathrm{d}A - \int_{A_r} u_n \,\mathrm{d}A + \int_{A_{\mathrm{surf}}} (P - E)\,\mathrm{d}A. \tag{5}$$

A_b describes the open boundary area, A_r the river boundary area, A_{surf} the surface area, and u_n denotes the normal velocity component (positive outwards).

Salinity

The Reynolds-averaged salinity equation reads as

$$\partial_t s + \partial_x (us) + \partial_y (vs) + \partial_z (ws) - \partial_x (K_h \partial_x s) - \partial_y \left(K_h \partial_y s\right) - \partial_z (K_v \partial_z s) = 0, \tag{6}$$

where we used the eddy-diffusivity assumption for turbulent salinity fluxes. K_h and K_v denote the horizontal and vertical eddy diffusivities, respectively, and s the salinity. Volume integration of the salinity equation (6) requires boundary conditions for the diffusive salt flux. We demand that there is no net salt flux through the surface and the bottom. The surface boundary condition for salt flux reads therefore as

$$K_h(\partial_x s)(\partial_x \eta) + K_h(\partial_y s)(\partial_y \eta) - K_v \partial_z s = -(E-P)\, s \quad \text{for} \quad z = \eta \tag{7}$$

(Beron-Vera et al. 1999; Warren 2009; Nurser and Griffies 2019) and at the bottom as

$$K_h(\partial_x s)(\partial_x(-H)) + K_h(\partial_y s)(\partial_y(-H)) - K_v \partial_z s = 0 \quad \text{for} \quad z = -H. \tag{8}$$

In (7) the diffusive salt flux at the surface is necessary to compensate the advective salt flux associated with (3). With these boundary conditions the volume-integrated salinity equation (6) reads as

$$\partial_t \int_V s \,\mathrm{d}V = -\int_{A_b} (s u_n - K_h \partial_n s)\,\mathrm{d}A \equiv -\int_{A_b} f_n^s \,\mathrm{d}A, \tag{9}$$

with ∂_n denoting the derivative normal to the transect. Furthermore, we define the tracer flux

$$f_n^c \equiv c u_n - K_h \partial_n c, \tag{10}$$

with c being a passive tracer, in eq. (9) $c = s$. Eq. (9) only allows exchanging salt through the open ocean boundary.

Salinity Square

Multiplication of (6) with $2s$ leads to an equation for s^2,

$$\partial_t s^2 + \partial_x\left(u s^2\right) + \partial_y\left(v s^2\right) + \partial_z\left(w s^2\right) - \partial_x\left(K_h \partial_x s^2\right) - \partial_y\left(K_h \partial_y s^2\right) - \partial_z\left(K_v \partial_z s^2\right) = -\chi^s, \tag{11}$$

with the local salt mixing

$$\chi^s = 2\left[K_h(\partial_x s)^2 + K_h(\partial_y s)^2 + K_v(\partial_z s)^2\right], \tag{12}$$

see Burchard and Rennau (2008). By multiplication of (7) and (8) with $2s$, one finds corresponding boundary conditions for s^2,

$$K_h(\partial_x s^2)(\partial_x \eta) + K_h(\partial_y s^2)(\partial_y \eta) - K_v \partial_z s^2 = -2(E-P)\, s^2 \quad \text{for} \quad z = \eta \tag{13}$$

and

$$K_h(\partial_x s^2)(\partial_x(-H)) + K_h(\partial_y s^2)(\partial_y(-H)) - K_v \partial_z s^2 = 0 \quad \text{for} \quad z = -H. \tag{14}$$

Volume integration of (11) and using the derived boundary conditions (13) and (14) yield

$$\partial_t \int_V s^2 \,\mathrm{d}V = -\int_{A_b} f_n^{s^2} \,\mathrm{d}A + \int_{A_{\mathrm{surf}}} s^2 (E-P) \,\mathrm{d}A - \int_V \chi^s \,\mathrm{d}V, \tag{15}$$

where the second term on the right hand side denotes the salinity squared transport due to the net surface freshwater transport.

Salinity variance

Similarly, an equation for the local salinity variance s'^2, with $s' = s - \bar{s}$, where $\bar{s}$ denotes the volume-averaged salinity, $\bar{s} = \frac{1}{V}\int s \,\mathrm{d}V$ can be derived. By subtracting $\partial_t \bar{s}$ from the salinity equation (6) and multiplying with $2s'$ one finds

$$\begin{aligned} \partial_t s'^2 + \partial_x \left(u s'^2\right) + \partial_y \left(v s'^2\right) + \partial_z \left(w s'^2\right) - \partial_x \left(K_h \partial_x s'^2\right) - \partial_y \left(K_h \partial_y s'^2\right) - \partial_z \left(K_v \partial_z s'^2\right) \\ = -\chi^s - 2s' \partial_t \bar{s}. \end{aligned} \tag{16}$$

The respective variance boundary conditions can be derived by multiplying (7) and (8) with $2s'$:

$$K_h(\partial_x s'^2)(\partial_x \eta) + K_h(\partial_y s'^2)(\partial_y \eta) - K_v \partial_z s'^2 = -2(E-P)\, s^2 - 2(E-P)\, s\bar{s} \quad \text{for} \quad z = \eta \tag{17}$$

and

$$K_h(\partial_x s'^2)(\partial_x(-H)) + K_h(\partial_y s'^2)(\partial_y(-H)) - K_v \partial_z s'^2 = 0 \quad \text{for} \quad z = -H. \tag{18}$$

By integration over the estuarine volume and considering the boundary conditions (17) and (18), (16) yields

$$\partial_t \int_V s'^2 dV = -\int_{A_b} f_n^{s'^2}\,\mathrm{d}A + \bar{s}^2 \int_{A_r} u_n\,\mathrm{d}A + \int_{A_{\mathrm{surf}}} \left(s^2 - \bar{s}^2\right)(E-P)\,\mathrm{d}A - \int_V \chi^s\,\mathrm{d}V, \tag{19}$$

where the first term on the right hand side denotes the variance exchange with the ocean, the second term accounts the change of the mean salinity due to river runoff and the third term accounts variance changes due to evaporation and precipitation. The integrated salt mixing χ^s denotes a sink in both the salinity squared equation (15) and the salinity variance equation (19). The formalism of the salinity squared equation (15) has the advantage that it only depends on boundary fluxes and not on any internal information of the estuary. The variance on the other hand depends on the mean salinity $\bar{s}$ which is a volume-integrated property. Therefore, the salinity squared formalism is easier to use and apply (Burchard et al. 2019).

b. Time averaging and reformulation in terms of TEF bulk values

Using the Total Exchange Flow analysis framework (MacCready 2011; Burchard et al. 2018; Lorenz et al. 2019), which allows proper computation of bulk values characterizing the net exchange flow of an estuary with the ocean, we want to express the volume, salinity, salinity squared and salinity variance budget in terms of bulk values. In the TEF analysis framework, the transport of any tracer c above a certain salinity S through any cross section is defined as

$$Q^c(S) = -\left\langle \int_{A(S)} f_n^c\,\mathrm{d}A \right\rangle, \tag{20}$$

with $A(S)$ being the fraction of the transect with $s > S$ (MacCready 2011) and $\langle\,\rangle$ denotes temporal averaging. The inflowing and outflowing bulk properties are defined as the fraction of inflow/outflowing tracer transport divided by the respective volume transport:

$$c_{\mathrm{in}} = \frac{Q^c_{\mathrm{in}}}{Q_{\mathrm{in}}}, \quad c_{\mathrm{out}} = \frac{Q^c_{\mathrm{out}}}{Q_{\mathrm{out}}}, \tag{21}$$

where $Q^c_{\text{in}} \geq 0$ and $Q^c_{\text{out}} \leq 0$ can be computed from $Q^c(S)$ with considerations of the extreme values, see Lorenz et al. (2019). With $c = 1$, the volume transport bulk values, Q_{in}, Q_{out}, their respective bulk salinities ($c = s$), s_{in}, s_{out}, bulk salinities squared ($c = s^2$), $(s^2)_{\text{in}}$, $(s^2)_{\text{out}}$, bulk salinity variances ($c = s'^2$), $(s'^2)_{\text{in}}$, $(s'^2)_{\text{out}}$, and with the definitions of river discharge

$$Q_r = -\left\langle \int_{A_r} u_n \, \mathrm{d}A \right\rangle, \tag{22}$$

surface fresh water transport

$$Q_{\text{surf}} = -\left\langle \int_{A_{\text{surf}}} (E - P) \, \mathrm{d}A \right\rangle = Q_{\text{evap}} + Q_{\text{precip}}, \tag{23}$$

with $Q_{\text{evap}} \leq 0$, $Q_{\text{precip}} \geq 0$, surface salinity transport

$$F^{s^2}_{\text{surf}} = \left\langle \int_{A_{\text{surf}}} s^2 (E - P) \, \mathrm{d}A \right\rangle, \tag{24}$$

and volume integrated salt mixing

$$M = \left\langle \int_V \chi^s \, \mathrm{d}V \right\rangle, \tag{25}$$

where $M \geq 0$, one can rewrite the time-averaged budget equations (5), (9), (15) and (19):

$$\begin{aligned} \delta V = \langle \partial_t V \rangle &= Q(0) + Q_r + Q_s \\ &= Q_{\text{in}} + Q_{\text{out}} + Q_r + Q_{\text{surf}}, \end{aligned} \tag{26}$$

$$\delta S = \left\langle \partial_t \int_V s \, \mathrm{d}V \right\rangle = Q^s(0) = Q^s_{\text{in}} + Q^s_{\text{out}} = Q_{\text{in}} s_{\text{in}} + Q_{\text{out}} s_{\text{out}} \tag{27}$$

$$\begin{aligned} \delta S^2 = \left\langle \partial_t \int_V s^2 \, \mathrm{d}V \right\rangle &= Q^{s^2}(0) + F^{s^2}_{\text{surf}} - M \\ &= Q_{\text{in}} \left(s^2\right)_{\text{in}} + Q_{\text{out}} \left(s^2\right)_{\text{out}} + F^{s^2}_{\text{surf}} - M, \end{aligned} \tag{28}$$

and

$$\begin{aligned} \delta S'^2 = \left\langle \partial_t \int_V s'^2 \, \mathrm{d}V \right\rangle &= Q^{s'^2}(0) + F^{s^2}_{\text{surf}} + \left\langle \bar{s}^2 \int_{A_r} u_n \, \mathrm{d}A \right\rangle - \left\langle \int_{A_{\text{surf}}} \bar{s}^2 (E - P) \, \mathrm{d}A \right\rangle - M \\ &= Q_{\text{in}} \left(s'\right)^2_{\text{in}} + Q_{\text{out}} \left(s'\right)^2_{\text{out}} + F^{s^2}_{\text{surf}} + \left\langle \bar{s}^2 \int_{A_r} u_n \, \mathrm{d}A \right\rangle - \left\langle \int_{A_{\text{surf}}} \bar{s}^2 (E - P) \, \mathrm{d}A \right\rangle - M. \end{aligned} \tag{29}$$

Combining (26) and (27) leads to the time dependent Knudsen relations (Knudsen 1900) including surface freshwater transport:

$$Q_{\text{in}} = \frac{s_{\text{out}}}{s_{\text{in}} - s_{\text{out}}} (Q_r - \delta V + Q_{\text{surf}}) + \frac{1}{s_{\text{in}} - s_{\text{out}}} \delta S, \tag{30}$$

$$Q_{\text{out}} = -\left(\frac{s_{\text{in}}}{s_{\text{in}} - s_{\text{out}}} (Q_r - \delta V + Q_{\text{surf}}) + \frac{1}{s_{\text{in}} - s_{\text{out}}} \delta S \right). \tag{31}$$

c. Exact and approximated mixing relations

Further combining (28) with (31) and (30) one finds an equation for the time averaged, volume-integrated mixing:

$$M_e = \frac{s_{\text{out}}(s^2)_{\text{in}} - s_{\text{in}}(s^2)_{\text{out}}}{s_{\text{in}} - s_{\text{out}}} (Q_r - \delta V + Q_{\text{surf}}) + \frac{(s^2)_{\text{in}} - (s^2)_{\text{out}}}{s_{\text{in}} - s_{\text{out}}} \delta S - \delta S^2 + F^{s^2}_{\text{surf}}, \tag{32}$$

which is the same result as in Burchard et al. (2019) but with the additional fresh water input Q_{surf} and an additional s^2-transport through the surface, $F^{s^2}_{\text{surf}}$. For $P = E = 0$ (32) reduces to equation (36) of Burchard et al. (2019). Assuming constancy, i.e. the temporal average of the squared property is the same as the time averaged quantity squared, e.g. $(s^2)_{\text{in}} = (s_{\text{in}})^2$, $(s^2)_{\text{out}} = (s_{\text{out}})^2$, (32) reduces to

$$M_c = s_{\text{in}} s_{\text{sout}} (Q_r - \delta V + Q_{\text{surf}}) + (s_{\text{in}} - s_{\text{out}}) \delta S - \delta S^2 + F^{s^2}_{\text{surf}}. \tag{33}$$

If we assume periodicity or apply long-term averaging, i.e. a tidally periodic estuary, or long-term average of the estuary, the storage terms are approximately zero. Under these assumptions (32) yields

$$M_p = \frac{s_{\text{out}}(s^2)_{\text{in}} - s_{\text{in}}(s^2)_{\text{out}}}{s_{\text{in}} - s_{\text{out}}} (Q_r + Q_{\text{surf}}) + F^{s^2}_{\text{surf}}. \tag{34}$$

Considering both assumptions at the same time, (32) reads as

$$M_{cp} = s_{\text{in}} s_{\text{out}} (Q_r + Q_{\text{surf}}) + F^{s^2}_{\text{surf}}, \tag{35}$$

which we can rewrite by defining a bulk surface salinity,

$$s_{\text{surf}} \equiv \left[(s^2)_{\text{surf}}\right]^{\frac{1}{2}} = \left(-\frac{F^{s^2}_{\text{surf}}}{Q_{\text{surf}}}\right)^{\frac{1}{2}}, \tag{36}$$

to

$$M_{cp} = s_{\text{in}} s_{\text{out}} Q_r + \left(s_{\text{in}} s_{\text{out}} - (s_{\text{surf}})^2\right) Q_{\text{surf}}. \tag{37}$$

The relation consists of two terms, each related to different forcing: the mixing term due to river discharge and a mixing term due to precipitation and evaporation. For vanishing surface freshwater fluxes (37) reduces to (1) established by MacCready et al. (2018).

Now we can also solve the problem stated in the introduction. For the case of evaporation only, (37) becomes

$$M_{cp} = \left(s_{\text{in}} s_{\text{out}} - (s_{\text{surf}})^2\right) Q_{\text{evap}} \quad \text{for} \quad Q_r = Q_{\text{precip}} = 0, \tag{38}$$

and shows that despite $Q_{\text{evap}} < 0$ a non-negative M_{cp} is obtained due the additional squared surface salinity term with $s_{\text{surf}} \geq (s_{\text{in}} s_{\text{out}})^{1/2}$. If the surface salinity of an inverse estuary does not fulfill this condition, the assumptions of stationarity and constancy are invalid.

For the case of precipitation only, (37) becomes

$$M_{cp} = \left(s_{\text{in}} s_{\text{out}} - (s_{\text{surf}})^2\right) Q_{\text{precip}} \quad \text{for} \quad Q_r = Q_{\text{evap}} = 0, \tag{39}$$

which requires $s_{\text{surf}} \leq (s_{\text{in}} s_{\text{out}})^{1/2}$. This condition is fulfilled, as for this kind of estuary the water column would be stratified and therefore $s_{\text{surf}} \leq s_{\text{out}} < s_{\text{in}}$.

3. Simplistic Box Model

To exemplify the derived mixing relation (35) for an inverse estuary, we assume a box model as shown in Fig. 1. A steady state with a surface layer of volume V_{surf} with salinity s_{surf} and a

bottom layer of volume V_b with salinity s_{out} (Fig. 1a) is maintained by the co-action of evaporation and inverse estuarine circulation during an infinitesimal time interval Δt. We describe the process of evaporation via $Q_{\text{surf}} < 0$ as spatially constant removal of fresh water from the saline surface volume. This fresh water loss increases the surface salinity from s_{surf} to s^*_{surf}, see Fig. 1b. The volume in the estuary is replenished by an exchange flow with inflowing ocean water ($Q_{\text{in}}, s_{\text{in}}$) and an outflow of estuarine bottom water ($Q_{\text{out}}, s_{\text{out}}$) keeping the salt in the estuary constant (Fig. 1c).

In the following the mixing necessary to maintain the steady state shown in Fig. 1a, more precise to return to it from the state shown in Fig. 1c, is calculated. The volume-integrated salinity squares for the different states are given by

$$\Sigma_a = V_{\text{surf}}(s_{\text{surf}})^2 + V_b(s_{\text{out}})^2, \tag{40}$$

$$\Sigma_b = (V_{\text{surf}} + \Delta t Q_{\text{surf}})(s^*_{\text{surf}})^2 + V_b(s_{\text{out}})^2, \tag{41}$$

$$\Sigma_c = (V_{\text{surf}} + \Delta t Q_{\text{surf}})(s^*_{\text{surf}})^2 + \Delta t Q_{\text{in}}(s_{\text{in}})^2 + (V_b + \Delta t Q_{\text{out}})(s_{\text{out}})^2. \tag{42}$$

The production of volume-integrated salinity square due to evaporation ($Q_{\text{surf}} < 0$) can be calculated as

$$\frac{\Sigma_b - \Sigma_a}{\Delta t} = -\frac{1}{1 + \frac{\Delta t Q_{\text{surf}}}{V_{\text{surf}}}}(s_{\text{surf}})^2 Q_{\text{surf}}, \tag{43}$$

where salt conservation between states a and b,

$$V_{\text{surf}} s_{\text{surf}} = (V_{\text{surf}} + \Delta t Q_{\text{surf}})\, s^*_{\text{surf}}, \tag{44}$$

has been used. With the help of the Knudsen relations (30) and (31) with $Q_r = \delta V = \delta S = 0$, the change of volume-integrated salinity square due to the exchange flow can be quantified as

$$\frac{\Sigma_c - \Sigma_b}{\Delta t} = s_{\text{in}} s_{\text{out}} Q_{\text{surf}}. \tag{45}$$

The mixing required to mix state c back to state a is given by $\frac{\Sigma_c - \Sigma_a}{\Delta t}$ and thus

$$M_{cp} = \lim_{\Delta t \to 0} \frac{(\Sigma_c - \Sigma_b) + (\Sigma_b - \Sigma_a)}{\Delta t} = \left(s_{\text{in}} s_{\text{out}} - (s_{\text{surf}})^2\right) Q_{\text{surf}}, \tag{46}$$

which is the same result as in (35) with $Q_r = 0$. The variance change $\frac{\Sigma_b - \Sigma_a}{\Delta t}$ in (43) is equivalent to the additional s^2-flux $F^{s^2}_{\text{surf}}$. From this simple box model the two components included in M_{cp} are well illustrated, balancing the salinity square (variance) loss due to the exchange flow and the salinity square (variance) gain due to evaporation.

4. Numerical model setups

To test the derived relations (32)–(35) in a numerical model, we employ a 2D model similar to the setup of Warner et al. (2005) and Burchard et al. (2019), and a realistic three-dimensional model of the Persian Gulf, also known as Arabian Gulf. The model of our choice is the General Estuarine Transport Model (GETM, Burchard and Bolding 2002), a coastal ocean model, solving the hydrostatic Boussinesq equations (Klingbeil et al. 2018). For turbulence closure the turbulence module of the General Ocean Turbulence Model (GOTM, Burchard and Bolding 2001) is coupled to the model. Here, we use the $k-\epsilon$-model in all simulations as well as the TVD-Superbee scheme (Pietrzak 1998) for the advection discretization. Further details on the different setups are described in the respective sections.

a. Calculation of mixing and $F^{s^2}_{surf}$ in the model

In GETM all forms of variance changes are quantified in every grid cell according to the discrete variance decay analysis method of Klingbeil et al. (2014). This also includes the application of (43) to the single surface grid cells. The corresponding variance change defines the local contribution to $F^{s^2}_{\text{surf}}$. The total mixing of the model $M^{\text{tot}}_{\text{model}}$ consists of physical $M^{\text{phy}}_{\text{model}}$ and numerical $M^{\text{num}}_{\text{model}}$ contributions, originating from the turbulence parameterization and the spurious mixing ubiquitous to advection schemes, respectively. All time-averaged quantities are calculated during runtime as thickness-weighted averages (Klingbeil et al. 2019).

b. Idealized two-dimensional Simulations

First we want to apply the relations (32)–(35) to an idealized setup with different forcing. Furthermore, we will investigate approximations of the surface salinity square transport, since the exact value is difficult to observe in high temporal and spatial resolution. The setup estuary is 100 km long, has a resolution of $\mathrm{d}x = \mathrm{d}y = 200$ m with a linearly sloping topography from 15 m depth at the ocean boundary to 5 m where the river is entering the domain, see Fig. 2. In the vertical 60 equally distributed σ-coordinates are used. The open boundary is prescribed with a constant salinity of 30 g/kg, and an M2 tidal amplitude of 0.5 m, if tides are applied. Freshwater transports, river discharge as well as spatially integrated precipitation or evaporation, are all $5.0\,\mathrm{m^3\,s^{-1}}$. The TEF analysis is done during the model run for each baroclinic time step using 250 equidistant salinity bins from 0-40.0 g/kg as proposed by Lorenz et al. (2019). Depending on the experiment, see Tab. 1, different combinations of forcing are applied. The potential temperature is kept constant in these simulations. The different experiment simulations are integrated into a quasi-periodic-state (500 tidal cycles) which is not a real periodic state due to waves forced by the surface flux gradients which propagate through the domain, flushing the high salinity water from the shallow part out of the estuary. Therefore, a long-term average of 100 tidal cycles is carried out to minimize the storage terms in the budget equations, see Fig. 2.

The first experiment A (Tab. 1, Fig. 2a) demonstrates the bottom water formation solely due to evaporation, without any tides. Over the inner half of the domain, constant evaporation is prescribed. Due to the slope of the bathymetry, the salinity increases towards the shallow water, creating a baroclinic pressure gradient. Opposing a barotropic pressure gradient due to the lower surface at the coast is formed. The water of high salinities flows down the slope at the bottom, whereas the water of less salinity enters the evaporation zone, indicated by the arrows in Fig.

2a. As shown in Tab. 2, $M^{\mathrm{tot}}_{\mathrm{model}} = M_e$ holds exactly down to machine accuracy. Evaluating the approximations, M_p shows a small discrepancy to M_e, whereas M_c shows a large deviation, although $(s^2)_{\mathrm{in}} \approx (s_{\mathrm{in}})^2$ and $(s^2)_{\mathrm{out}} \approx (s_{\mathrm{out}})^2$. Therefore, M_{cp} shows also a large deviation. This is due to the overall low mixing in this simulation.

Experiment B adds river discharge, $Q_r = 5\,\mathrm{m^3\,s^{-1}}$, to experiment A, while also shifting the evaporation area further offshore and reducing the area from half the domain to one-third of the domain, keeping the freshwater loss to $-5\,\mathrm{m^3\,s^{-1}}$. Furthermore, a semi-diurnal M2 tide of 0.5 m is prescribed. The resulting salinity distribution, see Fig. 2b, shows a salinity maximum near the left border of the evaporation zone of ~ 37 g/kg, a so-called salt plug which can be often found in tropical estuaries during dry season (Wolanski 1986; Valle-Levinson and Bosley 2003). In the salt plug, the mean velocity is downward. The circulation along the analyzed transect follows an inverse circulation. In addition, due to the river discharge, a classic estuarine circulation is created near the coast, extending into the evaporation zone. There the strong evaporation is able to transform the brackish water to higher salinities than the prescribed 30 g/kg at the open boundary. Compared to the first experiment the mixing is larger by a factor of ~ 20, although $F^{s^2}_{\mathrm{surf}}$ being smaller than in Exp. A. This is due to the net freshwater transport which is ≈ 0 across the transect in this case, compare (35). For this experiment in contrast to Exp. A, the constancy approximation is better than the periodicity approximation.

Experiment C replaces the river discharge with a precipitation region in the coastal area, see Fig. 2c. The results show a similar salinity distribution to Exp. B and the mixing is comparable as well. The major difference to Exp. B is the numerical mixing that has more than doubled.

Experiment D adds river discharge, yielding a net positive freshwater budget adding $5\,\mathrm{m^3\,s^{-1}}$ to the setup. The overall circulation follows a classical estuarine circulation with brackish water leaving the estuary at the surface, while saline water enters at the bottom, see Fig. 2d. The

evaporation is not enough to form a salt plug as shown in Exp. B. and Exp. C. $F^{s^2}_{\text{surf}}$ has the smallest value of all experiments due to the smallest surface salinities, but adding $\sim 1/3$ of the total mixing. The rest of the mixing is due to the classic estuarine mixing as already described by MacCready et al. (2018) and Burchard et al. (2019). For this experiment, the constancy approximation leads to an overestimation, whereas the periodicity approximation leads to an underestimation.

We did some approximations of the exact surface salinity square transport in Tab. 3, which involve the easier to observe quantities: average sea surface salinity and integrated surface fresh water transport for all four experiments. Furthermore, we compare the definition of s_{surf}, eq. (36), to model mean surface salinities. The best approximation for these experiments of the exact $F^{s^2}_{\text{surf}}$, where precipitation and evaporation occur in different regions, is achieved, when separately evaluating the salinity square transports due to evaporation and precipitation, i.e.

$$F^{s^2}_{\text{surf}} \approx -\langle (s_{\text{surf,model,evap}})^2 \rangle Q_{\text{evap}} + \langle (s_{\text{surf,model,precip}})^2 \rangle Q_{\text{precip}}. \tag{47}$$

c. Realistic three-dimensional Simulation

In this section we apply the mixing relations to a realistic model setup of a large, inverse estuary, the Persian Gulf, see Fig. 3.

We repeated the model simulation of Lorenz et al. (2020) for the year 2011 which is a representative year of the exchange flow of the Persian Gulf. The difference between this simulation and the results of Lorenz et al. (2020) is an online TEF analysis as proposed by Lorenz et al. (2019) rather than an offline analysis of hourly output. We used 250 salinity bins from 0 to 50 g/kg. The setup has a horizontal resolution of one nautical mile based on ETOPO1 (Amante and Eakins 2009), a vertical resolution of 40 vertically adaptive coordinates (Hofmeister et al. 2010, 2011; Gräwe et al. 2015), is forced with the NCEP Climate Forecast System Version 2 (CFSv2, Saha et al. 2011) for the atmosphere, and uses HYCOM boundary conditions (Chassignet et al. 2007) with tides from

the Oregon State University Tidal Prediction Software (OTPS, Egbert and Erofeeva 2002). For further details of the setup and the validation of the model, we refer to Lorenz et al. (2020).

The Persian Gulf is a semi-enclosed marginal sea with net freshwater loss due to evaporation. Its exchange flow is, therefore, following an inverse estuarine circulation. Although the evaporation is dominating the freshwater budget, there is an annual river discharge of $\approx 1600\,\mathrm{m^3 s^{-1}}$ with the Shatt Al Arab as the major contributor with $1400\,\mathrm{m^3 s^{-1}}$. The circulation of the Gulf is strongly dependent on the seasonal cycle. In winter the Gulf is well-mixed in most parts due to strong surface cooling, evaporation and winds, and due to its shallowness (mean depth $\approx 40\,\mathrm{m}$). In summer the Gulf is stratified and a general counter-clockwise circulation can be observed (Reynolds 1993; Kämpf and Sadrinasab 2006; Yao and Johns 2010a; Pous et al. 2015).

The seasonality of the forcing translates into the salt mixing, see in Fig. 4, where the vertically integrated, monthly mean χ^s is shown (χ^s includes both physical and numerical contributions). Four persistent salt mixing hotspots can be identified: the western shelf of the Gulf of Oman, the Strait of Hormuz, the river plume of the Shatt Al Arab, and the shallow zone north of Bahrain and west of Qatar.

The western shelf of Oman is the region where the Persian Gulf water stratifies into the Indian Ocean in around 250 m depth. The Gulf water interacts with the steep topography and forms eddies of mesoscale to sub-mesoscale size (L'Hégaret et al. 2015; Vic et al. 2015; Morvan et al. 2019). This process is not sufficiently resolved in the hydrostatic model (Klingbeil and Burchard 2013) and the mixing in our simulation is explained by numerical mixing due to internal pressure gradient errors within the terrain-following coordinates (Shchepetkin and McWilliams 2003).

The hotspot located in the Strait of Hormuz is where the exchange flow is occurring. The high mixing there is related to topographic features in the channel, strong tidal currents and eddy activity (Swift and Bower 2003), which mix the saline outflowing water with the inflowing water. Along

the Iranian coast in the Strait, there is only Indian Ocean water of almost constant salinity (Yao and Johns 2010b; Pous et al. 2015) which explains the low salt mixing values as there are only small salinity gradients. West of the Strait there is more mixing occurring in fall when the buoyancy loss due to the atmospheric forcing occurs. Almost all year there is a line of high mixing which is the front between the Iranian Coastal Jet of Indian Ocean Surface Water and the more saline Persian Gulf water (Kämpf and Sadrinasab 2006).

Two more mixing hotspots are located further inside the Gulf: the Shatt Al Arab river plume area and the area north of Bahrain and west of Qatar. The high mixing values are explained by the strong salinity gradients in those regions. The mixing of the Shatt Al Arab is due to its low salinity river plume which is mixed with ambient more saline water. The mixing of the Bahrain waters is due to hypersaline water of salinities greater than 50 g/kg, formed in the shallow south of Bahrain, mixing with the Gulf water. Despite the high mixing values in this area, it is negligible as a source of outflowing Persian Gulf Water (Lorenz et al. 2020).

Besides these persistent hotspots, seasonality can be observed also in other parts of the Gulf. The vertically integrated salt mixing is smaller in winter (JFM) and summer (JAS) than in spring (AMJ) and fall (OND). The explanation is found in the vertical structure of the Gulf: in winter most regions of the Gulf are well-mixed, i.e. there are no salinity gradients to be mixed. In spring stratification and the basin-wide circulation start to form, which is creating shear and therefore salt mixing. In summer stratification is strongest, inhibiting vertical mixing. In fall the stratification is mixed away due to surface cooling, strong evaporation, and winds, reflected in the high local mixing values.

The surface salinity-square transport is strongest in November and weakest in March, see contours in Fig. 4. From March onwards the transport grows from the shallow coasts offshore until September, before it decreases again starting from the shallows. The shallow areas have higher

surface salinities (Reynolds 1993; Kämpf and Sadrinasab 2006; Yao and Johns 2010a; Pous et al. 2015) which combined with the dry easterly to south-easterly winds cause this spatial distribution.

It is well-known that the outflowing water is formed in late fall and winter in the north-west and southern shallows, which then propagates as a bottom current to the Strait of Hormuz (Reynolds 1993; Kämpf and Sadrinasab 2006; Yao and Johns 2010b; Pous et al. 2015; Lorenz et al. 2020). Lorenz et al. (2020) show that in late July/early August a regime shift in the outflowing water occurs. From February to August, most outflowing water in the Strait of Hormuz, except entrained surface waters, originated in the southern shallows in fall and winter. The propagation time is 2-3 months. From August onwards most outflowing water was formed in the north-west during fall and winter, more than 6 months prior. During this time period, water from the southern shallows is not dense enough to become part of the bottom water (Yao and Johns 2010b). This shift in water masses is reflected in the increase of the salinity of the outflow in early August.

A time series for 2011 of the exchange flow properties across the blue transect in Fig. 3 and Fig. 4 reflects the described seasonality, see Fig. 5. The volume exchange is highly variable on a diurnal time scale. On a weekly time scale, a spring-neap cycle can be observed, especially in the outflow. The inflow is near the surface and therefore effected more by winds. On seasonal time scales, we find that the volume exchange is stronger in the first half of the year, when the well-mixed state transitions into the stratification state, than the second half where increased vertical mixing weakens the exchange flow (Yao and Johns 2010b; Pous et al. 2015; Lorenz et al. 2020). The salinity of the inflow, s_{in}, is $\sim 37\,\mathrm{g/kg}$ whereas the salinity of the outflow follows the seasonal cycle described before, see Fig. 5b. For this simulation, $(s^2)_{\mathrm{in,out}} \approx (s_{\mathrm{in,out}})^2$ and are therefore not shown. The basin-averaged model surface salinity, Fig. 5b, shows a seasonal cycle with the lowest salinities in summer and highest in winter (Kämpf and Sadrinasab 2006). The surface salinity bulk value, s_{surf} defined in eq. (36), is more variable than the model surface salinity and is highest in

summer and lowest in winter, contrary to the model surface salinity. This is due to the weighting of the model surface salinity with the evaporation rate which is most of the year higher near the shallow coasts where the highest surface salinities are found.

The described seasonality of the local salt mixing is visualized more clearly in the time series of the mixing M_e, see Fig. 5d. For this simulation the constancy assumption (33) shows only a small error, since the graphs of the bulk salinities and bulk salinity squares show the same temporal evolution, proving that for this exchange flow $s^2_{\text{in}} \approx (s^2)_{\text{in}}$ and $s^2_{\text{out}} \approx (s^2)_{\text{out}}$. The mixing is highly variable on a diurnal time scale which is expected when the exchange flow in itself is highly variable on that time scale. The volume budget on this time scale is dominated by the storage term δV, see Fig. 5c, as it is one order of magnitude larger than the surface freshwater forcing, Q_{surf}, see Fig. 5e, which in turn is one order of magnitude larger than the river discharge Q_r. The salinity storage, δS, and salinity square storage, δS^2, are proportionally larger than δV (not shown here). Due to the dominating storage terms, we do not show the mixing relations (34) and (35) in Fig. 5d as these assumptions are clearly not valid for a time series of daily values. The highly frequent changes are due to diurnal tides and wind events (Thoppil and Hogan 2009, 2010; Vasou et al. 2020). The wind events are called Shamal which brings dry air to the Gulf leading especially in fall to a great heat loss and high evaporation rates, as seen in November and December Fig. 5e and are investigated in detail by Thoppil and Hogan (2010). On a weekly time scale, the mixing is a result mixing due to surface transport, e.g. the higher mixing in June due to the high $F^{s^2}_{\text{surf}}$ and high mixing periods in October/November, plus of spring-neap variations. As the exchange flow is partly controlled by tides, M is as well (Wang et al. 2017; MacCready et al. 2018). The strongest signal is found to be time scales between 14-17 days, which is the time scale of the spring-neap cycle, but also the length of high/low evaporation over the Gulf, see Fig. 5e. As a measure of stratification and to show its relation to mixing, we used the potential energy relative to the mixed condition Φ (Simpson et al.

1978), see Fig. 5f. It clearly shows the seasonality of the stratification and changes on a bi-weekly time scale, visible more clearly for $\widehat{\Phi}$, which is Φ without the seasonal signal. The changes $\widehat{\Phi}$ are due to mixing. The temporal change of Φ, $\partial_t\Phi$, is well (negatively) correlated to the mixing M, see Fig. 5g where the anomalies of $\partial_t\Phi$, M_e, and $F^{s^2}_{\text{surf}}$ from their respective annual mean values, scaled by their respective standard deviation, are shown. When there is high mixing, the change in Φ is negative and the other way round. Furthermore, Fig. 5g suggests that most of the variation in M_e is due to $F^{s^2}_{\text{surf}}$.

On seasonal time scales the storage terms minimize and the seasonality of the exchange flow and the forcing is visible. The volume storage is orders of magnitude smaller than the freshwater forcing, see Tab. 4. The mixing is low from January to April, increases from May to July, decreases until October before reaching its maximum in November and December. This follows the seasonal exchange flow (Kämpf and Sadrinasab 2006; Yao and Johns 2010b; Pous et al. 2015; Lorenz et al. 2020) modulated with the seasonal surface salinity square transport $F^{s^2}_{\text{surf}}$, see Fig. 5f, which shows strong variations on scale of $\sim$ 16 days. The analyzed time series in this study is too short to investigate longer time scales, but as inter-annual variability exists in the exchange flow of the Gulf (Pous et al. 2015; Lorenz et al. 2020; Campos et al. 2020), the mixing should vary on inter-annual time scales. From the results of Lorenz et al. (2020) we would expect that the amplitude of this time scale should be a lot smaller than the amplitude of the variability of the diurnal and bi-weekly time scales.

The annual mean mixing of the Gulf in this simulation is $M \approx 4.7 \cdot 10^6\,(\mathrm{g/kg})^2\,\mathrm{m}^3\,\mathrm{s}^{-1}$, see Tab. 4 for the exact value. For this simulation the relative errors of the different assumptions are:

$$\begin{aligned}
\text{constancy:} &\quad \left|\frac{M_c - M_e}{M_e}\right| = 1.4‰,\\
\text{periodicity:} &\quad \left|\frac{M_p - M_e}{M_e}\right| = 2.1‰,\\
\text{constancy and periodicity:} &\quad \left|\frac{M_{cp} - M_e}{M_e}\right| = 3.6‰,\\
\text{approximated } F^{s^2}_{\mathrm{surf}}\text{:} &\quad \left|\frac{-\langle s_{\mathrm{surf,model}}\rangle^2 \cdot Q_{\mathrm{surf}} - F^{s^2}_{\mathrm{surf}}}{F^{s^2}_{\mathrm{surf}}}\right| = 1.2‰,\\
\text{constancy, periodicity, and approximated } F^{s^2}_{\mathrm{surf}}\text{:} &\quad \left|\frac{s_{\mathrm{in}} s_{\mathrm{out}} (Q_r + Q_{\mathrm{surf}}) - \langle s_{\mathrm{surf,model}}\rangle^2 \cdot Q_{\mathrm{surf}} - M_e}{M_e}\right| = 2.2‰,
\end{aligned} \tag{48}$$

where $s_{\mathrm{surf,model}}$ is the mean surface salinity of the model. The errors of all mixing relations and also the approximation of the exact $F^{s^2}_{\mathrm{surf}}$ are small. Based on these results the mixing of the Persian Gulf on long time scales can be well approximated by eq. (37), where s_{surf} can be the long-term average surface salinity, instead of the more complex definition (36).

Decomposing (37) into riverine and surface fresh water contributions, we find that both contribute almost equally to the total mixing:

$$M_{\mathrm{river}} = s_{\mathrm{in}} s_{\mathrm{out}} Q_r \approx 2.5 \cdot 10^6\,\mathrm{g/kg}^2\,\mathrm{m}^3\,\mathrm{s}^{-1} \tag{49}$$

$$M_{\mathrm{surface}} = \left(s_{\mathrm{in}} s_{\mathrm{out}} - (s_{\mathrm{surf}})^2\right) Q_{\mathrm{surf}} \approx 2.1 \cdot 10^6\,\mathrm{g/kg}^2\,\mathrm{m}^3\,\mathrm{s}^{-1}. \tag{50}$$

This is an interesting result, as the fresh water forcing due to evaporation is almost a factor of 10 greater than the river discharge. This makes sense, as the gradients associated to these processes are very different: for the surface mixing, the salinity gradients are very small but scaled with a large area. For the mixing due to river runoff, the gradients are large but confined to a small area. Assuming the freshwater has to be mixed approximately to the mean salinity of the Gulf (> 40 g/kg), and following the isohaline theory by Burchard (2020), the long-term averaged mixing due to river run-off integrated over the volume bounded by the river and the 40 g/kg isohaline has to

be $M = (40\,\mathrm{g/kg})^2\, Q_r$. This means that even though river discharge is almost an oder of magnitude smaller than evaporation, the riverine mixing is high due to the large salinity range the freshwater has to be entrained through.

5. Discussion and Conclusions

In this study, we derived a mixing relation that is obeyed by all estuaries since it includes surface freshwater fluxes. Crucial to this relation is the newly introduced integrated surface salinity-squared flux due to precipitation and evaporation, $F^{s^2}_{\mathrm{surf}}$. This term is essential when describing estuaries where the surface freshwater contributions by precipitation and evaporation cannot be neglected or are the main driver of the circulation, like in an inverse estuary. On the other hand, when the river discharge dominates the volume budget, the surface contributions may be neglected, resulting in the mixing relations presented in MacCready et al. (2018) and Burchard et al. (2019).

We showed that the derived mixing relation (32) exactly obeys the mixing directly diagnosed during the model runs, proofing the validity of this relation. We further analyzed the validity of approximated relations: i) assuming constancy, i.e. $(s^2)_{\mathrm{in}} = (s_{\mathrm{in}})^2$ and $(s^2)_{\mathrm{out}} = (s_{\mathrm{out}})^2$, eq. (33), ii) assuming periodicity/long-term averaging, i.e. vanishing storage terms, eq. (34), iii) assuming both at the same time, eq. (35). We performed four two-dimensional idealized simulations with different fresh water forcing, experiments A - D, see Section 4b, to exemplify the mixing relations. From the performed idealized simulations we can not generalize the errors of the assumptions as these seem to be setup-specific. For example, the constancy assumption fails for experiment A (only evaporation) but is a good approximation for experiments B (evaporation + river discharge) and C (evaporation + precipitation). On the other hand, the periodicity assumption is a good approximation when the temporal averaging becomes longer and longer. It is desirable to approximate the newly introduced term for the integrated surface salinity square flux, $F^{s^2}_{\mathrm{surf}}$, as this term requires a high temporal and

spatial resolution of surface salinity, precipitation and evaporation rates. Our results show that it can be approximated with

$$F^{s^2}_{\text{surf}} \approx -(s_{\text{surf}})^2 Q_{\text{surf}}, \tag{51}$$

when either precipitation or evaporation dominate the surface freshwater flux, i.e. $P \gg E$ or $E \gg P$, as it is in experiment A (evaporation, no precipitation), and also the Persian Gulf simulation ($E \gg P$), see Section c. When precipitation and evaporation are of the same magnitude, $E \approx P$, this approximation is not useful as $F_{\text{surf}} \propto Q_{\text{surf}} \approx 0$ in that case. We showed this in experiments C (evaporation + precipitation) and D (evaporation + precipitation + river discharge), where the net surface fresh water flux is zero. For this case evaporation and precipitation have to be evaluated separately with the respective surface salinities, see eq. (47). Based on these findings, we conclude that if the either E or P dominate the surface fresh water budget and if the averaging period is long enough, the mixing can be sufficiently approximated with eq. (37),

$$M \approx M_{cp} = s_{\text{in}} s_{\text{out}} (Q_r + Q_{\text{surf}}) - s^2_{\text{surf,model}} Q_{\text{surf}}, \tag{52}$$

with $s_{\text{surf,model}}$ being the modeled long-term mean, estuary-wide integrated surface salinity instead of the surface salinity bulk value we defined in eq. (36). For the one year Persian Gulf simulation, see Section 4c, the error of eq. (52) to the exact mixing is only 2.2%. For other applications outside modeling, $s_{\text{surf,model}}$ may also be replaced by direct observations of the surface salinity, if available. Relation, eq. (52), further allows to decompose the mixing contributions from river runoff and surface transports. For the Persian Gulf, with a total mixing of $\sim 4.7 \cdot 10^6$ (g/kg)^2 m^3 s^{-1}, the contributions are almost equal, despite the order of magnitude difference in the forcing, $|Q_{\text{surf}}| \approx 10\,|Q_r|$. The distinction of the competition between these two terms could become very useful when working with tropical estuaries, where the freshwater forcing may shift from wet to dry season (Wolanski 1986; Valle-Levinson and Bosley 2003) and with it the mixing contributions.

Acknowledgments. This publication is a contribution to the Training Group Baltic TRANSCOAST GRK 2000 funded by the German Research Foundation which also supported M.L. H.B. and K.K. were supported by the Collaborative Research Centre TRR 181 on Energy Transfer in Atmosphere and Ocean funded by the German Research Foundation (project number 274762653). The numerical simulations were performed with resources provided by the North-German Supercomputing Alliance (HLRN). Most of the analysis work was performed by computers financed by PROSO (FKZ: 03F0779A).

Data availability statement. Please contact one of the authors if you are interested in using the data.

References

Amante, C., and B. W. Eakins, 2009: *ETOPO1 1 arc-minute global relief model: procedures, data sources and analysis*. US Department of Commerce, National Oceanic and Atmospheric Administration, National Environmental Satellite, Data, and Information Service, National Geophysical Data Center, Marine Geology and Geophysics Division Colorado.

Beron-Vera, F., J. Ochoa, and P. Ripa, 1999: A note on boundary conditions for salt and freshwater balances. *Ocean Modelling*, **1 (2-4)**, 111–118.

Burchard, H., 2020: A Universal Law of Estuarine Mixing. *Journal of Physical Oceanography*, **50 (1)**, 81–93, doi:10.1175/JPO-D-19-0014.1.

Burchard, H., and K. Bolding, 2001: Comparative analysis of four second-moment turbulence closure models for the oceanic mixed layer. *Journal of Physical Oceanography*, **31 (8)**, 1943–1968.

Burchard, H., and K. Bolding, 2002: *GETM: A General Estuarine Transport Model; Scientific Documentation*. European Commission, Joint Research Centre, Institute for Environment and Sustainability.

Burchard, H., F. Janssen, K. Bolding, L. Umlauf, and H. Rennau, 2009: Model simulations of dense bottom currents in the western baltic sea. *Continental Shelf Research*, **29 (1)**, 205 – 220, doi:https://doi.org/10.1016/j.csr.2007.09.010, URL http://www.sciencedirect.com/science/article/pii/S0278434307002920, physics of Estuaries and Coastal Seas: Papers from the PECS 2006 Conference.

Burchard, H., X. Lange, K. Klingbeil, and P. MacCready, 2019: Mixing estimates for estuaries. *Journal of Physical Oceanography*, **49 (2)**, 631–648.

Burchard, H., and H. Rennau, 2008: Comparative quantification of physically and numerically induced mixing in ocean models. *Ocean Modelling*, **20 (3)**, 293–311.

Burchard, H., and Coauthors, 2018: The Knudsen theorem and the Total Exchange Flow analysis framework applied to the Baltic Sea. *Progress in Oceanography*, **165**, 268–286.

Campos, E. J., A. L. Gordon, B. Kjerfve, F. Vieira, and G. Cavalcante, 2020: Freshwater budget in the Persian (Arabian) Gulf and exchanges at the Strait of Hormuz. *Plos one*, **15 (5)**, e0233 090.

Chassignet, E. P., H. E. Hurlburt, O. M. Smedstad, G. R. Halliwell, P. J. Hogan, A. J. Wallcraft, R. Baraille, and R. Bleck, 2007: The HYCOM (hybrid coordinate ocean model) data assimilative system. *Journal of Marine Systems*, **65 (1)**, 60–83.

Egbert, G. D., and S. Y. Erofeeva, 2002: Efficient inverse modeling of barotropic ocean tides. *Journal of Atmospheric and Oceanic Technology*, **19 (2)**, 183–204.

Gräwe, U., P. Holtermann, K. Klingbeil, and H. Burchard, 2015: Advantages of vertically adaptive coordinates in numerical models of stratified shelf seas. *Ocean Modelling*, **92**, 56–68.

Hofmeister, R., J.-M. Beckers, and H. Burchard, 2011: Realistic modelling of the exceptional inflows into the central Baltic Sea in 2003 using terrain-following coordinates. *Ocean Modelling*, **39 (3-4)**, 233–247.

Hofmeister, R., H. Burchard, and J.-M. Beckers, 2010: Non-uniform adaptive vertical grids for 3D numerical ocean models. *Ocean Modelling*, **33 (1)**, 70–86.

Kämpf, J., and M. Sadrinasab, 2006: The circulation of the Persian Gulf: a numerical study. *Ocean Science*, **2 (1)**, 27–41.

Klingbeil, K., J. Becherer, E. Schulz, H. E. de Swart, H. M. Schuttelaars, A. Valle-Levinson, and H. Burchard, 2019: Thickness-Weighted Averaging in Tidal Estuaries and the Vertical Distribution of the Eulerian Residual Transport. *Journal of Physical Oceanography*, **49 (7)**, 1809–1826, doi:10.1175/JPO-D-18-0083.1.

Klingbeil, K., and H. Burchard, 2013: Implementation of a direct nonhydrostatic pressure gradient discretisation into a layered ocean model. *Ocean Modelling*, **65**, 64–77.

Klingbeil, K., F. Lemarié, L. Debreu, and H. Burchard, 2018: The numerics of hydrostatic structured-grid coastal ocean models: state of the art and future perspectives. *Ocean Modelling*, **125**, 80–105, doi:10.1016/j.ocemod.2018.01.007.

Klingbeil, K., M. Mohammadi-Aragh, U. Gräwe, and H. Burchard, 2014: Quantification of spurious dissipation and mixing–Discrete variance decay in a Finite-Volume framework. *Ocean Modelling*, **81**, 49–64.

Knudsen, M., 1900: Ein hydrographischer Lehrsatz. *Annalen der Hydrographie und Maritimen Meteorologie*, **28 (7)**, 316–320.

L'Hégaret, P., R. Duarte, X. Carton, C. Vic, D. Ciani, R. Baraille, and S. Corréard, 2015: Mesoscale variability in the Arabian Sea from HYCOM model results and observations: impact on the Persian Gulf Water path. *Ocean Science*, **11 (5)**, 667–693, doi:10.5194/os-11-667-2015, URL https://www.ocean-sci.net/11/667/2015/.

Lorenz, M., K. Klingbeil, and H. Burchard, 2020: Numerical Study of the Exchange Flow of the Persian Gulf Using an Extended Total Exchange Flow Analysis Framework. *Journal of Geophysical Research: Oceans*, **125 (2)**, e2019JC015 527, doi:10.1029/2019JC015527.

Lorenz, M., K. Klingbeil, P. MacCready, and H. Burchard, 2019: Numerical issues of the Total Exchange Flow (TEF) analysis framework for quantifying estuarine circulation. *Ocean Science*, **15 (3)**, 601–614, doi:10.5194/os-15-601-2019.

MacCready, P., 2011: Calculating estuarine exchange flow using isohaline coordinates. *J. Phys. Oceanogr.*, **41 (6)**, 1116–1124.

MacCready, P., W. Rockwell Geyer, and H. Burchard, 2018: Estuarine Exchange Flow is Related to Mixing through the Salinity Variance Budget. *J. Phys. Oceanogr.*, **48**, 1375–1384.

Morvan, M., P. L'Hégaret, X. Carton, J. Gula, C. Vic, C. de Marez, M. Sokolovskiy, and K. Koshel, 2019: The life cycle of submesoscale eddies generated by topographic interactions. *Ocean Science*, **15 (6)**, 1531–1543, doi:10.5194/os-15-1531-2019, URL https://www.ocean-sci.net/15/1531/2019/.

Nash, J. D., and J. N. Moum, 2002: Microstructure Estimates of Turbulent Salinity Flux and the Dissipation Spectrum of Salinity. *Journal of Physical Oceanography*, **32 (8)**, 2312–2333, doi:10.1175/1520-0485(2002)032<2312:MEOTSF>2.0.CO;2.

Nurser, A. J. G., and S. M. Griffies, 2019: Relating the Diffusive Salt Flux just below the Ocean Surface to Boundary Freshwater and Salt Fluxes. *Journal of Physical Oceanography*, **49 (9)**, 2365–2376, doi:10.1175/JPO-D-19-0037.1, URL https://doi.org/10.1175/JPO-D-19-0037.1.

Pietrzak, J., 1998: The use of TVD limiters for forward-in-time upstream-biased advection schemes in ocean modeling. *Monthly Weather Review*, **126 (3)**, 812–830.

Pous, S., P. Lazure, and X. Carton, 2015: A model of the general circulation in the Persian Gulf and in the Strait of Hormuz: Intraseasonal to interannual variability. *Continental Shelf Research*, **94**, 55–70.

Reynolds, R. M., 1993: Physical oceanography of the Gulf, Strait of Hormuz, and the Gulf of Oman - Results from the Mt Mitchell expedition. *Marine Pollution Bulletin*, **27**, 35–59.

Saha, S., and Coauthors, 2011: NCEP Climate Forecast System Version 2 (CFSv2) Selected Hourly Time-Series Products. Research Data Archive at the National Center for Atmospheric Research, Computational and Information Systems Laboratory, Boulder CO, URL https://doi.org/10.5065/D6N877VB.

Shchepetkin, A. F., and J. C. McWilliams, 2003: A method for computing horizontal pressure-gradient force in an oceanic model with a nonaligned vertical coordinate. *Journal of Geophysical Research: Oceans*, **108 (C3)**.

Simpson, J., C. Allen, and N. Morris, 1978: Fronts on the continental shelf. *Journal of Geophysical Research: Oceans*, **83 (C9)**, 4607–4614.

Stern, M. E., 1968: T-S gradients on the micro-scale. *Deep Sea Research and Oceanographic Abstracts*, **15 (3)**, 245 – 250, doi:https://doi.org/10.1016/0011-7471(68)90001-6.

Swift, S. A., and A. S. Bower, 2003: Formation and circulation of dense water in the Persian/Arabian Gulf. *Journal of Geophysical Research: Oceans*, **108 (C1)**.

Thoppil, P. G., and P. J. Hogan, 2009: On the mechanisms of episodic salinity outflow events in the Strait of Hormuz. *Journal of Physical Oceanography*, **39 (6)**, 1340–1360.

Thoppil, P. G., and P. J. Hogan, 2010: Persian gulf response to a wintertime shamal wind event. *Deep Sea Research Part I: Oceanographic Research Papers*, **57 (8)**, 946–955.

Valle-Levinson, A., 2010: Definition and classification of estuaries. *Contemporary Issues in Estuarine Physics*, doi:10.1017/CBO9780511676567.002.

Valle-Levinson, A., and K. T. Bosley, 2003: Reversing circulation patterns in a tropical estuary. *Journal of Geophysical Research: Oceans*, doi:10.1029/2003jc001786.

Vasou, P., V. Vervatis, G. Krokos, I. Hoteit, and S. Sofianos, 2020: Variability of water exchanges through the Strait of Hormuz. Springer, doi:10.1007/s10236-020-01384-2.

Vic, C., G. Roullet, X. Capet, X. Carton, M. J. Molemaker, and J. Gula, 2015: Eddy-topography interactions and the fate of the Persian Gulf Outflow. *Journal of Geophysical Research: Oceans*, **120 (10)**, 6700–6717.

Wang, T., W. R. Geyer, and P. MacCready, 2017: Total exchange flow, entrainment, and diffusive salt flux in estuaries. *Journal of Physical Oceanography*, **47 (5)**, 1205–1220.

Warner, J. C., W. R. Geyer, and J. A. Lerczak, 2005: Numerical modeling of an estuary: A comprehensive skill assessment. *Journal of Geophysical Research: Oceans*, **110 (C5)**.

572 Warren, B. A., 2009: Note on the Vertical Velocity and Diffusive Salt Flux Induced by
573 Evaporation and Precipitation. *Journal of Physical Oceanography*, **39 (10)**, 2680–2682, doi:
574 10.1175/2009JPO4069.1, URL https://doi.org/10.1175/2009JPO4069.1.

575 Wolanski, E., 1986: An evaporation-driven salinity maximum zone in Australian tropical estuaries.
576 *Estuarine, Coastal and Shelf Science*, doi:10.1016/0272-7714(86)90065-X.

577 Yao, F., and W. E. Johns, 2010a: A HYCOM modeling study of the Persian Gulf: 1. Model
578 configurations and surface circulation. *Journal of Geophysical Research: Oceans*, **115 (C11)**.

579 Yao, F., and W. E. Johns, 2010b: A HYCOM modeling study of the Persian Gulf: 2. Formation
580 and export of Persian Gulf Water. *Journal of Geophysical Research: Oceans*, **115 (C11)**.

LIST OF TABLES

Table 1. Overview of four idealized model experiments of different combinations of freshwater fluxes. Q_{evap} and Q_{precip} are the area integrated evaporation and precipitation velocities E and P. 33

Table 2. Results of the mixing analysis for the idealized model experiments listing the variables needed to compute the mixing with eq. (32)-(35). In the model mixing is directly diagnosed ($M^{\text{tot}}_{\text{model}}$) and split into physical and numerical contributions ($M^{\text{phy}}_{\text{model}}$, $M^{\text{num}}_{\text{model}}$) to compare to the relations (Klingbeil et al. 2014). Although we only show rounded values, $M^{\text{tot}}_{\text{model}}$ and M_e equal to machine accuracy. . . . 34

Table 3. Comparison of sea surface salinity and $F^{s^2}_{\text{surf}}$ to approximations using tidal averaged model results inside the estuary, i.e. right of the transects shown in Fig. 2. $\langle s_{\text{surf,model,evap}} \rangle$ and $\langle s_{\text{surf,model,precip}} \rangle$ are the respective mean surface salinities of the evaporation/precipitation zones, whereas $\langle s_{\text{surf,model}} \rangle$ is the mean surface salinity of the whole estuary. 35

Table 4. Results of the mixing analysis for the Persian Gulf in 2011: all variables needed to compute the mixing with eq. (32)-(35) are listed below. 36

597 TABLE 1. Overview of four idealized model experiments of different combinations of freshwater fluxes. Q_{evap}
598 and Q_{precip} are the area integrated evaporation and precipitation velocities E and P.

Experiment	Q_r / $m^3\ s^{-1}$	Q_{evap} / $m^3\ s^{-1}$	Q_{precip} / $m^3\ s^{-1}$	M_2 amplitude / m
A	0.0	-5.0	0.0	0.0
B	5.0	-5.0	0.0	0.5
C	0.0	-5.0	5.0	0.5
D	5.0	-5.0	5.0	0.5

599 TABLE 2. Results of the mixing analysis for the idealized model experiments listing the variables needed to
600 compute the mixing with eq. (32)-(35). In the model mixing is directly diagnosed ($M^{\mathrm{tot}}_{\mathrm{model}}$) and split into physical
601 and numerical contributions ($M^{\mathrm{phy}}_{\mathrm{model}}$, $M^{\mathrm{num}}_{\mathrm{model}}$) to compare to the relations (Klingbeil et al. 2014). Although we
602 only show rounded values, $M^{\mathrm{tot}}_{\mathrm{model}}$ and M_e equal to machine accuracy.

	Exp. A	Exp. B	Exp. C	Exp. D
s_{in} / (g/kg)	30.00	36.63	36.57	24.04
s_{out} / (g/kg)	32.67	37.34	37.12	13.98
$((s^2)_{\mathrm{in}})^{1/2}$ / (g/kg)	30.00	36.63	36.58	24.05
$((s^2)_{\mathrm{out}})^{1/2}$ / (g/kg)	32.73	37.38	37.18	15.24
δV / $\mathrm{m^3\ s^{-1}}$	0.00	0.36	0.34	0.30
δS / (g/kg) $\mathrm{m^3\ s^{-1}}$	1.18	5.55	6.94	8.48
δS^2 / $(\mathrm{g/kg})^2\ \mathrm{m^3\ s^{-1}}$	65.3	237	339.3	-35.16
$F^{s^2}_{\mathrm{surf}}$ / $(\mathrm{g/kg})^2\ \mathrm{m^3\ s^{-1}}$	5279	3982	3786	946.8
M_e / $(\mathrm{g/kg})^2\ \mathrm{m^3\ s^{-1}}$	212.3	3646	3464	2445
M_c / $(\mathrm{g/kg})^2\ \mathrm{m^3\ s^{-1}}$	403.9	3678	3495	2884
M_p / $(\mathrm{g/kg})^2\ \mathrm{m^3\ s^{-1}}$	203.6	3982	3786	2193
M_{cp} / $(\mathrm{g/kg})^2\ \mathrm{m^3\ s^{-1}}$	396.7	3982	3786	2628
$M^{\mathrm{tot}}_{\mathrm{model}}$ / $(\mathrm{g/kg})^2\ \mathrm{m^3\ s^{-1}}$	212.3	3646	3464	2445
$M^{\mathrm{phy}}_{\mathrm{model}}$ / $(\mathrm{g/kg})^2\ \mathrm{m^3\ s^{-1}}$	103.5	3438	2911	2413
$M^{\mathrm{num}}_{\mathrm{model}}$ / $(\mathrm{g/kg})^2\ \mathrm{m^3\ s^{-1}}$	108.8	208	553	32

603 TABLE 3. Comparison of sea surface salinity and $F^{s^2}_{\text{surf}}$ to approximations using tidal averaged model results
604 inside the estuary, i.e. right of the transects shown in Fig. 2. $\langle s_{\text{surf,model,evap}} \rangle$ and $\langle s_{\text{surf,model,precip}} \rangle$ are the respective
605 mean surface salinities of the evaporation/precipitation zones, whereas $\langle s_{\text{surf,model}} \rangle$ is the mean surface salinity
606 of the whole estuary.

	Exp. A	Exp. B	Exp. C	Exp. D
$F^{s^2}_{\text{surf}}$ / (g/kg)^2 m^3 s^{-1}	5279	3982	3786	946.8
s_{surf} with eq. (36) / (g/kg)	32.56	28.22	∞	∞
$\langle s_{\text{surf,model}} \rangle$ / (g/kg)	32.49	17.62	14.99	6.63
$\langle s_{\text{surf,model,evap}} \rangle$ / (g/kg)	32.49	27.19	26.89	12.31
$\langle s_{\text{surf,model,precip}} \rangle$ / (g/kg)	-	-	3.10	0.95
$-\langle s_{\text{surf,model}} \rangle^2 \cdot Q_{\text{surf}}$ / (g/kg)^2 m^3 s^{-1}	5258	1552	0.00	0.00
$-\langle s_{\text{surf,model,evap}} \rangle^2 \cdot Q_{\text{evap}}$ / (g/kg)^2 m^3 s^{-1}	5258	3697	3614	757.6
$-\langle s_{\text{surf,model,precip}} \rangle^2 \cdot Q_{\text{precip}}$ / (g/kg)^2 m^3 s^{-1}	-	-	-48.00	-4.51
$-\langle (s_{\text{surf,model}})^2 \rangle \cdot Q_{\text{surf}}$ / (g/kg)^2 m^3 s^{-1}	5276	2169	0.00	0.00
$-\langle (s_{\text{surf,model,evap}})^2 \rangle \cdot Q_{\text{evap}}$ / (g/kg)^2 m^3 s^{-1}	5276	3967	3914	958.4
$-\langle (s_{\text{surf,model,precip}})^2 \rangle \cdot Q_{\text{precip}}$ / (g/kg)^2 m^3 s^{-1}	-	-	-137.1	-17.86

607 TABLE 4. Results of the mixing analysis for the Persian Gulf in 2011: all variables needed to compute the
608 mixing with eq. (32)-(35) are listed below.

variable / unit	value
s_{in} / (g/kg)	36.98
s_{out} / (g/kg)	39.93
$((s^2)_{\mathrm{in}})^{1/2}$ / (g/kg)	36.98
$((s^2)_{\mathrm{out}})^{1/2}$ / (g/kg)	39.93
s_{surf} with eq. (36) / (g/kg)	40.68
$\langle s_{\mathrm{surf,model}} \rangle$ / (g/kg)	40.43
δV / $\mathrm{m}^3\,\mathrm{s}^{-1}$	-62
δS / (g/kg) $\mathrm{m}^3\,\mathrm{s}^{-1}$	-9887
δS^2 / $(\mathrm{g/kg})^2\,\mathrm{m}^3\,\mathrm{s}^{-1}$	-568866
Q_r / $\mathrm{m}^3\,\mathrm{s}^{-1}$	1691
Q_{surf} / $\mathrm{m}^3\,\mathrm{s}^{-1}$	-13340
$F^{s^2}_{\mathrm{surf}}$ / $(\mathrm{g/kg})^2\,\mathrm{m}^3\,\mathrm{s}^{-1}$	22080406
$-\langle s_{\mathrm{surf,model}} \rangle^2 \cdot Q_{\mathrm{surf}}$ / $(\mathrm{g/kg})^2\,\mathrm{m}^3\,\mathrm{s}^{-1}$	21810458
M_e / $(\mathrm{g/kg})^2\,\mathrm{m}^3\,\mathrm{s}^{-1}$	4714700
M_c / $(\mathrm{g/kg})^2\,\mathrm{m}^3\,\mathrm{s}^{-1}$	4782332
M_p / $(\mathrm{g/kg})^2\,\mathrm{m}^3\,\mathrm{s}^{-1}$	4815712
M_{cp} / $(\mathrm{g/kg})^2\,\mathrm{m}^3\,\mathrm{s}^{-1}$	4882160
$M^{\mathrm{tot}}_{\mathrm{model}}$ / $(\mathrm{g/kg})^2\,\mathrm{m}^3\,\mathrm{s}^{-1}$	4714700
$M^{\mathrm{phy}}_{\mathrm{model}}$ / $(\mathrm{g/kg})^2\,\mathrm{m}^3\,\mathrm{s}^{-1}$	4309199
$M^{\mathrm{num}}_{\mathrm{model}}$ / $(\mathrm{g/kg})^2\,\mathrm{m}^3\,\mathrm{s}^{-1}$	405501

LIST OF FIGURES

Fig. 1. Descriptive box model of a steady state, instantaneous process of an inverse estuarine circulation due to evaporation: a) The two-layered box with two well-mixed layers, a surface and bottom layer with different salinities. b) The fresh water volume, $\Delta t Q_{\text{surf}}$, $Q_{\text{surf}} < 0$, is removed from V_{surf} which reduces the volume of the surface layer to $V_{\text{surf}} + \Delta t Q_{\text{surf}}$. The salt left behind by the evaporation process is mixed into the reduced surface volume, increasing the salinity s_{surf} to s^*_{surf}. c) The exchange flow is added. Its net volume flux replaces the evaporated fresh water. The inflow Q_{in} of salinity s_{in} enters the estuary and V_{b} is reduced by the outflow Q_{out} to $V_{\text{b}} + \Delta t Q_{\text{out}}$. The salt content is not changed by the exchange flow. The state a) is the long-term average result of states b) and c). 38

Fig. 2. Idealized simulations: long-term average states of salinity distribution and residual circulation (w scaled with the local aspect ratio) averaged over 100 tidal cycles for different freshwater forcing: a) evaporation prescribed over half the domain, b) evaporation prescribed over one third in the middle of the domain with river discharge, c) evaporation over one third in the middle of the domain with precipitation over the right third of the domain, d) evaporation over one third in the middle of the domain with precipitation over the right third of the domain with additional river discharge, see Tab. 1 for more details. The dashed lines mark the transects that are evaluated to compute the mixing inside the estuary, i.e. right of the transect. The results of this evaluation are listed in Tab. 2. 39

Fig. 3. Bathymetry and used model domain of the Gulf: the shallow north-west and southern regions are bounded by a trench in the north, which is deepening towards the Strait of Hormuz. Outside the Strait of Hormuz, the depth is increasing to $\sim 2000\,\text{m}$ (note the non-uniform color scale). The blue line denotes the transect across which the exchange flow is analyzed. . 40

Fig. 4. Monthly mean mixing map of the Gulf for 2011: color coded is the vertically integrated local salt mixing, χ^s, see eq. (12). The black contour shows the surface salinity-square flux in $10^{-6}\,(\text{g/kg})^2\,\text{m}\,\text{s}^{-1}$, see also eq. (24). The transect across the exchange flow analysis is carried out is shown in blue. 41

Fig. 5. Time series of the daily exchange flow and mixing quantities for 2011: a) bulk volume transport values, b) bulk salinities of the exchange flow and surface salinities, eq. (36) and model salinity, c) volume storage δV, d) mixing computed from the exchange flow bulk values using relation (32) and (33), and physical, numerical mixing of the model, e) surface freshwater flux Q_{surf} and surface salinity squared flux $F^{s^2}_{\text{surf}}$, f) potential energy relative to the mixed condition Φ (Simpson et al. 1978) and Φ without the seasonal signal, $\widehat{\Phi}$, and g) the temporal change of Φ, $\partial_t \Phi$, M_e and $F^{s^2}_{\text{surf}}$ (anomaly from the annual mean and scaled with the respective standard deviation). The thick lines are smoothed with a 1-week running mean filter. Note the different scaling of the y-axis in each panel. If there is a blank in the time series, e.g. in b), then the respective inflow or outflow is zero and the bulk values are zero as well. Further note that the bulk salinity squares are very closely following the squared bulk salinities. The annual results of the mixing relation are listed in Tab. 4. 43

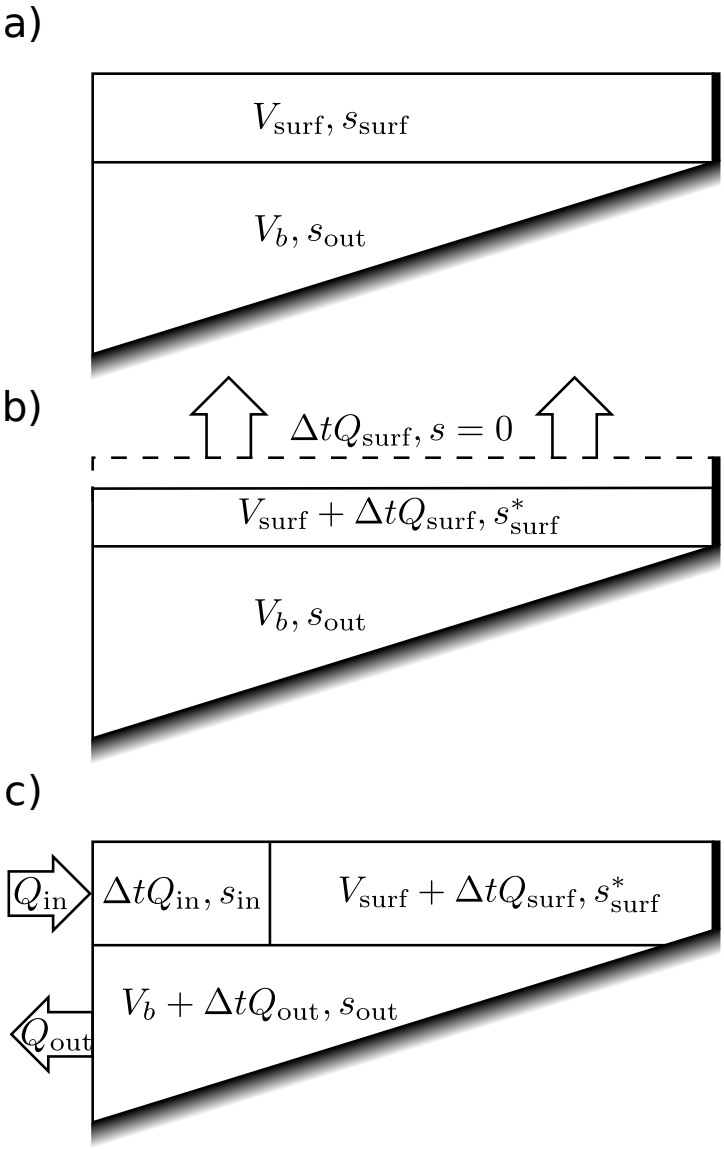

FIG. 1. Descriptive box model of a steady state, instantaneous process of an inverse estuarine circulation due to evaporation: a) The two-layered box with two well-mixed layers, a surface and bottom layer with different salinities. b) The fresh water volume, $\Delta t Q_{\mathrm{surf}}$, $Q_{\mathrm{surf}} < 0$, is removed from V_{surf} which reduces the volume of the surface layer to $V_{\mathrm{surf}} + \Delta t Q_{\mathrm{surf}}$. The salt left behind by the evaporation process is mixed into the reduced surface volume, increasing the salinity s_{surf} to s^*_{surf}. c) The exchange flow is added. Its net volume flux replaces the evaporated fresh water. The inflow Q_{in} of salinity s_{in} enters the estuary and V_{b} is reduced by the outflow Q_{out} to $V_{\mathrm{b}} + \Delta t Q_{\mathrm{out}}$. The salt content is not changed by the exchange flow. The state a) is the long-term average result of states b) and c).

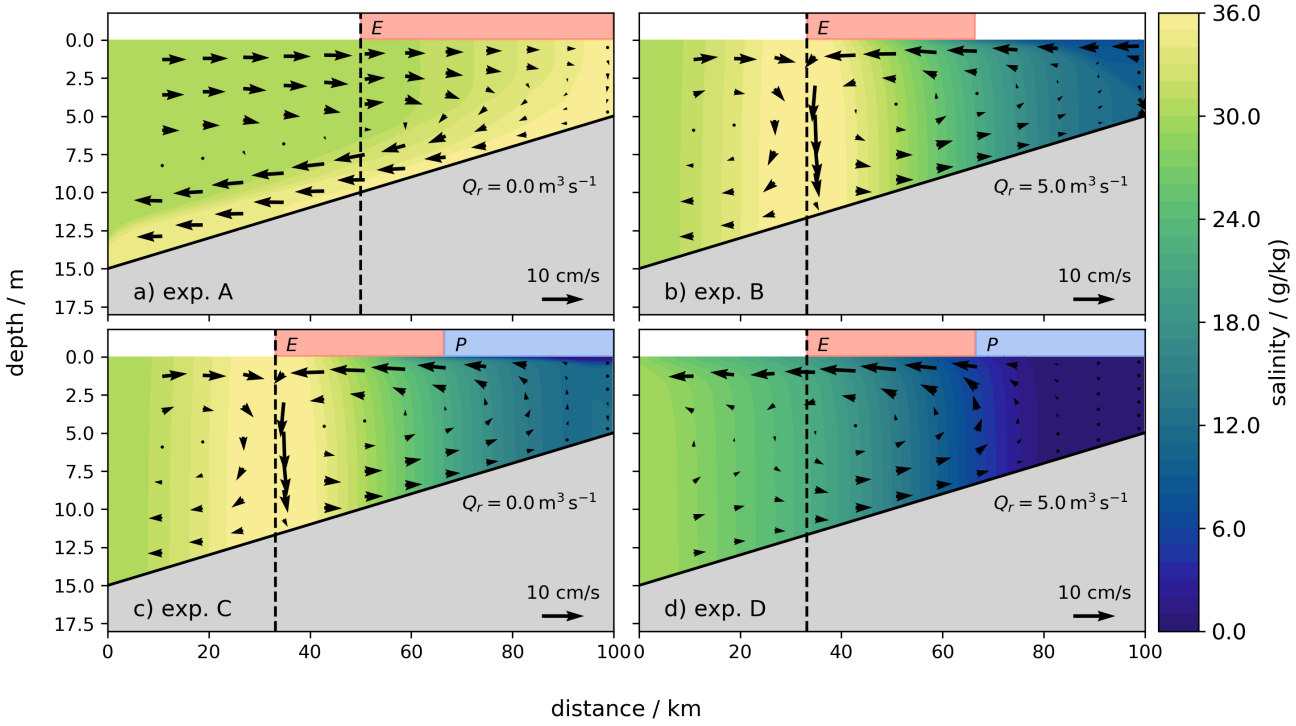

656 FIG. 2. Idealized simulations: long-term average states of salinity distribution and residual circulation (w
657 scaled with the local aspect ratio) averaged over 100 tidal cycles for different freshwater forcing: a) evaporation
658 prescribed over half the domain, b) evaporation prescribed over one third in the middle of the domain with river
659 discharge, c) evaporation over one third in the middle of the domain with precipitation over the right third of the
660 domain, d) evaporation over one third in the middle of the domain with precipitation over the right third of the
661 domain with additional river discharge, see Tab. 1 for more details. The dashed lines mark the transects that are
662 evaluated to compute the mixing inside the estuary, i.e. right of the transect. The results of this evaluation are
663 listed in Tab. 2.

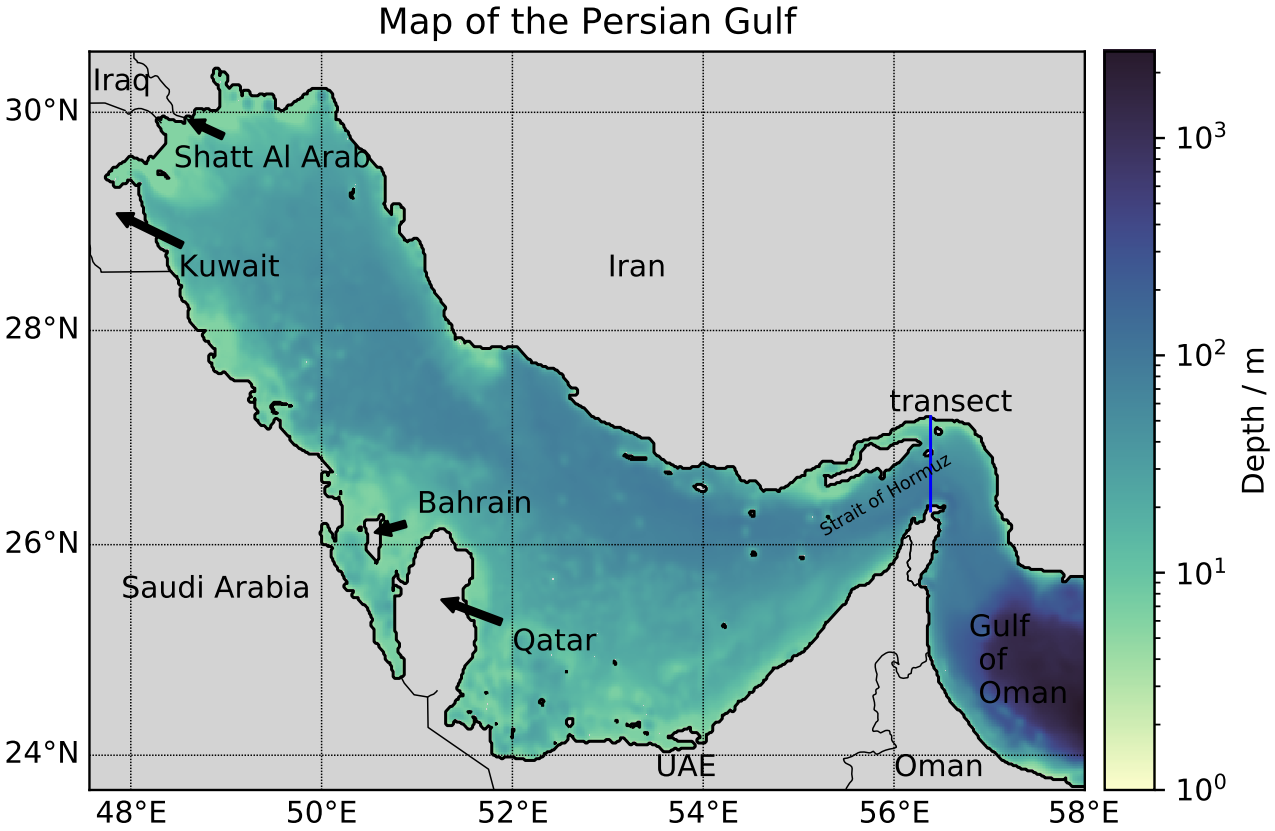

664 FIG. 3. Bathymetry and used model domain of the Gulf: the shallow north-west and southern regions are
665 bounded by a trench in the north, which is deepening towards the Strait of Hormuz. Outside the Strait of Hormuz,
666 the depth is increasing to ~ 2000 m (note the non-uniform color scale). The blue line denotes the transect across
667 which the exchange flow is analyzed.

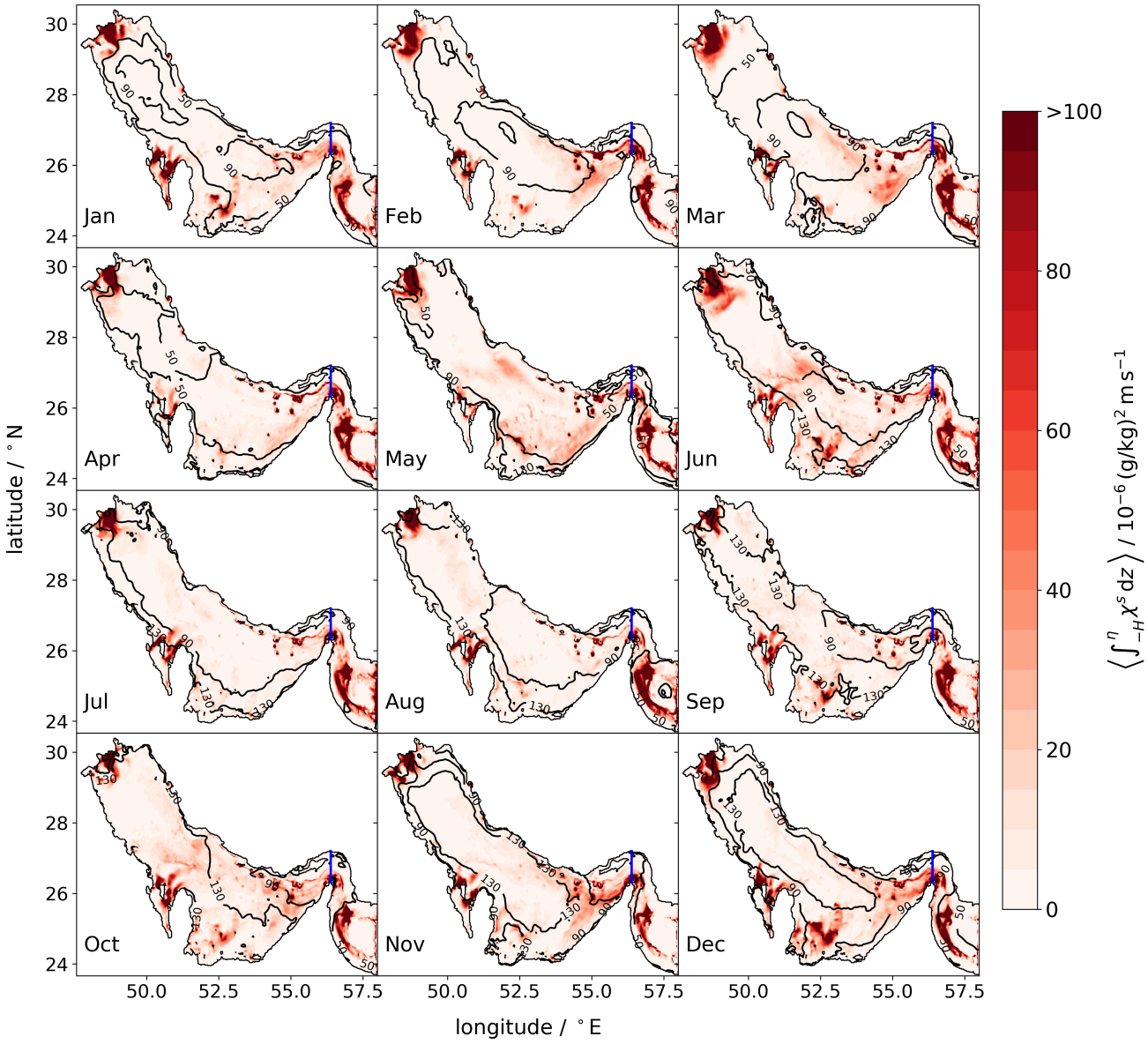

668 FIG. 4. Monthly mean mixing map of the Gulf for 2011: color coded is the vertically integrated local salt
669 mixing, χ^s, see eq. (12). The black contour shows the surface salinity-square flux in 10^{-6} (g/kg)^2 m s^{-1}, see also
670 eq. (24). The transect across the exchange flow analysis is carried out is shown in blue.

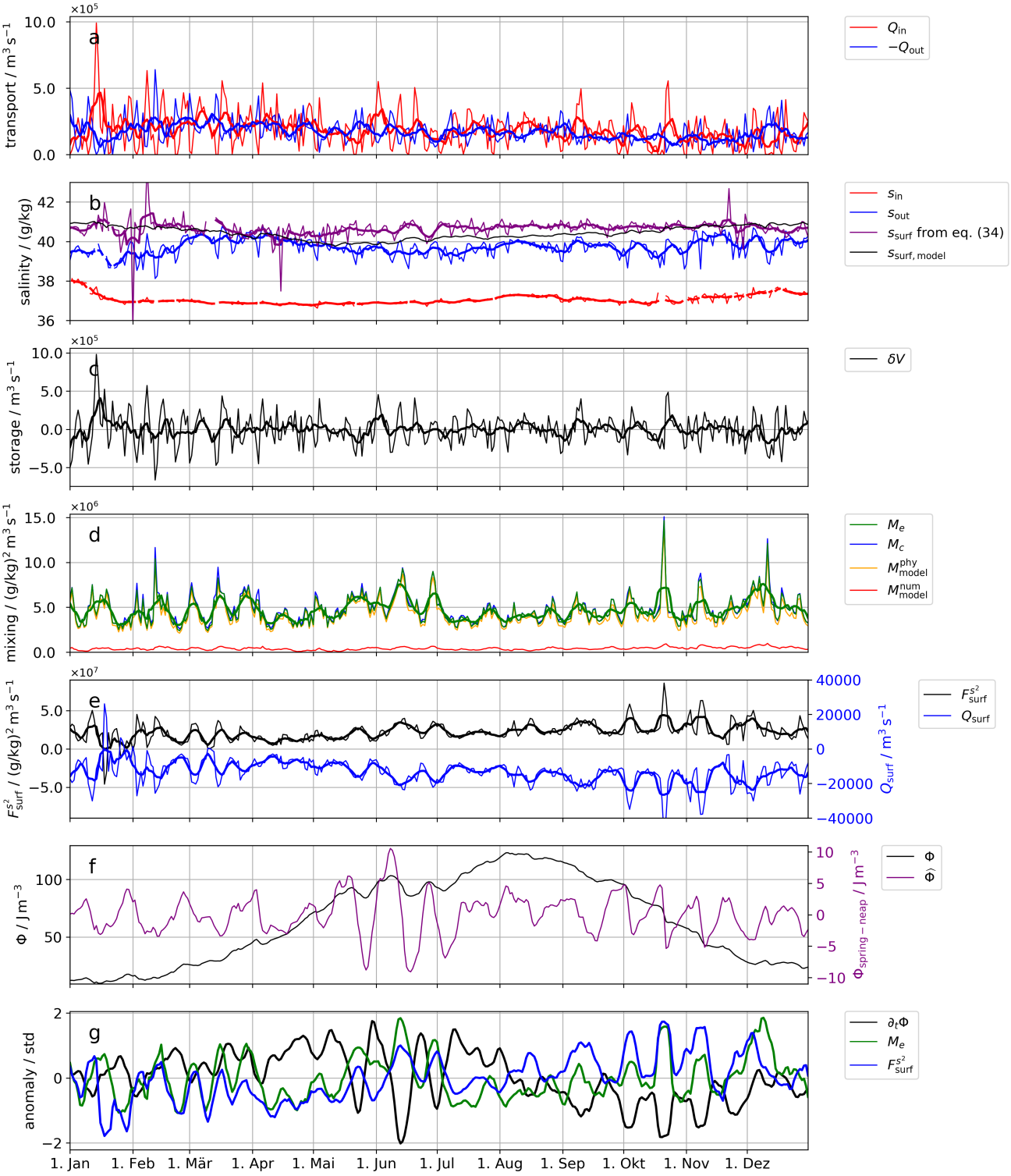
a
transport / m³ s⁻¹
×10⁵
10.0
5.0
0.0
Q_{in}
$-Q_{out}$
b
salinity / (g/kg)
42
40
38
36
s_{in}
s_{out}
s_{surf} from eq. (34)
$s_{surf,\,model}$
c
storage / m³ s⁻¹
×10⁵
10.0
5.0
0.0
−5.0
δV
d
mixing / (g/kg)² m³ s⁻¹
×10⁶
15.0
10.0
5.0
0.0
M_e
M_c
M^{phy}_{model}
M^{num}_{model}
e
$F^{s^2}_{surf}$ / (g/kg)² m³ s⁻¹
×10⁷
5.0
0.0
−5.0
40000
20000
0
−20000
−40000
Q_{surf} / m³ s⁻¹
$F^{s^2}_{surf}$
Q_{surf}
f
Φ / J m⁻³
100
50
10
5
0
−5
−10
$\Phi_{spring-neap}$ / J m⁻³
Φ
⟨Φ⟩
g
anomaly / std
2
0
−2
$\partial_t\Phi$
M_e
$F^{s^2}_{surf}$
1. Jan
1. Feb
1. Mär
1. Apr
1. Mai
1. Jun
1. Jul
1. Aug
1. Sep
1. Okt
1. Nov
1. Dez

FIG. 5. Time series of the daily exchange flow and mixing quantities for 2011: a) bulk volume transport values, b) bulk salinities of the exchange flow and surface salinities, eq. (36) and model salinity, c) volume storage δV, d) mixing computed from the exchange flow bulk values using relation (32) and (33), and physical, numerical mixing of the model, e) surface freshwater flux Q_{surf} and surface salinity squared flux $F^{s^2}_{\text{surf}}$, f) potential energy relative to the mixed condition Φ (Simpson et al. 1978) and Φ without the seasonal signal, $\widehat{\Phi}$, and g) the temporal change of Φ, $\partial_t \Phi$, M_e and $F^{s^2}_{\text{surf}}$ (anomaly from the annual mean and scaled with the respective standard deviation). The thick lines are smoothed with a 1-week running mean filter. Note the different scaling of the y-axis in each panel. If there is a blank in the time series, e.g. in b), then the respective inflow or outflow is zero and the bulk values are zero as well. Further note that the bulk salinity squares are very closely following the squared bulk salinities. The annual results of the mixing relation are listed in Tab. 4.